Discrete Crack Dynamics

and its Application to Study Fracture in Polycrystalline Diamond



Mahdieh T. Ebrahimi

Department of Physics
Imperial College London

This dissertation is submitted for the degree of
Doctor of Philosophy and Diploma of Imperial College

February 2018

Acknowledgements

I would like to express my gratitude to my supervisors, Prof. Daniele Dini, Dr. Daniel Balint and Prof. Adrian Sutton, for all their supports, guidances, encouragements, and stimulating discussions throughout the duration of this project which made it possible to bring the project to an end.

I would also like to acknowledge the EPSRC Centre for Doctoral Training in Theory and Simulation of Materials at Imperial College London and Element Six co-funding the project via the award of a Ph.D. studentship.

This thesis work is dedicated to everyone in my family especially to my husband Ali for his support and encouragement. I am truly thankful for having you in my life. This work is also dedicated to my parents, who have always loved me unconditionally and believed in me in my moment of weakness.

Declaration

I hereby declare that except where specific reference is made to the work of others, the contents of this dissertation are original and have not been submitted in whole or in part for consideration for any other degree or qualification in this, or any other university. This dissertation is my own work and contains nothing which is the outcome of work done in collaboration with others, except as specified in the text and Acknowledgements.

Mahdieh T. Ebrahimi
February 2018

©

"The copyright of this thesis rests with the author and is made available under a Creative Commons Attribution Non-Commercial No Derivatives licence. Researchers are free to copy, distribute or transmit the thesis on the condition that they attribute it, that they do not use it for commercial purposes and that they do not alter, transform or build upon it. For any reuse or redistribution, researchers must make clear to others the licence terms of this work"

Abstract

Mechanical properties of polycrystalline materials are affected by the microstructure of the components. All cracks and inclusions present in a body subjected to external forces cannot act independently even if their density is relatively low. The elastic fields generated by the presence of each crack and inclusion extends throughout the system. Thus, not only the external load but also the neighbouring cracks and inclusions determine the stress experienced by each individual defect. In this work, the Multipole Method (MM) is used to simulate the many-body self-consistent problem of interacting elliptical micro-cracks and inclusions in an unbounded solid. Finite-sized problem can be solved using the superposition scheme and incorporating the complex variable boundary element method.

A criterion is employed to determine the crack propagation path based on the stress distribution; the evolution of individual micro-cracks and their interactions with existing cracks and inclusions is then predicted using what we coin the Discrete Crack Dynamics (DCD) method. DCD is fast (semi-analytical) and particularly suitable for the simulation of evolving low-speed crack networks in brittle or quasi-brittle materials.

Furthermore, effects of the grain boundary strength and the interfacial strength of inclusions on the deflection of crack paths were studied. Results of each step of the analysis are validated against finite element analysis predictions and previously published experimental data and modelling results. New results for propagating cracks interacting with hard and soft inclusions in finite bodies are presented.

Finally, the methodology developed by the author is used to determine the effect of residual stresses in general, and the residual thermal stresses associated with the second phase inclusion in particular, on the crack propagation path. The study is then extended to characterise the influence of residual stresses and thermal stresses on crack propagation in PCD structures.

Keywords: Crack-Inclusion interactions, Multipole Method, Discrete crack dynamics, Grain boundary, Interface strength, Residual stress, Thermal stress

Table of contents

List of figures **xv**

List of tables **xxv**

Abbreviations **xxvii**

1 Introduction **1**
1.1 Thesis Structure 2
1.2 Research Objectives 3

2 Background And Literature Review **5**
2.1 Background 5
2.1.1 Diamond 5
2.1.2 Polycrystalline Diamond 7
2.1.3 Fracture And Failure of PCDs 9
2.2 Background In Continuum Mechanics 10
2.2.1 Linear Elastic Fracture Mechanics (LEFM) 10
2.2.2 Mixed Mode Fracture 13
2.3 Predicting Crack Trajectories in Brittle Materials 13
2.3.1 Methods to Study Inclusions and Cracks Interactions 14
2.3.2 Method to Study Crack Propagation 28
2.4 New Methodology to Study Media Containing Cracks and Inclusions 29

3 Interaction Between Elements Of A System **31**
3.1 Introduction 31
3.2 Conformal Mapping And Complex Variable Analysis 31
3.2.1 Conformal Mapping From Elliptical To Cartesian Coordinate Systems 32
3.3 In-Plane Elasticity Problem 33
3.4 Solid With Elliptical Inclusions And Cracks 34

3.4.1 Single Elliptic Inclusion In An Infinite Plane 34
3.4.2 Finite Array Of Aligned Inclusions 38
3.5 Finite Array Of Arbitrary Oriented Inclusions 42
3.5.1 Method 43
3.5.2 Numerical Results 46
3.5.3 Total Stress Fields Of The System 48
3.5.4 Stress Intensity Factors (SIFs) 50

4 Crack Propagation: Discrete Crack Dynamic 53
4.1 Introduction 53
4.2 Discrete Crack Dynamics (DCD) 54
4.2.1 Crack Propagation Criteria 54
4.2.2 Crack Propagation: Length Scale 59
4.2.3 New Elliptical Micro-Crack Coordinate 61
4.3 Stress Intensity Factors of a Kinked Crack 62
4.3.1 Correction to the Problem of Two Cracks (Kinked Cracks) 64
4.4 Crack Propagation: Simulation 69
4.4.1 Crack Propagation: Simulation Steps 69
4.5 Finite-Size Problems 75
4.5.1 The Complex Variable Boundary Element Method 76
4.6 Numerical Results 82

5 Interface and Grain Boundary Effects 87
5.1 Introduction 87
5.2 Interface Effect 89
5.2.1 Crack Propagation At The Interface 90
5.2.2 New Deflection Mechanism 91
5.3 Numerical Study of Problems at the Interface 93
5.3.1 Crack Propagation And Grain Boundary 94
5.3.2 Crack Propagation And Inclusions 96
5.3.3 Crack Propagation, Inclusion And Grain Boundary 100
5.4 Toughening Mechanism 106
5.4.1 Array of Soft Inclusions on a Grain Boundary 107
5.4.2 Array of Hard Inclusions on a Grain Boundary 111
5.4.3 Array Of Inclusions On A Grain Boundary; General Case 112
5.5 Grain Boundary Engineering of Polycrystalline Diamond 112
5.5.1 Effect Of Alloying Elements 116

5.6 Conclusion 117

6 Residual Stress and Temperature Effects 119
6.1 Introduction 119
6.2 Residual Stress Effect On The Crack Propagation Path 120
6.2.1 Method Of Approach 120
6.2.2 Numerical Results 122
6.3 Temperature Effect On The Crack Propagation Path 127
6.3.1 Thermal Stress Distribution Around The Circular Inclusions 128
6.3.2 Numerical Results 129
6.4 Fracture Of PCD And Residual Stresses 133

7 Conclusions and Future Work 137
7.1 Conclusion 137
7.1.1 Development of the New Methodology 137
7.1.2 Failure Mechanism In PCDs And DCD Method 139
7.2 Suggestions For Future Work 140
7.3 Summary of Achievements and Algorithms 143

References 149

Appendix A Conformal Mapping And Branch Points 169

Appendix B Finite Array Of Inclusion; Expansion Coefficient 173
B.1 Introduction 173
B.1.1 Expansion Coefficients: a_{npq} 176
B.1.2 Expansion Coefficients: b_{npq} 177
B.1.3 Expansion Coefficient Of Uniform Far-Field Load 179

Appendix C Minimum Distance From A Point To An Ellipse 183

Appendix D Notes On The Use Of Atomistic Simulations 185

List of figures

1.1 Bright field TEM images showing respectively the microstructure of Quadmodal PCD at different length scale. a) Cobalt material decorates boundaries between diamond grains of various sizes. b) Diamond grains with portions of highly deformed areas (plastic deformation cores encircled). White arrow points to the area containing residual stresses associated with second phase inclusions. c) Cobalt pools, inclusions, and other defects are shown at higher magnification [1]. 2

2.1 Diamond unit cell structure: cell dimension a = 0.3567 *nm*, and $c-c$ bond length of 0.154 *nm*. 6

2.2 PCD cutter structure: a) photography of a cutter, b) schematic of the microstructure (leached out "holes" in white and binder pools in dark grey) of a leached PCD sample, c) microstructure of the failed PCD sample at high temperature ($1,395\ ^0C$) [2]. 9

2.3 The three modes of loading that can be applied to a crack. 12

2.4 A typical and fully enriched FEM mesh with an arbitrary crack. circled nodes and squared nodes are enriched. Partially and fully enriched elements are the elements whose nodes are enriched [3]. 17

2.5 The Kachanov method, (a) decomposition of two interacting cracks under the σ^{∞} far-field load, (b) the unknown traction on each crack is sum of the average and the non-uniform term (with zero average) [4]. 22

2.6 Interaction between two cracks, (a) decomposition of two interacting cracks under the σ^{∞} far-field load, (b)Traction on each crack is sum of its linear varying term and a non-uniformity with zero average [5]. 25

3.1 Elliptic inclusion in a cartesian coordinate system. Local coordinates associated with the inclusion's surface are also displayed. 34

3.2 Normalised stress field distributions of (a) an elliptical void with aspect ratio 0.5×10^{-5} in a diamond matrix (b) crack of length $4\mu m$ in an infinite plate with uniform far-field stress [6]. 37

3.3 Local (individual inclusion) and global coordinate systems. 38

3.4 Finite array of aligned elliptical inclusions 40

3.5 Stress fields halfway between two aligned cracks are calculated by multipole ($n_{max} = 27$), Kachanov, and complex analytical methods are illustrated by red, blue and green colour respectively. Black dots illustrate the FEM calculated fields. The distance between two cracks of the same size (L) is equal to Δ. . 42

3.6 Stress fields of two aligned cracks between 0 and $\Delta/2$. Calculated fields by finite element method, multipole ($n_{max} = 27$), Kachanov, and complex analytical methods are illustrated by black, red, blue and green colour respectively [7, 8]. 43

3.7 Local and global coordinate systems. 44

3.8 The flow chart of the multipole method displacement and stress fields calculation. 47

3.9 Stress fields on the perimeter (distance along the perimeter has been normalised to the total perimeter length) of a hole with a 45^0 angle of inclination to the horizon and the aspect ratio of 0.5 ($l_1 = 1\mu m$ and $l_2 = 0.5\mu m$) subjected to a remote uniform tension in the x_{2q} direction. Fields calculated by the multipole method and FEM are represented by the blue and black lines respectively. 48

3.10 Plot of stress components in the direction orthogonal to the major axis of the elliptical hole under consideration along its perimeter for various configurations. The stress fields calculated by the multipole method and FEM are represented by blue and black lines, respectively. 49

3.11 Stress fields along the x_1 axis are calculated using FEM (black) and MM (blue) for a system of two collinear cracks. Schematic of the problem is shown in (a) and the distance between two cracks is set to be $0.1L_2$. Normalised $\sigma_{x_2x_2}$ presented for the cases where a) $L_1/L_2 = 100$, and b) $L_1/L_2 = 10$. 50

3.12 Schematic representation of the problem; SIF of a crack emanating from an elliptical hole, in an unbounded solid subjected to remote Mode I loading. . 52

3.13 SIF of a crack emanating from an elliptical inclusion with various aspect ratios l_2/l_1. The blue and black lines are derived from analytical calculations for $l/l_1 = 0.05$, and 0.005 respectively. Data shown by triangles are computed by the average SIF method along the distance l. 52

4.1 Main and extended crack directions. 57

4.2 Schematic of the general fracture criterion at the crack-tip. Energy varies at the crack-tip as a function of the polar angle θ. 59

4.3 Critical distance methods: The point method uses the stress at a point $r = L/2$ from the notch root rather than the maximum stress at the notch root; the line method uses the average stress on a line drawn from the notch over a distance $r = 0$ to $2L$ [9]. 60

4.4 Schematic of mode-I traction-sepration law used to model brittle crack propagation. 61

4.5 Schematic of a crack-tip with the extension point (y_{10q}, y_{20q}) on the perimeter of the crack and the new crack-tip at (y_{11}, y_{21}). 62

4.6 Two small cracks of length L_1 and L_2 are separated by distance δ. A single crack has a length $L_1 + L_2 + \delta$. 63

4.7 Macrocrack and a micro-crack 64

4.8 Displacement field (u_{x_2}) of two cracks under uniform tension in x_2 direction. Sizes of cracks are $L_1 = 10\mu m$ and $L_2 = 1\mu m$. 65

4.9 a) Two small cracks of length L_1 and L_2 are separated by distance δ, b) an equivalent kinked crack, and c) two aligned cracks. 65

4.10 The ratio of the optimised distance between two inclusions, δ, to the second crack/inclusion length, L_2, is plotted versus the ratio of the second to the first crack/inclusion length, L_2/L_1. 67

4.11 a) Kinked crack benchmark problem. Appropriate δ is selected according to Figure 4.10; b) Normalised SIF of a kinked crack with b/a=1 using the MPM method. 67

4.12 Schematic representation of simulation steps. a) propagated kinked crack, b) an equivalent crack, c) merge micro-cracks, d) micro-cracks orientations. . 69

4.13 Schematic representation of (a) zig-zag cracks, and (b) the approximated kinked cracks used to describe the system in DCD. 72

4.14 The flow chart of the DCD method to calculate the crack propagation path and its associated energy in the system. 74

4.15 Decomposition of the finite elastic body with inclusions into the problem of interacting elliptical inclusions and the complementary problem for the finite body without inclusions. 75

4.16 The flow chart of static analysis of CVBEM [10]. 79

4.17 The flow chart of the stress and displacement fields in step 2 of the DCD method (Figure 7.5) to calculate the crack propagation path and its associated energy in the finite size system. 80

4.18 Square plate with the circular hole. 81

4.19 Crack propagation path (dashed line) of cracks with different inclination angles under uniform tension. The initial size of the crack is 5 μm. The initial inclination angles of $5^0, 25^0, 45^0, 65^0, 85^0$ are presented by black, purple, blue, green, and red lines respectively. 82

4.20 Boundary element simulation of crack propagation process in pre-cracked specimens for 30°, 45° and 65°. (a) calculation with DCD and (b) Boundary Element Method [11]. 83

4.21 Deviation of the crack propagation path in the vicinity of a circular inclusion. a) crack path predicted using different harmonic terms n; green (n=1), blue (n=3) and red (n=9). This one shows the effect of harmonic terms on the accuracy of the results. Crack path deviations are shown for several relative stiffnesses of the inclusion to the matrix b) with correct aspect ratio, c) a comprised aspect ratio to zoom closer, and d) a comprised aspect ratio provided in [12]. 84

4.22 Experimental crack trajectory (red) compared to the asymptotic model (blue)[13], and the DCD method (black) for interaction with elliptical voids. 85

5.1 Schematic representation of problems. Crack propagation in a polycrystalline material: (a) overall view of potential interaction; effect of the interfacial strength of (b) grain boundaries, (c) inclusions and (d) inclusions along the grain boundaries, on the crack propagation path. 88

5.2 Schematic diagram of crack propagation mechanisms at the interface: (a) He and Hutchinson approach, i.e. check the crack energy for both possible propagation paths [14, 15], (b) Cook and Gordon mechanism based on the stress distribution and crack coalescence [16, 17], and (c) Crack propagation mechanism based on the energy distribution at the crack tip and crack coalescence, adopted in this study. 89

5.3 (a) Schematic of the problem. Stress fields are calculated using the MM method in the vicinity of an elliptical hole (with the aspect ratio = 0.01), with uniaxial stress applied in the x_2- direction. Zoom-in of the crack-tip stress fields are shown; the distance along the crack axis is in ellipse curvature (ρ) unit. (b) Contours of $\sigma_{x_2x_2}$, (c) Contours of $\sigma_{x_1x_1}$. 90

5.4 Variation of the relative stress fields in the vicinity of the crack tip in x_1-direction; The distance along the crack axis is normalised using the crack tip ellipse curvature (ρ), and stress fields are calculated using the MM method. 91

5.5 The normalised energy at the crack tip as a function of the polar angle θ. Energy plots are depicted for 3 cracks with different aspect ratios 0.001 (blue), 0.01 (black), and 0.1 (red). 92

5.6 Crack propagating toward a grain boundary. (a) Schematic of a general problem, (b) schematic of the simulated problem of a bi-crystal subjected to uniaxial remote vertical load and different GB orientations (φ). GB is shown in red and crack in black. 94

5.7 Crack propagation paths at a grain boundary for a bi-crystal subjected to uniaxial remote vertical load and different GB orientations. GB shown in red and crack propagation path in black. 95

5.8 Schematic diagram of a crack propagating towards an inclusion in (a) the polycrystalline structure and (b) in an abounded solid. The inclusion is assumed to be elliptical in shape and the lengths of the ellipse major and minor axes are denoted by l_1 and l_2, respectively. 96

5.9 Schematic representation of the interface problem when a crack propagates toward an inclusion. 97

5.10 Crack propagation trajectory computed for $\mu_i/\mu_0 = 10$, $\Gamma_i/\Gamma_0 = 10$ and values of a) $\Gamma_{int}/\Gamma_0 = 1$, b) $\Gamma_{int}/\Gamma_0 = 0.9$, and c) $\Gamma_{int}/\Gamma_0 = 0.5$ 99

5.11 Crack propagation trajectory computed for $\mu_i/\mu_0 = 0.5$, $\Gamma_i/\Gamma_0 = 0.5$ and values of a) $\Gamma_{int}/\Gamma_0 = 1$, b) $\Gamma_{int}/\Gamma_0 = 0.5$, and c) $\Gamma_{int}/\Gamma_0 = 0.2$ 99

5.12 Crack propagation trajectory computed for $\mu_i/\mu_0 = 0.2$, $\Gamma_i/\Gamma_0 = 0.4$ and values of a) $\Gamma_{int}/\Gamma_0 = 1$, b) $\Gamma_{int}/\Gamma_0 = 0.5$, and c) $\Gamma_{int}/\Gamma_0 = 0.2$ 99

5.13 Crack propagation trajectory computed for $\mu_i/\mu_0 = 0.1$, $\Gamma_i/\Gamma_0 = 0.2$ and values of a) $\Gamma_{int}/\Gamma_0 = 1$, b) $\Gamma_{int}/\Gamma_0 = 0.5$, and c) $\Gamma_{int}/\Gamma_0 = 0.2$ 99

5.14 Photographs of fractured specimen with hard (stiff) and soft (compliant) inclusion showing different crack–inclusion interaction scenarios: (a) Weakly bonded hard inclusion. (b) Weakly bonded soft inclusion. (c) Strongly bonded hard inclusion. (d) Strongly bonded soft inclusion. The black dot adjacent to initial crack-tip denotes the reference mark and the broken arrow indicates crack propagation direction [18]. 100

5.15 Schematic diagram of a crack propagating towards an inclusion at the GB in (a) the polycrystalline structure and (b) in an unbounded solid. The inclusion is assumed to be elliptical in shape and the lengths of the ellipse major and minor axes are denoted by l_1 and l_2, respectively. 101

5.16 Schematic diagram of an inclusion (shaded area) on a grain boundary (red line). A distribution of the interfacial energies at the point along the grain boundaries which intersects the inclusion interface is shown by γ_{int} and γ_{GB}. 101

5.17 Schematic diagram showing the relationship between interface angle and aspect ratio for a lenticular inclusion. 102

5.18 Crack propagation path and evolution of the crack energy and the Mode-I SIF on a GB containing an elliptical hard inclusion are predicted for each set of simulations. Material properties are selected as: $\mu_i/\mu_0 = 10$, $\Gamma_i/\Gamma_0 = 1.1$, $\Gamma_i/\Gamma_{int} = 4$. a) Inclusion size is $e = l_2/l_1 = 0.5$, and, $\Gamma_{GB}/\Gamma_{int} = 0.25$, b) Inclusion size is $e = l_2/l_1 = 0.8$, and $\Gamma_{GB}/\Gamma_{int} = 2.4$. The red line on the schematic of the system shows the GB line. 104

5.19 Crack propagation path and evolution of the crack energy and the Mode-I SIF on a GB containing an elliptical soft inclusion are predicted for each set of simulations. Material properties are selected as: $\mu_i/\mu_0 = 0.10$, $\Gamma_i/\Gamma_0 = 0.5$, $\Gamma_0/\Gamma_{int} = 4$. a) Inclusion size is $e = l_2/l_1 = 0.5$, and $\Gamma_{GB}/\Gamma_{int} = 1.60$, b) Inclusion size is $e = l_2/l_1 = 0.2$, and $\Gamma_{GB}/\Gamma_{int} = 0.30$. 105

5.20 Crack propagation path and evolution of the crack energy and the Mode-I SIF on a GB containing an elliptical hole were predicted for each set of simulations. Material properties are selected as: $\mu_i/\mu_0 = 0.0$, $\Gamma_i/\Gamma_0 = 0.0$, $\Gamma_0/\Gamma_{int} = 1$. a) hole size is $e = l_2/l_1 = 0.5$, and $\Gamma_{GB}/\Gamma_0 = 1.20$, b) hole size is $e = l_2/l_1 = 0.2$, and $\Gamma_{GB}/\Gamma_0 = 1.85$. 106

5.21 Schematic diagram of a crack propagating towards an array of inclusions on the GB in (a) the polycrystalline structure and (b) in an unbounded solid simulated here as a simplified scenario. Inclusions are assumed to be elliptical in shape and equispaced on a GB. 107

5.22 Energy evolution of the crack while it is propagating along the GB containing 4 equispaced soft inclusions with different spacing. 109

5.23 Energy evolution of the crack while it is propagating along the GB containing 4 equispaced elliptical voids with different spacing. 110

5.24 Energy evolution of the crack while it is propagating along the GB containing 4 equispaced elliptical hard inclusions with different spacing. 113

5.25 Crack propagation path can be deflected by a GB containing soft inclusions. Deflection mechanisms depend on the GB, the inclusion interface, and the matrix material strength as well as, the relative orientation of GB and the propagating crack. 114

6.1 Schematic representation of the crack trajectory and the maximum principle stress fields normalised with respect to the remote load (σ_1/σ_∞). Black and red dashed lines show crack trajectories predicted using SIFs in Equation 4.2 and the two proposed crack propagation criteria. Crack at each simulation step is approximated by a kinked crack, and a kink crack by two sequential cracks. Stress fields at the tip of the second crack are illustrated in different steps where black arrows predict the crack propagation direction in that particular configuration. The crack starts propagating from point 1 and continues until it is far away from the influence of the residual stresses in point 8. 123

6.2 Deflection of the crack by the proposed residual stress in Equation 6.1 and the external far-field load. Propagating crack will first be deflected where the compressive hoop stress in the matrix material is normal to crack plane. As the crack moves around, it will be deflected away where the crack plane is normal to the tensile radial stress. 124

6.3 Schematic representation of the crack propagation path for an initial crack of length 2.6 μm, under far-field tension and tensile radial residual stress. The blue, red, and black lines are crack trajectories associated with residual stresses where the magnitude of the stress on the perimeter of the circle relative to the external load are set to 0, 1, and 2. 124

6.4 Schematic representation of the crack propagation path for an initial crack of length 2.6 μm, under far-field tension and compressive radial residual stress. The blue, red, and black lines are crack trajectories associated with residual stresses where the magnitude of the stress on the perimeter of the virtual circle relative to the external load were set to 0, -1, and -2. 125

6.5 Schematic representation of crack propagation paths under the uniform far-field tension and compressive radial residual stress. The blue, red, and black lines are crack trajectories associated with the initial crack of length 12, 4, and 2.6 μ m respectively. 126
6.6 Schematic representation of the crack propagation path of an inclined crack under the far-field tension and tensile radial residual stress. 126
6.7 The problem of inclusion in the matrix material is decomposed into two systems: a) a matrix material with a circular void under an internal radial pressure of p_0, b) a circular inclusion under an external radial pressure of p_0. 129
6.8 Graph showing the effect of thermal stress and the second phase inclusion on the crack propagation path. Black and red lines illustrate the crack propagation trajectories in the presence and in the absence of thermal stresses respectively. 131
6.9 Graph showing the effect of thermal stress, the second phase inclusion and interface strength on the crack propagation path. Black and red lines illustrate the crack propagation trajectories in the presence and in the absence of thermal stresses respectively. 132
6.10 Graph showing the effect of thermal stress relative to the external load, the second phase inclusion and interface strength on the crack propagation path. Black, and blue lines illustrate the crack propagation trajectories for cases where thermal stress was considered and thermal stress on the surface of inclusion relative to the external load was 2 and $2/3$ respectively. The red line shows the crack propagation trajectories for case where thermal stresses were not considered 132
6.11 PCD cutter structure: a) photography of a cutter, b) X-ray image of PCD cross-section showing the leach depth of an example cutter (E6 2017). The black, light grey and dark grey parts are showing the substrate, the non-leached, and the leached part of PCD respectively. 134
6.12 PCD cutter structure: a) a cross-section of a typical cutter after field evaluation showing all the cracks initiating at/near the wear front then propagating into the bulk (E6 2017), b) microstructure of an ideal leached PCD sample. 134
6.13 Crack deflection towards holes in a symmetric system containing holes and cobalt inclusions. 135
6.14 Crack deflection towards holes in a symmetric system containing holes and cobalt inclusions. Red and black lines present crack trajectories in which the thermal stresses are and are not considered respectively. 135

7.1 A scanning electron microscope (SEM) test of the crack slit in a failed PCD [19]. 140
7.2 Residual and thermal stresses of fine and coarse unleached PCD samples provided by E6. 142
7.3 The flow chart of the multipole method displacement and stress fields calculation. 143
7.4 The flow chart of static analysis of CVBEM [10]. 144
7.5 The flow chart of the DCD method to calculate the crack propagation path and its associated energy in the system. 145
7.6 The flow chart of the method used to compute stress and displacement fields in step 2 of the DCD method (Figure 7.5) employed to calculate the crack propagation path and its associated energy in the finite size system. 146

A.1 Mode I stress fields and displacement fields of elliptic inclusion with aspect ratio $l_2/l_1 = 1/2$. Matrix material and inclusion have the same material. . . 170
A.2 Mode I stress fields and displacement fields of elliptic inclusion with aspect ratio $l_2/l_1 = 1/2$. Matrix material and inclusion are selected with mechanical properties $\mu_0 = 478$ GPa and $\nu_0 = 0.07$, and $\mu_1 = 75$ GPa and $\nu_1 = 0.31$ respectively. 171

C.1 Minimum distance from point $\mathbf{P} = (y_{11}, y_{21})$ to an ellipse in the local y_q coordinate system. 183

D.1 (a) Unphysical behaviour at diamond crack tip using REBO2 potential, a crack in diamond blunts. (b) Bond braking in diamond using REBO2Scr potential. 186

List of tables

4.1 Comparison of stress fields 63

4.2 Comparison of the SIFs at the crack-tip and the left and right-hand side of the second crack in Figure 4.7 using analytical approach [20] and the MM method. 64

4.3 Variation of the normalised SIF ($K/\sigma\sqrt{\pi a}$) with angle for a kinked crack of the same size as the original crack under a uniform tensile stress. Suffix B refers to the endpoint (tip B) of the kinked crack (see Fig. 4.11). Methods 1, 2, 3 and 4 are the MPM method, the complex potential formulation, discrete dislocation density and Greens function technique, respectively [21–23]. . 68

4.4 Variation of the normalised SIF ($K/\sigma^{\infty}\sqrt{\pi a}$) with angle for systems given in Figure 4.13 using the singular integral equation containing the COD and the multiple method. Suffix B refers to the endpoint (tip B) of the crack and m denotes the number of zig-zag kinks. 72

5.1 The average normalised energy and Mode I SIF at the crack-tip are calculated for different toughening mechanisms where soft inclusions, voids, and hard inclusions were located on the GB. The percentage difference of the results for the soft inclusions and voids are calculated. In the last two columns present the normalised quantities for a GB containing hard inclusions. . . . 111

5.2 Results of ab initio molecular dynamics simulations at T = 1500 C^0 under a pressure of 5 GPa followed by cooling to room temperature and energy minimisation. 116

Abbreviations

Roman Symbols

σ_u Ultimate tensile strength

ε_{ij} Kronecker delta

Λ_{ij} Transmission factor

$\psi(z)$ Complex Muskelishvili's potential

t_{ij} The traction generated by the $j-th$ crack at the $i-th$ crack position.

t_i The average traction vector for the i-th crack.

$(\widehat{\zeta O \eta})$ Elliptical coordinate system

$(X_1 + iX_2)$ Point force

$<>$ Average

$\alpha_{ij}(\theta)$ Angular function

κ Kolosov's constant

ε_{ij} Strain tensor

η_{nm}^{pq} Re-expansion coefficients

Γ_0 Fracture energy of the matrix material

$\Gamma_{1,2}$ Far-field linear coefficient

Γ_{int} Fracture energy of the interface

$\Gamma_{surface}$ Surface energy

μ	Shear Modulus
μ_{nm}^{pq}	Re-expansion coefficients
∇^2	Laplacian
∇^4	Bilaplacian or the biharmonic operator
ν	Poisson's ratio
$\omega(\xi)$	Transformation function
$\overline{K}$	Average SIF
σ^{∞}	Far-field load
σ^{ij}	The stress field generated by the $j-th$ crack at the $i-th$ crack site.
σ^{i}	The amount of stress fields that $i-th$ crack experiences.
σ_{ij}	Stress fields components
τ_n	Normal traction
θ_p	The angle between y_p, and global coordinate system.
$\underline{u}$	$\underline{u}=(u_1,u_2)^T$ Displacement vector
$\varphi(z)$	Complex Muskelishvili's potential
ξ	$\xi=\zeta+i\eta$; ζ and η are variable in Cartesian coordinate system.
ζ_{0q}	Interface of the $q-th$ inclusion
ζ_0	Ellipse interface
a_{npq}	Expansion coefficient of $p-th$ inclusion in the $q-th$ coordinate system
A_{np}	Expansion coefficient of $p-th$ inclusion in the $p-th$ coordinate system
A_n	Expansion coefficient of one inclusion
b_{npq}	Expansion coefficient of $p-th$ inclusion in the $q-th$ coordinate system
B_{np}	Expansion coefficient of $p-th$ inclusion in the $p-th$ coordinate system
B_n	Expansion coefficient of one inclusion

d Ellipse inter-foci distance

D_q Inter-foci distance of the $q-th$ inclusion in its local coordinate system.

d_q Inter-foci distance of the $q-th$ inclusion

e Ellipse aspect ratio

E' The effective Young's modulus

e_η Normal vector in the elliptical coordinate system.

e_ζ Normal vector in the elliptical coordinate system.

G Energy release rate

G_C Critical energy release rate

G_d Maximum energy release rate of the deflecting crack

G_p Maximum energy release rate of the penetrating crack

$K_p^{\pm}$ SIF of the right and left hand side of the $p-th$ crack

K_C Critical stress intensity factor

K_{IC} Mode I critical stress intensity factor

K_{mode} Stress intensity factors

l_1 Ellipse major axis

l_2 Ellipse minor axis

n_i Unit normal vector

R Rotational transformation tensor

s_{11}, s_{12}, s_{22} Far-field load

u_{pq}^r Disturbance induced by the $p-th$ inclusion in the q coordinate system

u_p^s Disturbance induced by the $p-th$ inclusion in the p coordinate system

$u_{p(y)}$ Displacement in the y local coordinate of $p-th$ inclusion

u_p Displacement in the local coordinate of $p-th$ inclusion

v $= e^{\xi}$ is a basis function for complex potentials.

v_q $= e_q^{\xi}$ is a basis function for complex potentials.

w Weight function

z $z = x + iy$; x and y are variable in Cartesian coordinate system.

Z_{pq} Distance between two local coordinates of $p-th$, and $q-th$ inclusions

z_p Local coordinate of $p-th$ inclusion, coordinate system is parallel to the global coordinate system.

$(\widehat{x_1 o x_2})$ Cartesian coordinate system

2D Two-dimension

3D Three-dimension

BEM Boundary Element Method

CRSS Critical Resolved Shear Stress

CVBEM Complex variable boundary element method

DCD Discrete Crack Dynamic

FEM Finite Element Method

GB Grain Boundary

HPHT High Pressure And High Temperature

LEFM Linear Elastic Fracture Mechanics

MM Multipole Method

MSERR Maximum Strain Energy Release Rate

MTS Maximum Tangential Stress

SEM Scanning Electron Microscope

SIF Stress Intensity Factor

TEM Transmission Electron Microscopy

XFEM eXtended Finite Element Method

Chapter 1

Introduction

The author conducts this Ph.D. thesis under the joint guidance and advice of supervisors from Imperial College London and Element Six (E6), a De Beers Group Company. E6 (a reference to carbon, the sixth element of the periodic table) is the world's leading manufacturer of synthetic diamond for hard abrasive materials. Synthetic diamonds are used throughout many industrial applications such as cutting, grinding, drilling, and polishing. Of particular interest is Polycrystalline Diamond (PCD) that is formed by sintering diamond powders using metallic catalysts at very high temperatures ($> 1500^oC$) and pressures (> 5 GPa). PCD is a hard abrasive material with a broad range of applications in the oil and gas, and hard rock mining industries. Understanding the failure mechanisms of the PCD materials is a technological problem with scientific significance. Cracks, inclusions, catalyst binders, and any imperfections which are left after manufacturing, could have a significant impact upon the cracking process either in single crystals or grain boundaries of PCDs. Figure 1.1 illustrates bright field mode of transmission electron microscopy (TEM) images of PCD's grain boundaries. It shows the variety of diamond imperfections such as dislocations, defects, and Cobalt (or other metallic catalysts') pools that can produce failure in the system.

PCDs failure mechanisms involve crack nucleation, crack-inclusion interactions, and crack propagation. The objective of this project is to develop a method to calculate the micro-crack and inclusion interactions, and then using the interaction information to predict low-speed crack propagation paths in brittle or quasi-brittle materials at the continuum scale. Once fully developed and validated, the method should be extended to study more realistic problems including PCDs, therefore studying the effect of the presence of multiple inclusions, manufacturing residual stresses and grain boundaries.

PCDs have low fracture toughness and plastic deformation is extremely limited. The investigation of this thesis may be used to help in the design process by shedding light on the

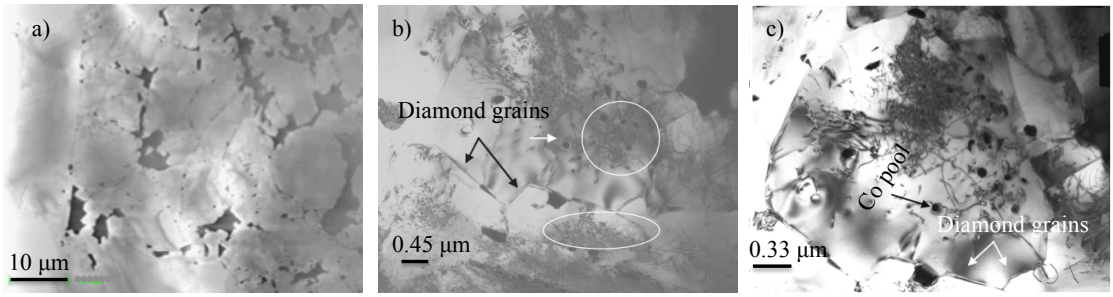


Fig. 1.1 Bright field TEM images showing respectively the microstructure of Quadmodal PCD at different length scale. a) Cobalt material decorates boundaries between diamond grains of various sizes. b) Diamond grains with portions of highly deformed areas (plastic deformation cores encircled). White arrow points to the area containing residual stresses associated with second phase inclusions. c) Cobalt pools, inclusions, and other defects are shown at higher magnification [1].

failure mechanisms. Before studying PCD structures, we focus on understanding the failure mechanisms and crack propagation problems in brittle polycrystalline materials.

1.1 Thesis Structure

Crack propagation is an inherently multi-scale problem, where the crack propagation path depends on phenomena and mechanisms occurring at different length and time-scales, from the loading conditions prescribed at the macroscopic scale all the way down to the bond breaking events responsible for failure at the crack tip that can only be resolved at the atomistic level. Multi-scale simulations of crack propagation involving all the scales from atomistic simulations are not computationally practical due to the very large number of scales involved; so micro-scale and meso-scale crack propagation analyses have been suggested to supplement the continuum scale for fracture modelling. In this study, a new tool to study the crack propagation at the micro-scale is proposed and developed to study the effect of microstructure on the main crack propagation path, and the strength of the grain boundaries (GBs) and micro-structural features on the development of fracture in quasi-brittle systems.

In Chapter 2 a general overview of diamond and polycrystalline diamond is provided. Then, a short introduction of the theoretical background and relevant concepts of fracture mechanics followed by a comprehensive literature review on various analytical and numerical methods to study micro-crack and inclusion interactions are presented. Their strengths and drawbacks are then investigated, and the multipole method is selected for the simulation of the problem.

In Chapter 3 the multipole method is explained in details and extended to treat a limited array of cracks and inclusions. This method provides a solution in a complex potential formulation for 2D plane elasticity problems where close interactions between inclusions are taken into account. The local field at each point in the system is obtained through the superposition of the incident far-field and the disturbance fields caused by neighbouring defects around all inclusions.

In Chapter 4, a novel method is proposed to predict the crack propagation path in two-dimensional finite-sized systems. Once the distribution of stresses and stress intensity factors (SIFs) in a system are computed using the multipole method, the evolution of individual micro-crack and its interaction with existing cracks/inclusions is then explicitly modelled using the new technique named "Discrete Crack Dynamic". Details of the method development and its application to some benchmark problems are reported in this chapter.

Chapter 5 is focused on the effect of the interfacial strength of the grain boundaries and elliptical inclusions on the deflection of the crack path. The method is developed to channel the crack into a toughening configuration (array of elliptical holes and soft inclusions) in order to obtain the optimised microstructure required to enhance toughness through different mechanisms. Numerical results at each step are validated with other experimental and computational results.

Chapter 6 utilises the capabilities of the method to determine the effect of residual stresses in general, and the residual thermal stresses associated with the second phase inclusion in particular, on the crack propagation path. Both compressive and tensile residual stresses can deflect crack trajectories. Tensile residual stresses can reduce the wear and fracture resistance performance or cause failure in materials; on the contrary, compressive residual stresses are mostly beneficial and may arrest or retard the crack propagation. The study is extended to characterise the influence of residual stresses and thermal stresses on crack propagation in PCD structures. This thesis is closed by summarising the achievements of the project and the proposed future work, which are discussed in Chapter 7.

1.2 Research Objectives

In order to gain a better understand of the failure mechanisms that govern crack propagation in brittle polycrystalline materials, the effect of the microstructure and the interaction between cracks, grain boundaries and inclusions has to be studied. Therefore, a fracture model that can predict microstructural interactions is required. The aim of this work is to develop an accurate and potentially computationally inexpensive fracture model for brittle and quasi-

brittle fracture in 2D and to implement it to solve problems involving realistic polycrystalline structures. The main objectives of this thesis can be summarised as follows:

- Calculating the full stress fields in an unbounded solid containing elliptical inclusions and cracks.
- Including the finite size effects using the linear superposition principle and a boundary element methodology.
- Developing a new method, called *Discrete Crack Dynamic* (DCD), to model the propagation of individual micro-cracks and their interactions with existing cracks/inclusions and grain boundaries.
- Incorporating *interface* and *grain boundary* effects in the crack propagation model. Interfaces and grain boundaries are modelled explicitly using inter- and intra-granular fracture energies as to establish the likelihood of propagation and crack path.
- Studying the effect that *residual* and *thermal stress* have on the crack propagation path.

Chapter 2

Background And Literature Review

2.1 Background

2.1.1 Diamond

Graphite and diamond are forms of carbon with different hybridizations. The common sp^2 and sp^3 allotropes of carbon exist in various crystallographic forms of graphite-like and diamond-like phases. Each carbon atom in diamond's structure is covalently bonded to four other carbon atoms, which results in a highly stable structure. Diamond is a metastable allotrope of carbon in nature, but the large value of cohesive energy (7.46 eV) as well as the significant energy barrier, result in its high metastability and extreme melting temperature, in the order of 5000 K [24].

Crystallographic structure

Diamond has a complex internal structure that reflects the growth conditions, impurity contents and deformations. A common cubic structure of diamond (Figure 2.1) can be described as two interpenetrating face centre cubic lattice (FCC) with $a/4 < 111 >$ displacement and the same slip system of FCC crystals: $< 110 >$ directions and $\{111\}$ planes. The bonds are 154 pm in length and at an angle of 109.5^0 to each other [25].

Impurities

Elements other than carbon exist in the diamond lattice and affect its optical, electrical, thermal and mechanical properties. Sixty elements have been identified in natural and synthesised diamond, the major impurities being nitrogen, oxygen and hydrogen both present at the surface and in the bulk [26]. Inclusions are most likely to be found at lattice imperfections, dislocations and platelets.

Synthesised diamond, or man-made diamond, is used for various industrial purposes. Synthetic diamonds are grown by many different techniques such as, high pressure, high

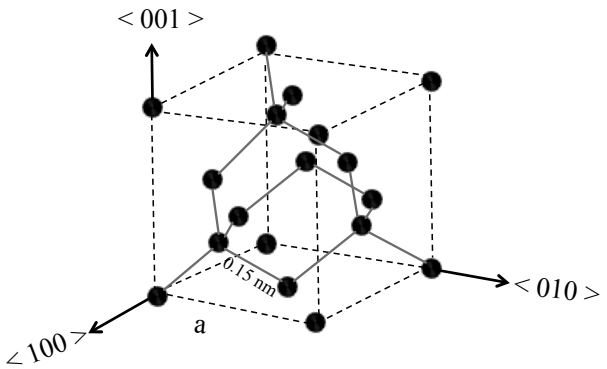


Fig. 2.1 Diamond unit cell structure: cell dimension a = 0.3567 *nm*, and $c-c$ bond length of 0.154 *nm*.

temperature (HPHT) sintering, shock wave synthesis, and chemical vapour deposition techniques [26]. Synthesised diamond contains inclusions such as nitrogen, nickel, cobalt and other catalytic metals in both bulk and at the surface with diameter size smaller than 60 nm and in many cases even as small as 2 or 3 nm [27].

Mechanical properties

The elastic constants have been measured using variety of techniques "wedge" technique, x-rays scattering, Brillouin scattering, and ultrasonic pulse method [28–36]. The measurements indicate that elastic stiffness constants are pressure and temperature dependent. Due to FCC symmetry in the crystal structure, only three constants are needed to describe the stiffness of diamond; Vogelgesang [36] obtained parameters at room temperature and pressure as follows: $C_{11} = 1080.4$, $C_{12} = 127.0$, $C_{44} = 576.6$ GPa. [1] A yield strength of 130-140 *GPa*, and a critical resolved shear stress (CRSS) of about 70 *GPa* were suggested by [37]. However, the CRSS specifically in covalently bonded materials depends on the experimental conditions [38]. The critical stress intensity factor values depend on which surface fracture occurs. Fileds and Freeman [39] recorded values for synthesised and natural diamond in the range $3.4 - 7\ MN\ m^{-3/2}$.

Plastic deformation

Stressed diamond can be relaxed by emission of dislocations and plastic deformations at high enough temperature; for example multiple slip can occur below 700 ^0K by point loading characterised by pressure around 10 GPa [40]. At lower temperature, relaxation corresponds to the formation of stacking faults, mechanical micro-twins, micro-cracks, and graphitisation.

[1] Elastic constants C_{ij} determine the linear relationship between stresses and strains, for example, C_{11} relates σ_{11} to ε_{11}.

Plastic deformation is uncommon at low temperature and therefore diamond is classified as a brittle material.

Diamond defects

It has been empirically observed that the inclusion-rich areas can be also characterised by the area of high density dislocations as well as numerous stacking faults and microtwins on (111) planes [41]. The reason why diamond has specific types of dislocations and defects, is related to the carbon structure and phase transformations that take place when it is exposed to high pressure [42–45].

2.1.2 Polycrystalline Diamond

Diamond exhibits experimentally and numerically brittle cleavage usually along the (1 1 1) plane, but cleavage has also been observed on the (1 1 0) plane, and, to a lesser extent, along some other planes [46, 47]. Anisotropy in most of the properties of a single crystal diamond provides disadvantages for many applications. PCDs, consisting of numerous diamond particles sintered together with metallic binders (usually cobalt) have the advantages of being effectively isotropic at a macroscopic level and having a greater toughness while still maintaining a reasonably high thermal conductivity. PCDs are often described by the average grain size of the original powder, which has a significant effect on the consolidation process during the early stage of sintering. For instance, by selecting two different initial grain sizes, the porosity of the mixture can be reduced; this reduction depends on the relative ratio of the fine and coarse grains and operation pressure [48, 49].

Polycrystalline aggregates of diamonds consist of a number of small grains and are produced using very specific technological processes. Fine-grained aggregate is synthesised by sintering diamond crystallites into a coherent structure at a high temperature and pressure in two ways: i) solid-state sintering of diamond grains without additives under high pressure [50, 51], ii) liquid phase sintering of diamond using catalysts, which is the conventional method for industrial production of PCDs [48]. Industrial PCDs sintering process comprises of three stages, cold compaction, hot compaction, and infiltration and liquid phase sintering [52].

The cold compaction process profoundly affects the final diamond size distribution, binder content, binder phase distribution and homogeneity, diamond grit inter growth, and densification kinetics. Three processes take place during the cold compaction, (i) particle rearrangement, (ii) crushing of diamond particles, and (iii) filling of voids with crushed fine particles. The second stage of sintering is the hot compaction. In this stage, at temperature below 700°C mainly crushing and rearrangement of particles take place and at temperature above 700°C, diamond plastic deformation are detected. Also, graphitisation, and densifica-

tion by plastic deformation and filling the pores by graphite occur at this stage. During the infiltration and liquid phase sintering process, diamond particles are mixed with a solvent catalyst (Fe, Ni, or Co mixture) under high pressure, and with tungsten carbide, which is released from the substrate into the diamond layers. At this stage, the molten additive metal has a role of a solvent/catalyst and also fills in the gaps amongst the grains. These molten solutions reduce the pressure and temperature necessary for phase transformation to diamond and enhance the rate at which phase transformation occurs by overcoming the large kinetic barrier and acting as a transport agent for carbon. The other roles of the molten catalysts in the sintering process are to dissolve any graphite formed in the cold compaction stage and to round off sharp corners of the grains and the necks between bonded diamonds. The presence of the second phase with highly plastic properties in the local zone of contact between the grains promote redistribution and relaxation of the contact stresses and consequently prevents crack propagation and brittle fracture to occur. Re-precipitation of diamond and intergrowth, and consequently grain growth, are the main features of this sintering stage.

Small modifications to the manufacturing processes can alter significantly the properties of the final PCD products. PCDs have generally superior performance to those of a single crystal diamond: high hardness and strength, toughness, abrasion resistance and thermal conductivity [53, 1]. The improvement in the toughness of PCDs is associated with the random orientation of grains in its structure which forces any propagating crack to take a strolling zigzagging path, and consequently consuming more strain energy in such a way.

PCD materials are vulnerable to thermal degradation when exposed to elevated temperature and as a result they have a safe operational temperature limit. This vulnerability results from the thermal expansion differences that exist between metallic catalysts and diamond. This differential thermal expansion can induce thermal stresses and consequently break binder and diamond bonds, and form cracks in the structure. Also, the solvent metal catalysts at high temperature can cause an undesirable phase transformation in diamond (converting it to carbon monoxide, carbon dioxide, or graphite). Investigations have been conducted to improve the limiting operational temperature of PCDs [54, 55]. The graphitisation of the diamond depends markedly on the atmosphere around the diamond. In the presence of Oxygen, even in minute quantities, apparent graphitisation can be observed at temperatures above 700°C. Also, graphitisation can occur at diamond grain boundaries where the cobalt binder "wets" the diamond surfaces. Keshavan *et.al.* provided a solution to this problem by leaching and removing the metallic binders from the working surface of PCDs [56]. The leaching process gradually removes the binder from the specimen, or at least from a portion of the polycrystalline aggregate, generally reaching depths of about 0.01 to 0.1 *mm* from the surface (as shown in the structure of the PCD cutters in Figure 2.2).

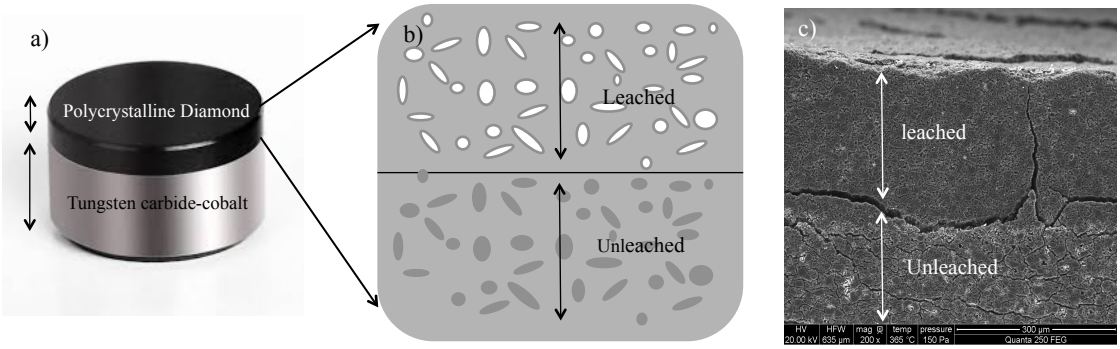


Fig. 2.2 PCD cutter structure: a) photography of a cutter, b) schematic of the microstructure (leached out "holes" in white and binder pools in dark grey) of a leached PCD sample, c) microstructure of the failed PCD sample at high temperature ($1,395\ ^0C$) [2].

These unique properties of PCDs are best utilised in cutting tools for machining a wide variety of abrasive materials. The combination of hardness, toughness and strength make PCDs excellent cutters for a variety of drilling operations. PCDs are incorporated in the oil and gas industries for drilling purpose, where the cutting tool has to resist fracture (toughness), plastic deformation (hot hardness) and (abrasive, adhesive and tribo-chemical) wear. A frequent problem in the drilling industry is the failure of cutting tools which is caused by PCDs fracture and chipping. Considering the large costs associated with the need to change the cutting tools in the middle of the drilling process (usual costs are in the range of hundreds of thousands of euro) the most significant challenge when designing the cutting tool is to resist abrupt component fracture and to improve its lifetime.

2.1.3 Fracture And Failure of PCDs

Understanding deformation and failure mechanisms is critical for improvements in brittle polycrystalline structure performance. Failure of polycrystalline materials is associated with the fracture toughness, wear mechanisms, effect of loading rate and fatigue mechanism, existing thermal residual stresses, and microstructure distribution. Failure mechanisms of PCDs can be classified into three stages; surface depreciation, cracks formation, and crack growth. Surface depreciation is a consequence of surface graphitisation and carbon removal. Removal of carbon atoms includes chemical and mechanical procedures [57]. A stressed PCD with depreciated surface is prone to experience micro-cracking either inside the grains (transgranular) or at the grain boundaries (intergranular). Depending on the amount of applied stress, residual stress and temperature variation, diamond can undergo structural relaxation, which exhibits itself in dislocation movement and plastic deformation, graphitisation and/or

crack nucleation. At extreme condition activated defects, inclusions, and micro-cracks can break the coherence of the stressed material and produce macro-cracks and failure [58].

Material inhomogeneities and defects such as impurities, inclusions, and micro-cracks play a fundamental role in dictating the modes of fracture and failure for both macroscopic brittle cracks and typical fatigue crack propagation [59–61]. Grain boundaries, elastic modulus, and toughness of the individual microstructural constituents and interfaces are critical parameters that control the failure mechanisms in brittle polycrystalline materials. The ability to predict the material behaviours and the failure mechanisms of such materials can lead to better designs, improved performance, reduced costs and enhanced safety. This work is focused on developing a two-dimensional (2D) numerical model to predict microstructure, and temperature variation effects on crack propagation and failure of brittle polycrystalline structures in the quasi-static regime, with the aim of optimising the design of PCDs. Before presenting the development of the new numerical tool, some theoretical background and relevant concepts related to continuum fracture mechanics are presented to provide an overview of the state-of-the-art methodologies used to study mixed mode crack propagation in the linear elastic regime.

2.2 Background In Continuum Mechanics

2.2.1 Linear Elastic Fracture Mechanics (LEFM)

Fracture mechanics was developed to understand the causes of failure in materials. A large amount of work has been built in the framework of continuum mechanics starting from the 1920s, by Inglis [62] and Griffith [63] to establish a model for crack propagation, and for the determination of the stress, strain, and displacement fields in a cracked medium, with particular attention focused on describing the neighbourhood of an elliptical cavity and the behaviour of crack-tips in a material under load.

2.2.1.1 The energy release rate

Griffith's theory states that a crack will propagate when the reduction in potential energy that occurs due to crack growth is greater than or equal to the increase in surface energy due to the creation of two new fracture surfaces. This theory is applicable to elastic materials that fracture in a brittle manner.

Irwin extended the Griffith approach and developed the energy release rate concept. The energy release rate G is the change of potential energy per unit crack area as the crack propagates throughout the system; i.e. G is the energy dissipated by fracture per unit of new

fracture surface area.

$$G = -\frac{dU}{da} \tag{2.1}$$

where U is the potential energy of an elastic body, and $2a$ is the crack length. According to Griffith's theory and the energy release rate concept, crack can propagate only if the energy release rate becomes greater than or equal to the surface energy per unit area (γ). In other words, the energy dissipated at the crack-tip has to be balanced by the cost of creating two new surfaces. At the moment of fracture, the energy release rate reaches the critical value G_C and the fracture condition becomes:

$$G_C = 2\gamma. \tag{2.2}$$

G_C is the material's resistance to fracture which means it is the measure of fracture toughness.

2.2.1.2 Stress Intensity Factor

Irwin [64] incorporated the Westergaard [65] approach and introduced a new crack-tip characterising parameter, the stress-intensity factor (SIF). Irwin stated that stress and displacement fields near the crack-tip could be described by a single constant "SIF". The SIF is the magnitude of the dominant component of the local stress fields near the crack-tip. It accounts for the geometry of the body containing the crack and the type of loading to which it is subjected. The importance of this concept is laid on the fact that a macroscopic parameter, SIF, overcomes the lack of adequate knowledge about the microscopic fracture events at the crack-tip. The SIF is usually expressed by K in equations with a subscript to denote the mode of loading (Figure 2.3), i.e., K_I, K_{II}, and K_{III}. Stress field components ahead of a crack-tip in an isotropic linear elastic material and in a polar coordinate system (r,θ) can be written (in first approximation - this is a first term expansion) as:

$$\lim_{r\to 0} \sigma_{ij}^{(I)} = \frac{K_I}{\sqrt{2\pi r}} f_{ij}^{(I)}(\theta) \tag{2.3}$$

$$\lim_{r\to 0} \sigma_{ij}^{(II)} = \frac{K_{II}}{\sqrt{2\pi r}} f_{ij}^{(II)}(\theta) \tag{2.4}$$

$$\lim_{r\to 0} \sigma_{ij}^{(III)} = \frac{K_{III}}{\sqrt{2\pi r}} f_{ij}^{(III)}(\theta) \tag{2.5}$$

for Modes I, II, and III, respectively [66]. f_{ij} is a dimensionless function that varies with the load and geometry. In a mixed-mode problem (i.e., when more than one loading mode is present), using the principle of linear superposition, the total distribution of the stresses is given by:

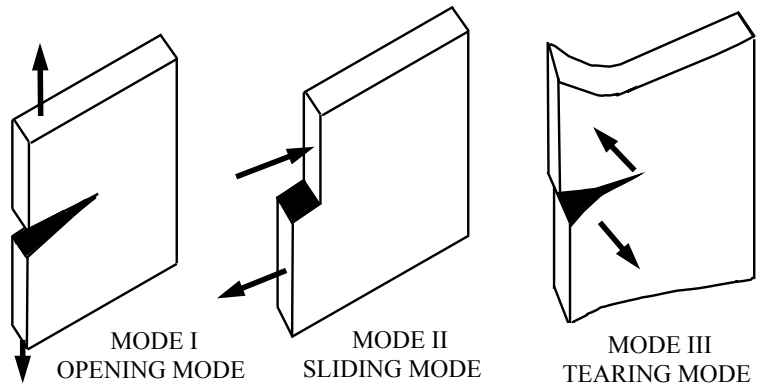


Fig. 2.3 The three modes of loading that can be applied to a crack.

$$\sigma_{ij} = \sigma_{ij}^{(I)} + \sigma_{ij}^{(II)} + \sigma_{ij}^{(III)} \tag{2.6}$$

2.2.1.3 Relation between K and G

The energy release rate quantifies the net change in potential energy that accompanies an increment of crack extension. The SIFs can be used to quantify the stresses, strains, and displacements fields near the crack-tip. Considering the energy differences between a body before and after crack growth, and the fact that the energy release rate G can be written in terms of the stress and displacement fields at the crack-tip [67], it is clear that G and SIFs (K_I, K_{II}, K_{III}) are related. In 2D linear elasticity, when all modes of loading are present, the energy release rate of a crack propagating a unit length along its extension is related to the SIFs via:

$$G = \frac{K_I^2}{E'} + \frac{K_{II}^2}{E'}, \tag{2.7}$$

where E' is the effective Young's modulus and it differs for conditions of plane stress or plane strain according to:

$$E' = \begin{cases} E & \texttt{for plane stress} \\ E/(1-\nu^2) & \texttt{for plane strain} \end{cases} \tag{2.8}$$

and ν is the Poisson's ratio. Using Formula 2.7, failure conditions can be expressed in terms of critical SIFs; K_{IC}, and K_{IIC} determines the material resistance to the crack

propagation in mode *I* and *II* respectively. These critical values are intrinsic properties that only depend on the material and experimental conditions.

2.2.2 Mixed Mode Fracture

Equation 2.7 was obtained by assuming that a crack under combined loading moves along its extension and in its initial plane. Unfortunately, for the crack subjected to the mixed mode loading, when two or more modes of loading are present, the extension is not collinear and the crack kinks at an angle from its original plane. Hence, Equation 2.7 can not be used to apply the Griffith-Irwin energy release rate criterion for cracks under mixed mode loads.

For the case of pure-mode loading and according to Griffith's theory, a fracture in the direction of the crack extension will occur when the corresponding SIF or energy release rate reaches its critical value. Analogous to the pure-mode loading, a criterion is required to predict the failure condition and the crack propagation direction for the generally mixed mode loading problems. For a crack under mixed-mode I/II loading conditions, a number of fracture criteria have been developed by many researchers. Various fracture criteria are reviewed and discussed in Gdoutos's book [68], where he reflects on the limitations and applications of different criteria. For each problem, depending on the fracturing media, an appropriate crack propagation criterion has to be selected. Crack propagation direction can also be predicted according to the selected criterion.

Erdogan and Sih [69] proposed the maximum circumferential stress (MCS) criterion, which assumed that the crack kinks in the direction where the circumferential stress surrounding the crack-tip is the maximum. Alternatively, Sih [70, 71], introduced the minimum strain energy density (MSED) criterion and assumed that fracture occurs in the direction where the strain energy density is the minimum. Smith *et al.* [72, 73] developed a maximum tensile stress criterion by considering T-stress. The maximum energy release rate (MERR) criterion based on Griffith's theory was proposed by Palaniswamy and further developed by Hossein *et al.* [74–76]. Later, the general mixed-mode brittle fracture criterion based on the concept of maximum potential energy release rate (MPERR) was introduced by Chang *et al.* [77]. The aforementioned criteria can be applied to forecast fracture in brittle materials. Mixed mode crack propagation and the direction of crack propagation are studied in details in Chapter 4.

2.3 Predicting Crack Trajectories in Brittle Materials

Studying crack propagation in elastic materials requires solving three distinct problems. Firstly, a numerical or analytical method to calculate interactions between cracks and inclu-

sions and to determine the stress and displacement fields around the crack must be available. Secondly, the method needs to be capable of computing the fracture parameters, such as stress intensity factors and energy release rate. Thirdly, one has to decide on criteria to characterise under which conditions and into what direction the crack will propagate.

To address the first and second problems, a critical review of the various existing methods of stress analysis in elastic solids with many cracks and inclusions is provided in the following section. Ideally, the method should be capable of predicting stress and strain fields as well as the fracture parameters. Then, the third problem is approached by providing a review of several methodologies used to model crack propagation in various media. The intention is to present a rational justification of the method that is used in this study to predict the interaction between elements of the system and also on the necessity of the new method to be able to study crack propagation in brittle materials.

2.3.1 Methods to Study Inclusions and Cracks Interactions

In mechanics of elastic solids containing a network of cracks and inclusions, the problem can be formulated respecting the local and effective properties. Interactions between cracks and inclusions significantly modify the local properties; hence they are sensitive to the positions of individual cracks and inclusions. However, the effective properties are generally derived as volume averaged quantities that are less influenced by the geometry and positions of cracks and inclusions. As studying the fracture-related problems at the microscopic level, which is the focus of this thesis, requires information of the local properties such as SIFs, this review is confined to methods that investigate the local properties and interactions between all elements of the system.

2.3.1.1 Numerical investigations

Finite Element Method

Engineering analysis of mechanical systems has been addressed by solving partial differential equations which are used to capture the behaviour of matter and physical principles. In general, deriving an analytical solution for these differential equations is often impossible except only for simple problems of regular geometries with most straightforward boundary conditions. Hence, several numerical methods, such as finite difference method (FDM) [78], finite element method (FEM) [79–81], mesh less methods [82], boundary element method (BEM) [83] and discrete element method (DEM) [84] have been developed during the last decades to tackle various problems in all branches of Physics and Engineering; particularly

relevant here are the techniques developed in the fields of Material Science and Applied Mechanics.

Finite element method (FEM) is the dominant discretisation technique for finding approximate solutions to many engineering boundary value problems. The fundamental concept in the physical interpretation of the FEM is the subdivision of the large model into smaller (non-overlapping) components of simple geometry called finite elements. The response of each element is expressed regarding the values of the unknown functions at a set of nodal points. The response of the original model is then approximated by assembling the collection of all elements. Comprehensive reviews of FEM can be found in [79–81].

Basic theory: In the FEM, the unknown parameters are obtained by minimising an energy functional. An energy functional consists of the total energies associated with the particular finite element model. Based on the law of conservation of energy, the variation of energy functional must be equal to zero. The basic equation for finite element analysis of solid materials is $\frac{\partial F}{\partial u} = 0$, where the energy functional and displacement parameter are expressed as F and u. This is based on the principle of virtual work (δW), which states that for a system under the static equilibrium the net force and net torque acted upon the system is zero. Each finite element will have its own unique energy functional. In stress analysis, the work form of the equilibrium equations for a continuous rigid body Ω with the surface Γ is:

$$\begin{aligned} \delta W &= \int_{\Omega} \nabla.\sigma d\Omega + \int_{\Omega} f d\Omega + \int_{\Gamma} T d\Gamma \\ &= \sum_{i} (\int_{\Omega_i} \nabla.\sigma d\Omega_i + \int_{\Omega_i} f d\Omega_i + \int_{\Gamma_i} T d\Gamma_i) = 0, \end{aligned} \tag{2.9}$$

where, σ is the stress tensor, f is total the body forces, and $T = n.\sigma$ is the total boundary tractions describing the contribution of the external boundary conditions. The domain Ω is covered by sub-domains Ω_i with the supported surface Γ_i. The first integral on the right hand side of the equation demonstrates the internal strain energy and the second and third integrals are, respectively, the potential energy contributions of the body force loads and distributed surface loads. In FEM, the displacement field is approximated by:

$$u = \sum_{i} \phi_i u_i \tag{2.10}$$

where u_i is the nodal value of the displacement components and ϕ_i is the piecewise polynomial shape function associated with node i. The orthogonality condition requires the functions ϕ_i to satisfy the partition of unity principle ($\sum_i \phi_i = 1$) [85]. The displacement equation and its piecewise polynomial functions are the key points to express that the classical FEM can

not support the large gradients and discontinuity problems of cracks and voids. Piecewise polynomials are more suitable for the approximation of smooth functions and they are not tailored for the approximation of non-smooth functions.

Also, FEM is a very versatile numerical approach, but this flexibility comes at a price of mesh-generation. Construction of good quality meshes is not convenient and often accounts for large computational costs in finite element simulations. Therefore, conventional FEM has been modified and extended by changing the smoothness of the shape functions, node distributions and a local mesh refinements. Intensive research over the past 3 to 4 decades has extended conventional FEM to new FEM-based methods available to model cracks and discontinuities, for example extended FEM, generalised FEM and partition of unity FEM [86–90]. Extended finite element method, which is commonly used for the problem of crack propagation [12, 91, 92], is briefly revisited in more details in the following section.

Extended Finite Element Method

The eXtended Finite Element Method (XFEM) is an extension of the FEM. The method is developed by Belytschko *et al.* [92] using a new approximation for the displacement field. In XFEM, Displacement field can be decomposed into the standard part u^{fem} and into an enriched part u^{enr} as:

$$\begin{aligned} u &= u^{fem} + u^{enr} \\ &= \sum_{i \in N^{fem}} u_i \phi_i + \sum_{j \in N^{enr}} a_j \phi_j \rho \end{aligned} \tag{2.11}$$

where u_i and a_j are the standard and the enriched nodal variables associated with node i and node j, respectively. N^{fem} is the set of all the nodes in the finite element mesh and N^{end} is the set of nodes that are enriched with the enrichment function ρ. The enrichment function ρ carries the information about the underlying physics of the problem. For example, for the problem with strong discontinuities such as crack, ρ can be selected as the Heaviside function.

In XFEM simulation the enrichment can be done on all the nodes in the finite element mesh (global enrichment) or on some of the nodes (local enrichment). In most of the simulations such as cracks and interfaces, the region of interest is localised and the enrichment can be restricted close to the region of interest. For the case of linear elastic fracture mechanics, the displacement proposed in Equation 2.10 is replaced by a generalised displacement function that contains two sets of functions, a jump enrichment functions to describe the

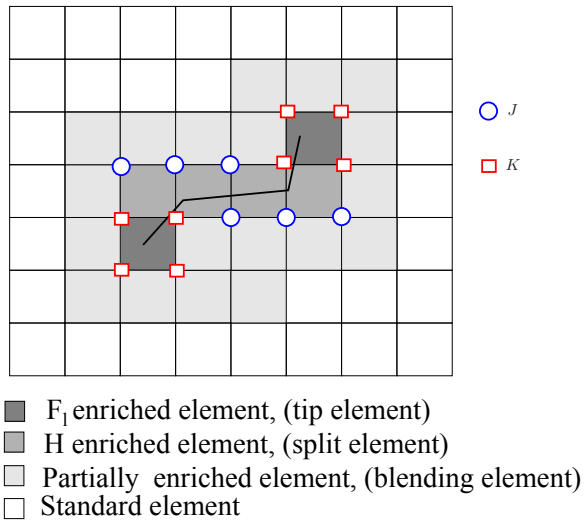


Fig. 2.4 A typical and fully enriched FEM mesh with an arbitrary crack. circled nodes and squared nodes are enriched. Partially and fully enriched elements are the elements whose nodes are enriched [3].

discontinuity of crack faces and asymptotic branch functions that span the two-dimensional asymptotic crack-tip fields. The approximation of u takes the form:

$$u = \sum_{i \in I} u_i \phi_i + \sum_{j \in J} b_j \phi_j H + \sum_{k \in K} \phi_k (\sum_{l=1}^{n} c_k^l F_l) \tag{2.12}$$

As shown in Figure 2.4, H is a jump enrichment function of the circular nodes (J), and in this case only provides for the modelling of the discontinuity up until the crack-tip. The H function has the value 1 "above" and -1 "below" the crack. b_j and c_k^l present the nodal enrichment degree of freedom vectors. n is the total number of near-tip asymptotic functions. The squared nodes (K) are enriched with the asymptotic crack-tip functions F. The function F for isotropic elasticity is defined as:

$$F(r,\theta) = \{\sqrt{r}\sin(\theta/2), \sqrt{r}\cos(\theta/2), \sqrt{r}\sin(\theta/2)\sin\theta, \sqrt{r}\cos(\theta/2)\sin\theta\} \tag{2.13}$$

where (r,θ) are the local polar-coordinates at the crack-tip. Details of models and simulations can be found in [93, 94]. In the complex system where cracks and inclusion are

interacting, the enriched approximation takes the following form:

$$u = \sum_{i \in I} u_i \phi_i + \underbrace{\sum_{j \in J} b_j \phi_j H + \sum_{k \in K} \phi_k (\sum_{l=1}^{n} c_k^l F_l)}_{for\ cracks} + \underbrace{\sum_{m \in M} d_m \phi_m \psi}_{for\ inclusions} \tag{2.14}$$

where, d_m is the nodal degrees of freedom that corresponds to the enrichment function, ψ, given by Equation 2.14 to capture the inclusions discontinuity. M is the set of nodes enriched with the enrichment function.

Implementation of the XFEM involves several stages. The calculation begins by producing the usual finite element mesh, and then determining the interfaces or discontinuities explicitly. For the case of local enrichment the nodes that needs enrichment have to be selected using area criterion or the nodal values. Later, depending on the physics and geometry of the problem, different enrichment function should be selected and added to the finite element approximation and integrated over the system.

Although XFEM is powerful and applicable to the variety of problems, the flexibility provided by this method leads to its associated difficulties; specifically in numerical integration over the enriched elements. Problems encountered during the implementation of this method include issues with (i) singular and discontinuous enrichment functions in integrating over the elements that are intersected by the discontinuous surfaces, (ii) oscillations in the results over the elements that are partially enriched, (iii) poor convergence rate, (iv) necessity of the post-processing stage to extract the SIFs from the computed displacement field, and (v) ill condition stiffness matrix caused by addition of enrichment functions to the finite element approximation basis. Significant amount of work has been done to improve the method [3, 91, 95–97], and more investigations are required.

Boundary Element Method

The boundary element method (BEM) is an integral equation technique for solving a wide variety of problems in science and engineering [83]. In FEM, the entire system must be discretised to set up the algebraic equations and get the solutions. Creating a suitable mesh for the problem is a curtail and time-consuming process. The particular feature of BEM is the fact that the discretisation of the problem domain is confined to the boundary alone. Reduction in the dimension of the mesh generation problem results in a significant saving in computational costs.

In BEM, the problem is solved by superposing singular solution of all segment distributed over the entire boundary of the problem. The singular point on the boundary exerts influences

on every point on the boundary. In the final calculations, the impacts of single sources have to be summed over all boundary segments. After the unknowns on the boundary points have been derived, stress and strain fields inside the domain can be determined.

Boundary value problems in linear elasticity are formulated in two ways; the direct formulation, which constitutes the basis of most modern BE codes, and the indirect one which is an unmediated outcome of the superposition principle [98, 99]. In the case of the direct approach, the elasticity problem can be formulated in terms of displacements or stress fields, to give the basis of the conventional or hypersingular formulation of BEM. In the direct BEM the integrals are carried over the field points while in the indirect BEM, they are taken over the source points. In both methods, the boundary integral formulations give rise to ill-conditioned problems at points characterised by geometric discontinuities. Integrals have to be evaluated numerically using various methods, such as Gaussian quadrature. Analytical evaluation of the integrals is not straightforward, especially in the direct BE scheme.

BEM is highly flexible while several features can be easily incorporated in the analysis. Interaction between inclusions and cracks, and effects of material properties such as young modulus mismatch and variation of poisson ratio ratio have been studied by many authors [100–105]. Although substantial research has been conducted on the field of BEM, it is by no means complete. This method and its associated computer codes are in an experimental stage, and there might exist problems of reliability. Also, this technique is applied mostly to two-dimensional problems, due to its semi-analytical nature (and the limited number of analytical solutions available for 3D problems) and a lack of supporting commercial software. Nevertheless, BEM can be combined with different methods, in which the strength of several approaches can be exploited to optimise the process of numerical calculations. This particular aspect of the BEM is used later in our implementation of the methodology used to treat finite size problems in Chapter 4.

Meshless Method

As the use of elements or mesh in the previously proposed methods is the main root of computational costs and problems, the idea to avoid the explicit use of elements and meshes has been recently explored and the concept of meshfree or meshless methods have been proposed by various researchers. Meshfree methods use a set of nodes, named field nodes, distributed within the problem domain and on the boundaries. Field nodes require no prior information on the relationship between the nodes to approximate the unknown field distributions. The density of the nodes is not necessarily uniform and depends on the accuracy desired. Meshless methods are more accurate than FEMs and do not have a mesh generation problem but imposition of the essential boundary conditions may require special treatments.

Also speedwise, it can be more computationally demanding than the FEM because of the complex nature of meshless shape functions and evaluation of integrals in the domains under investigation. The meshfree method has been implemented in various types of fracture mechanics applications, such as single and mixed mode crack problems, fatigue crack growth, and dynamic crack analysis as well as other typical engineering applications such as vibration of cracked structures [106–111]. Barbieri *et al.* [112–114] introduced a new enriched weight function and used the meshless method to study the evolution of multiple arbitrary and branching cracks in two dimensions in an elastic isotropic body. They have shown that the method is capable of handling heavily kinked and branching cracks with accurate stress intensity factors and optimal convergence rates in two but also in three dimensions. Although meshless methods have shown good potential to become powerful numerical tools, these methods are are still in their development stage. There are technical issues that have to be resolved before the methods can become practical tools for complex engineering problems.

Summary: Several techniques have been developed to predict stress field distributions in a system. The finite element method (FEM) is one of the most widely used tools for studying stationary cracks and fracture along a pre-defined path [79–81], but localised features such as cracks, holes, and inclusions are not efficiently resolved by mesh refinement, and interactions between elements of the system and consequently general path crack growth cannot be modelled accurately and efficiently using conventional FEM, which in part led to the development of the extended finite element method (XFEM) by Belytschko *et. al* [92] and by many researchers [91, 95–97]. Another alternative to FEM is the boundary element method (BEM), also referred to as the boundary integral equation method (BIEM) [98, 83]. The main attraction of BEM is the reduction of the spatial dimensions of the problem since only the boundary needs to be discretised. Despite the fact that the simulation of the full stress field distributions is possible with the XFEM and BEM and meshless methods, they become computationally expensive techniques when the number of localised features is increased. Therefore, there is scope to develop more efficient tools to study a complex crack network interacting with inclusions.

2.3.1.2 Analytical and semi-analytical investigations

The Kachanov Method

Interactions between cracks can be studied in terms of far-field tractions and stress superpositions. Kachanov proposed a simple method based on the superposition technique and the principle of self-consistency [4, 115]. A linear elastic solid with N cracks subjected to

the external far-field load σ^{∞}, can be equivalently formulated as a problem where all the crack faces with unit normals n_i are subjected to traction $t_i = n_i.\sigma^{\infty}$. Using the superposition principle the system is decomposed into the N subsystems each containing one crack loaded by an unknown traction t_i. As cracks can not act independently in the system and the stress fields of any crack extend throughout the system, each crack should be considered as a source of external fields for the rest of the cracks. Thus, the amount of stress fields experienced by each crack σ^i is the summation of the far-field load and the disturbance fields. Disturbance fields are induced at the crack site by other cracks in the system. Hence, σ^i is formulated by:

$$\sigma^i = \sigma^{\infty} + \sum_j{}' \sigma^{ij}, \tag{2.15}$$

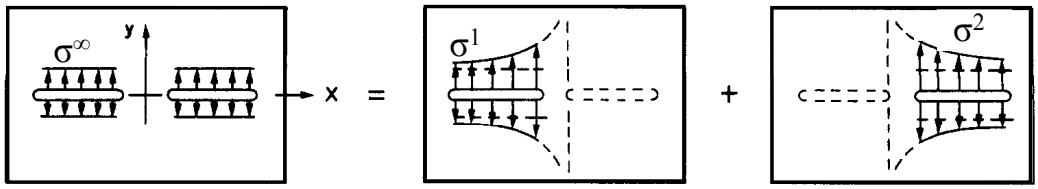
and the unknown traction t_i formula is derived by:

$$t_i = -n_i.\sigma^{\infty} + \sum_j{}' t^{ij}. \tag{2.16}$$

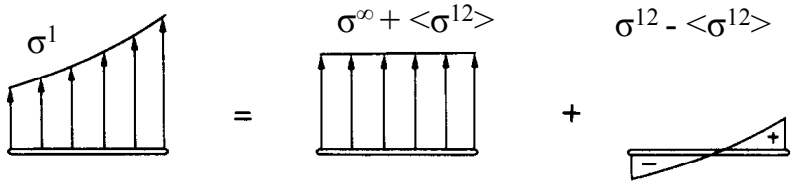
Where σ^{ij} is the stress field generated by the $j-th$ crack at the $i-th$ crack site, and $\sum'_j \sigma^{ij}$ is the disturbance stress field created at the $i-th$ crack faces by other cracks. Likewise, t^{ij} is the traction generated by the $j-th$ crack at the $i-th$ crack faces. The principle of self-consistency requires that all cracks and micro-cracks experience the same amount of averaged effective stress field [116], i.e. the traction induced on a given crack by other cracks is approximated using the average traction generated by all other cracks.

Figure 2.5 shows that the average traction on each crack corresponds to the uniform average traction as well as the non-uniform term. Neglecting the impact of the non-uniform traction is the key assumption of the method. The assumption is acceptable where the cracks are well separated and the short range interactions are negligible. However, short range interactions are noticeable in fracture of real material. The first step to solve the problem is determining the uniform average traction on each crack; $< t_i >$ is the average traction vector for the $i-th$ crack.

The average traction induced on the $i-th$ crack by the $j-th$ crack is taken as ($< t^{ij} >= \Lambda_{ij} < t^j >$), where Λ_{ij} is the interaction factor and reflects the geometry of the cracks. Therefore, by knowing the average tractions $< t_j >$, and interaction factors the problem would be solved. With respect to Equation 2.16, tractions on each crack can be calculated by a linear equation containing the far-field stresses and uniform average traction of other cracks. Similarly, the total equation of tractions produce a system of $2N$ linear algebraic equations. These equations can be written systematically using the interaction matrix $[\Lambda_{ij}]$.



(a)



(b)

Fig. 2.5 The Kachanov method, (a) decomposition of two interacting cracks under the σ^{∞} far-field load, (b) the unknown traction on each crack is sum of the average and the non-uniform term (with zero average) [4].

$$(\delta_{ij}I - \Lambda_{ij}).< t_i >= t_j^{\infty} \tag{2.17}$$

The interaction matrix is not symmetric and it reflects the geometry of the crack system independent of the remote loading conditions (t_j^{∞}). Kachanov derived formulas to obtain crack's SIFs using $< t_i >$ [4, 115, 117]. Depending on the geometrical configuration of the crack system, SIFs can decrease ("shielding") or increase ("amplification"). The errors in the evaluation of the SIFs depend on the geometry of the crack network (crack sizes and distance between cracks), and they are typically small and negligible if the spacing between cracks is on the same scale as the length of the crack.

Crack-micro-crack interaction: Interactions between a main crack-tip and a cluster of micro-cracks is an example of the application of this method. Simulation results are summarised here [118, 116]:

"Short range" and "long range" interactions; two distinct zones are defined for crack and micro-crack interaction. A region consists of several micro-cracks [119–121] located in the proximity of the main crack-tip is a short range interaction zone. The interaction in this field is highly sensitive to the exact positions of micro-cracks.

Fluctuation of the interaction effect: SIF is highly sensitive to the local geometry of the micro-cracks, thus, for the random field of micro-cracks the SIF can potentially fluctuate significantly from shielding ($K/K_0 < 1$) to amplification ($K/K_0 < 1$); K_0 denote SIF of the main-crack in the absence of micro-cracks. Crack propagation initiates at local peaks of amplification. Therefore, the nonlocal properties of the material, such as effective elastic constants at the micro-crack zone, can not adequately predict local fluctuations and consequent crack propagation in brittle materials.

Impact of the "wake region" of micro-cracking: The presence of micro-cracks in the wake region produces a shielding effect. Due to the low stress level in the wake region, the shielding effect is typically smaller than the fluctuation of the SIFs from sample to sample. Thus, the effect shielding in the wake region is not statistically notable.

"Clusters" of micro-cracks: the effect of micro-crack clusters on the main crack-tip: The crack-tip is in-sensitive to the position of individual micro-cracks in the cluster system. This means that the cluster can be simulated by one effective micro-crack. The density (D) and the relative position of the cluster to the main crack-tip determine the effective micro-crack length ($L \propto D^{1/2}$).

Despite the simplicity of the method, the results summarised above can provide a good understanding of the system size and the number of cracks and inclusions that are required in the simulation in order to predict the crack propagation path.

However, like most of the simulation methods, this method has some limitations. For example, using the method requires knowledge of the full stress field for one crack when tractions applied along the crack faces. The full field solution is available for only special shapes, thus the model is restricted to crack's shape. Later, Kachanov used effective properties and density matrix to include the effect of inclusions [122, 123], but his optimal method is only applicable to solve crack interaction problems. In 2D, the polynomial method is more efficient while in 3D configurations, the Kachanov method is more accurate. Also, the method is not applicable to the problems with non-uniform external field; in this case other methods such as polynomial expansion of traction are recommended [124]. Further issues with the method are associated to the relationship between the uniform far-field and the effective field at the surface of each crack. Feng suggested a field correction for this problems; details of his method can be found in [125–127]. Finally, the accuracy of the model depends on the configuration and the distances between the cracks. The non-uniform traction becomes important as the spacing between cracks reduces. Corrections have been applied to the Kachanov method for the problems containing closely spaced cracks. In the subsequent section, two of these attempts are presented.

Modified Kachanov method for closely crack interactions

A) Garbatikh proposed a method to calculate SIFs for closely spaced cracks in 2D problems [128]. His model is inspired by the analytical method of Kachanov, who neglected the non-uniform traction; hence, the accuracy of calculations depends on the arrangement and geometry of cracks. For closely spaced cracks, the use of average tractions is not adequate and $t_j(\xi_j) - < t_j >= \Delta t_j \neq 0$, where ξ_j and t_j are the local axis and traction of the $j-th$ crack. Significant changes in Δt_j within a small area lead to non-negligible changes in SIFs.

In the Garbatikh method, the total traction on each crack (t_j) is divided into symmetric and asymmetric parts. For the symmetric part, the average traction along the crack is non-zero, while it becomes zero for the asymmetric one.

$$t_j(\xi_j) - < t_j >= \Delta t_j \neq 0 \tag{2.18}$$

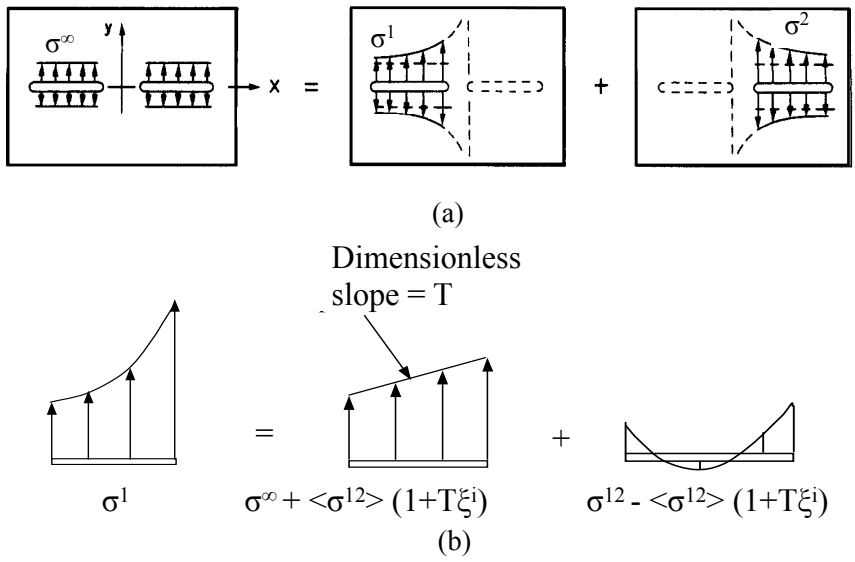


Fig. 2.6 Interaction between two cracks, (a) decomposition of two interacting cracks under the σ^{∞} far-field load, (b)Traction on each crack is sum of its linear varying term and a non-uniformity with zero average [5].

$$\begin{aligned} t_j &= < t_j > + \Delta t_j \\ &= < t_j >^s + \Delta t_j^s + < t_j >^a + \Delta t_j^a \\ &= < t_j >^s + \Delta t_j^s + \Delta t_j^a \\ &= t_j^s + t_j^a \end{aligned} \tag{2.19}$$

In this notation, the same formulation as the Kachanov approach can be used to solve the SIF of the cracks. However, the total number of equations are doubled because of the separation of symmetric and asymmetric parts. This model could improve SIFs of two stack-like cracks compared with Kachanov method by a factor of ten. Although, the method has been developed for SIF calculations and other quantities, some calculations like stress fields or displacements may not be derived correctly. Furthermore, calculations have been done for stack-like cracks and other configurations require more investigation.

B) Results of Kachanov method based on uniform tractions are considered as the zeroth order approximation for the interacting cracks problem. The first order approximation is defined when tractions between two cracks have linearly varying components and non-uniform terms (Figure 2.6); again the average value of the non-uniform term is neglected. Using the higher order approximation with a perturbation approach similar to the method originally proposed by Kachanov can enhance the accuracy of the calculations. Li *et al.*

proposed the first order approximation by including the effect of a linearly varying component [5]. This means that t^{ij} term in Equation 2.16 becomes:

$$t^{ij} =< t^{ij} > (1 + T\xi^{i}), \tag{2.20}$$

and T is the dimensionless slope of average field at the $i-th$ crack demonstrated in Figure 2.6. The average tractions $< t^{i} >$ can be derived using the equation 2.17, and disturbance fields t^{ij}, and tractions t^{i} can be calculated afterward. These calculations enable us to predict the evaluation of the first order tractions of closely-spaced cracks. A similar process can be utilised to obtain crack interactions with higher order approximations. The accuracy of this method has to be studied in more detail. Computing higher order terms requires computationally expensive algorithms, so a trade-off between accuracy and computational cost must be found.

2.3.1.3 Polynomial approximation of traction:

In an elastic solid, a problem containing N cracks (inclusions) is decomposed into a sub-problem of homogeneous solid and N subproblems containing a single crack (inclusion) with unknown tractions. In the polynomial approximation method, the unknown traction on each crack (inclusion) is expanded into a polynomial of degree M with the unknown coefficients. Coefficients of the polynomial have to be found by solving $2N(M+1)$ linear algebraic equations [129].

A Maxwell's Method:

This model has been used in multiple fields in physics. The logic behind the method everywhere is similar to the Maxwell's method in conductivity [130]. Maxwell described the effect of a cluster of spherical particles in an infinite space and in a presence of the far-field with an equivalent sphere whose conductivity is equal to the effective sphere. Likewise, the effective properties of composite, porous and micro-cracked isotropic materials with a periodic or random structure can be estimated using an equivalent spherical particle. The aim of the Maxwell's model is to establish the impact of the impurities in an infinite matrix of the host material at larger distances from the cluster [131, 132].

However, the drawbacks of this method restrict its applications. One of the difficulties is that the resultant effective properties must be isotropic. In this approach, neither the interaction between particles nor their geometrical arrangements are taken into account. Thus, the Maxwell method has to be combined with other methods to lessen its limitations; several attempts can be found in [133, 134]. One of the examples that is explained later

in this report is the finite cluster method of the multipole expansion. It can be viewed as the generalised Maxwell's approach where the interactions between particles are taken into account [135].

Multipole Method

The multipole method (MM) is a powerful theoretical based method that can be used for heterogeneous solids. MM is a series based method that reduces the boundary value problem in the homogeneous domain to an ordinary system of linear algebraic equations. In this method, interactions between several different inclusions can be taken into account. microstructural effects on the local field and, consequently the effective properties can be derived. The MM method can be viewed as a generalised Eshelby's model expanded for the case of the non-uniform field load [135, 136].

In the expansion method, coordinate systems and appropriate basis functions, which form full orthogonal sets, are selected analytically according to the shape of the inclusions, basic differential equations for equilibrium, matrix-to-inclusion bonding conditions at the interface, and, finally, asymptotic behaviour at infinity. Study of the system with different shapes of inclusions is restricted to the availability of the well-known analytical expansion functions. Expansion functions are available for the spherical and spheroidal shapes as well as unidirectional fibres with circular or elliptical area [137–140]. In addition to the above restriction, this method can be applied only to linear boundary value problems.

Nonetheless, because most of the calculations are done analytically, the efficiency of the model is high. The efficiency of the method for the effective properties, in which require average quantities, becomes more prominent for larger scale calculation. Using the fast multiple scheme, consideration of the more realistic larger scale problem is possible. Due to the analytical nature of the method, it can provide a good insight into the physical essence of the problem. Also, unlike other methods, both inclusions and cracks can be investigated in a system for some specific shapes [135]. Mandatory steps of the method are outlined below:

1. Writing the solution using the linear superposition method.
2. performing a local regulation expansion of the sum in the vicinity of the inclusions (cracks).
3. Finding a linear set of equations by fulfilling the boundary condition.
4. Calculating the numerical solution of the linear system.
5. Calculating stress and displacement fields using the derived numerical solution.

Summary: Micro-crack and inclusion interactions have been studied using analytical and numerical methods before: notably the Kachanov method [115, 4, 116–121], the modified Kachanov method for closely interacting cracks [128, 5], the polynomial approximation method [129], Maxwell's method [130–134] and the Multipole method (MM) [135–140]. Kachanov considered the average traction exerted on a crack by the other cracks in the system; this was later modified [128, 5] to account for linearly varying traction along the crack. Another method approximated the traction using a polynomial expansion [129], which further improved the accuracy of the representation of the traction along the crack. This method was used and developed in both Maxwell's method and the Multipole method.

The Maxwell's method is extended to the problem of linear elasticity by McCartney *et al.* [131, 132]. The aim of the method is to establish the impact of the impurities in an infinite matrix of the host material at larger distances from the cluster. However, in this approach, neither the interaction between particles nor their geometrical arrangements are considered. The main concept of this method is used and extended by Kuchsh to develop a new method named the multipole method [135]. The MM is a series method that reduces the boundary value problem in the homogeneous domain to an ordinary system of linear algebraic equations [135–140].

The multipole method is a powerful theoretical based method that can be used for heterogeneous solids. In this method, interactions between several different inclusions can be taken into account. Consequently, microstructural effects on the local field and, the effective properties can be derived. The method can evaluate both local fields and effective properties of the material. Due to the analytical nature of the method, it can provide a good insight into the physical essence of the problem. Also, interactions between inclusions (for some specific shapes) and cracks can be calculated in one system [135]. Investigation of all methods indicates that the multipole method is likely to be the most suitable one to analyse stress and strain fields in elastic solids in the presence of multiple cracks and inclusions. Details of the method are provided in the next chapter.

2.3.2 Method to Study Crack Propagation

In Section 2.3.1, several methods to study interaction between cracks and inclusions are reviewed and the most appropriate one is introduced. Once the stress field distributions and SIFs are calculated, and the fracture criterion and the condition on which the crack can propagate are selected, all the requirements to study crack propagation in quasi-static region are provided.

Crack propagation is a step by step process, in which the crack advances incrementally at each simulation step. The general algorithm to study a crack propagation regardless of the numerical method is as follow. First, stress and displacement field distributions and SIFs are computed for the current state of the system. Second, in the case where the crack growth becomes possible, an appropriate fracture criterion determines the crack increment and propagation direction. Third, the crack size is updated and the iterative process is continued.

Many techniques have been developed to predict crack propagation path. Several stress analysis methods, such as FEM, XFEM, and BEM have been incorporated in the general crack propagation farm work. Intensive works have been done to improve the crack propagation techniques [85–90], [92], [141–144]. The most promising method in the problems of crack propagation is the XFEM. Benzley [141] introduced an enrichment to FEM using asymptotic solutions of static fracture problems. For static crack propagation problems, Black and Belytschko [85], Moes et al. and Dolbow et al. [92, 142] developed XFEM method. The method was also generalised to arbitrary discontinuities by [89, 143, 144].

Despite the popularity of the XFEM in predicting the crack propagation, studying fractures in composites, where networks of cracks, inclusions, and grain boundaries are present, is often not computationally feasible using this method. According to the previous investigation proposed in Section 2.3.1, the multipole method is a promising method to study the interactions between crack/inclusions. However, there is no available crack propagation framework that uses the multipole method. A solution to the problem is developing a new technique that uses the general crack propagation algorithm but employs a semi-analytical method to calculate stress fields and SIFs at each simulation step. In this work, the author aims to develop a new tool to predict fracture in brittle and semi-brittle materials containing cracks and inclusions.

2.4 New Methodology to Study Media Containing Cracks and Inclusions

Fracture is a limiting factor in the sustainable development of brittle materials. Engineering and tailoring the structure of these materials can enhance their toughness and consequently their performance. The ability to guide and deflect the crack is fundamental to enhance the performance of the brittle materials, as the crack deflections from the straight line elevates the material's toughness [59–61]. Interactions between the main crack and imperfections such as inclusions specially with weak interfaces, small voids, and grain boundaries can deflect and channel the crack along the predefined path [13, 12, 100, 103, 145]. Thus, predicting

crack trajectory in materials containing cracks, inclusions and interfaces is essential for the design purposes.

The objective of this thesis is to develop a new technique to predict the evolution of the crack networks in heterogeneous solids containing elliptical inclusions. Similar to other computational methods, such as Molecular Dynamics or Discrete Dislocation Dynamics [146–148], the validity of the calculations relies upon resolving the elastic interactions of defects in the system. In the new method proposed by the author, elliptical inclusions and cracks are the basic constituent elements of the system and play a role analogous to that played by dislocations in discrete dislocation dynamics. The initial step in developing a method is to accurately characterise the the localised stress fields caused by micro-structures, and their interactions. Calculating interactions between elements of the system is the main objective of Chapter 3. Evolution of individual micro-cracks and their interaction with existing cracks/inclusions is then predicted using what we refer to as the Discrete Crack Dynamics (DCD) method. This approach is fast (semi-analytical) and reliable, and particularly suitable for the prediction of evolving low-speed crack networks in brittle or quasi-brittle materials. Details of the method development and its application to some benchmark problems are reported in Chapter 4.

Chapter 5 is focused on the effect of the interfacial strength of elliptical inclusions and grain boundaries in crack deflection. Results of this chapter are valuable for engineering design purposes. The method is developed to channel a crack into a toughening configuration (array of elliptical voids and soft inclusions) to obtain the optimal toughening configuration in a simple problem.

Finally the method is further developed in Chapter 6 to determine the effects of residual stresses in general, and the residual thermal stresses associated with inclusions in particular, on the crack propagation path. The study is extended to characterise the influence of residual stresses and thermal stresses on crack propagation in PCDs.

Chapter 3

Interaction Between Elements Of A System

" A multipole expansion is a series expansion of the effect produced by a given system in terms of an expansion parameter which becomes small as the distance away from the system increases [149]."

3.1 Introduction

The multipole method provides a fast, accurate solution for multi-inclusion systems (where cracks may be thought of as collapsed elliptical inclusions). The method evaluates the local stress field in the vicinity of the inclusions using the linear superposition principle. The local field is the linear sum of the incident far-field and the fields generated by all inclusions. The problem has to be solved for the entire array of inclusions simultaneously. With the exception of the basis functions, which must be chosen according to the geometry of the inclusions, the solution procedure is identical for different shapes of inclusions [135–140]. In this chapter, the basic notation of the stress and displacement fields in terms of the complex potentials and terminology of the multipole method are introduced. Then, a general solution for a system comprising a finite array of elliptical inclusions and cracks is proposed.

3.2 Conformal Mapping And Complex Variable Analysis

Conformal mapping is a mathematical technique that converts one problem into another that is easier to solve. This technique involves a conformal map function $f(z) = w$ that maps a domain U to an image V in the complex plane. More precisely,

$$f : U \to V \quad with \quad U, V \subset C^n \tag{3.1}$$

where in general, f is a holomorphic (analytical) function that preserve local angles and can be uniquely written as

$$f(z) = u(x,y) + iv(x,y). \tag{3.2}$$

u and v are two real harmonic functions of x and y variable. *f(z)* is a conformal mapping if and only if $f'(z) \neq 0$ everywhere on the domain. Applications of conformal mapping can be found in many physical problems that obey Laplace and Biharmonic equations. The Laplace equation ($\nabla^2\Phi(x,y) = 0$) is invariant under conformal mapping. Due to the uniqueness of Laplace solutions, this method can facilitate obtaining the analytical solution for the 2D potential field ($\Phi(x,y)$). Problems of plane elasticity can be reduced to solution of Biharmonic equations ($\nabla^4\Phi = 0$). Biharmonic equations are invariant under conformal mapping, however, the invariance is more restricted. The potential Φ can satisfy the biharmonic equation only if it is continuous up to and including the fourth order. It is also necessary that the function and its derivatives be single valued throughout the region under consideration. In section 3.2.1, a conformal mapping to transform elliptical objects in one coordinate system into straight lines in another coordinate system is presented.

3.2.1 Conformal Mapping From Elliptical To Cartesian Coordinate Systems

The most convenient conformal mapping for problems containing elliptical objects is [140] $z = x_1 + ix_2 = \omega(\xi) = d\cosh\xi$, where $\xi = \zeta + i\eta$. Setting ζ equal to a constant, ζ_0, the Cartesian axes become $x_1 = d\cosh\zeta_0\cos\eta$ and $x_2 = d\sinh\zeta_0\sin\eta$, which describes an ellipse in the $x_1 - x_2$ plane with major and minor axes $2d\cosh\zeta_0$ and $2d\sinh\zeta_0$ respectively, for which the aspect ratio is $e = \tanh\zeta_0$, and d is again the distance between the foci. Thus the locus of the ellipse in the z-plane corresponds to a straight line $\zeta = \zeta_0$ in the ξ-plane. Assuming the $\cosh^{-1}(z/d) = \ln[(z/d) + \sqrt{(z/d)+1}\sqrt{(z/d)-1}]$, the definition of the inverse mapping $\xi = \cosh^{-1}(z/d)$ requires branch points at $(\pm d, 0)$ and branch cuts at $(-\infty, -d]$ and $[d, \infty)$. As analytical functions are permitted to have singularities and branch points, where they cannot be differentiable, all properties pertinent to the conformal mapping are not satisfied at these locations.

3.3 In-Plane Elasticity Problem

In the 2D framework, both plane strain and plane stress basic equations of elasticity can be studied with complex potentials [136, 135]. The Muskhelishvili-Kolosov complex analytic potential functions $\varphi(z)$ and $\tilde{\psi}(z)$ are introduced, in terms of which the stress tensor components σ_{ij} and displacement vector $\mathbf{u} = (u_1, u_2)$ may be expressed in plane strain as follows:

$$\begin{aligned} \sigma_{11} + \sigma_{22} &= 4\mu \left[\varphi'(z) + \overline{\varphi'(z)} \right] && (3.3) \\ \sigma_{22} - \sigma_{11} + 2i\sigma_{12} &= 4\mu \left[\bar{z}\varphi''(z) + \tilde{\psi}'(z) \right] && (3.4) \\ u_1 + iu_2 &= \kappa\varphi(z) - z\overline{\varphi'(z)} - \overline{\tilde{\psi}(z)} && (3.5) \end{aligned}$$

where μ is the shear modulus, ν is the Poisson's ratio, and κ is Kolosov's constant factor equal to $3-4\nu$ for plane strain and $\frac{3-\nu}{1+\nu}$ for plane stress. The complex conjugate of a function $f(z)$ is written as $\overline{f(z)}$ and the primes denote differentiation. The displacement vector $\mathbf{u}$ in the complex form is $u = u_1 + iu_2$. Following Kushch [150] a potential $\psi(z) = \tilde{\psi}(z) + z\varphi'(z)$ is defined, in terms of which equations 3.3 to 3.5 become:

$$\begin{aligned} \sigma_{11} + \sigma_{22} &= 4\mu(\varphi' + \overline{\varphi'}) && (3.6) \\ \sigma_{22} - \sigma_{11} + 2i\sigma_{12} &= 4\mu \left[(\bar{z} - z)\varphi''(z) - \varphi'(z) + \psi'(z) \right] && (3.7) \\ u_1 + iu_2 &= \kappa\varphi(z) - (z - \bar{z})\overline{\varphi'(z)} - \overline{\psi(z)}. && (3.8) \end{aligned}$$

Under the conformal mapping from the z-plane to the ω-plane, the fundamental stress combinations in Equations 3.6 and 3.7 transform according to the following equations:

$$\begin{aligned} (\sigma_{11} + \sigma_{22})_z &= (\sigma_{11} + \sigma_{22})_\omega \\ (\sigma_{22} - \sigma_{11} + 2i\sigma_{12})_z &= \frac{\omega'(\xi)}{\overline{\omega'(\xi)}} (\sigma_{22} - \sigma_{11} + 2i\sigma_{12})_\omega . \end{aligned} \qquad (3.9)$$

The transformation Jacobean is given by $\frac{\omega'(\xi)}{\overline{\omega'(\xi)}}$. Also, let the displacement vector in the z-plane and the ω-plane be presented by u_z and u_ω respectively. The displacement vector transforms as:

$$u_z = \frac{|\omega'(\xi)|}{\overline{\omega'(\xi)}} u_\omega \qquad (3.10)$$

Details of transformation with conformal mapping of $z = \omega(\xi)$ can be found in reference [151]. Using the transformations given in Equations 3.9 and 3.10, the components of the

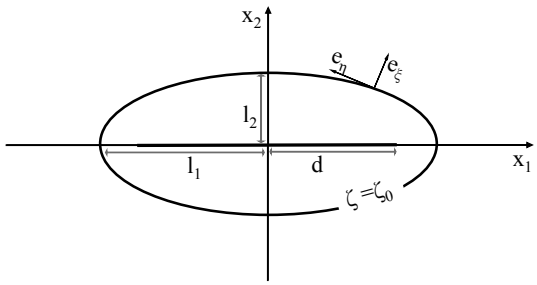


Fig. 3.1 Elliptic inclusion in a cartesian coordinate system. Local coordinates associated with the inclusion's surface are also displayed.

traction and displacement in the ω-plane are expressed by

$$\begin{aligned} \frac{t}{2\mu} &= \varphi' + \overline{\varphi'} - \frac{\omega'(\xi)}{\overline{\omega'(\xi)}}\left[(\bar{z}-z)\varphi'' - \varphi' + \psi'\right] \\ u &= \frac{\overline{\omega'(\xi)}}{|\omega'(\xi)|}\left(\kappa\varphi(z) - (z-\bar{z})\overline{\varphi'(z)} - \overline{\psi(z)}\right). \end{aligned} \tag{3.11}$$

In the following section, the conformal maping function and its attributed transformations are applied to the field components to study interactions between elliptical inclusions and cracks in an unbounded solid.

3.4 Solid With Elliptical Inclusions And Cracks

A general problem contains a distribution of shapes of cracks and inclusions, and the latter may deviate considerably from perfectly circular. Using elliptical inclusions instead of circular is of particular interest because both straight cracks and inclusions can be treated at the same time and with the same formalism, by regarding the former as collapsed, zero stiffness inclusions. We apply the multipole method here to a brittle material containing cracks, and elliptical inclusions with initially perfectly bonded (*i.e.* displacement compatible) interfaces. Basis functions for elliptical inclusions were introduced by Kushch *et al.* [135, 136].

3.4.1 Single Elliptic Inclusion In An Infinite Plane

Consider a single elliptic inclusion, embedded at the origin of the Cartesian coordinate system $(\widehat{x_1Ox_2})$, in an infinite isotropic elastic solid (Figure 3.1). The Ox_1 and Ox_2 axes are along the major and minor axes of the ellipse, which have lengths $2l_1$ and $2l_2$ respectively. The aspect

ratio and the distance between the foci of the ellipse are $e = l_2/l_1 < 1$ and $d = \sqrt{l_1^2 - l_2^2}$ respectively. Perfect bonding is assumed at the matrix-inclusion interface ($\zeta = \zeta_0$), thus displacement $\mathbf{u}$ and traction $\mathbf{t}$ are continuous there:

$$[[\mathbf{u}]]_{\zeta_0} = \mathbf{u}^{(0)} - \mathbf{u}^{(1)} = 0; \quad [[\mathbf{t}]]_{\zeta_0} = \mathbf{t}^{(0)} - \mathbf{t}^{(1)} = 0 \tag{3.12}$$

Upper indices 0 and 1 refer to the matrix material and inclusion respectively. Using the elliptical coordinate system and following Equation 3.11, the displacement and traction vectors can be written as

$$u = u_\zeta + iu_\eta = \frac{\overline{\omega'(\xi)}}{|\omega'(\xi)|}\left[\kappa\varphi(z) - (z-\bar{z})\overline{\varphi'(z)} - \overline{\psi(z)}\right] \tag{3.13}$$

$$t = \sigma_{\zeta\zeta} - i\sigma_{\zeta\eta} = 2\mu\left[\varphi' + \overline{\varphi'} - \frac{\omega'(\xi)}{\overline{\omega'(\xi)}}[(\bar{z}-z)\varphi'' - \varphi' + \psi']\right] \tag{3.14}$$

Finding suitable basis functions and potential functions are of paramount importance to facilitating the problem-solving process. Selection of the elliptical coordinate system for calculations determines the four $e^{\pm n\xi}$ and $\overline{e^{\pm n\xi}}$ fundamental basis functions for the complex potentials. Selection of basis functions depends on the location of the field, the source of the field, and inclusions [152, 153]. Kushch [136, 135] defined potential functions φ and ψ as power series based on the v function, where $v = e^{\xi} = z/d \pm \sqrt{(z/d)^2 - 1}$ and $v_0 = e^{\zeta_0}$.

$$\varphi = \sum_n A_n v^{-n} \tag{3.15}$$

$$\begin{aligned} \psi &= \psi_0 - \psi_1; \quad \psi_0 = \sum_n B_n v^{-n} \\ \psi_1 &= \frac{\sinh\zeta_0}{\sinh\xi}\left(\frac{v}{v_0} - \frac{v_0}{v}\right)\sum_n nA_n v^{-n} \end{aligned} \tag{3.16}$$

The sign and valid domain of parameter n can be determined according to the region where potentials are expanded. Here, a function is defined to be regular if it and its derivatives are bounded within the region, otherwise, it is singular (irregular). Potentials inside the inclusions caused by the far-field load, where the source field is placed at infinity are regular functions so, the parameter n includes both negative and positive values ($-\infty < n < \infty$). Stress fields around the inclusion in the matrix material have two sources: (i) the far-field load at infinity which necessitates regular potential functions ($-\infty < n < \infty$), and (ii) the mismatch in elastic properties of the inclusion and the matrix material. The disturbance fields in the vicinity of the inclusion caused by the mismatch in elastic properties have a

finite source in the plane and should vanish at infinity. The boundedness of the fields at infinity imposes a constraint on the solutions, so the disturbance fields caused by the material mismatch have to be singular ($n > 0$ where $\lim_{\xi \to \infty} v^{-n} = 0$). Furthermore, potentials have to be analytic and continuous throughout the domain and at the boundaries, this provides extra conditions for the expansion coefficient of the regular potential functions such that

$$A_n = A_{-n}; \quad B_n = B_{-n} + 2n sinh(2\zeta_0) A_{-n} \ \ (n > 0) \tag{3.17}$$

This information will be used to calculate displacement and stress fields. The solution procedures in the multiple method are summarised below:

- Finite fields inside and outside the inclusion are illustrated by $f^{(1)}(\mathbf{r})$ and $f^{(0)}(\mathbf{r})$ respectively and can be expanded by appropriate basis functions. The function f is a representation for both displacement and traction fields.

$$f(\mathbf{r}) = f_{far} + f_{dis} \tag{3.18}$$

  Where f_{far}, and f_{dis} are fields caused by an external far-field load, and a total disturbance field induced by all inclusions respectively; it is evident that $\lim_{r \to \infty} f(\mathbf{r}) = f_{far}$.

- A linear set of equations can be derived by implementing potential functions 3.15, 3.16, and 3.17 in the displacement and traction equations (3.13 and 3.14). The number of equations is truncated by applying boundary conditions of perfectly bonded inclusion-matrix interface.

$$[[f]]_s = 0 \tag{3.19}$$

  Where $[[f]]_s = (f^{(0)} - f^{(1)})|_s$ shows the continuity of the function f (displacement and normal traction) across the interface S. Details of calculations can be found in [135, 136]. A linear set of $4n$ equations for one inclusion under a far-field load is:

$$\begin{aligned}
\kappa_0 A_n - \kappa_1 C_n + (\overline{D_n} - 2n \sinh 2\zeta_0 \overline{C_n}) v_0^{2n} &= -\kappa_0 a_n + \overline{b_{-n}} v_0^{2n} \\
\overline{B_n} + \kappa_1 C_n v_0^{2n} - \overline{D_n} &= \kappa_0 a_{-n} v_0^{2n} - \overline{b_n} \\
A_n - \frac{\mu_1}{\mu_0} C_n - \frac{\mu_1}{\mu_0} (\overline{D_n} - 2n \sinh 2\zeta_0 \overline{C_n}) v_0^{2n} &= -a_n - \overline{b_{-n}} v_0^{2n} \\
\overline{B_n} - \frac{\mu_1}{\mu_0} (C_n v_0^{2n} + \overline{D_n}) &= -a_{-n} v_0^{2n} - \overline{b_n} \\
n = 1, 2, 3, \cdots &
\end{aligned} \tag{3.20}$$

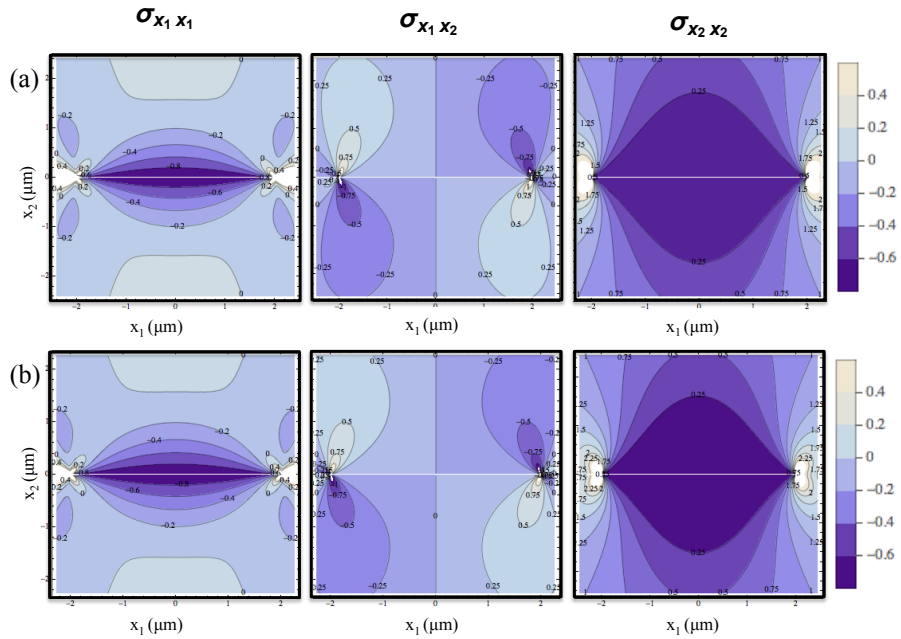


Fig. 3.2 Normalised stress field distributions of (a) an elliptical void with aspect ratio 0.5×10^{-5} in a diamond matrix (b) crack of length $4\mu m$ in an infinite plate with uniform far-field stress [6].

Where A_n and B_n are coefficients of the disturbance field in the matrix and C_n and D_n are fields coefficients in the inclusion region and finally, a_n and b_n are fields coefficients in the matrix resulting from the far-field load.

- From here, solving the problem is equivalent to deriving the expansion coefficients of Equation 3.20. Once the expansion coefficients are obtained, the potential functions and consequently displacement and stress fields can be calculated.

The problem is significantly simplified for the uniform far-field traction because all coefficients are $a_n = 0$ and $b_n = 0$ excluding $a_{\pm 1}$ and $b_{\pm 1}$. The $4n$ set of equations are reduced to only four equations.

3.4.1.1 Simulation results

To verify the reliability of the method two systems, first a pure material with an inclusion made of the same material as the matrix, and, second a crack-like inclusion were studied. When the inclusion and the matrix material were the same, the results given in appendix A

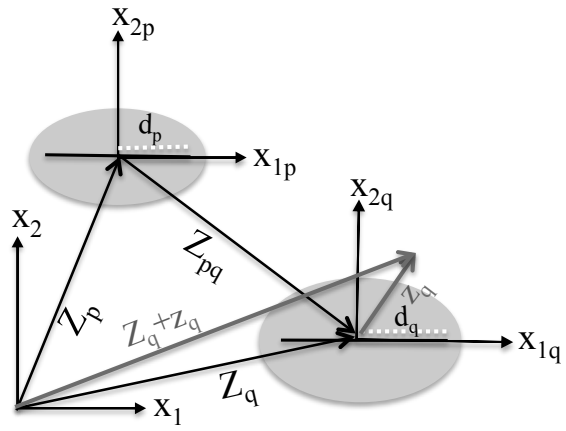


Fig. 3.3 Local (individual inclusion) and global coordinate systems.

were such that no trace of inclusion was found in the fields of matrix material. Figure 3.2a illustrates stress field distributions of a crack-like inclusion by a 0.5×10^{-5} aspect ratio under uniform normal traction. Results of crack-like inclusion are compared with stress fields of a crack of the same length (Figure 3.2b) calculated by complex analysis given in [6].

3.4.2 Finite Array Of Aligned Inclusions

In a system of N elliptical inclusions, one has to define N parallel "*local*" coordinate systems (x_{1p}, x_{2p}), each with its origin at the centroid of an ellipse (Fig 3.3); another parallel coordinate system is designated as the global coordinate system (x_1, x_2). Defining $z_p = x_{1p} + ix_{2p}$ and $z = x_1 + ix_2$, the coordinates of a point expressed in the global coordinate system (x_1, x_2) relates to the coordinates of the point expressed in the local system (x_{1p}, x_{2p}) by $z = z_p + Z_p$, where Z_p is the coordinate of the centroid of the pth inclusion in the global coordinate system. Each inclusion in the local coordinate system (z_p) can be mapped from the cartesian to the elliptical coordinate system using the $\omega(\xi_p)$ transformation.

$$z_p = d_p \omega(\xi_p) = d_p \cosh \xi_p \tag{3.21}$$

This transformation produces a branch-cut for each inclusion in its local coordinate system. For non-overlapping elliptical inclusions, fields of all inclusions are regular at the branch-cut [1] of the other inclusions. Branch-cuts in the system produce a limitation for close neighbours [153, 152]. This will not cause problem for the cross over inclusions or

[1] For an analytic multivalued function, branch cuts connect branch points to one another, or to infinity.

cracks, because stress fields are continues across the branch cuts (like dislocations) and only displacements change discontinuously across the branch cuts.

3.4.2.1 Re-expansion method

Consider an interacting multi-inclusion system where each inclusion experiences a total disturbance field generated by all inclusions as well as the external far-field load. To calculate the fields at each point in the system, one should start from determining the field distributions in one of the inclusion's local coordinate system. Obtaining the stress and displacement fields at each inclusion's local coordinate (for instance, at the qth local system) requires the re-expansion of the fields created by the rest of the inclusions into the same local coordinate system of the (qth) inclusion. Kushch [140] proposed a method to re-expand fields of the pth inclusion in the local coordinate system of the qth inclusion by

$$v_p^{-n} = \sum_m \eta_{nm}^{pq} v_q^{-m} \quad (n \geqslant 1) \tag{3.22}$$

where $\eta_{nm}^{pq} = \eta_{nm}(z_{pq}, d_p, d_q)$ is the re-expansion coefficient. A series of coefficients is derived using hypergeometric functions to expand $v_p^{-n} = [z_p/d_p \pm \sqrt{(z_p/d_p)^2 - 1}]^{-n}$, then Taylor expansion of the z_p in the vicinity of the z_q, and finally re-expansion of z_q^n to hypergeometric functions. The obtained series of expansion coefficients is

$$\eta_{nm}^{pq} = n(\frac{d_p}{2})^n (-1)^m \sum_{l=0}^{\infty} (\frac{d_q}{2})^{2l+m} M_{nml}(d_p, d_q) \frac{(n+m+2l-1)!}{(Z_{pq})^{n+m+2l}} \tag{3.23}$$

and,

$$M_{nml}(d_p, d_q) = \sum_{k=0}^{l} \frac{(d_p/d_q)^{2k}}{k!(l-k)!(k+n)!(m+l-k)!} \tag{3.24}$$

$$Z_{pq} = Z_q - Z_p \tag{3.25}$$

Converting a "singular" elliptical harmonic v_p^{-n} to a series of hypergeometric functions and applying an additional Taylor expansion provides an additional geometric restriction on the convergence of η_{nm}^{pq} series. Therefore, for the nearest neighbours another computationally expensive formula [153] shall be used. This integral form of coefficient converged for any two non-overlapping ellipses.

$$\eta_{nm}^{pq} = \frac{1}{\pi} \int_0^{\pi} e^{-n \cosh^{-1}(\frac{d_q \cos \eta_q + z_{pq}}{d_p})} \cos(m\eta_q) d\eta_q \tag{3.26}$$

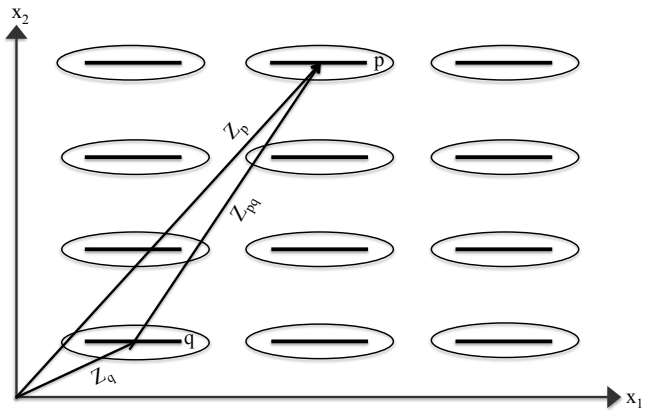


Fig. 3.4 Finite array of aligned elliptical inclusions

Another useful formula that is used in this context is a differentiation of the re-expansion formula with respect to the z_p.

$$\frac{\partial v_p^{-n}}{\partial z_p} = \sum_k \mu_{nk}^{pq} (v_q)^{-k} \tag{3.27}$$

The above mentioned re-expansion method, is used to evaluate fields in a system containing a finite array of aligned inclusions.

3.4.2.2 Method

Figure 3.4 shows a homogeneous plane contains a finite number of N non-overlapping elliptical inclusions. Due to the linearity of the system, the superposition principle is used to solve the problem. Using the linear superposition principle, the displacement $u(z)$ for the multiply connected matrix in the global, and local z_q coordinate system, is written as:

$$u(z) = u_{far}(z) + u_{dis}(z) = u_{far}(z) + \sum_{p=1}^{N} u_p^s(z_p) \tag{3.28}$$

where u_{far}, and u_{dis} are displacement fields caused by an external far-field load, and a total disturbance field induced by all inclusions respectively. This formula contains fields in $N+1$ different coordinate system, so to have a comprehensive solution, one has to re-write all the fields in one coordinate system. To do so, fields of the various coordinate systems have to be mapped to one of the inclusion's coordinate system, and then, the solution in the local coordinate system can be converted to the global coordinate system. A disturbance field in the vicinity of the qth inclusion requires a total disturbance field generated by other inclusions.

Singular fields of other inclusions in their local coordinate system must be re-expanded into regular fields in the qth coordinate system.

$$\sum_{p=1}^{N} u_p^s(z_p) = u_q^s(z_q) + \sum_{p\neq q} u_p^s(z_p) = u_q^s(z_q) + \sum_{p\neq q} u_{pq}^r(z_q) \tag{3.29}$$

Therefore $u(z)$ can be written in the local z_q coordinate system as:

$$\begin{aligned} u(z) &= \left[u_{far}(z_q + Z_q) + \sum_{p\neq q} u_{pq}^r(z_q) \right] + u_q^s(z_q) \\ &= u'_{far}(z_q) + u_q(z_q) \end{aligned} \tag{3.30}$$

which means that the condition experienced by each inclusion is that of a single equivalent inclusion. In other words, the problem is reduced to the one inclusion problem with a modified far-field traction and a $4N \times n$ set of linear equations. By applying the boundary conditions of a perfectly bonded inclusion-matrix interface, the problem becomes:

$$\begin{aligned} \kappa_0 A_n^{(q)} - \kappa_q C_n^{(q)} + (\overline{D_n^{(q)}} - 2n\sinh 2\zeta_{q0}\overline{C_n^{(q)}})v_{q0}^{2n} &= -\kappa_0 a_n^{(q)} + \overline{b_{-n}^{(q)}} v_{q0}^{2n} \\ \overline{B_n^{(q)}} + \kappa_q C_n^{(q)} v_{q0}^{2n} - \overline{D_n^{(q)}} &= \kappa_0 a_{-n} v_{q0}^{2n} - \overline{b_n^{(q)}} \\ A_n^{(q)} - \frac{\mu_q}{\mu_0} C_n^{(q)} - \frac{\mu_q}{\mu_0}(\overline{D_n^{(q)}} - 2n\sinh 2\zeta_{q0}\overline{C_n^{(q)}})v_{q0}^{2n} &= -a_n^{(q)} - \overline{b_{-n}^{(q)}} v_{q0}^{2n} \\ \overline{B_n^{(q)}} - \frac{\mu_q}{\mu_0}(C_n^{(q)} v_{q0}^{2n} + \overline{D_n^{(q)}}) &= -a_{-n}^{(q)} v_{q0}^{2n} - \overline{b_n^{(q)}} \\ n \geqslant 1,\ \ 1 \leqslant q \leqslant N \end{aligned} \tag{3.31}$$

where upper index q refers to the qth inclusion. From this point onwards the problem reduces to solving a set of linear equations where the unknown coefficients A and B can be obtained. Once all coefficients are derived, the other scalar potentials and consequently the stress and displacement fields can be calculated.

The infinite set of equations (3.31) are reduced to a finite number of equations by applying the reduction method and defining the maximum number of harmonic terms n_{max}. Depending on the distance between the inclusions, the appropriate choice of n_{max} should be selected; the closer the inclusions, the higher n_{max} is required. Kushch [140] conducted a series of numerical experiments for the problem of two inclusions and showed that $n_{max} = 27$, or equivalently 27 harmonic terms are adequate to obtain a convergent solution for nearly touching inclusions. The stress fields of two aligned cracks under uniform traction are calculated here using the commercial finite element package ABAQUS (FEM), the multipole

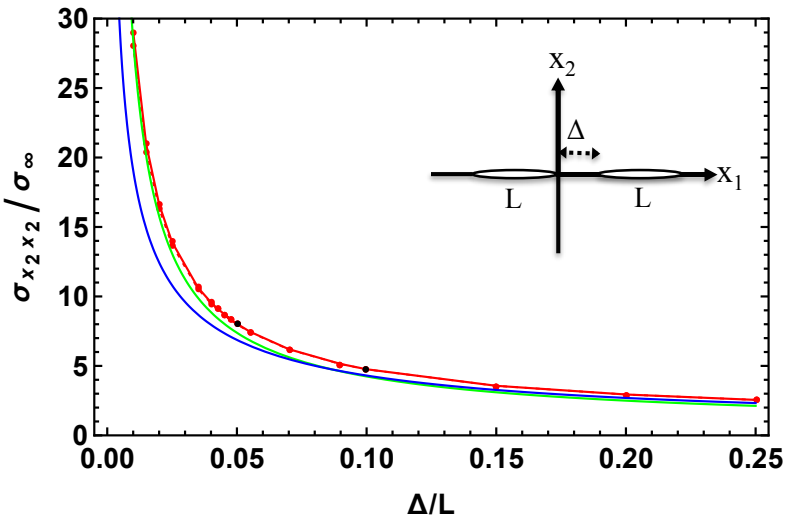


Fig. 3.5 Stress fields halfway between two aligned cracks are calculated by multipole ($n_{max} = 27$), Kachanov, and complex analytical methods are illustrated by red, blue and green colour respectively. Black dots illustrate the FEM calculated fields. The distance between two cracks of the same size (L) is equal to Δ.

method, the Kachanov method [4], and the analytical solutions presented in [7, 8]. Results of these calculations are illustrated in Fig 3.5 and 3.6.

Figure 3.5 shows the value of the stress $\sigma_{x_2x_2}$ normalised with respect to the remote stress σ_∞ at the centre between the two cracks. All methods are in good agreement where the distance between two cracks (Δ) is larger than 10% of the crack length. For smaller distances, the Kachanov method deviates considerably from the other methods. The stress field derived using the multipole method is in good agreement with both FEM calculations and the analytical approach. Figure 3.6 shows the normalised full stress field $\sigma_{x_2x_2}/\sigma_\infty$ between the two cracks of the same size (L) for the ratios $\Delta/L = 0.1$ and $\Delta/L = 0.05$, where Δ is the distance between the cracks. The full stress field simulated via the multipole method is in good agreement with the FEM calculations.

3.5 Finite Array Of Arbitrary Oriented Inclusions

By generalising the problem of one inclusion to the system of N arbitrarily oriented inclusions, coordinate systems similar to the one that are introduced for the finite array of aligned inclusions are required. Additionally, another term to describe the orientation of inclusions is incorporated.

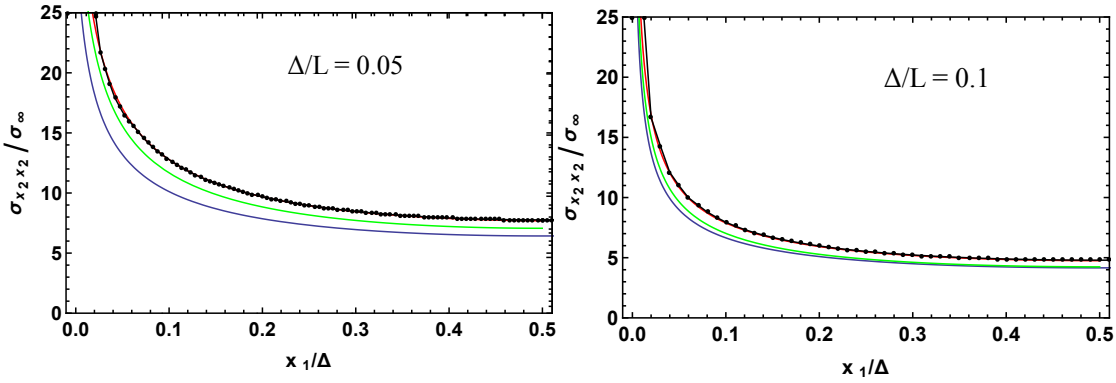


Fig. 3.6 Stress fields of two aligned cracks between 0 and $\Delta/2$. Calculated fields by finite element method, multipole ($n_{max} = 27$), Kachanov, and complex analytical methods are illustrated by black, red, blue and green colour respectively [7, 8].

To describe the differences in the relative orientations of the ellipses another set of N local "*rotated*" coordinate systems (y_{1p}, y_{2p}) is required, aligned along the major and minor axes of each ellipse (Figure 3.7). If the coordinate axes (y_{1p}, y_{2p}) are related by an anti-clockwise rotation of θ_p relative to the local coordinate axes (x_{1p}, x_{2p}) then $y_p = y_{1p} + iy_{2p} = e^{-i\theta_p} z_p$. The conformal transformation $y_p = D_p \cosh \xi_p$, where $2D_p$ is the distance between the foci of the pth ellipse, introduces the local elliptic coordinates $\xi_p = \zeta_p + i\eta_p$. Then $z_p = D_p e^{i\theta_p} \cosh \xi_p$.

3.5.1 Method

The process of calculating the stress fields and scalar potentials is similar to what was done for the finite array of aligned inclusions. The difference lies in the definition of the expansion coefficients of the scalar potentials in three sets of coordinate systems (z,z_p, and y_p).

For a 2D solid that contains a finite array of arbitrarily oriented elliptical inclusions, the displacement field of the pth inclusion in the local parallel coordinate system z_p is $u_p(z_p) = u_p(x_{1p}, x_{2p})$. When this displacement field is expressed in the local rotated coordinate system y_p it has the form $u_p(y_p) = u_p(y_{1p}, y_{2p})$. The displacement field induced by the pth inclusion in its coordinate system is singular as the pth inclusion is approached, but it is regular in the vicinity of other inclusions. Upper indices s and r refer to singular and regular functions. The complex displacement caused by the pth inclusion in its coordinate system is shown by u_p^s; in the local qth coordinate system, this field is denoted by u_{pq}^r.

$$u_p^s(z_p) = u_{pq}^r(z_q) \tag{3.32}$$

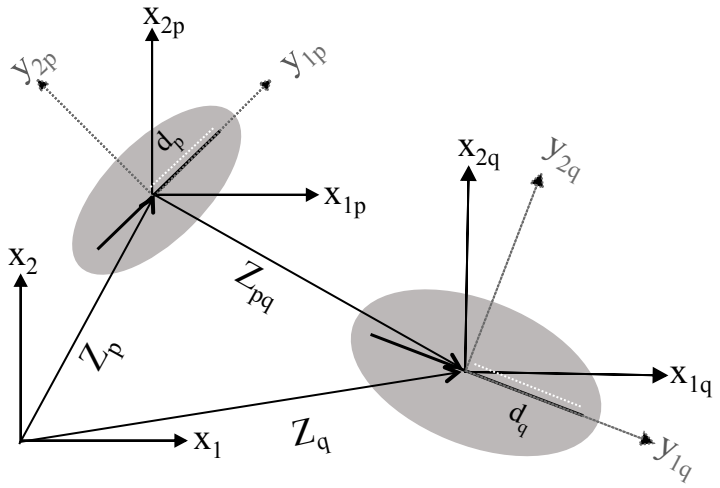


Fig. 3.7 Local and global coordinate systems.

Eq. 3.32 becomes $u_p^s(y_p)e^{i\theta_p} = u_{pq}^r(y_q)e^{i\theta_q}$ in the local y coordinate systems. The displacements $u_p^s(y_p)$ and $u_{pq}^r(y_q)$ can be expressed in terms of complex potentials using Eq. 3.8:

$$\begin{aligned} u_p^s(y_p) &= \kappa\varphi_p^s(y_p) - (y_p - \bar{y_p})\overline{\varphi_p^{s\prime}(y_p)} - \overline{\psi_p^s(y_p)} \\ u_{pq}^r(y_q) &= \kappa\varphi_{pq}^r(y_q) - (y_q - \bar{y_q})\overline{\varphi_{pq}^{r\prime}(y_q)} - \overline{\psi_{pq}^r(y_q)} \end{aligned} \tag{3.33}$$

where $\varphi_{pq}^{r\prime}(y_q) = \frac{\partial\varphi_{pq}^r}{\partial y_q}$ and $\varphi_p^{s\prime}(y_p) = \frac{\partial\varphi_p^s}{\partial y_p}$. The scalar potentials that solve the problem in the p and q coordinate systems are:

$$\begin{aligned} \varphi_p^s(y_p) &= \sum_{n=1}^{\infty} A_{np} v_p^{-n} \\ \psi_p^s(y_p) &= \sum_{n=0}^{\infty} \left[B_{np} - nA_{np} \frac{\sinh\zeta_{0p}}{\sinh\xi_p} \left(\frac{v_p}{v_{0p}} - \frac{v_{0p}}{v_p} \right) \right] v_p^{-n} \end{aligned} \tag{3.34}$$

$$\begin{aligned} \varphi_{pq}^r(y_q) &= \sum_{m\pm} a_{mpq} v_q^{-m} \\ \psi_{pq}^r(y_q) &= \sum_{m\pm} \left[b_{mpq} - ma_{mpq} \frac{\sinh\zeta_{0q}}{\sinh\xi_q} \left(\frac{v_q}{v_{0q}} - \frac{v_{0q}}{v_q} \right) \right] v_q^{-m} \end{aligned} \tag{3.35}$$

By equating similar terms in $u_p^s(z_p)$ and $u_{pq}^r(z_q)$ and transforming the basis functions, the expansion coefficients a_{mpq} and b_{mpq} in the q coordinate system can be derived in terms of A_{np} and B_{np}. Details of the derivation of the coefficients a and b can be found in Appendix B. Superimposing the disturbance fields of all inclusions in the vicinity of the qth inclusion and adding it to the far-field gives the total disturbance for a finite array of N non-overlapping elliptical inclusions:

$$u(z) = u_{far}(z) + \sum_{p=1}^{N} u_p^s(z_p) \tag{3.36}$$

Transforming all the disturbance fields into one coordinate system gives:

$$\sum_{p=1}^{N} u_p^s(z_p) = u_q^s(z_q) + \sum_{p\neq q} u_p^s(z_p) = u_q^s(z_q) + \sum_{p\neq q} u_{pq}^r(z_q) \tag{3.37}$$

Finally, the displacement $u(z)$ in the local z_q coordinate system becomes:

$$\begin{aligned} u(z) &= \left[u_{far}(z_q + Z_q) + \sum_{p\neq q} u_{pq}^r(z_q) \right] + u_q^s(z_q) \\ &= u'_{far}(z_q) + u_q(z_q) \end{aligned} \tag{3.38}$$

which means that the field experienced by each inclusion is that of a single equivalent inclusion. In other words, the problem is reduced to the one inclusion problem with a modified far-field traction and a $4N \times n$ set of linear equations. By applying the boundary conditions of a perfectly bonded inclusion-matrix interface, the unknown coefficients A and B can be obtained. Once all coefficients including a_{npq} and b_{npq} are derived, the other scalar potentials and consequently the stress and displacement fields can be calculated.

For simplicity, the problem of one inclusion is solved in the y local coordinate system. Therefor, the far-field for each inclusion has to be rotated according to its y local coordinate system. For instance, for a uniform far-field tension, the scalar potentials φ_{0far} and ψ_{0far} have to be expanded as follows

$$\begin{aligned} \varphi_{0far}(y_q) &= \sum_{m\pm} a_{m0q} v_q^{-m} \\ \psi_{0far}(y_q) &= \sum_{m\pm} \left[b_{m0q} - m a_{m0q} \frac{\sinh \zeta_{0q}}{\sinh \xi_q} \left(\frac{v_q}{v_{0q}} - \frac{v_{0q}}{v_q} \right) \right] v_q^{-m} \end{aligned} \tag{3.39}$$

The non-zero coefficients of the field in the local y coordinate system are as below; details of the derivation can be found in Appendix B.1.3:

$$\begin{aligned} a_{10q} &= \frac{d_q e^{-i\theta_q}}{2}\left(\frac{s_{11}+s_{22}}{8\mu_0}\right) \\ b_{-10q} &= \frac{a_{10q}}{v_{0q}^2} + \frac{d_q e^{i\theta_q}}{8\mu_0}(s_{22}-s_{11}+2is_{12}), \end{aligned} \tag{3.40}$$

where $d_q = D_q e^{i\theta_q}$. After the problem is solved in the local y_q coordinate system, a rotational transformation is applied to the calculated fields to transform them into the local z_q coordinate system using $\sigma(z_q) = R\,\sigma(y_q)R^T$ where R is the rotational transformation tensor. Additional transformation is required to convert the stress fields from the local z_q system into the global coordinate system.

3.5.1.1 Flow diagram

A flow diagram of the multipole method code developed here is illustrated in Figure 7.3 for an unbounded solid; the multipole method predicts the full stress and displacement of the system. In this case, the boundary conditions (step 4) required for the multipole method are provided from the far-field load expansion in the same basis functions that are used for expansion of the complex potentials.

The analysis is finalised in six steps. Generating the expansion coefficients η_{mn}^{pq}, and μ_{mn}^{pq} (step 2) and solving the linear system (step 5) are the most computationally expensive steps in the analysis.

3.5.2 Numerical Results

To verify the accuracy of the multipole method, stress fields of one, two, and three miss-oriented elliptical holes are analysed. All simulations are performed under a uniform tensile load in the x_2 direction. In the first set of simulations, stress fields on the perimeter of one elliptical hole oriented at 45 degrees with respect to the global axes and subjected to remote tensile load (σ_∞) in the x_2 direction are calculated using the commercial finite element package ABAQUS (FEM), and the multipole method. Stress fields are illustrated along the perimeter of the inclusion starting from the point $(y_1, y_2) = (0, l_1)$ following the inclusion in the anticlockwise direction in the local y coordinate system. Results of simulations are in good agreement with each other.

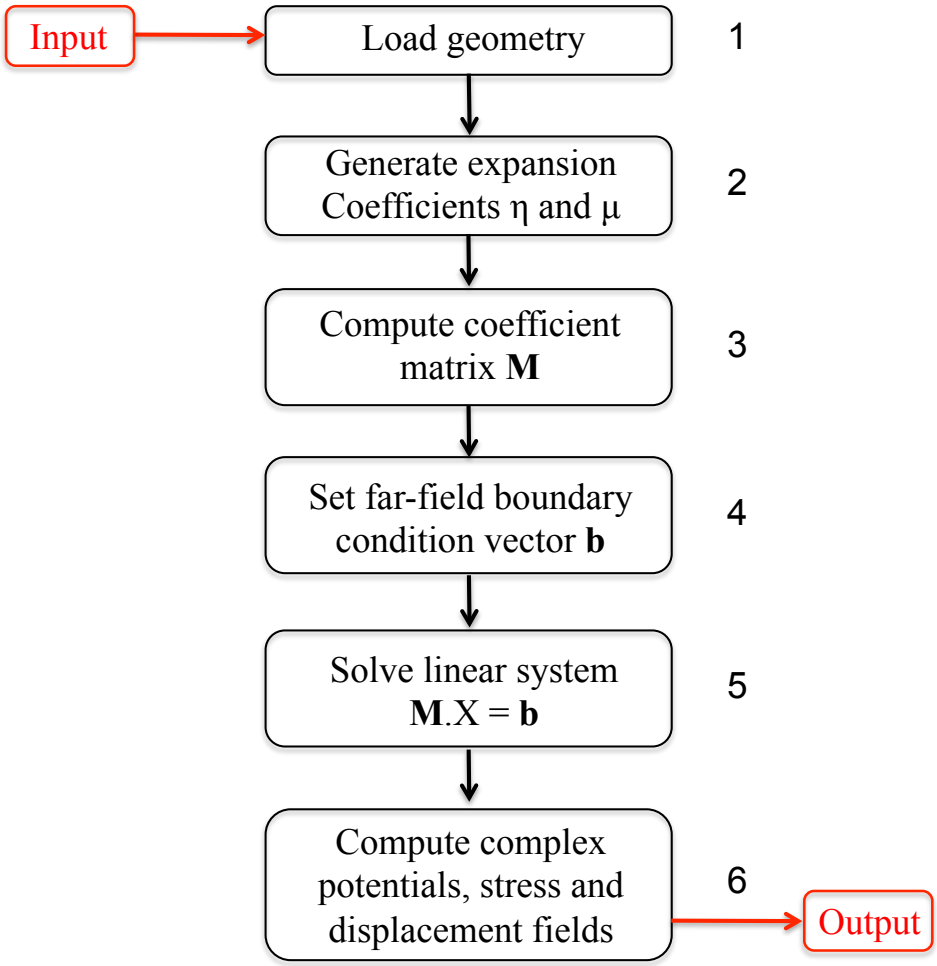


Fig. 3.8 The flow chart of the multipole method displacement and stress fields calculation.

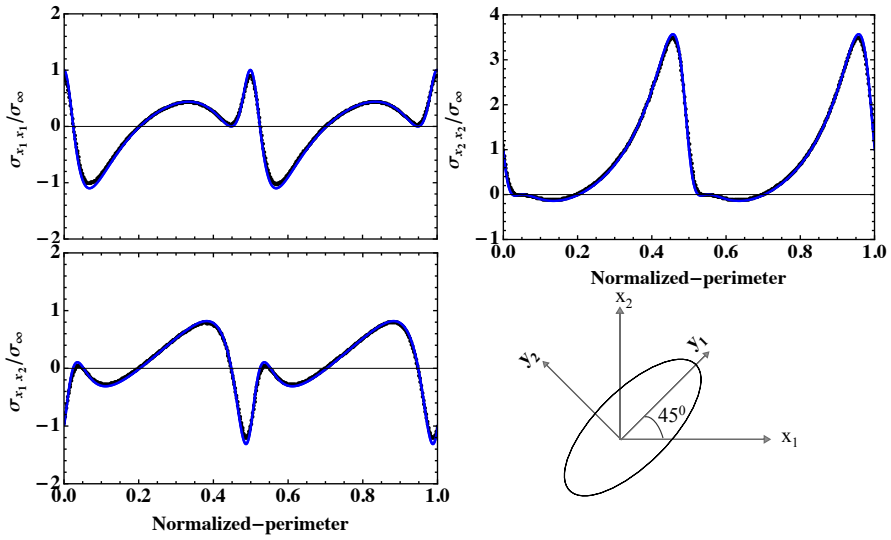
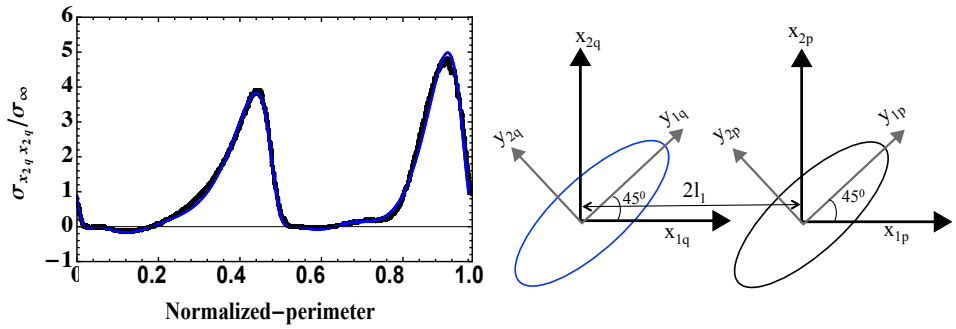


Fig. 3.9 Stress fields on the perimeter (distance along the perimeter has been normalised to the total perimeter length) of a hole with a 45^0 angle of inclination to the horizon and the aspect ratio of 0.5 ($l_1 = 1\mu m$ and $l_2 = 0.5\mu m$) subjected to a remote uniform tension in the x_{2q} direction. Fields calculated by the multipole method and FEM are represented by the blue and black lines respectively.

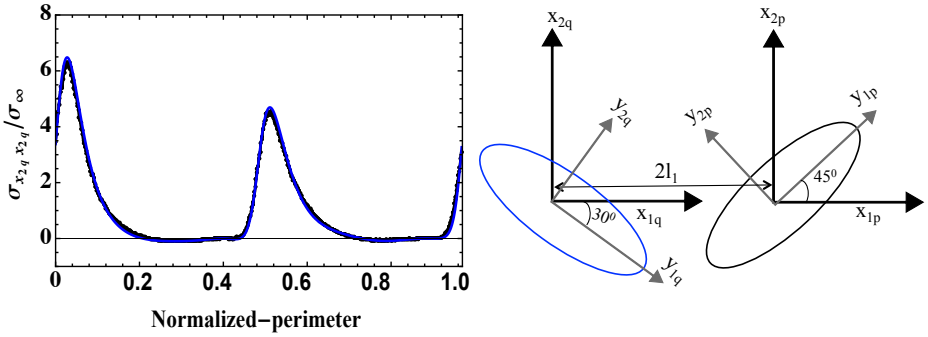
Another set of simulations was run to calculate stress fields on the perimeter of two and three arbitrarily placed elliptical holes with aspect ratio 0.5 ($l_1 = 1\mu m$ and $l_2 = 0.5\mu m$). Figure 3.10 illustrates the stress component $\sigma_{x_2x_2}/\sigma_\infty$ along the perimeter of the qth inclusion starting from the point $(y_{1q}, y_{2q}) = (0, l_1)$ following the inclusion in the anticlockwise direction in the local y_q coordinate system; in Figure 3.10d calculations were done for the first inclusion (shown in blue) starting from the point: $(y_{11}, y_{21}) = (x_{11}, x_{21}) = (0, l_1)$. Fields calculated using the multipole method and FEM are represented by the blue and black lines, respectively. Figures show that they agree well with each other.

3.5.3 Total Stress Fields Of The System

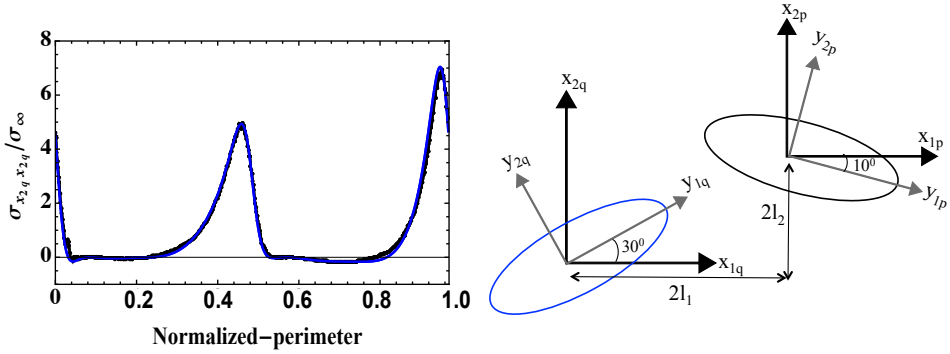
In order to obtain the stress fields of the qth inclusion, the singular stress fields of other inclusions are expanded as regular fields in the qth coordinate system. The fields close to the surface are accurate. Nevertheless, these calculated fields tend to infinity as the distance from the surface of the inclusion increases. The increase in the stress and displacement fields is associated with the presence of the regular terms $e^{n\xi}$ in the complex potentials. Therefore, to predict correct fields, regular terms should vanish as the distance from the inclusion increases.



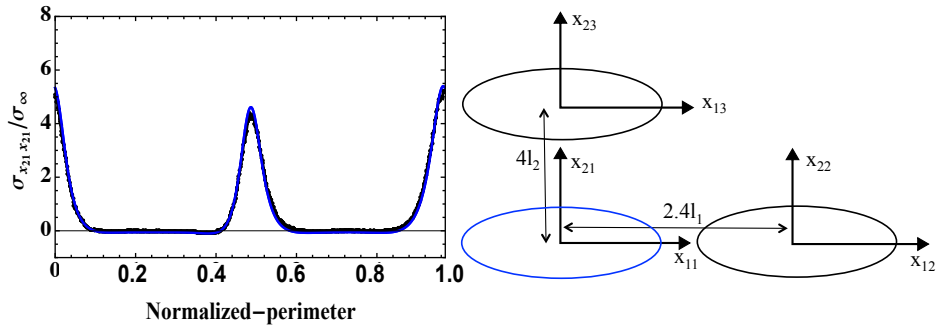
(a) Two aligned 45^0 inclusions.



(b) Two aligned 45^0 inclusions with -30^0 and 45^0 inclination slopes.



(c) Two inclusions with 30^0 and -10^0 inclination slopes and separation distance $z_{pq} = 2\,l_1 + i\,2l_2$.



(d) Three 0^0 inclusions with separation distances of $z_{12} = 2.4l_1$ and $z_{13} = i\,4l_2$.

Fig. 3.10 Plot of stress components in the direction orthogonal to the major axis of the elliptical hole under consideration along its perimeter for various configurations. The stress fields calculated by the multipole method and FEM are represented by blue and black lines, respectively.

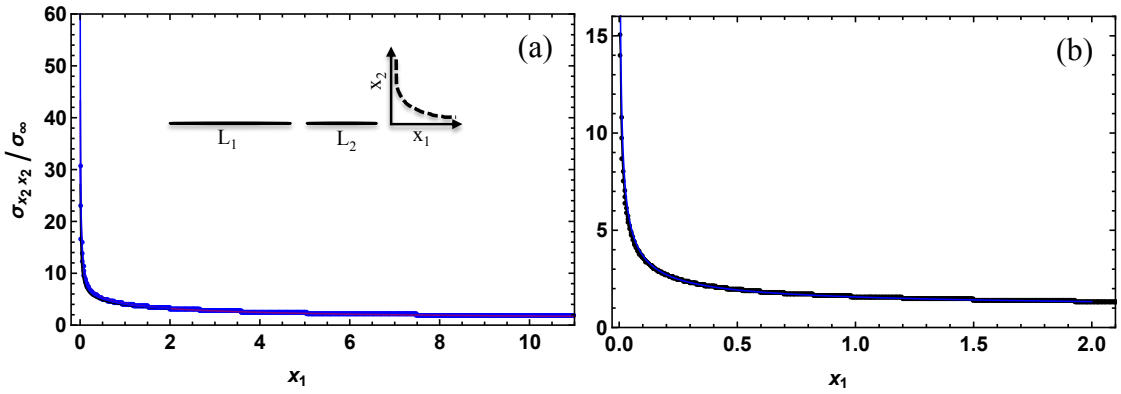


Fig. 3.11 Stress fields along the x_1 axis are calculated using FEM (black) and MM (blue) for a system of two collinear cracks. Schematic of the problem is shown in (a) and the distance between two cracks is set to be $0.1L_2$. Normalised $\sigma_{x_2x_2}$ presented for the cases where a) $L_1/L_2 = 100$, and b) $L_1/L_2 = 10$.

To obtain the stress fields, a system with correct coefficients for short range interactions and decaying fields $e^{-n\xi}$ at infinity is required. To calculate the exact expansion coefficients, a large enough number of harmonic terms (n) has to be used in the first run of the simulation. Then, by using the correct expansion coefficients and removing regular fields (by equating the η and μ coefficients to zero), stress fields can be calculated at any point in the system. To validate the method, stress fields of a system containing two aligned cracks under uniform tension are simulated using FEM and MM. Figure 3.11 shows the stress field $\sigma_{x_2x_2}$, normalised with respect to the remote load, directly ahead of the second crack-tip.

3.5.4 Stress Intensity Factors (SIFs)

Studies of the crack propagation in the vicinity of inclusions are of considerable interest for both practical applications and fracture mechanics. In fracture analysis, SIFs are used to measure the amplification of stresses in the proximity of a crack-tip, and to calculate the energy of the crack. Analytical expressions for the stress intensity factor of the cracks and stress concentrations of the inclusions can be derived using the complex potential technique [135]. Here, K^+ and K^- refer to the right and left crack-tips with respect to the local coordinate system. For inclusions the stress concentrations are calculated at the rounded edges intercepting the major axis of the inclusion. In linear elastic fracture mechanics the SIF is defined as:

$$K_{Iq}^{\pm} + iK_{IIq}^{\pm} = \lim_{z_q \to \pm d_q} t_q \sqrt{2\pi(z_q \mp d_q)} \tag{3.41}$$

where the term $(z_q \mp d_q)$ defines the distance between the branch point and the surface of the inclusion.

$$t_q = 2\mu[\overline{\varphi'(z_q)} + (\overline{z_q} - z_q)\varphi''(z_q) + \psi'(z_q)] \tag{3.42}$$

in the z_q coordinate system. For the case where $e_q \to 0$, terms containing $z - \overline{z}$ become zero, thus the SIFs become:

$$K_{Iq}^{\pm} + iK_{IIq}^{\pm} = 2\mu_0 \lim_{z_q \to \pm d_q} (\overline{\varphi_q'} + \psi_q')\sqrt{2\pi(z_q \mp d_q)} \tag{3.43}$$

After some algebra, and considering the fact that complex potentials are singular potential in the local coordinate system, one can obtain the formula for the case where $\zeta_q \to 0$ as:

$$K_{Iq}^{\pm} + iK_{IIq}^{\pm} = -2\mu_0\sqrt{\frac{\pi}{D_q}}\sum_{k=1}^{\infty}(\pm 1)^{k-1}(A_{nq} + \overline{B_{nq}}) \tag{3.44}$$

This formulation enables calculating the SIFs without any additional numerical effort. The formula is valid for inclusions with nearly zero aspect ratio and arbitrary far load. As the stress field singularity at the crack-tip and the elliptical inclusion are different, SIFs for elliptical inclusions/voids cannot be predicted with the same method. In the next section the problem of elliptical inclusions and their relevant SIFs are addressed.

3.5.4.1 A crack emanating from an ellipse

The SIF cannot be determined for an ellipse unless we assume that a crack is emanating from the ellipse. Analytical solutions for cracks emanating from elliptical inclusions are very difficult to obtain. Here the evaluation of SIFs for cracks emanating from elliptical inclusions is addressed by averaging over a short distance from where the crack emanation is predicted. Once the distribution of stress fields is calculated, the average SIFs is computed using $\overline{K} = (1/l)\int_0^l \sqrt{2\pi r}\sigma dr$. The influence of the length l is investigated and results of calculations are compared with an analytical method given by Berezhnitskii *et.al*. [154–156], for an elastic plane weakened by an elliptical hole with a crack terminating at its edge.

Figure 3.12 shows a schematic representation of the problem; a crack emanating from an elliptical hole, in an unbounded solid subjected to remote Mode *I* loading. The host material is assumed to behave elastically and isotropically. SIFs are calculated analytically using formulas:

$$K_I = \sigma^{\infty}\sqrt{\pi(l_1 + l)}F(m, \varepsilon_1) \tag{3.45}$$

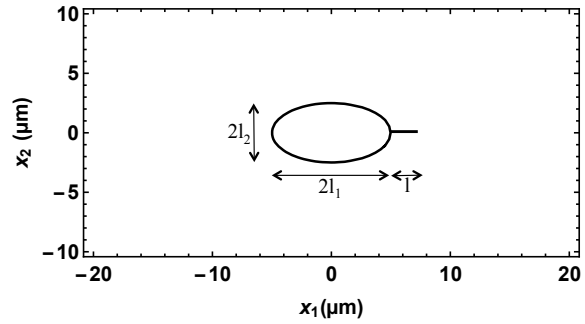


Fig. 3.12 Schematic representation of the problem; SIF of a crack emanating from an elliptical hole, in an unbounded solid subjected to remote Mode I loading.

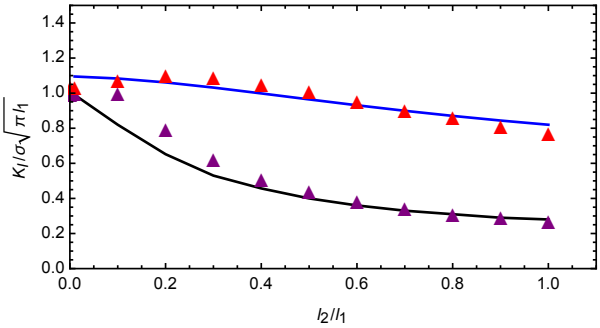


Fig. 3.13 SIF of a crack emanating from an elliptical inclusion with various aspect ratios l_2/l_1. The blue and black lines are derived from analytical calculations for $l/l_1 = 0.05$, and 0.005 respectively. Data shown by triangles are computed by the average SIF method along the distance l.

$$F(m,\varepsilon_1) = \left\{ \frac{[1-\frac{m}{(1+\varepsilon_1)^2}][1+\frac{m}{1+\varepsilon_1}]}{[1-\frac{1}{(1+\varepsilon_1)^2}][1+\frac{1}{1+\varepsilon_1}]} \right\}^{1/2} \tag{3.46}$$

$$1+\varepsilon_1 = \frac{l_1+l+\sqrt{(l_1+l)^2-(l_1^2-l_2^2)}}{(l_1+l_2)}, \tag{3.47}$$

where $m = \frac{l_1-l_2}{l_1+l_2}$; l_1, l_2, and l are respectively, the semi-major, semi-minor axes of the ellipse, and emanating crack length. SIFs are calculated for an ellipse with various aspect ratios. The SIFs are averaged over the lengths $l/l_1 = 0.05$ and 0.005. Results of simulations are presented in Figure 3.13. For comparison purpose, the figure also shows results obtained by Berezhnitskii. It is observed that the present numerical results are in excellent agreement with the analytical results especially for voids with larger aspect ratios.

Chapter 4

Crack Propagation: Discrete Crack Dynamic

4.1 Introduction

The path followed by a slowly propagating crack depends on the microstructure of the material, comprising features such as inclusions, grain boundaries and other cracks. The primary objective of this chapter is to investigate the process of micro-crack deflection and capture crack propagation at low crack speed.

The simulation of crack propagation presented here uses the multipole method and is developed based on 4 postulates: (i) each crack can be modelled as a collapsed zero-stiffness inclusion, (ii) crack growth is incremental and quasi-static, (iii) crack growth can be modelled by introducing a small crack (or pseudo-inclusion) ahead of the existing crack-tip in the predetermined propagation direction at each step. Crack growth can be thought of as comprising sequential micro-crack initiation events ahead of the main crack-tip followed by merging of the crack ensemble [157–162], (iv) two cracks (psudo-inclusions) can be approximated by a single kinked crack if their sizes and the distance between them satisfy specific criteria, which will be studied in detail later.

The first postulate makes it possible to find the interactions between cracks and inclusions of the system simultaneously. The second and third postulates allow the introduction of a small crack at the existing tip to model incremental crack propagation. The direction of crack propagation can be determined using a suitable mixed mode crack propagation criterion. The fourth postulate is valid only if the SIF at the tip of the second crack can approximate the SIF of the two-crack ensemble, which might not be straight. A consequence of the fourth postulate is that the stress fields between two adjacent cracks becomes critically high and the field at the “junction" between the two cracks (see figure 4.9) affects the stress fields and

the SIFs at crack-tips far away from the junction. Thus, a modification has to be applied to derive the SIFs of kinked cracks from two adjacent cracks; details of the correction are provided in Section 4.3.

Once the distribution of stresses and strains is computed using MM and the correction to the SIFs is included, a crack propagation criterion is employed to determine the crack propagation path. The evolution of individual micro-cracks and their interaction with existing cracks/inclusions is then explicitly modelled using what we refer to here as the discrete crack dynamic (DCD) method. This approach is fast and suitable for the prediction of low-speed crack propagation paths in brittle or quasi-brittle materials.

4.2 Discrete Crack Dynamics (DCD)

Here an approximate method to determine the propagation path of the main crack in a system of many-inclusions/cracks is introduced. It is implicitly assumed that the elastic fields of microstructures are propagated instantaneously. In the Discrete Crack Dynamics method, the term dynamics is used to imply evolution of micro cracks in structures, rather than elastodynamics. This assumption enables the stress fields at an instant in time to be evaluated by considering the static elastic fields of the cracks and inclusions at their current positions. This is reasonable for quasi-static analysis, where the crack propagates continuously, ideally at some constant slow speed. Quantitatively, the slow speed means that the crack speed becomes a small fraction of a transverse speed of sound; the slowest speed at which information can be propagated in an elastic medium.

Studying crack propagation in elastic materials requires solving three distinct problems. Firstly, a method to calculate interactions between cracks and inclusions and determine the stress and displacement fields around the crack must be available. Secondly, the method needs to be capable of computing the fracture parameters, such as the stress intensity factors or the energy release rate. In this study, the multipole method is used to address the first two problems. Thirdly, a criterion is needed to characterise the conditions leading to crack propagation, as well as the direction and length of propagation. The last problem is addressed in the following sections.

4.2.1 Crack Propagation Criteria

A fracture criterion is required to accurately determine the crack propagation path. A number of fracture criteria has been developed for a crack under critical mixed mode loading [69, 74–76, 163]. Here a concise overview of the most common and widely applied criteria such

as the maximum tangential stress, the maximum strain energy release rate, and a general fracture criterion are provided.

4.2.1.1 Maximum tangential stress (MTS)

Erdogan and Sih [69] proposed the simplest and the most widely used theory for evaluating the crack propagation direction under mixed mode conditions. They presented the maximum tangential stress criterion based on two hypotheses for the extension of a crack in brittle materials. Firstly, the crack extension starts at the crack-tip in a radial direction. Secondly, the crack extension is along the direction where the $\sigma_{\theta\theta}$ is maximum, and $\sigma_{r\theta}$ is zero. The crack propagation condition in MTS is:

$$\cos\frac{\theta_0}{2}\left[K_I\sin\theta_0 + K_{II}(3\cos\theta_0 - 1)\right] = 0 \tag{4.1}$$

where

$$\theta_0 = \pm\arccos[(3K_{II}^2 + K_I\sqrt{K_I^2 + 8.0K_{II}^2})/(K_I^2 + 9K_{II}^2)]. \tag{4.2}$$

Equation 4.2 confines the crack propagation angle to a domain between $-\pi/2$ and $\pi/2$. To ensure that the energy release associated with the crack extension is maximum, the sign of the propagation angle θ should be opposite to the sign of K_{II} [164]. Once the crack initiation angle is determined, fracture starts when

$$\cos\frac{\theta_0}{2}\left[K_I\cos^2\frac{\theta_0}{2} + \frac{3}{2}K_{II}\sin\theta_0\right] = K_C, \tag{4.3}$$

where K_C is the critical stress intensity factor. The MTS criterion can be summarised as finding the crack initiation angle θ_0 using

$$\frac{\partial\sigma_{\theta\theta}}{\partial\theta} = 0, \qquad \frac{\partial^2\sigma_{\theta\theta}}{\partial^2\theta} \leqslant 0 \quad \Rightarrow \theta = \theta_0 \tag{4.4}$$

and then, the crack propagation condition using

$$\sqrt{2\pi r}(\sigma_{\theta\theta})_{\theta_0} = K_C. \tag{4.5}$$

Equations 4.3 to 4.5 are valid only if the singular terms in the stress fields are considered while, in general, other terms in stress field distributions are involved in fracture. In a linear elastic system, the stresses of a homogeneous and isotropic cracked body can be written as an infinite series expansions introduced by Westergaard [65] and Williams [165]. In the polar coordinate system, the tangential stress ($\sigma_{\theta\theta}$) is written as

$$\sigma_{\theta\theta}(r,\theta) = \frac{1}{\sqrt{2\pi r}}(K_I \cos\frac{\theta}{2} - 3K_{II}\sin\frac{\theta}{2}\cos^2\frac{\theta}{2}) + T\sin^2\theta + O(r^{1/2}) \tag{4.6}$$

The accuracy of the method can be improved if extra terms in the expansion series, given in Equation 4.6, are considered. For example, Ayatollahi and co-workers use the second term, T stress [1], as well as singular terms, in the series expansion of the stress fields. They extended the MTS condition to the Generalised Maximum Tangential Stress (GMTS) condition[73, 166, 167]. In the elliptical coordinate system, the tangential stress $\sigma_{\eta\eta}$ can be calculated using the multipole method. Knowing the expansion series of the tangential stress, the propagation angle θ_0 can be calculated using the formula 4.4 and the crack initiation condition should be checked using Equation 4.5.

4.2.1.2 Minimum strain energy density (MSED)

The fundamental quantity in this criterion is the strain energy contained in a unit volume of the material at a given instant of time. The principle of minimum energy states that at equilibrium the internal energy of a system decreases and approaches a minimum value. The strain energy density for linear isotropic materials undergoing small strain can be written as:

$$W = 1/2\sigma_{ij}\varepsilon_{ij} = S/r \tag{4.7}$$

where σ_{ij} and ε_{ij} are stress and strain components, S is the strain energy density factor and r is the distance form the crack-tip. The MSED states that the crack propagates in a direction along which the strain energy density factor possesses a minimum value [70, 71], i.e.,

$$\partial S/\partial\theta = 0, \quad \partial^2 S/\partial\theta^2 > 0. \tag{4.8}$$

The crack propagation angle, denoted by θ_0, can be calculated using Equation 4.8. The crack initiation condition is given by $S_{min} = S(\theta_0) = S_C$, where S_C is the critical value of the strain energy density factor.

4.2.1.3 Maximum strain energy release rate (MERR)

This criterion is based on the energy balance concept in the crack propagation process. The amount of released energy during the crack initiation and propagation is equal to the stored strain energy of the local stretched atomic bonds. The MSERR is proposed by Palaniswamy and developed by Hossein *et al* [74–76] for a crack subjected to the mixed mode loading. It

[1] The singular stress term contribution of the stress field in the vicinity of the crack-tip is characterised by the stress intensity factor and the first regular stress term is represented by the T-stress.

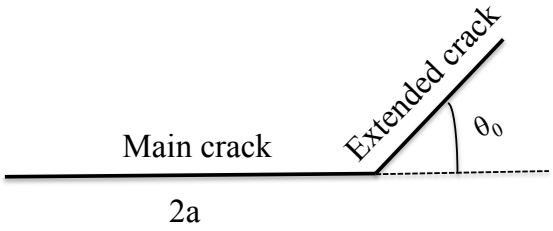


Fig. 4.1 Main and extended crack directions.

is postulated that the crack propagates along the direction where the strain energy release rate is maximum. Also, the crack starts to propagate when the maximum energy release rate reaches a critical value.

Hossein *et al.* [76] calculated the energy release rate $G(\theta)$ using path independent integrals and complex potentials for any propagation branch with angle θ, where the propagation branch size was assumed to be nearly zero (*Extended crack* $\rightarrow 0$ in Figure 4.1). The main crack is an edge crack of length $2a$.

$$G(\theta) = \frac{2\pi a}{E}\left(\frac{1-\theta/\pi}{1+\theta/\pi}\right)^{\theta/\pi}\left(\frac{4}{3+\cos^2\theta}\right)^2\Big\{$$

$$(1+3\cos^2\theta)\sigma^{\infty^2}_{x_2x_2} + 4\sin 2\theta\,\sigma^{\infty}_{x_2x_2}\tau^{\infty}_{x_1x_2} \tag{4.9}$$

$$+ (9-5\cos^2\theta)\tau^{\infty^2}_{x_1x_2}\Big\}$$

where E is Young's modulus, and $\sigma^{\infty}_{x_2x_2}$ and $\tau^{\infty}_{x_1x_2}$ are the stress components of the far-field load. The crack initiation angle θ_0 was derived using the $\partial G/\partial\theta = 0$ and $\partial^2 G/\partial\theta^2 < 0$ formulas. The crack initiation condition is given by $G(\theta_0) = G_c$, where $G_c = \frac{K_{IC}^2+K_{IIC}^2}{E'}$. $E' = E$ for the plane stress and $E/(1-\nu^2)$ for the plane strain problems.

4.2.1.4 General fracture criterion

The energy release rate of a crack propagating a unit length along its extension is:

$$G = \frac{K_I^2 + K_{II}^2}{E'} \tag{4.10}$$

However, in general, the energy release rate is angularly dependent, $G(\theta)$, and the fracture direction under mixed mode loading is not necessarily along the crack extension. Calculating the energy release rate without considering any approximations for the method is mathematically involved and somewhat cumbersome. An approximate expression of $G(\theta)$ was presented by Chang *et al.* who introduced effective SIFs [77] using singular terms of the stress fields.

$$G(\theta) \approx \frac{\kappa+1}{8\mu}[K^2_{I_{eff}}(\theta) + K^2_{II_{eff}}(\theta)] \tag{4.11}$$

An approximate expression for $G(\theta)$ in terms of stress field distributions in the polar coordinate system is given by:

$$G(\theta) = \frac{\pi r}{4\mu}[(\kappa+1)(\sigma^2_{\theta\theta} + \sigma^2_{\theta r})] \tag{4.12}$$

This formula can also be derived by considering the definition of SIFs in the polar coordinate system.

$$K_I = \lim_{r\to 0}\sqrt{2\pi r}(\sigma_{\theta\theta})_{\theta=0} \tag{4.13}$$

$$K_{II} = \lim_{r\to 0}\sqrt{2\pi r}(\sigma_{\theta r})_{\theta=0} \tag{4.14}$$

In the above equations both $\sigma^2_{\theta r}$ and $\sigma^2_{\theta\theta}$ are maximised at $\theta = 0$. Using this concept, $K_I(\theta)$, $K_{II}(\theta)$, and $G(\theta)$ can be written as: [2]

$$K_I(\theta) + iK_{II}(\theta) = \lim_{r\to 0}\sqrt{2\pi r}(\sigma_{\theta\theta} + i\sigma_{\theta r}) \tag{4.15}$$

$$G(\theta) = \frac{K^2_I(\theta) + K^2_{II}(\theta)}{E'} \tag{4.16}$$

In the case where $\sigma^2_{\theta r} = 0$, both MSERR and MTS conditions are equivalent and they predict a similar propagation angle. In the elliptical coordinate system, using the multipole method notation the SIF formulas are:

$$K_I(\theta) + iK_{II}(\theta) = \lim_{r\to 0}\sqrt{2\pi r}(\sigma_{\eta\eta} + i\sigma_{\eta\zeta}) \tag{4.17}$$

Thus,

[2] It should be noted that in general SIFs can be obtained using the formula $K_{ij}(\theta) = \lim_{r\to 0}\sqrt{2\pi}r^{1-\lambda_i}\tau_{ij}(r,\theta)$, where λ_i depends on the distance between the crack-tip and an interface joining two dissimilar materials [168].

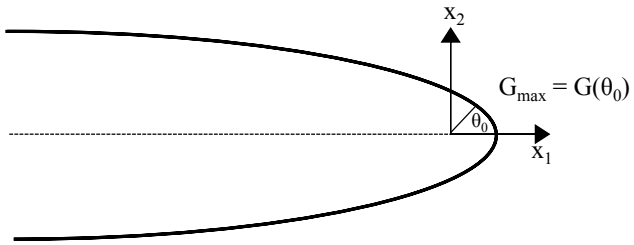


Fig. 4.2 Schematic of the general fracture criterion at the crack-tip. Energy varies at the crack-tip as a function of the polar angle θ.

$$K_I^2(\theta) + K_{II}^2(\theta) = \lim_{r \to 0} 2\pi r(\sigma_{\eta\eta}^2 + \sigma_{\eta\zeta}^2) \tag{4.18}$$

Since at the surface of the elliptical hole $\sigma_{\eta\zeta}^2$ is zero, the MTS and MSERR provide very similar results in our calculations. Then, the crack initiation condition can be derived using the computed stress fields. In this work, the general fracture criterion, demonstrated in Figure 4.2, is selected for the computations. Figure 4.2 shows the energy at the crack tip as a function of the polar angle θ. Crack propagates in the direction of the maximum energy release rate.

4.2.2 Crack Propagation: Length Scale

Predictions of crack propagation based on the stress fields at the notch root (and/or the crack-tip) are notoriously inaccurate. The calculated maximum stress on the surface is unsuitable for predicting crack propagation in situations where the gradient of the stress near the notch is high [169–172]. Such high stress fields decrease significantly over short distances; it is not the entire stress field that is important in studying crack propagation, only the field over a critical finite distance ahead of the crack-tip. This critical distance (Figure 4.3) relates to the microstructure of the material and it can be determined using e.g. the finite fracture method (FFM) [173, 174].

The FFM is based on the assumption that crack growth is not smooth and continuous, but instead occurs in a discontinuous manner. The size of the extension ($2L$) is determined by the microstructure and deformation behaviour of the material. In the FFM the failure condition is obtained using an energy balance similar to that of Griffith, but assuming a finite amount of crack extension. For the case of a sharp crack, the value of $L = \frac{1}{\pi}(\frac{K_C}{\sigma_0})^2$ is expressed as a function of two other material constants, the fracture toughness K_C and the inherent strength parameter σ_0. This formula may require corrections for crack blunting. A similar material

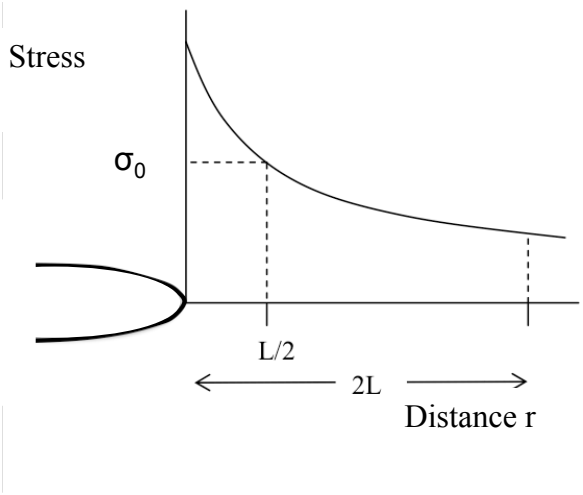


Fig. 4.3 Critical distance methods: The point method uses the stress at a point $r = L/2$ from the notch root rather than the maximum stress at the notch root; the line method uses the average stress on a line drawn from the notch over a distance $r = 0$ to $2L$ [9].

constant was proposed by Peterson [175], Neuber [176], and El Haddad [177] using the point method, line method, and imaginary crack method respectively. For a brittle material, such as diamond, $L = \frac{1}{\pi}(\frac{K_{IC}}{\sigma_u})^2$ where σ_u and K_{IC} represent the material ultimate tensile strength and mode I critical SIF [174]. Using σ_u and K_{IC} reported by Field [26], the critical distance for diamond is predicted to be $2L = \frac{2}{\pi}(\frac{5\times10^{-3}}{4.03})^2 \simeq 1\mu m$.

Dugdale [178] and Barentblatt [179] introduced the concept of the Cohesive Zone Model based on the idea that a crack surface can be divided into two regions, i) the inner region of the crack where the crack surfaces are separated (open crack) and ii) the edge region of the crack (near the crack tips), where the faces interact with each other and the forces of cohesion are present. They predicted that deformation and stresses experienced over the edge region are linked to the likelihood of the crack to propagate and they introduced the length s measured from the end of the crack-tip to identify the process zone, i.e. the region over which damage takes place. It was suggested that the crack propagates under the action of the stress field distributions which the crack is subjected to over the length s; this is equivalent to the point mentioned in the FFM method, which states only the field over a critical finite distance ahead of the crack-tip is important when studying crack propagation. Dugdale [178] has shown that for the problem of a straight crack propagating in an idealised infinite medium the length $s \sim 1.23/\pi(K_c/\sigma_u)$ which is very close to the length L proposed above.

Crack propagation model used in this study can be better explained as analogous to the Cohesive Zone Model (CZM) [180–182]. In the CZM model, it is assumed that the damage

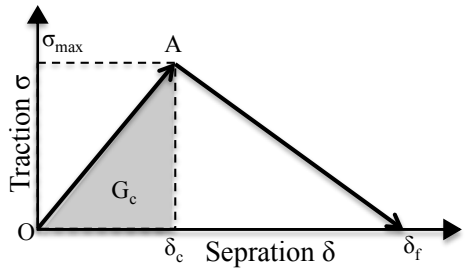


Fig. 4.4 Schematic of mode-I traction-sepration law used to model brittle crack propagation.

is localised in the cohesive zone (interface) while the rest of the material remains undamaged. The mixed-mode triangle traction-separation law has to be used for the mixed mode crack propagation problems. However, to make it easier to explain, the traction-separation law of Mode-I brittle fracture is used in Figure 4.4 to describe the different parameters required in a typical CZM and the DCD model. In the CZM, the interface is assumed to be undamaged when the separation, δ, is less than the critical separation distance, δ_c (in Figure 4.4). Thus, the interface behaves elastically; however beyond δ_c the interface undergoes damage evolution (irreversible process) until the system approaches the separation at failure δ_f. The energy release rate of the cohesive low is calculated from

$$G = \frac{1}{s}\int_0^{\delta_f} \sigma(\delta) d\delta. \tag{4.19}$$

In the case of brittle material with reversible elastic behaviour, which is the case of this study, $\delta_f = \delta_c$. Therefore, the crack propagation model used in the DCD method is somewhat similar to what is proposed in CZM in the sense that the grey triangle in Fig. 4.4 represent the energy required for the crack to propagate; this means that, given also the similarity in the definition the two methodologies of the critical length, s, the DCD is also similar to CZM in terms of fracture energy and energy release rate, although it does not use the concept of traction-separation.

4.2.3 New Elliptical Micro-Crack Coordinate

In the DCD method, the crack advances step by step by adding a new micro-crack at the main crack-tip. The exact position of each additional crack is determined by i) the maximum tangential stress criterion and SIFs at the crack-tip (Section 4.2.1.1), and ii) searching for where the generalised energy release rate is maximised at the crack-tip surface; which is

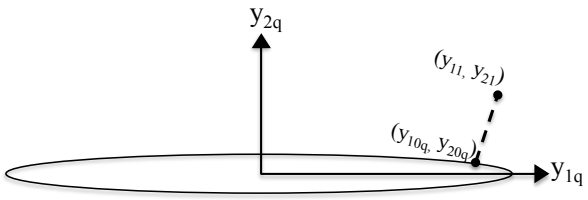


Fig. 4.5 Schematic of a crack-tip with the extension point (y_{10q}, y_{20q}) on the perimeter of the crack and the new crack-tip at (y_{11}, y_{21}).

where crack extension occurs. If the material has a homogenised fracture energy the new crack propagates in direction that minimise the distance from the specified point on the elliptical crack [183]. The effect of variations in the fracture energy on the crack propagation path will be studied in Chapter 5.

In Figure 4.5, an extension point on the crack surface is at (y_{10q}, y_{20q}) in the local y_q coordinate system. In order to add a new micro-crack to the system, a new coordinate system with origin O_{New} and inclination angle θ_{New} have to be introduced:

$$\begin{aligned} O_{New} &= Z_q + (y_{11} + iy_{21}) \exp(i\theta_q) \\ \theta_{New} &= \theta_q + \arctan[\frac{y_{21} - y_{20q}}{y_{11} - y_{10q}}], \end{aligned} \tag{4.20}$$

where (y_{11}, y_{21}) denotes the centre of the new crack in the main crack local y_q coordinate system, and $\exp(i\theta_q)$ rotates the local y_q system into the z_q coordinate system. The coordinate (y_{11}, y_{21}) is calculated using the minimum distance principle [184] and the predetermined length of the crack extension; details of the calculations are provided in Appendix C.

4.3 Stress Intensity Factors of a Kinked Crack

It is important at this point to confirm the validity of the last postulate, namely that two adjacent cracks can be approximated by a single kinked crack. Three ways to test this assumption are investigated below: comparing stress fields, SIFs, and displacement fields of two cracks with a single kinked crack. Stress fields, SIFs, and displacement fields are calculated for cracks positioned along the x_1 direction, are under uniform tension in the x_2 direction.

Stress fields

A test was conducted on the average stress fields ahead of a second small crack with length L_2 and an equivalent crack as shown in Figure 4.9. The average stress fields are compared over a distance of 10% of the equivalent crack length using the multipole method and FEM method. The differences between the fields of the second micro-crack and the equivalent crack are written in terms of a percentage error for several stress fields. Results of simulations are presented in table 4.1 for different size of cracks.

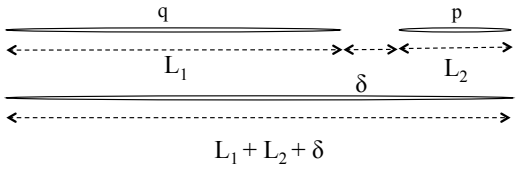


Fig. 4.6 Two small cracks of length L_1 and L_2 are separated by distance δ. A single crack has a length $L_1 + L_2 + \delta$.

Table 4.1 Comparison of stress fields

Crack Size: $L_1/L_2 = 100$			
δ/L_2	Error (%)		
	$\sigma_{x_2x_2}$	Von Mises	Pressure
0.01	9.1	10.1	12.2
0.03	9.9	11.1	13.3
0.05	10.4	11.5	13.6
0.07	11.5	12.8	14.9
0.10	12.6	13.9	16.1

Crack Size: $L_1/L_2 = 10$			
δ/L_2	Error (%)		
	$\sigma_{x_2x_2}$	Von Mises	Pressure
0.01	18.3	19.2	24.1
0.03	21.2	22.2	28.0
0.05	18.1	18.6	23.6
0.07	17.3	17.7	22.2
0.10	21.4	21.8	27.1

Stress intensity factors

Second, the SIFs of adjacent cracks and the main crack are compared using the multipole method and an analytical solution obtained in terms of complex potentials [20]. The SIFs located at the tip of the semi-infinite crack and the left and right hand side of the second crack in Figure 4.7 are represented by K_{I0}, K_{Ia}, and K_{Ib} respectively in Table 4.2. The SIFs are calculated both analytically and using the multipole method. The table shows some discrepancy between the K_{I0} values calculated by the two methods. This resulted from the different assumptions that are made in the multipole method simulations; the semi-infinite

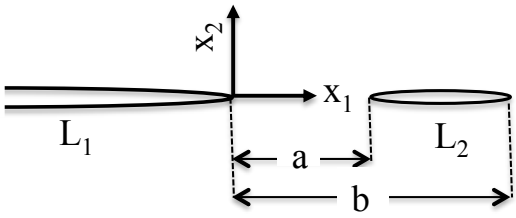


Fig. 4.7 Macrocrack and a micro-crack

crack of the analytical formulation is approximated by a large crack in the multipole method. Comparison of the results show the accuracy of the MM and the fact that two adjucent cracks can not represent the equivalent larger crack.

Table 4.2 Comparison of the SIFs at the crack-tip and the left and right-hand side of the second crack in Figure 4.7 using analytical approach [20] and the MM method.

$b-a=1\mu m$ Analytical approach				Crack size: $L_1=100$ & $L_2=1\mu m$		
$\frac{\delta}{L_2}=\frac{a}{(b-a)}$	K_{I0}/K_∞	K_{Ia}/K_∞	K_{Ib}/K_∞	K_{I0}/K_∞	K_{Ia}/K_∞	K_{Ib}/K_∞
0.01	2.76	2.67	0.73	1.71	2.38	0.73
0.03	1.92	1.78	0.68	1.52	1.72	0.68
0.05	1.65	1.47	0.65	1.42	1.45	0.66
0.07	1.51	1.30	0.63	1.39	1.29	0.63
0.10	1.39	1.14	0.61	1.29	1.14	0.62

Displacement fields

The displacement field (u_{x_2}) of two cracks under uniform tension in the x_2 direction is illustrated in Figure 4.8. In reality, two adjacent cracks require energy to merge and produce one crack. However as the propagation concept is not included in the mathematical framework of the multipole method, cracks can not merge. Consequently, the stress fields between two cracks become critically high and affect the stress fields and SIFs at crack-tips.

4.3.1 Correction to the Problem of Two Cracks (Kinked Cracks)

In general, two cracks cannot be approximated as one larger crack [20] unless modifications are applied to the system. In this section, a method to derive the SIFs of a kinked crack comprising two adjacent cracks is discussed.

Consider a pair of cracks, p and q where crack p is short compared to crack q, and their separation δ is small compared to the length of either crack (Figure 4.9a). Under external loading, crack q produces disturbance fields in the vicinity of Z_p and vice versa. Kushch *et al.*

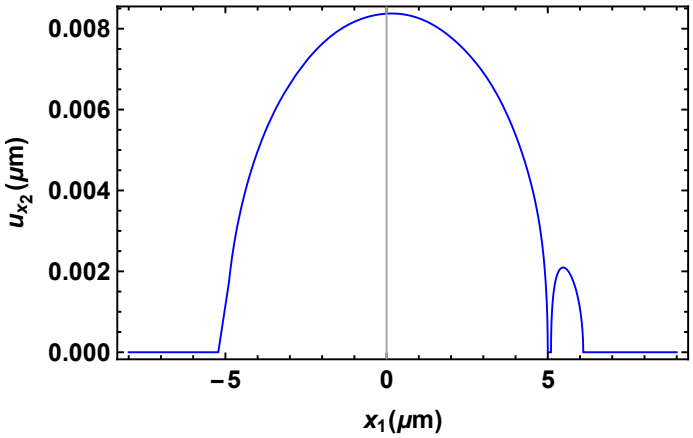


Fig. 4.8 Displacement field (u_{x_2}) of two cracks under uniform tension in x_2 direction. Sizes of cracks are $L_1 = 10\mu m$ and $L_2 = 1\mu m$.

[185, 186] derived a formula for the average stress in the pth inclusion $< \sigma >_p$, caused by the qth inclusion in terms of expansion coefficients $a_{n,q,p}$ and $b_{n,q,p}$. The same results were derived by Buryachenko [140] using the Green's functions in Eshelby's [187] and Mura's [188] studies.

Berezhnitskii *et al.* [189] showed in a system containing two cracks that under the critical external load, cracks grow towards each other and merge, and consequently a single kinked crack is formed. In our DCD, cracks propagate by inserting a micro-crack a small distance ahead of the crack-tip, in the direction of crack propagation, as depicted in Figure 4.9a. Therefore, it is necessary to establish that this ensemble can, to a very good approximation, represent the equivalent contiguous kinked crack (in terms of the SIFs and energy release rate) shown in Figure 4.9b, by suitable choice of the micro-crack length and separation distance. Hence SIFs and energy release rate are computed for the pth crack at tip B (see Figure 4.9a) incorporating the disturbance field at tip B caused by the longer qth crack. To simplify the calculation, the average disturbance fields introduced in [140] are used.

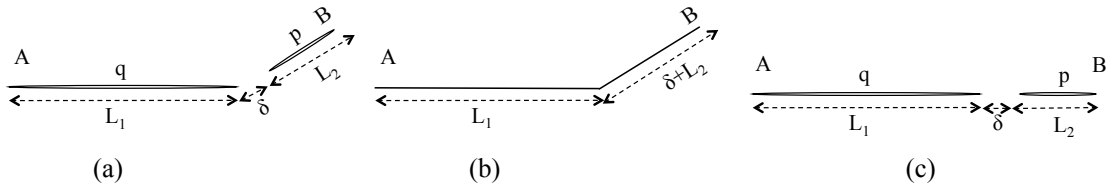


Fig. 4.9 a) Two small cracks of length L_1 and L_2 are separated by distance δ, b) an equivalent kinked crack, and c) two aligned cracks.

The average disturbance fields in one crack in the binary crack system caused by the other depends on the distance δ (Figure 4.9a). If cracks are positioned very close to each other, the large stress fields of the adjacent tips will reduce the accuracy of the approximation. Also, if they are positioned too far from each other, the ensemble in Figure 4.9a is incapable of representing the equivalent kinked crack in 4.9b. Therefore, there is an optimum δ that makes the approximate SIFs and energy release rate of Figure 4.9a maximally accurate. The case of two aligned cracks in Figure 4.9c is more sensitive to δ than any other configuration [190–192], hence δ is optimised for that case and the value is used for all configurations.

Since the optimisation of δ also depends upon the crack lengths, a number of simulations were run using different values of the crack lengths and junction size δ, to find the optimum δ. The optimum δ is the distance for which the two crack ensemble of Figure 4.9a (of length $L_1 + L_2 + \delta$) differs by no more than 1% in its SIFSs at tip B compared to those of the equivalent contiguous crack for the aligned cracks case (see Figure 4.9c). Figure 4.10 shows the optimum value of δ for different crack lengths L_1 and L_2.

Figure 4.11 and Table 4.3 present results for a successful validation test performed using kinked crack systems. Normalised SIFs of the kinked cracks calculated by analytical methods using the complex potential formulation and Greens function technique [21, 22], and the discrete dislocation density method [23] are compared with results obtained using the multipole method for two adjacent cracks separated by the optimum distance δ; the value of δ was obtained from the results of Figure 4.10 for the corresponding b/a ratios used in the comparison, noting that $a = L_1$ and $b = L_2 + \delta$. Analysing the results shows that normalised SIFs calculated using the MPM never differ by more than 5% for the $\phi = 15^\circ$, 30°, 45° and 60° degree cases, compared to the results of Lo *et al* [21], Hills [23] and Chen [22] respectively. Accuracy of the MPM depends on the number of harmonic terms, n, used in the calculations. According to the study performed by Kushch [135], *n=25* gives accurate results, which was also confirmed in this study by comparing predictions to FEM results; hence that value was used here. Data in Table 4.3 shows that discrepancies are larger for larger angles ϕ.

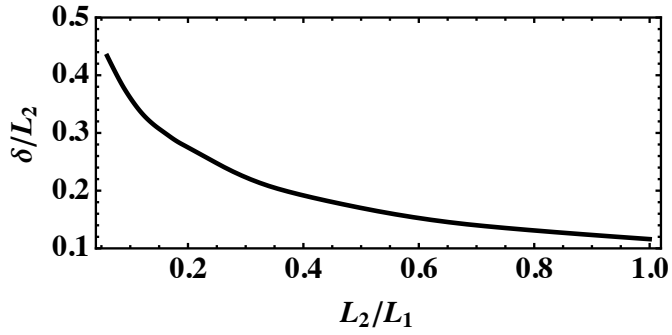


Fig. 4.10 The ratio of the optimised distance between two inclusions, δ, to the second crack/inclusion length, L_2, is plotted versus the ratio of the second to the first crack/inclusion length, L_2/L_1.

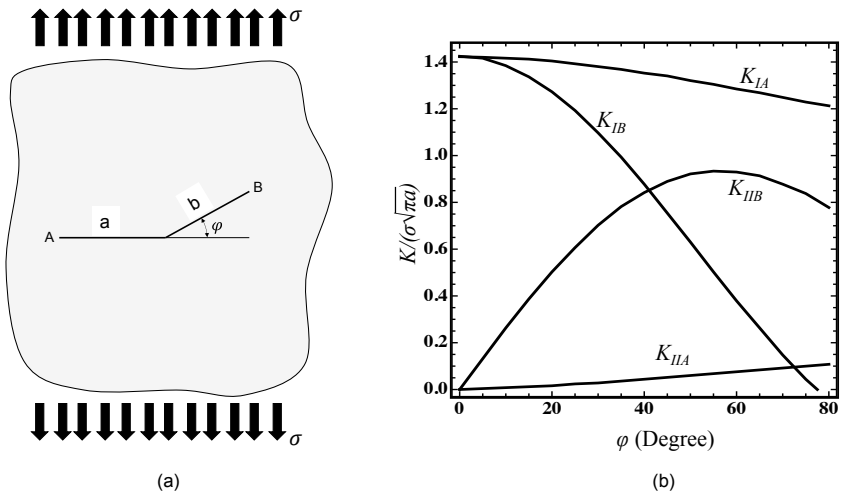


Fig. 4.11 a) Kinked crack benchmark problem. Appropriate δ is selected according to Figure 4.10; b) Normalised SIF of a kinked crack with b/a=1 using the MPM method.

Table 4.3 Variation of the normalised SIF ($K/\sigma\sqrt{\pi a}$) with angle for a kinked crack of the same size as the original crack under a uniform tensile stress. Suffix B refers to the endpoint (tip B) of the kinked crack (see Fig. 4.11). Methods 1, 2, 3 and 4 are the MPM method, the complex potential formulation, discrete dislocation density and Greens function technique, respectively [21–23].

Angle (φ^0)	Method	K_{IB}				K_{IIB}			
		Size b/a				Size b/a			
		1	0.5	0.1	0.05	1	0.5	0.1	0.05
15^0	1	1.3	1.15	0.98	0.97	0.38	0.31	0.21	0.20
	2	-	1.15	1.01	0.98	-	0.32	0.23	0.19
	3	1.32	-	0.97	-	0.41	-	0.22	-
	4	1.32	1.15	0.99	0.98	0.38	0.32	0.22	0.19
30^0	1	1.07	0.96	0.85	0.86	0.68	0.58	0.4	0.38
	2	-	-	-	-	-	-	-	-
	3	1.08	-	0.83	-	0.69	-	0.41	-
	4	1.08	0.95	0.86	0.86	0.68	0.57	0.4	0.36
45^0	1	0.73	0.67	0.64	0.69	0.87	0.76	0.52	0.49
	2	-	0.66	0.66	0.69	-	0.72	0.54	0.47
	3	0.76	-	0.66	-	0.83	-	0.52	-
	4	0.74	0.66	0.66	0.69	0.84	0.72	0.52	0.46
60^0	1	0.37	0.34	0.41	0.49	0.90	0.82	0.58	0.53
	2	-	-	-	-	-	-	-	-
	3	0.38	-	0.41	-	0.82	-	0.55	-
	4	0.39	0.35	0.43	0.49	0.83	0.74	0.56	0.50
75^0	1	0.04	0.01	0.15	0.28	0.81	0.79	0.56	0.55
	2	-	0.1	0.23	0.28	-	0.64	0.51	0.48
	3	0.08	-	0.19	-	0.67	-	0.52	-
	4	0.09	0.07	0.2	0.29	0.68	0.65	0.52	0.48

4.4 Crack Propagation: Simulation

In the DCD method, crack propagation is a discretised process (based on the concepts of FFM [173, 174]), in which the crack advances incrementally at each simulation step. The general algorithm to study a crack propagation is as follows. *(i)* Values of stress fields and SIFs are computed for the current state of the system. *(ii)* If the crack propagation condition is fulfilled, the direction of propagation and the increment length have to be determined using the fracture criterion. *(iii)* The crack size (crack/inclusion distribution) is updated and the iterative process is continued.

4.4.1 Crack Propagation: Simulation Steps

The general algorithm to study an evolution of a main crack in a system containing other cracks and inclusions is as follows.

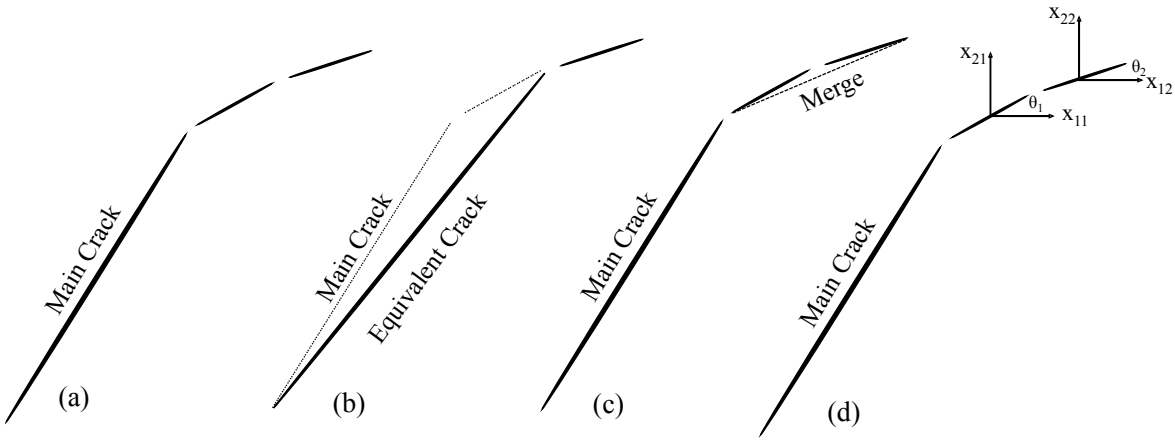


Fig. 4.12 Schematic representation of simulation steps. a) propagated kinked crack, b) an equivalent crack, c) merge micro-cracks, d) micro-cracks orientations.

- If the crack propagation condition is satisfied, a further crack is added ahead of the main crack-tip with the optimal spacing determined in 4.3, the crack extension determined from the theory of FFM and at an angle prescribed by the adopted fracture criterion. The arrangement of the original crack and the new crack is an approximation of a kinked crack, using the theory developed in Section 4.3. Accordingly, the SIFs and the energy of the approximated kinked crack are calculated.

- The problem arises in the next step of simulation when the kinked crack propagates. The discretised process of crack propagation requires introducing a new micro-crack at the tip of the crack/micr-crack ensemble. At this point, calculating the SIFs of a propagated kinked crack, which is a system of one main crack and two micro-cracks given in Figure 4.12a is not straightforward. Before addressing the current problem, it is better to answer the question of whether it is even possible to determine the crack propagation path with a succession of small micro-cracks?

  Although in the DCD method, crack propagation is simulated by adding new micro-cracks at the main crack-tip, the whole process of crack propagation can not be modelled by introducing a series of micro-cracks ahead of the main crack-tip due to the shielding effect associated with the micro-cracks. Crack-tip shielding caused by micro-cracking were studied by Kachanov *et al.* [193] and Hutchinson *et al.* [194, 195]. An analytical study was given by Asher [20] for an array of aligned micro-cracks ahead of a main crack-tip. It was proved that by increasing the number of micro-cracks, the local SIFs and stress field distributions at the micro-crack tips are not significantly affected by the presence of the main crack, and mostly are influenced by the local stress fields. As the effect of the main crack is lost by far away micro-cracks, the estimated crack propagation direction and energy based on the leading micro-cracks becomes unreliable. Therefore, another method to approximate crack propagation path is required. Precise prediction of the SIFs and crack energy are necessary to determine the crack propagation path. Here a solution is given for a system of three cracks. The solution is then generalised for a problem of the crack propagation in the DCD method, where the concept of a kinked crack and its SIFs are used to model crack evolution.

  The problem of a propagating kinked crack may be addressed by approximating a set of three cracks, comprising a main crack and two micro-cracks, with two cracks by either replacing the main crack and the first micro-crack with an equivalent crack (Figure 4.12b) or merging the two micro-cracks (Figure 4.12c). Before using any of these estimations, it is necessary to be confident in the correctness of these approximations. The point of this is to always have a main crack and a single crack ahead of it representing the crack extension. For which it has been shown in Section 4.3 that the approximation is very good for the optimal distance and crack extension.

  The problem of SIFs at the tip of the kinked crack has been studied in [196–198]. It was shown that the SIFs of a kinked crack depend on the inclination angle of the crack extension and the SIFs of the main crack. Kitagawa *et al.* [199] and Bechtle *et al.* [200] showed that, from the standpoint of SIFs, a kinked crack can be replaced by a straight line crack, in which the direction at the crack-tip is the same as the crack

extension. Chen [22] showed that for a kinked crack, an angle between the tangent to the crack-tip and load direction determines the proportion of Mode I and II stress intensity factors while the distance between the two extends of the crack ensemble is a dominant factor on the crack-tip SIFs.

Considering the previous studies and knowing that the ratio of Mode I and II stress intensity factors determines the crack deflection direction in the next step of simulations [14, 15], in the problem of three cracks in Figure 4.12a, the orientation of the last micro-crack must remain the same. If the main crack and the first micro-crack is replaced with an equivalent crack as shown in Figure 4.12b, the length of the equivalent crack is roughly the same as the distance between the extents of the crack ensemble, thus, according to Chen [22] the SIFs in Figure 4.12b should be a good approximation of those at the propagated crack-tip.

Simulations were conducted to establish the validity of this assumption. The SIFs of zig-zag cracks shown in Figure 4.13a under a uniform tension in the x_2 direction were calculated by Chen [22]. The distance between the crack-tips is $2a$ and α denote the angle of zig-zag section. Here the SIFs of the zig-zag cracks at crack-tip B are estimated by the approximated kinked crack systems employed in the DCD to approximate branched cracks as depicted in Figure 4.13b. Table 4.4 presents the results of this validation test. Normalised SIFs of the zig-zag cracks, calculated by a numerical method using a singular integral equation containing the crack opening displacement (COD), are compared with the results obtained using the multipole method for two equivalent adjacent cracks separated by the optimum distance δ as described in the crack propagation methodology proposed here. The value of δ was obtained from the results of Figure 4.10. Analysing the results shows that normalised SIFs calculated using the MM are in good agreement with Chen's calculations, especifically for the cases with $\alpha <= 45^0$. The quality of the match also seem to affect mode II SIF more than mode I. If the zig-zag crack is modelled with the DCD method using the micro-cracks, the relative angular differences between the two subsequent micro cracks are equal to 2α. In the crack propagation problems, crack-tip angular variation corresponding to branching larger than 90^0 are rarely experienced in reality, except in the cases where the fracture energy has a very strong spatial bias. It can therefore be concluded that the approximation made when simulating crack propagation using the DCD method is acceptable and special care will only be taken when abrupt changes in the material properties of the material under investigation may lead to sudden and sharp changes in crack trajectories.

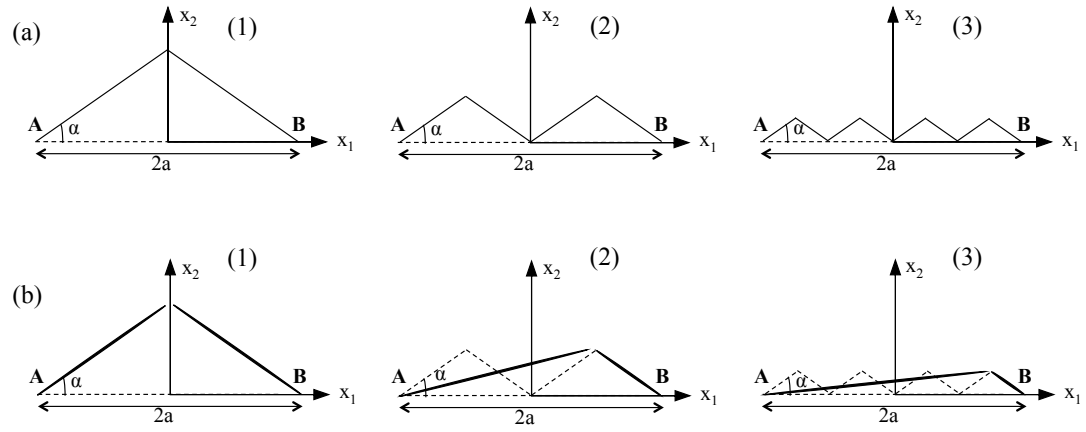


Fig. 4.13 Schematic representation of (a) zig-zag cracks, and (b) the approximated kinked cracks used to describe the system in DCD.

Table 4.4 Variation of the normalised SIF ($K/\sigma^{\infty}\sqrt{\pi a}$) with angle for systems given in Figure 4.13 using the singular integral equation containing the COD and the multiple method. Suffix B refers to the endpoint (tip B) of the crack and m denotes the number of zig-zag kinks.

SIF	m	$\tan\alpha$									
		Chen [22]					Multiple method				
		0.1	0.2	0.5	1	2	0.1	0.2	0.5	1	2
$K_{IB}/\sigma^{\infty}\sqrt{\pi a}$	1	0.99	0.97	0.81	0.52	0.21	0.98	0.95	0.81	0.54	0.23
	2	0.99	0.97	0.84	0.53	0.32	0.99	0.96	0.83	0.59	0.23
	4	0.99	0.97	0.86	0.65	0.41	0.99	0.98	0.87	0.66	0.30
$-K_{IIB}/\sigma^{\infty}\sqrt{\pi a}$	1	0.11	0.22	0.47	0.64	0.65	0.11	0.21	0.43	0.62	0.63
	2	0.09	0.19	0.40	0.54	0.54	0.08	0.16	0.36	0.55	0.57
	4	0.08	0.16	0.34	0.47	0.48	0.07	0.14	0.31	0.46	0.51

Figure 4.12d demonstrates the orientation of the last two micro-cracks in their local coordinate systems. To increase the accuracy of the simulation before introducing the equivalent crack, it might be better to check if it is more accurate to merge last two new cracks rather (Figure 4.12c) than replacing the first two cracks with an equivalent one. The criterion for whether to merge the two consecutive micro-cracks is a function of the relative angular difference between them ($\Delta\theta = \theta_2 - \theta_1$): If the mismatch in orientation of the two cracks is less than a predefined amount, then the cracks will be merged. The angular mismatch, below which the merging is allowed, is a function of whether or not the merging produces a better estimate of the SIFs compared to the alternative combination of equivalent crack extended by the outermost new crack. This, therefore, depends on the materials and the geometry of the problem.

- The same method can be used at all iterations to predict the crack trajectory.

4.4.1.1 Flow diagram

A flow diagram of the developed discrete crack dynamic code is illustrated in Figure 7.5; the DCD method predicts the crack propagation path and its associated energy in the system. In this case, crack propagation criteria (step 3) are provided by considering the host material that is used. The analysis is finalised in six steps. At each iteration, interactions between all elements of the system are calculated and the failure criterion at the main crack-tip is examined (step 4). The crack propagates in a direction determined by the fracture criteria, by introducing a new pseudo-crack in the system (step 5). In the first iteration, a main crack propagates by introducing a new micro-crack. The ensemble of the main crack and the micro-crack is an approximation of a kinked crack. Then, if the kinked crack propagates, a new micro-crack has to be added to the system; thus two micro-cracks have to be added. However, in the next iterations, there exists a kinked crack; thus only one micro-crack has to be added to the system. Then the main crack is replaced by an equivalent one (step 6).

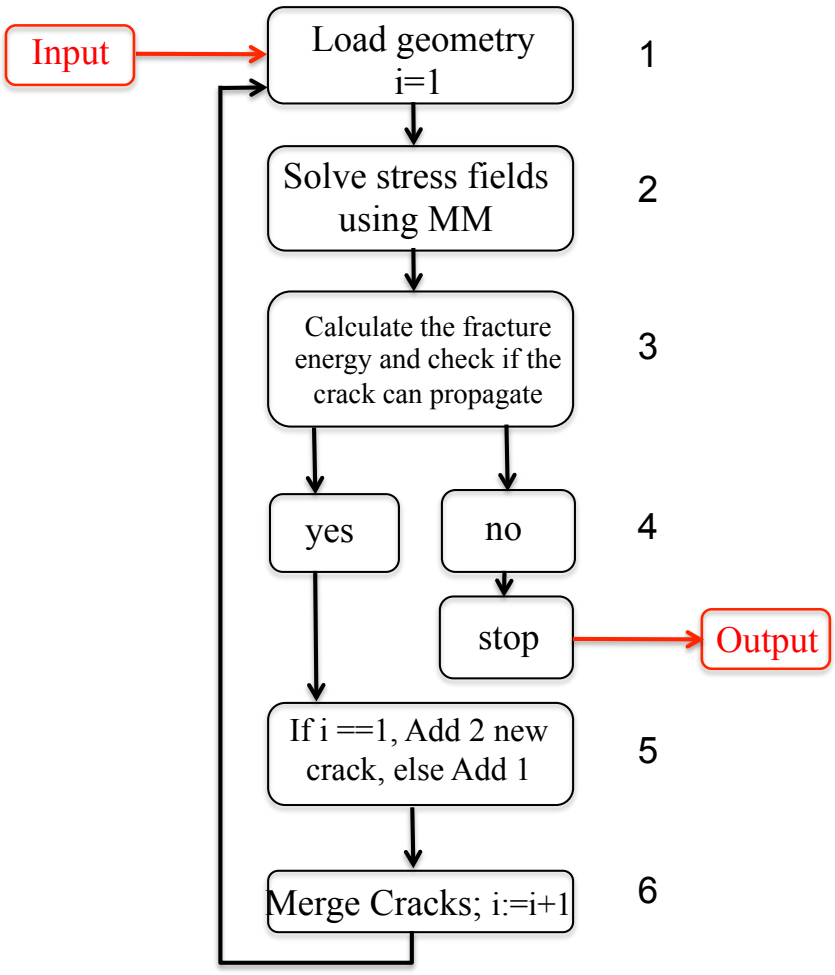


Fig. 4.14 The flow chart of the DCD method to calculate the crack propagation path and its associated energy in the system.

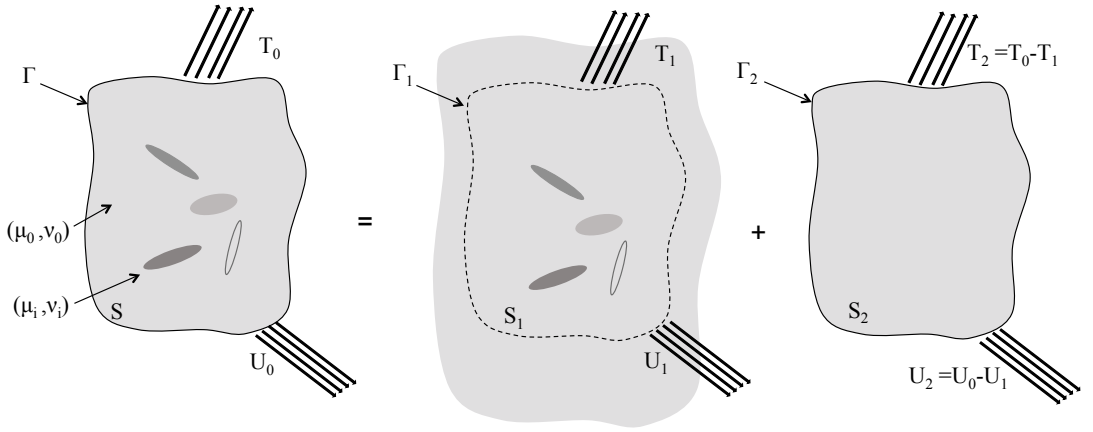


Fig. 4.15 Decomposition of the finite elastic body with inclusions into the problem of interacting elliptical inclusions and the complementary problem for the finite body without inclusions.

4.5 Finite-Size Problems

The behaviour of the main crack-tip at the macroscopic level in an unbounded solid has been successfully modelled by DCD method. The aim of this section is to simulate finite-size problems using a superposition scheme to incorporate boundary effects. Within linear elasticity the superposition principle is exact at each simulation step and requires no modification in the multipole method described here. Let S be the domain of the boundary-value problem with boundary Γ delimiting a solid body characterised by stress and displacement fields $\sigma_0(x,y)$ and $U_0(x,y)$. By virtue of the linear superposition principle, these can be written as the sum of two fields: $\sigma_0 = \sigma_1 + \sigma_2$ and $U_0 = U_1 + U_2$ where suffix 1 and 2 represent fields of the infinite domain containing the inclusions, and finite-size inclusion-free medium S_2 coinciding with S. As a result of inclusion interaction fields, surface Γ_1, which coincides with Γ, experiences a traction T_1 and displacement U_1. In order for the superposition of the fields in S_1 and S_2 to equate the fields in S, the surface Γ_2 must have, for every simulation step, -T_1 and -U_1 applied over it in addition to the boundary conditions applied on Γ.

To summarise, the problem under consideration is a 2D linear elastic body of area S, comprising elastic inclusions and holes (Figure 4.15). The elastic properties of the matrix material are governed by the shear modulus μ_0, and Poisson's ratio ν_0, and the elastic modulus of inclusions and holes are denoted by the shear modulus μ_i, and Poisson's ratio ν_i. This body is now considered to be subjected to the remote far-field traction.

It is assumed that the crack propagation process is quasi-static and to involve finite development at each step of simulation. Each simulation step involves two main computational

stages. First, for the current inclusions arrangement, the current stress field of the problem in the solid is determined. Second, if the propagation criterion is fulfilled, the position of the new micro-crack in the crack propagation process is specified.

The current state of the system is determined by decomposing the problem of the finite body with inclusions into two problems: the problem of interacting inclusions in the homogeneous infinite solid and the complementary problem for the homogeneous body without inclusions. The former problem is solved using the multipole method formulation, and the latter can be solved using a numerical scheme such as finite-element or boundary-element methods. The complex variables boundary element method (CVBEM) uses the same mathematical framework as the MM method and is therefore chosen to solve the finite boundary value problem in the absence of inclusions.

4.5.1 The Complex Variable Boundary Element Method

The Complex Variable Boundary Element Method is a generalisation of the Cauchy integral formula into a boundary integral equation method. The method produces approximation functions that are analytic within the domain enclosed by the problem boundary. In the CVBEM method, the integrations of the boundary integrals along each boundary element are solved exactly without the need for numerical integration. The modeling approach is extremely useful to deal with the two-dimensional elasticity problems [98, 83, 10]. In this study the indirect formulation of the CVBEM is employed; the associated code developed by the Zografos [10, 201] was used to calculate the effect of finite-size on crack propagation. The code is based on the complex form of Kelvin's Green function [83], and the influence functions of the respective boundary elements which are evaluated by analytical integration.

4.5.1.1 Formulation

In 2D elasticity, all the components of elastic fields can be expressed via Muskheloshvili's potentials φ and ψ.

$$\begin{cases} 2\mu u(z) = \kappa\varphi(z) - z\overline{\varphi'(z)} - \overline{\psi(z)} \\ \sigma_{11} + \sigma_{22} = 4Re\varphi'(z) \\ \sigma_{22} - \sigma_{11} + 2i\sigma_{12} = 2\left[\bar{z}\varphi''(z) + \psi'(z)\right] \end{cases} \tag{4.21}$$

where σ_{ij} are stress components in the global coordinate system (x_1, x_2); $u = u_1 + iu_2$ is the displacement vector in this system.

The expression of complex potentials for a point force in a plane (Kelvin's solution [151]) is given by:

$$\begin{aligned}\varphi'(z) &= -\frac{X_1+iX_2}{2\pi(1+\kappa)}\frac{1}{z-z_0}\\ \psi'(z) &= \kappa\frac{X_1-iX_2}{2\pi(1+\kappa)}\frac{1}{z-z_0}-\frac{X_1+iX_2}{2\pi(1+\kappa)}\frac{\overline{z_0}}{(z-z_0)^2}\end{aligned} \tag{4.22}$$

where (X_1+iX_2) is a point force loaded at the point z_0 in the normal and tangential directions. Denoting $U_i(\tau,z)$, and $\sigma_i(\tau,z)$ as the $i-th$ component of the displacements and stress functions corresponding to the unit point force loaded at the point τ. Using Equations 4.21 and 4.22, $U_i(\tau,z)$, and $\sigma_i(\tau,z)$ can be derived for a point source; this is equivalent to the concept of the Green's function. Having the displacement and stress functions produced by a unit point source, the displacement field within a finite region with a smooth boundary s at any point z inside the boundary can be written as:

$$\begin{aligned}u(z) &= u_1(z)+iu_2(z)\\ &= \int_s [U_1(\tau,z)+iU_2(\tau,z)]w(\tau)ds_\tau, \quad \tau\in s\\ &= \int_s U(\tau,z)w(\tau)ds_\tau\end{aligned} \tag{4.23}$$

where, $w(\tau)$ is a weight function that represents the magnitude of the continuous force on s. Similar expression can be written for the stress fields as:

$$\sigma(z) = \int_s \sigma(\tau,z)w(\tau)ds_\tau. \tag{4.24}$$

In 2D elasticity, $w(\tau)$, $U(\tau,z)$, and $\sigma(\tau,z)$ are 1×2, 2×2 and 3×2 matrixes respectively. The boundary value problem can be formulated in terms of boundary integral equations 4.23 and 4.24 by taking τ to be part of the larger boundary Γ; suppose that the s is a finite region with the Γ boundary. By discretising the boundary Γ to N segments of length s_i at points c_i (the midpoint in s_i boundary segment), the displacement and stress fields at any point $z\in s$ can be calculated using formulas:

$$\begin{aligned}u(z) &= \sum_{i=1}^{N}\int_{s_i} U(\tau_i,z)w(\tau_i)ds_{\tau_i}\\ \sigma(z) &= \sum_{i=1}^{N}\int_{s_i} \sigma(\tau_i,z)w(\tau_i)ds_{\tau_i}.\end{aligned} \tag{4.25}$$

where the integration has to be performed over each elements. It is more convenient to find the integrals in a local coordinate system of each boundary segment; transformation of the stress fields requires tensor rotation. The stress tensor σ', and displacement vector u' in the

rotated coordinate system are obtained using the formula $\sigma'(z) = R\sigma(z)R^T$ and $u' = Ru(z)$, where R is a rotational transformation tensor. By selecting $w(\tau_i) = w_i f(\tau_i)$, displacement and stress fields in equations 4.25 can be expressed as:

$$\begin{aligned} u(z) &= \sum_{i=1}^{N} \left[\int_{s_i} U(\tau_i, z) f(\tau_i) ds_{\tau_i} \right] w_i \\ \sigma(z) &= \sum_{i=1}^{N} \left[\int_{s_i} \sigma(\tau_i, z) f(\tau_i) ds_{\tau_i} \right] w_i \end{aligned} \tag{4.26}$$

which can be expressed in matrix form as:

$$\begin{aligned} u^* &= U.w \\ \sigma^* &= C.w \ . \end{aligned} \tag{4.27}$$

u^*, σ^*, and w are two vectors of $2N \times 1$ dimensions in 2D, where N is the number of the collection points multiplied by the dimension of the system. U and C are $2N \times 2N$ influence coefficient matrices, in which the elements are derived using the integrals in Equation 4.26. The elements of these matrices are the displacement/traction at the i-th collection point associated with the unit $f(\tau_i)$ traction acting on the $j-th$ element. w is the vector of the unknown weight functions at each collection point. Equation 4.27 provides $4N$ linear equations. However, depending on the mixed boundary conditions only $2N$ linear equations are involved. These linear equations can be solved by applying displacement and stress boundary conditions to u^* and σ^* vectors. By reordering the equations appropriately and solving the matrix equation, the unknown weight functions w_i can be determined; more details on matrix form of the equation can be found in [10]. Once the vector w is determined, the displacement and stress fields are fully calculated using equation 4.26.

4.5.1.2 Flow diagram

A flow diagram of the boundary element code is illustrated in Figure 7.4 for finite size problems, the multipole method and CVBEM are combined to predict the full stress and displacement of the system. In this case, the boundary conditions (step 4) required for CVBEM are provided by the multipole calculation at each nodal point.

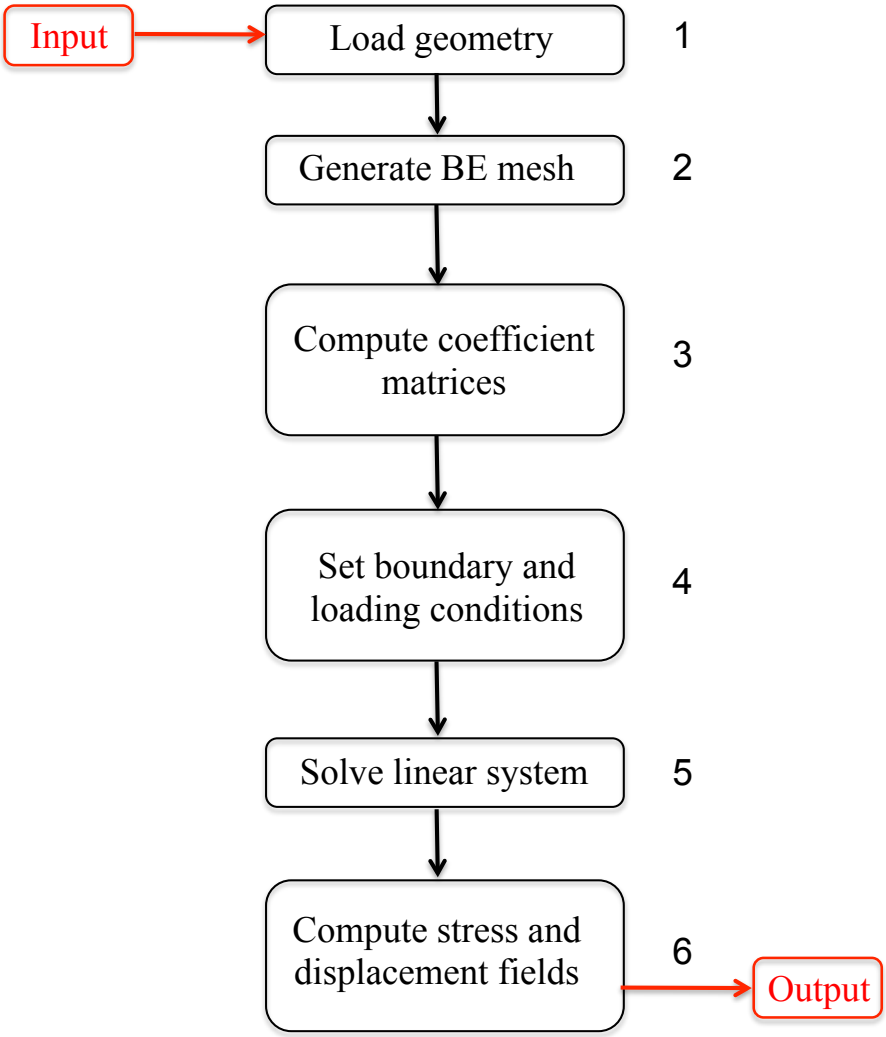


Fig. 4.16 The flow chart of static analysis of CVBEM [10].

The static analysis can be finalised in six steps. Calculating the influence coefficient matrices (step 3) and the stress and displacement fields (step 6) are the most computationally expensive steps in the analysis. In the crack propagation problems, where an iterative solution process is required, the iteration is performed over steps 4 and 5.

To predict the crack propagation for finite size problems, the stress and displacement fields in step 2 of the DCD chart (Figure 7.5) have to be calculated in the way shown in Figure 7.6.

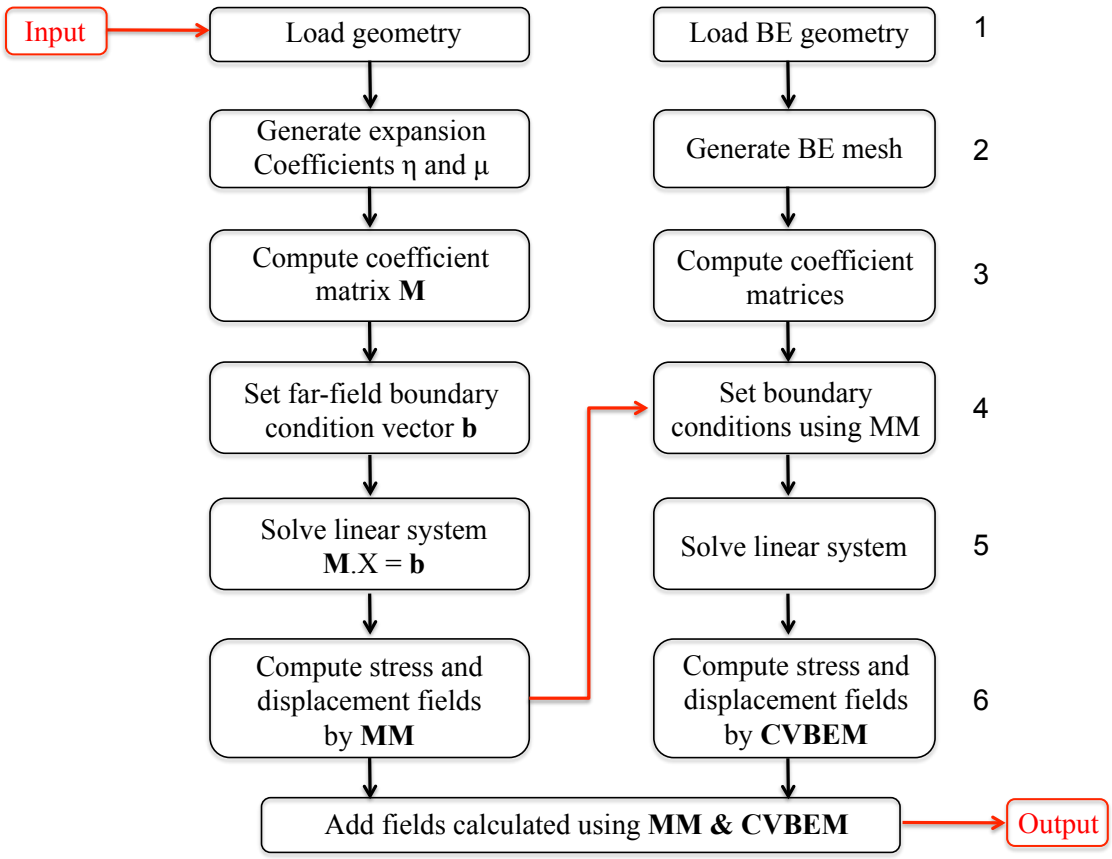


Fig. 4.17 The flow chart of the stress and displacement fields in step 2 of the DCD method (Figure 7.5) to calculate the crack propagation path and its associated energy in the finite size system.

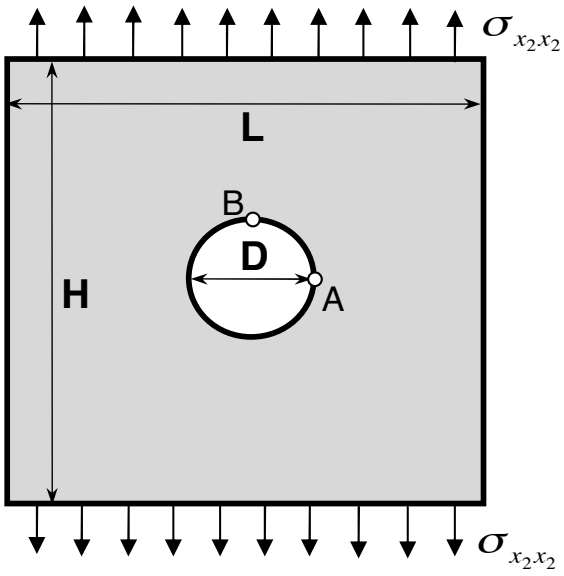


Fig. 4.18 Square plate with the circular hole.

4.5.1.3 Benchmark test: Square plate with a circular hole

A simple case of a square plate with a hole under uniform tension was examined to test the performance of the technique. This test assesses the accuracy of the method for the current state of the system at each simulation step. Figure 4.18 shows the geometry of this benchmark problem. For an unbounded plate the normalised value of the hoop stress, $\sigma_{\theta\theta}/\sigma_{x_2x_2}$, at points A and B is 3 and -1 respectively. However, for the finite plate problem, the values of 3.021 and -1.0167 for $L = 20$, $H = 20$, $D/2 = 1$ unit length was reported by Fenner [202] and confirmed by [10]. Here, the normalised value of the hoop stresses was derived using the multipole method, and the boundary element mesh consisted of uniform size straight elements distributed along the outer boundaries of the square plate. The number of elements distributed along the sides of the plate is increased to 100 to obtain sufficient accuracy. It should be noted that the required number of elements is almost half that calculated by Zografos [10].

4.6 Numerical Results

Simulations of this section were conducted to establish the validity of the fundamental building blocks of what I hope will become a standard micromechanics model for dealing with cracks near inclusions in real materials.

An Inclined Crack: Tension

To start, the DCD method was used to predict the propagation of an inclined crack under uniaxial tension, loaded in the x_2 direction. Figure 4.19 shows the propagation path of an inclined crack with various inclination angles. Although, the crack deflection angle depends on the applied fracture criterion, Figure 4.19 shows that there is a tendency for the crack propagation to occur mainly in mode I. This agrees with previous calculations [203, 66, 204].

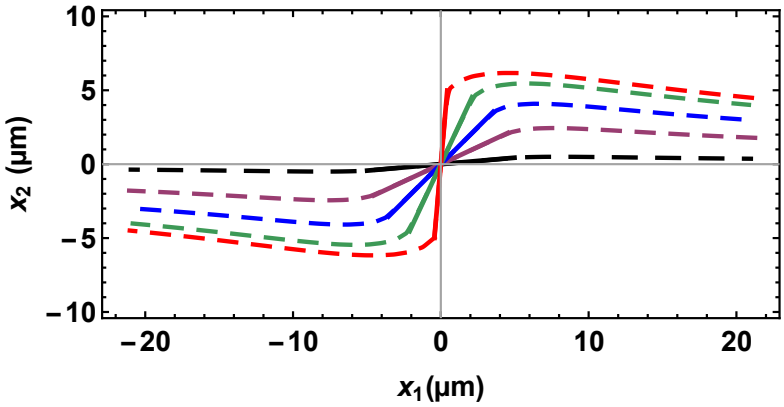


Fig. 4.19 Crack propagation path (dashed line) of cracks with different inclination angles under uniform tension. The initial size of the crack is 5 μm. The initial inclination angles of $5^0, 25^0, 45^0, 65^0, 85^0$ are presented by black, purple, blue, green, and red lines respectively.

An Inclined Crack: Compression

The same problem was solved under uniform compression in the x_2 direction. Figure 4.20 graphically compares the numerical results obtained using DCD and Boundary Element methods given by Haeri [11], and demonstrates the accuracy and validity of the DCD method. Results are in agreement with other predictions given by Horri and Nemat Nasser [205, 206].

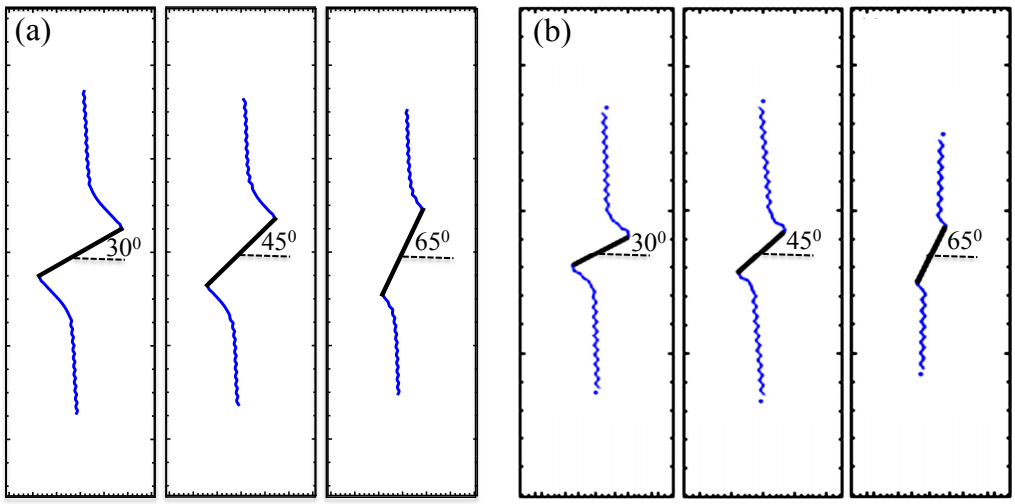


Fig. 4.20 Boundary element simulation of crack propagation process in pre-cracked specimens for 30°, 45° and 65°. (a) calculation with DCD and (b) Boundary Element Method [11].

Crack Path Deflection: Effect Of Soft And Hard Inclusions

Sets of simulations were run to establish the effect of impurity and micro-crack interactions on the deflection of the main crack-path. The crack propagation trajectory in the vicinity of a circular soft and hard inclusion were studied on a plate with side lengths of 10 μm. The plate was loaded remotely in tension in the x_2 direction. The initial crack length a and the inclusion radius r were set to $1\ \mu m$, and the inclusion was centered at the origin of the coordinate system. Figure 4.21a shows the effect of accuracy of the interaction fields between cracks and inclusions on the crack propagation path and its deflection in an unbounded system. The relative stiffnesses of the inclusion to the matrix was selected as 10. The green (n=1), blue (n=3) and red (n=9) curves represent crack paths for different number of harmonic terms. The crack paths are indistinguishable for $n = 9$ and higher values of n.

Figure 4.21 parts b and c present the crack path deflection in the presence of a circular hard and soft inclusion in a finite plate. The plate was fixed at the bottom edge and the load distributed uniformly on the top edge. The relative stiffnesses of the inclusion to the matrix were selected as $2, 10, 100$ and $1/2, 1/10$ for the hard and soft inclusion respectively. Figure 4.21d shows that simulated results are comparable with modelling provided in [12]. Results agree with other simulations and experimental predictions given by [207, 145, 208, 13].

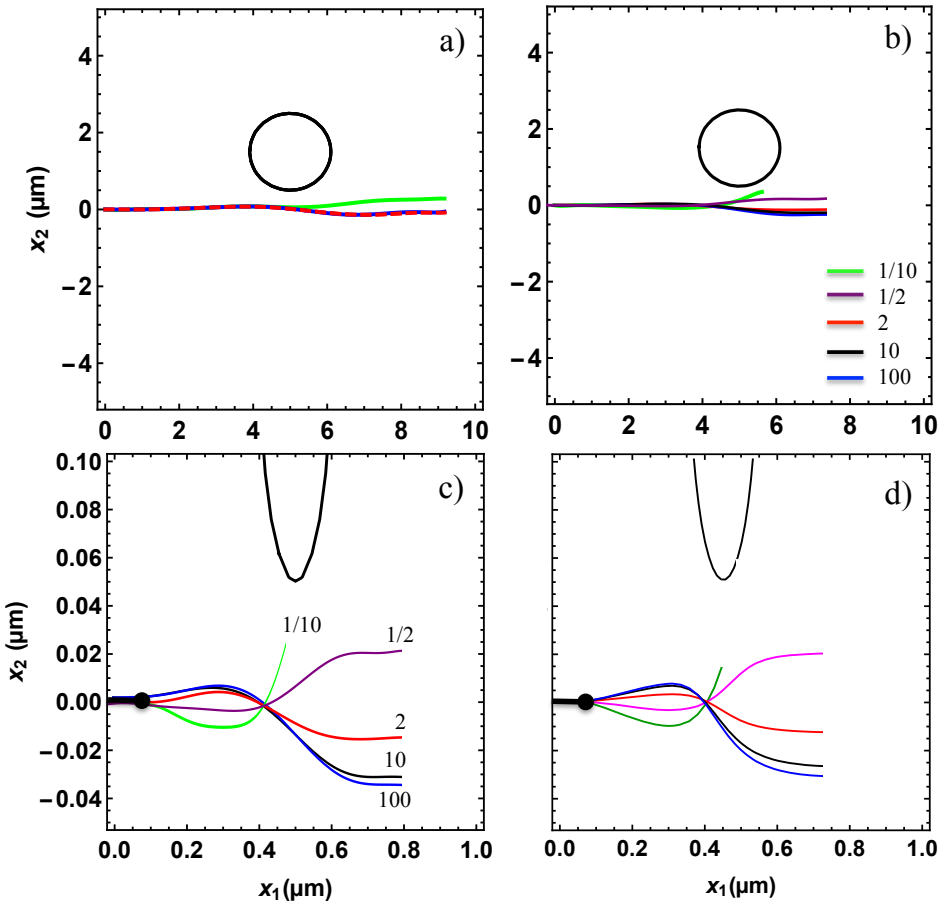


Fig. 4.21 Deviation of the crack propagation path in the vicinity of a circular inclusion. a) crack path predicted using different harmonic terms n; green (n=1), blue (n=3) and red (n=9). This one shows the effect of harmonic terms on the accuracy of the results. Crack path deviations are shown for several relative stiffnesses of the inclusion to the matrix b) with correct aspect ratio, c) a comprised aspect ratio to zoom closer, and d) a comprised aspect ratio provided in [12].

Crack Path Deflection: Effect Of Elliptical Holes

The DCD method was employed, to compare the crack paths in brittle materials with the asymptotic model and experimental result presented in Ref. [13]. A plate containing elliptical holes was subjected to Mode-I loading; the origins of elliptical holes with the major and minor axis of 4, and 0.6 *mm* are placed at $(x_{1a}, x_{2a}) = (75, -9)$ and $(x_{1b}, x_{2b}) = (105, 8)$ *mm* coordinates. The associated inclination angles of elliptical voids are $\theta_a = 0$ and $\theta_b = \pi/2$ respectively. The experimental set up is reproduced in the simulations as reported in Figure 4.22. Excellent agreement between analytical results of the asymptotic solution, the DCD method and experiment is observed. All methods predict fracture deflection toward the small void, where the interaction of the crack with elliptical voids deviates the fracture path from the straight line. In Figure 4.22, the blue and dark blue dashed curves represent the shape predicted by the asymptotic model [13] and the DCD method, whereas the red curve shows the actual shape obtained in the experiment. From the figure, it can be deduced that the DCD method can be applied to problems involving impurities and inclusions.

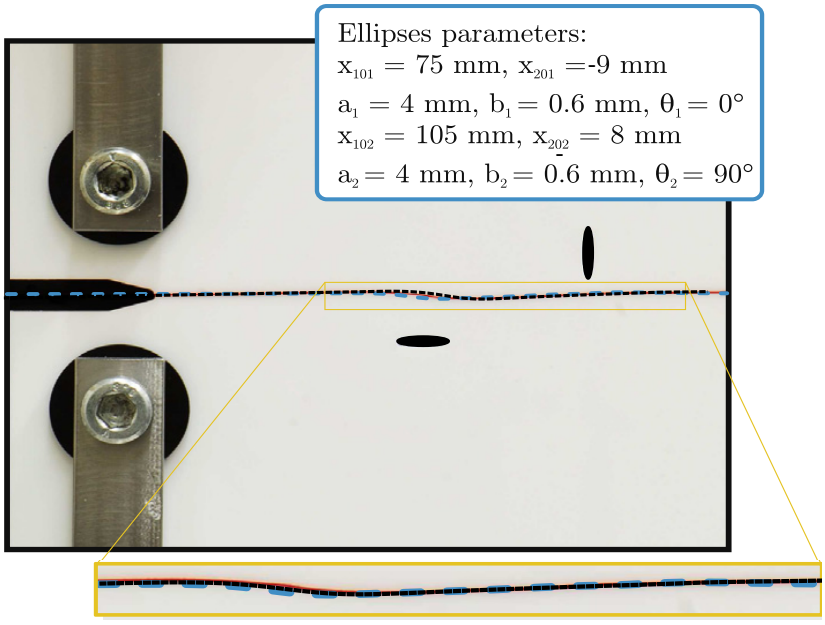


Fig. 4.22 Experimental crack trajectory (red) compared to the asymptotic model (blue)[13], and the DCD method (black) for interaction with elliptical voids.

In this chapter a new computational method, which is named discrete crack dynamics, is developed to address the elasticity problems of two-dimensional finite-size systems characterised by short range interactions between inclusions with particular application to crack propagation. The method may be applied to realistic complex structures to establish the effect of size and mechanical properties of inclusions on crack propagation paths. Interface energy, and the interactions between cracks/inclusions and grain boundaries are the subject of the next chapter.

Chapter 5

Interface and Grain Boundary Effects

5.1 Introduction

The main purpose of this chapter is to further develop a fracture model for polycrystalline materials considering the effect of interfacial strength on the crack trajectory. This study presents how the interactions between the main crack and imperfections such as inclusions, especially when characterised by weak interfaces, small voids, and grain boundaries (GB) can deflect and channel the crack along a predefined path [13, 100, 103, 12, 145]. The ability to guide and deflect the crack is fundamental to enhance the performance of brittle materials because the toughness of materials is increased by crack deflections [59–61]. Thus, the results provided by this investigation are valuable for design purposes as this information can be used to improve strength and toughness of materials.

Figure 5.1a is a schematic representation of a polycrystalline material where the crack propagates through several grains and propagation involves interactions with inclusions, cracks, voids and grain boundaries. In Chapter 4, the Discrete Crack Dynamics method was developed to predict an evolution of the individual micro-crack and its interaction with existing cracks/ inclusions in two-dimensional finite-sized systems. In the DCD the interactions between elements of a system are accurately computed using the multipole method, which has been presented in Chapter 3. To develop a complete fracture model for polycrystalline materials, one has to address the influences of the interfacial strength of grain boundaries (Figure 5.1b), inclusions (Figure 5.1c), and interactions between inclusions at the grain boundaries (Figure 5.1d), on the crack propagation path.

In this chapter, a method to study interfacial effects is introduced in Section 5.2. Then, the effect of the presence of grain boundaries on the evolution of the crack propagation path is studied in Section 5.3.1. The influence of the interface strength of an elliptical inclusion on the deflection of evolving cracks is investigated in Section 5.3.2. Crack interaction with an

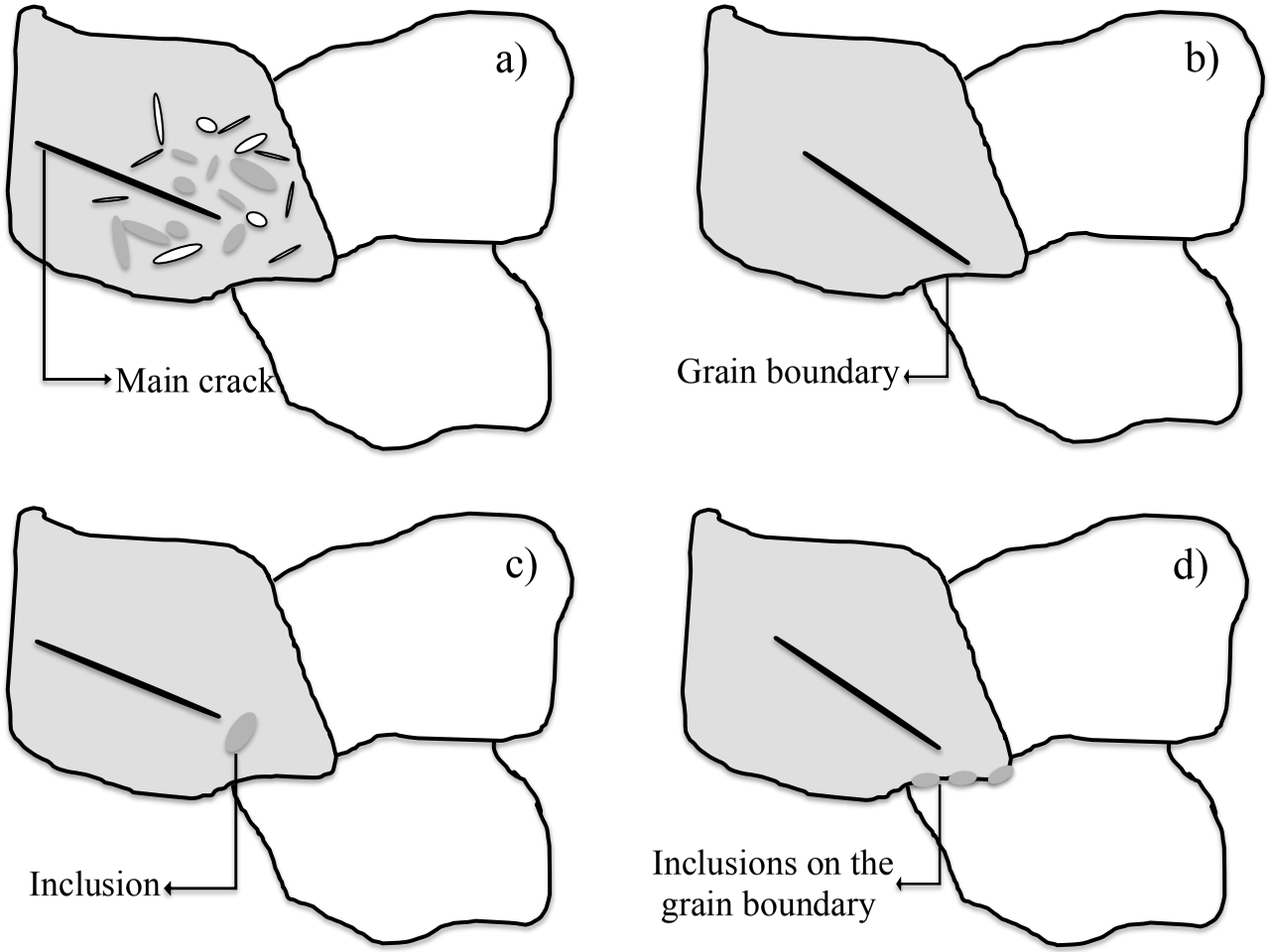


Fig. 5.1 Schematic representation of problems. Crack propagation in a polycrystalline material: (a) overall view of potential interaction; effect of the interfacial strength of (b) grain boundaries, (c) inclusions and (d) inclusions along the grain boundaries, on the crack propagation path.

inclusion located at the the grain boundary is investigated in Section 5.3.3. Finally, the method is employed to demonstrate how to channel a crack into a toughening configuration using an array of elliptical holes and soft inclusions to obtain the optimal configuration (Section 5.4). Numerical results at each step are validated with experimental and computational results available from the literature.

5.2 Interface Effect

Simulation results presented in Section 4.6 demonstrate that inclusions/cracks interactions can deflect the main crack-path. However, in those calculations, inclusion's interfacial strength when a crack interacts with an inclusion or a grain boundary was not considered. Generally, crack approaching an interface joining two dissimilar materials may arrest or advance by either deflecting into the interface or penetrating the interface.

Interfacial domains are critical parts of composite materials. Strength of materials are influenced by the orientation of existing cracks to the material interfaces and the strength of these interfaces. If an interface domain is weak enough, then a matrix crack can be arrested via deflection mechanisms. At the same time, the interface should also be strong enough so the matrix material can carry a significant part of the load. Consequently, tailoring and optimising interfacial strength with the aim to arrest and deflect cracks can enhance material strength.

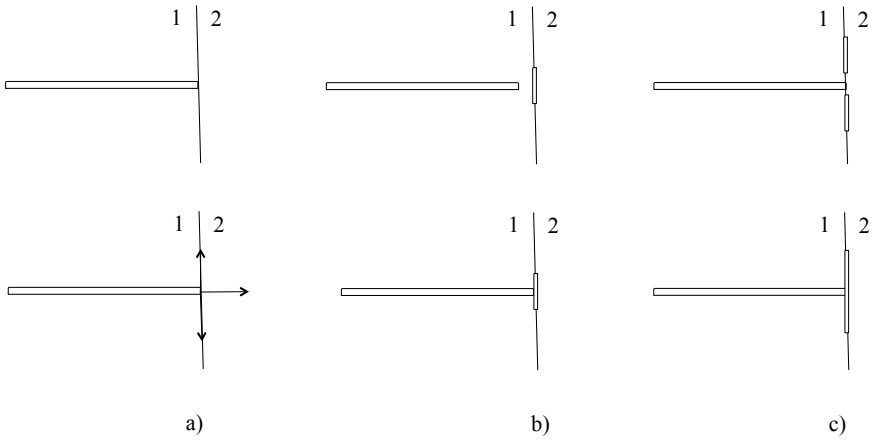


Fig. 5.2 Schematic diagram of crack propagation mechanisms at the interface: (a) He and Hutchinson approach, i.e. check the crack energy for both possible propagation paths [14, 15], (b) Cook and Gordon mechanism based on the stress distribution and crack coalescence [16, 17], and (c) Crack propagation mechanism based on the energy distribution at the crack tip and crack coalescence, adopted in this study.

5.2.1 Crack Propagation At The Interface

Various scenarios of crack propagation at the interface have been studied to look at the competition between the penetration and the deflection of the crack where the materials on either side of the interface are elastic and isotropic [14–17, 168, 209–212]. Different mechanisms are schematically shown in Figure 5.2. The first two mechanisms are the so called energy approach proposed by He and Hutchinson [14, 15], and the approach based on the stress distribution and crack coalescence proposed by Cook and Gordon [16, 17]. In the former approach, the energy release rate for the deflected crack is compared with the maximum energy release rate for the penetrating crack. The competition between deflection and penetration depends on the direction of the impinging crack with respect to the interface; the more oblique the crack, the more the deflection becomes favourable.

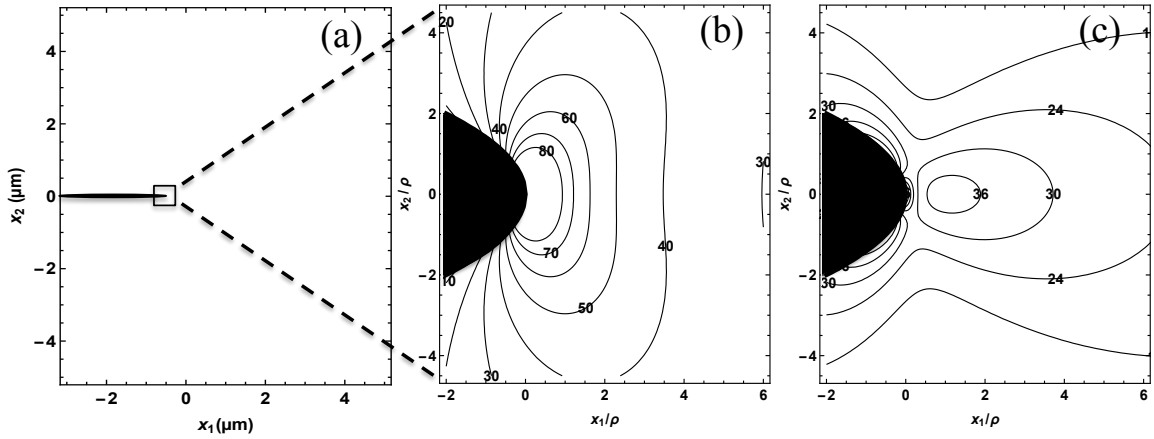


Fig. 5.3 (a) Schematic of the problem. Stress fields are calculated using the MM method in the vicinity of an elliptical hole (with the aspect ratio = 0.01), with uniaxial stress applied in the x_2- direction. Zoom-in of the crack-tip stress fields are shown; the distance along the crack axis is in ellipse curvature (ρ) unit. (b) Contours of $\sigma_{x_2x_2}$, (c) Contours of $\sigma_{x_1x_1}$.

The second mechanism, given by Cook and Gordon, is based on the stress distribution further ahead of the crack with finite tip radius. The influence of the crack-tip radius on the nature of stress fields and the question of how big the radius can be without invalidating the singular stress field at the crack-tip are addressed by Dini *etal*. [169–172]. Figure 5.3 shows stress contours for the equivalent elliptical hole modelled to simulate the finite radius crack subjected to uniform tension in the x_2 direction. Proceeding along the major axis of the crack away from the crack tip, the stress distributions are as shown in Figure 5.4. The $\sigma_{x_2x_2}$ is initially high and falls sharply (square root singular field [170]) while, from the crack boundary, $\sigma_{x_1x_1}$ increases from zero and at a distance roughly equal to the hole

curvature reaches the maximum value where $\sigma_{x_1x_1,max}/\sigma_{x_2x_2} \simeq 0.2$. Note that $\sigma_{x_1x_1}$ exhibits a mild stress concentration a little distance away from the hole; if the material has planes of weakness along the x_2 direction the stress $\sigma_{x_1x_1}$ could cause a crack to initiate in the x_2 direction just ahead of the main crack. This additional crack can either arrest or deflect the main crack depending on the energy of the main crack and the strength of the material. In this study the energy distribution (the third approach in Figure 5.2) at the crack tip is used to determine whether the crack can propagate and where the new micro-crack nucleates at the interface. This mechanism is explained in more details in the next section.

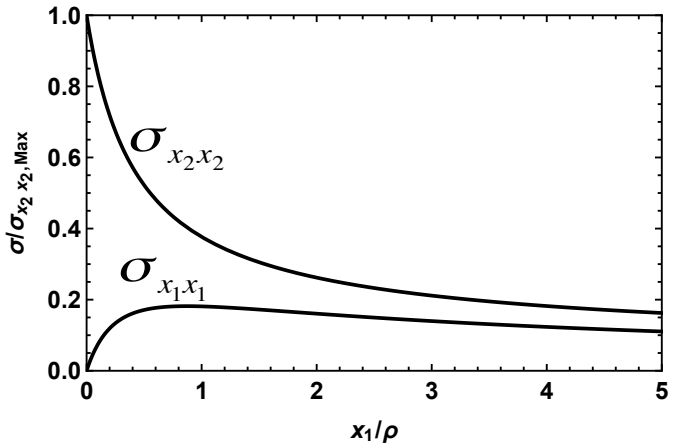


Fig. 5.4 Variation of the relative stress fields in the vicinity of the crack tip in x_1-direction; The distance along the crack axis is normalised using the crack tip ellipse curvature (ρ), and stress fields are calculated using the MM method.

5.2.2 New Deflection Mechanism

In homogeneous brittle material the crack propagates in a direction where Mode I condition is maintained at the crack tip. This criterion is not valid for a crack advancing into the interface region because the relative magnitude of the fracture energy between the materials joined at the interface and the interface itself are also involved. Fracture at the bi-material interface can be evaluated by the fracture energy, Γ, and the energy release rate G. The fracture energy is a property that characterises fracture resistance to the extension of a crack while the energy release rate G is the driving force for the extension of a crack. A crack can propagate if $G \geqslant \Gamma$, so, in a system where Γ varies from point to point, the crack propagates in the direction with lower fracture energy Γ and greater G/Γ. In this study, the crack propagation direction at the interface is determined by searching the point at the crack tip where the parameter (G/Γ) is

maximised. Deflection of the main crack results from the crack coalescence of the interfacial newly formed micro-crack with the main crack.

Interfacial effects are incorporated into the simulation codes developed based on the formulations reported in Chapters 3 and 4. The overall iterative process of predicting the crack propagation path using the DCD method is outlined in the flow chart displayed in Figure 7.5. At each iteration, interactions between all elements of the system are calculated and the failure criterion at the main crack tip is examined. The crack is propagating by introducing a new pseudo-crack in the system in the direction where G/Γ is maximised. Then the main crack is replaced by an equivalent one. Cracks with finite tip radius are again modelled as elliptical holes with nearly zero thickness. Before proceeding further, the effect of the crack thickness and curvature on the accuracy of calculations at the interface has to be investigated.

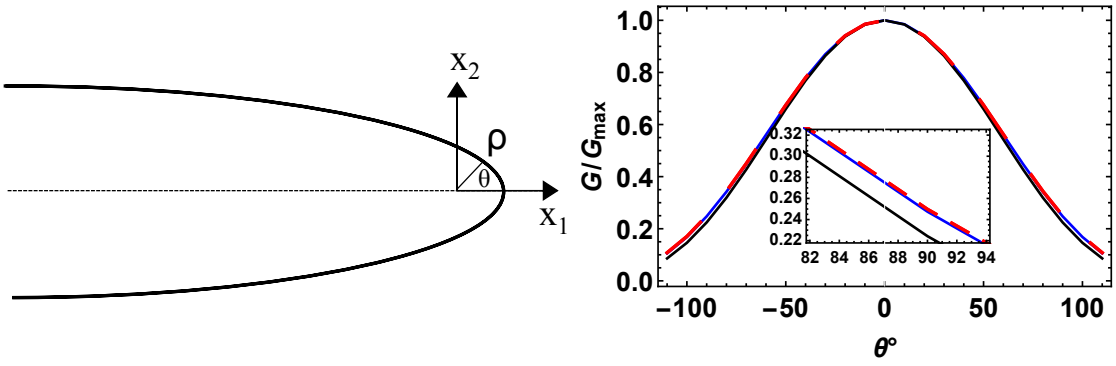


Fig. 5.5 The normalised energy at the crack tip as a function of the polar angle θ. Energy plots are depicted for 3 cracks with different aspect ratios 0.001 (blue), 0.01 (black), and 0.1 (red).

In the case of the collapsed elliptical hole, if the singular stress fields dominate the solution at the crack-tip, the crack propagation laws can be reasonably used to predict crack growth. Dini and Hills [171] showed that to approximate a blunt crack (with a finite curvature at the crack tip) to a crack, the applied load on the system should be in a permissible range with a minimum and a maximum load. The former is defined as the load below which the crack radius affects the stress fields, and the latter is the load associated with the concept of "small-scale yielding" in fracture mechanics and depends on the geometry of the problem [213]. Their calculations show for example that for a maximum of 5% to 6% discrepancy between two cases (crack and crack with blunt tip of finite curvature), the relative amount of crack curvature (ρ) and crack length ($2a$) should be around $\rho/2a \leqslant 0.00005$. For the case of

an elliptical hole, the value of ρ/a is equal to e^2, where e is the ellipse aspect ratio. Therefore, elliptical holes with small aspect ratio ($e \leqslant 0.01$) can be used to approximate cracks.

The full stress field distributions and energy at the tip of an elliptical crack with 5 μm length in an infinite plane are calculated using the multipole method. The crack is under uniform tension in the x_2 direction. Figure 5.5 presents the normalised energy at the crack tip for a range of polar angle θ. The energy is normalised by the maximum energy at the perimeter of the ellipse. The process of calculating the maximum energy is explained in Section 4.2.1.3. Different colours of the normalised energy plots express the influence of the crack's aspect ratio. The normalised energies were evaluated for three different aspect ratios ($e = 0.001,\ 0.01,\ 0.1$) and plotted with red, blue and black colours respectively. It is shown that this parameter has no significant effect on the results specifically for the cases with $e < 0.01$, but increasing the aspect ratio further can change the normalised energy distribution. Results of this calculation is compatible with the above discussion.

For the problem of elliptical cracks at the interface, one can use the fact that the interface of real materials has a physical thickness in the order of nanometer [214]. In the microscopic calculations, cracks can detect the interfacial effects only if their crack tip blunting have the same length scale. Using the information given above suggest that elliptical cracks with 0.01 aspect ratio can be used to study micro-cracks with nano-meter curvature.

5.3 Numerical Study of Problems at the Interface

A new method to determine crack propagation at the interface is introduced in the previous section using the fact that a crack tip in the interface domain experiences directional fracture energy. The direction corresponding to the angle at which the maximum G/Γ is reached determines the crack propagation direction. To develop a full fracture method for polycrystalline materials, a series of simulations were conducted to solve different problems of crack dealing with interfaces demonstrated in Figure 5.1. In this section, the effect of grain boundaries followed by influence of the interfacial strength of an elliptical inclusion on deflection of the evolving crack is investigated. Then, a combination of both cases where an inclusion is located at the grain boundary is studied. Finally, the method is employed to determine an optimal toughening configuration using an array of inclusions located at the GB.

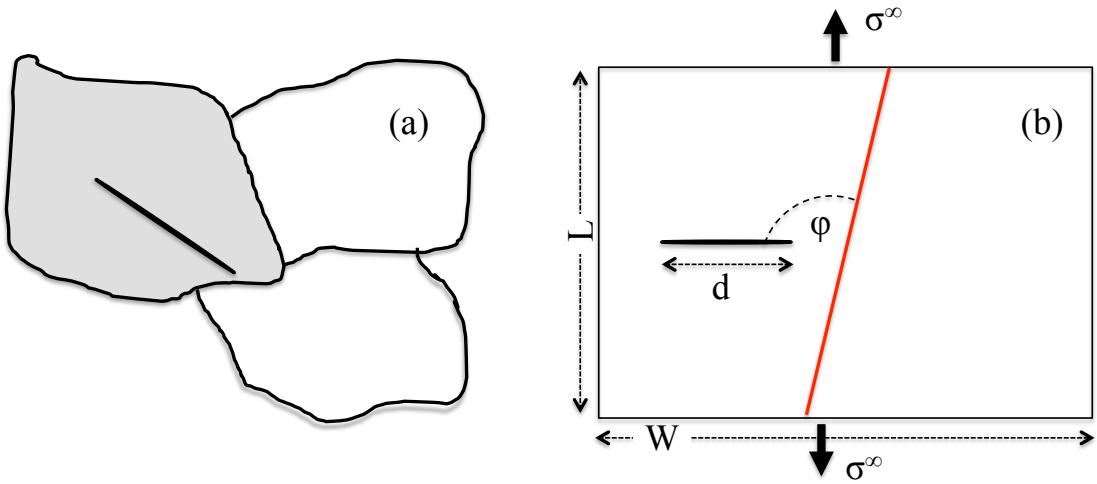


Fig. 5.6 Crack propagating toward a grain boundary. (a) Schematic of a general problem, (b) schematic of the simulated problem of a bi-crystal subjected to uniaxial remote vertical load and different GB orientations (φ). GB is shown in red and crack in black.

5.3.1 Crack Propagation And Grain Boundary

Much research has been conducted to study GB effects. It has been proved that grain boundaries orientation and strength can also modify the crack propagation path [215, 216]. Cracks are prone to propagate through grain boundaries with low fracture energies but bypass grains when the fracture energies of the associated GBs are high. Here, a parametric study is presented for a single crack propagating near a GB using the DCD method. Figure 5.6 shows the schematic of the problem where a crack propagates towards a) a GB in a polycrystalline structure and b) an interface of a bi-crystal (GB) subjected to uniaxial remote load (σ^{∞}). Commonly, the interface (here GB) fracture energy Γ_i defers from the matrix material fracture energy Γ_0. Crack deflection at a GB depends on the the fracture energy of the GB compared with the matrix material and on the mis-orientation between the GB and the impinging crack (φ). To exclusively study the effect of GB orientation on the crack propagation path, the relative energy of the interface with respect to the matrix material, Γ_i/Γ_0, is fixed in the simulations of this section.

Graphs in Figure 5.5 show that $G/G_{max} \simeq 0.24$ for a 90^0 polar angle. This means that the energy required for a 90^0 deflection of a straight crack under mode-I loading is four times as much as the energy needed for the crack propagates along its axis. This result is in good agreement with other numerical and analytical calculations given by Hutchinson *etal*.

and cook *etal*. [14–16, 168, 209]. Thus, in these simulations the ratio of fracture energies $\Gamma_{int}/\Gamma_0 \simeq 0.24$ was fixed to ensure that the 90^0 deflection at the interface can take place.

Simulations were conducted to establish the effect of a GB orientation. An initial configuration of the system is shown in Figure 5.6b, where grains were assumed to be made of homogeneous material ($\nu = 0.07$, $\mu = 570$ GPa and $\Gamma_0 = 10.18\ J/m^2$). The initial size of the crack (10 μm) was selected in such a way that the crack can propagate under the external uniform tension. The system width and length were $W = 35\ \mu m$ and $L = 20\ \mu m$ respectively. Crack propagation paths for different orientations of the GB are illustrated in Figure 5.7. Simulation results show that the propagating crack was arrested under the influence of the GB after kinking at the by-crystal interface for the cases in which the slope between the propagating crack direction and the interface were 90^0 to 70^0. The load was increased to force the crack to propagate further into the second grain, showing that the GBs produce an effective increase in fracture toughness under the specific conditions considered here. For the lower angle GBs, the crack deflects and propagates trough the grain boundaries; crack propagation across the GB was not observed. It should be noted that the crystallography disorientation at the GBs were neglected in all these simulations.

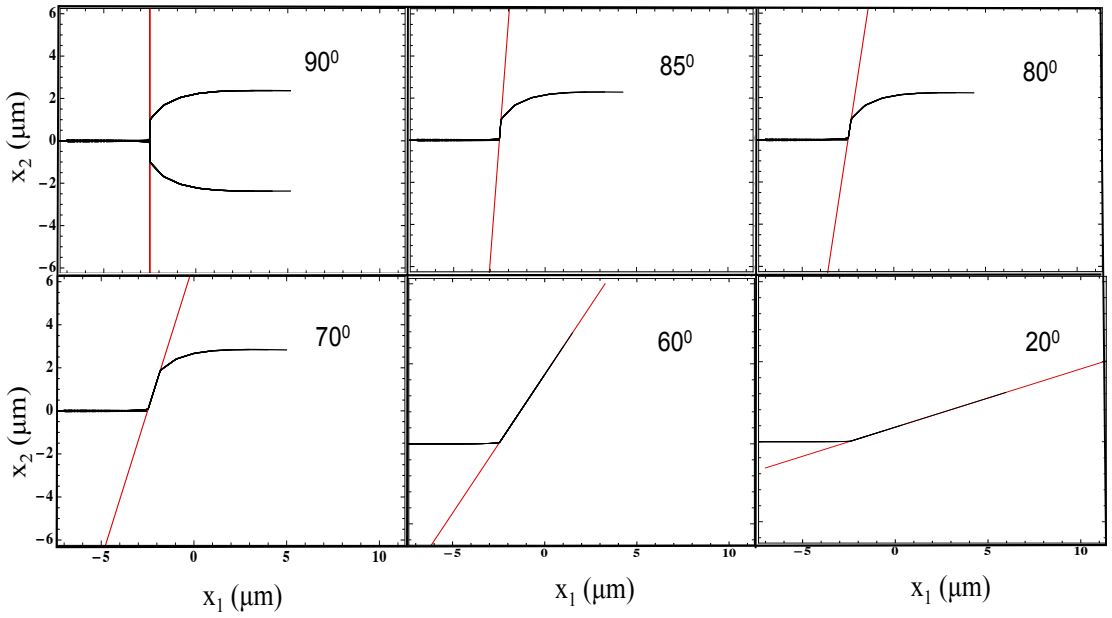


Fig. 5.7 Crack propagation paths at a grain boundary for a bi-crystal subjected to uniaxial remote vertical load and different GB orientations. GB shown in red and crack propagation path in black.

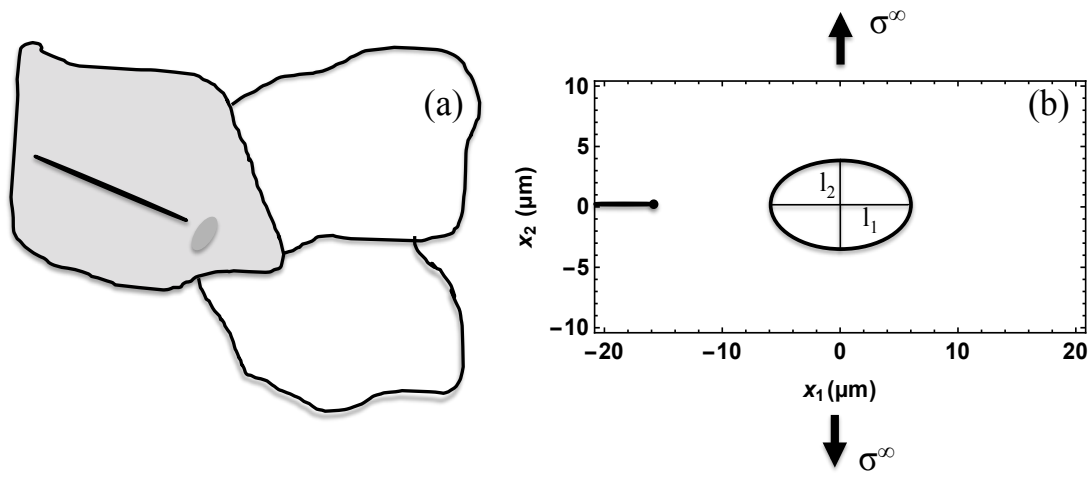


Fig. 5.8 Schematic diagram of a crack propagating towards an inclusion in (a) the polycrystalline structure and (b) in an abounded solid. The inclusion is assumed to be elliptical in shape and the lengths of the ellipse major and minor axes are denoted by l_1 and l_2, respectively.

5.3.2 Crack Propagation And Inclusions

Figure 5.8a shows a crack propagating toward an inclusion. In this scenario, the stress field distributions ahead of the crack interact with the inclusion's interface and consequently, such interactions must be considered carefully when estimating the crack propagation path. In this section, the effect of the interfacial strength of the inclusion on deflection of the crack propagation path, in the quasi-static regime, is studied.

Previously, a simple case where a crack approaches a line interface (e.g. a grain boundary) with different orientations was examined. The same method is used to simulate interfacial effects of a soft and hard (i.e. when the shear modulus of the inclusion is lower or higher than that of the matrix, respectively) inclusions when they interact with an advancing crack. The only difference between a GB and the interface of an inclusion in these simulations is that the inclusion is assumed to have a finite-sized interface rather than a sharp interface.

Figure 5.9 shows a zoom-in picture of a crack approaching an inclusion. To study the effect of the interface in the simulations, the area around any inclusion is divided into three regions. These areas which are numbered $1, 2$ and 3, and identify regions outside the inclusion, interface layer, and inside the inclusion with critical fracture energy Γ_0, Γ_{int}, and Γ_i respectively. The interface layer (region 2) is incorporated to represent a realistic scenario

and to avoid computational errors and costs due to the high singularity in the matrix of coefficients. The interface layer depth is an important parameter because once the crack tip reaches the interface it has to "decide" in which direction it will continue i.e., it will either penetrate through the inclusion or deflect and follow the path through the interface layer. Therefore, the crack-tip should be close to the inclusion to predict correct interactions with the inclusion, nevertheless it must be far enough away to avoid computational difficulties.

Selecting the interface layer depth correctly can minimise the uncertainty in predicting crack propagation path at an interface. From a pragmatic point of view, while the extent of the transition between materials may vary significantly depending on the particular matrix/inclusion combination, under consideration, the layer depth here is chosen, without loss of generality, to satisfy stability in the numerical procedure. In order to consider close interactions between the crack and the inclusion, the interface layer depth must be selected smaller than the crack increment at each simulation step. This fixes the maximum distance between the crack and the inclusion. Also, the interface layer depth has to be chosen according to the method that has been introduced in Chapter 4.3 to determine the distance between pseudo-cracks (δ) at each simulation step; δ was determined in such a way that calculated average stress fields and SIFs for neighbouring cracks and inclusions become reliable.

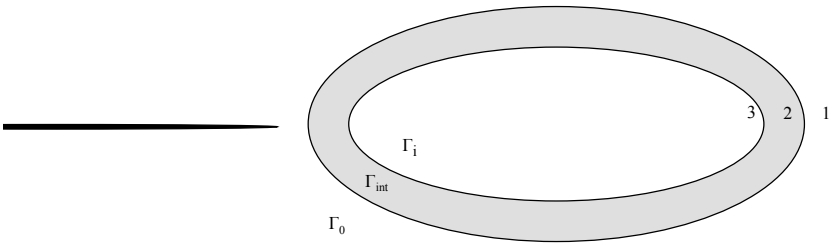


Fig. 5.9 Schematic representation of the interface problem when a crack propagates toward an inclusion.

The effect of surface interactions, and interfacial fracture energies were included in the computational code and tested to predict crack deflection close to soft and hard inclusions. Numerical simulations are carried out in the 2D Cartesian coordinate system. The computational system is depicted in Figure 5.8b, where the specimen containing the crack is subjected to a uniform uniaxial tensile loading in the x_2 direction. In this problem, deflection of the crack propagation trajectory is studied as a function of the rigidity ratio and fracture energy

ratio between a matrix and an inclusion for various interfacial energies of the inclusion. Both the matrix and the inclusion are assumed to be homogenous linear elastic materials.

Simulations were performed for various relative shear moduli ratios (μ_0/μ_{inc}), and fracture energies (Γ_0/Γ_i, Γ_{int}/Γ_0, and Γ_{int}/Γ_i); the Poisson's ratio was kept constant (ν_0/ν_{inc}=1/3). Indexes *0*, *i*, and *int* are used for matrix material, inclusion, and interface layer respectively. The initial crack with 5 μm length starts propagating from a certain distance (-12 μm) towards the inclusion with the $e = l_2/l_1 = 3/5$ aspect ratio. Le *etal*. [217] showed that crack deflection/penetration behaviour depends on a local curvature of an elliptical inclusion's interface near the crack-tip as well as an external load. Therefore, in each set of simulation the external load and the inclusion size are kept the same. Figures 5.10, to 5.13 illustrate that the crack propagation trajectory depends not only on the relative shear modulus of bulk and inclusion but also on the interfacial strength.

The case of a crack propagating toward the hard inclusion is shown in Figure 5.10. Although the interface layer is weak enough for the crack to be deflected along the interface, the propagation trajectory can still change depending on the interface fracture energy. Figures 5.11, 5.12, and 5.13 show cracks approaching different soft inclusions for different values of the interfacial strengths and fracture energy ratios. Numerical simulations show that for an interface with a higher strength, the crack penetrates the interface and propagates along its almost unperturbed crack growth direction. On the contrary, for a lower interfacial strength, the crack will deflect into and propagate along the interface.

Simulation results demonstrate that the DCD method can predict whether the crack penetrates into the inclusion or deflects at the interface. In the case of penetration, the method cannot explicitly predict the crack path inside the inclusions, because the simulation results become unreliable when the crack-tip approaches the branch points inside the inclusion. However, simple energetic considerations predict that the crack will propagate along the minimum energy path, which is the path from the point that the crack penetrates into the inclusion to the point where the crack is expected to exit. For example in Figure 5.13, assuming that all the inclusion's atoms have the same bonding energy, the minimum energy path should be the shortest path inside the inclusion as displayed in the figure.

Few researchers have paid attention to the experimental study of crack-inclusion interactions. The role of inclusion stiffness and interfacial strength on the crack propagation path was studied experimentally by Tippur *etal*. [18, 218]. It was shown that the crack growth behaviour is a function of the matrix-inclusion interfacial strength and the initial location of the crack relative to the inclusion. Experimental results of the crack propagation path are illustrated in Figure 5.14 and they are qualitatively in agreement with the predicted paths in Figures 5.10, to 5.13.

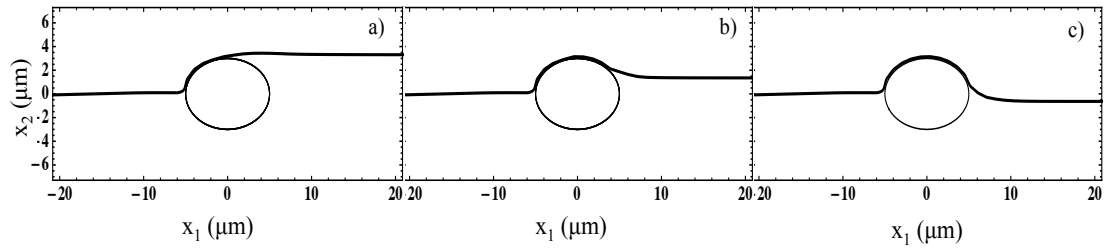


Fig. 5.10 Crack propagation trajectory computed for $\mu_i/\mu_0 = 10$, $\Gamma_i/\Gamma_0 = 10$ and values of a) $\Gamma_{int}/\Gamma_0 = 1$, b) $\Gamma_{int}/\Gamma_0 = 0.9$, and c) $\Gamma_{int}/\Gamma_0 = 0.5$

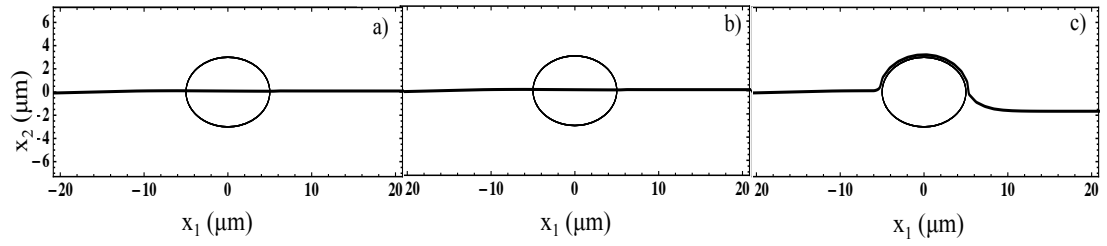


Fig. 5.11 Crack propagation trajectory computed for $\mu_i/\mu_0 = 0.5$, $\Gamma_i/\Gamma_0 = 0.5$ and values of a) $\Gamma_{int}/\Gamma_0 = 1$, b) $\Gamma_{int}/\Gamma_0 = 0.5$, and c) $\Gamma_{int}/\Gamma_0 = 0.2$

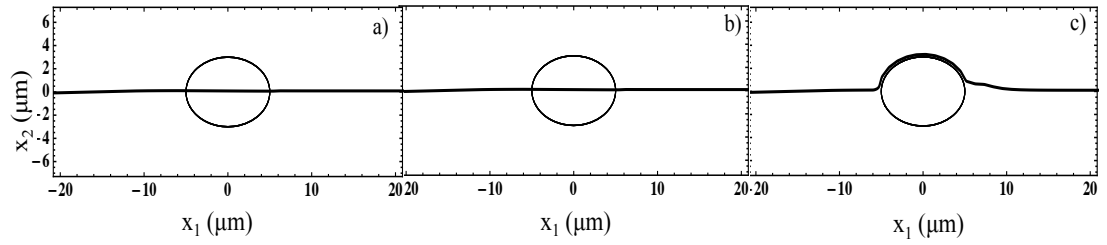


Fig. 5.12 Crack propagation trajectory computed for $\mu_i/\mu_0 = 0.2$, $\Gamma_i/\Gamma_0 = 0.4$ and values of a) $\Gamma_{int}/\Gamma_0 = 1$, b) $\Gamma_{int}/\Gamma_0 = 0.5$, and c) $\Gamma_{int}/\Gamma_0 = 0.2$

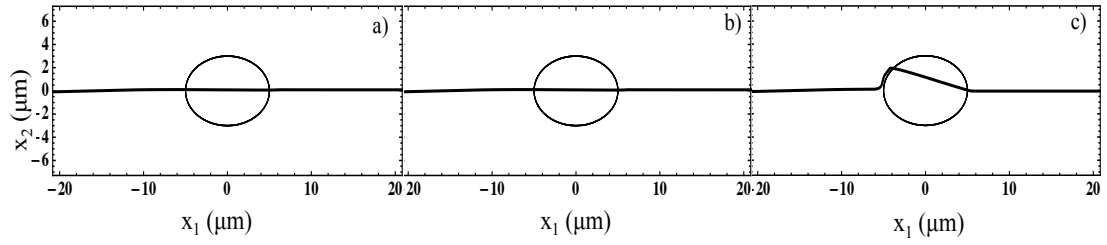


Fig. 5.13 Crack propagation trajectory computed for $\mu_i/\mu_0 = 0.1$, $\Gamma_i/\Gamma_0 = 0.2$ and values of a) $\Gamma_{int}/\Gamma_0 = 1$, b) $\Gamma_{int}/\Gamma_0 = 0.5$, and c) $\Gamma_{int}/\Gamma_0 = 0.2$

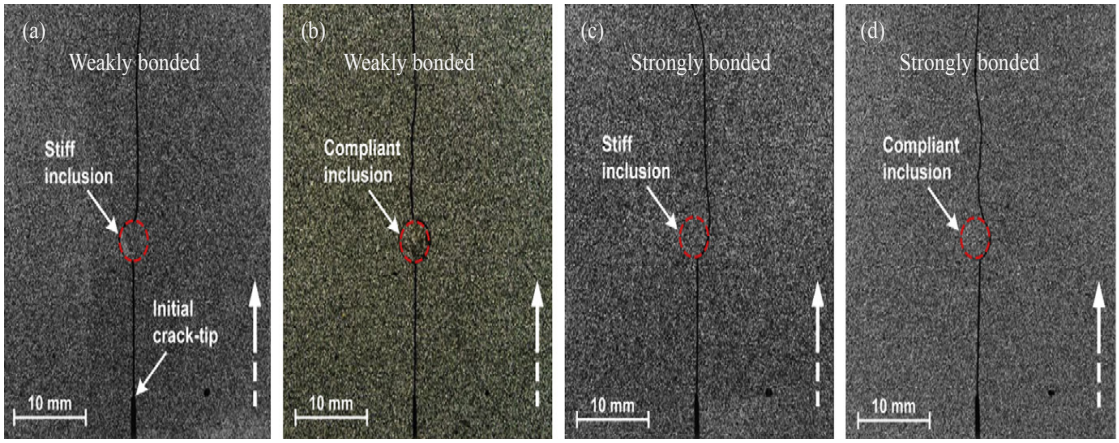


Fig. 5.14 Photographs of fractured specimen with hard (stiff) and soft (compliant) inclusion showing different crack–inclusion interaction scenarios: (a) Weakly bonded hard inclusion. (b) Weakly bonded soft inclusion. (c) Strongly bonded hard inclusion. (d) Strongly bonded soft inclusion. The black dot adjacent to initial crack-tip denotes the reference mark and the broken arrow indicates crack propagation direction [18].

Experimental results in Figure 5.14 cannot be quantitatively compared with results given by the DCD method because the former are obtained using a dynamic crack growth experiment while the simulations are performed in the quasi-static regime. This could be circumvented by deriving elastodynamic solutions for the problem; however, this is outside the scope of this thesis. An elastodynamic BEM solver for the computation of stresses and displacements in the finite domain is already available in [10], so maybe this is not an insurmountable task and it can be a topic of the future work.

5.3.3 Crack Propagation, Inclusion And Grain Boundary

Interfacial effects of GBs and inclusions on the crack propagation trajectory are studied separately in the previous sections. Figure 5.15a shows that a grain boundary may enter and pass through several inclusions. In this section, interaction of a crack with an inclusion at a grain boundary is investigated; interactions between GBs and inclusions and crystallography disorientation at GBs are neglected.

The geometry of microstructures in polycrystalline materials is linked to the interfacial energies of the constituents [219]. In general, studying the effect of microstructures on the GBs consists of several parameters such as inclusion strength (Γ_i), inclusion interfacial strength (Γ_{int}), GB strength (Γ_{GB}) and the matrix material strength (Γ_0). The energy required to fracture a brittle material along a GB plane without plastic deformation can be determined

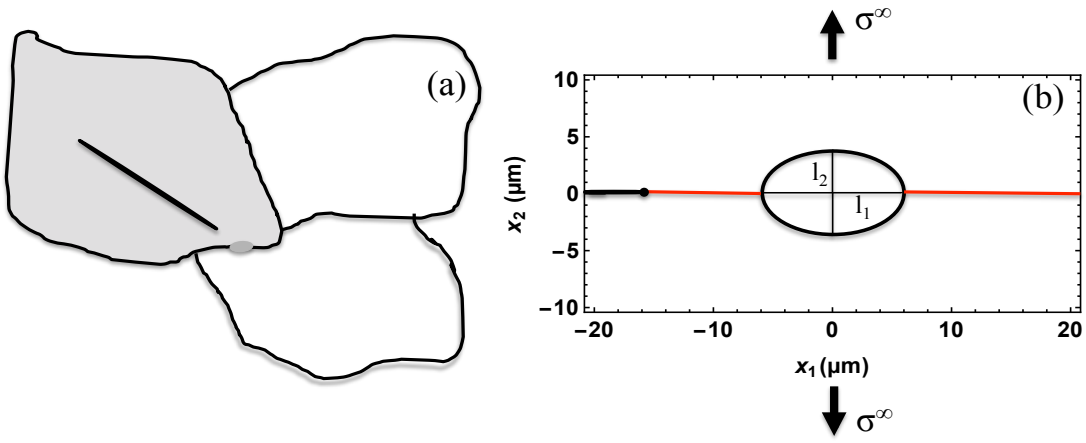


Fig. 5.15 Schematic diagram of a crack propagating towards an inclusion at the GB in (a) the polycrystalline structure and (b) in an unbounded solid. The inclusion is assumed to be elliptical in shape and the lengths of the ellipse major and minor axes are denoted by l_1 and l_2, respectively.

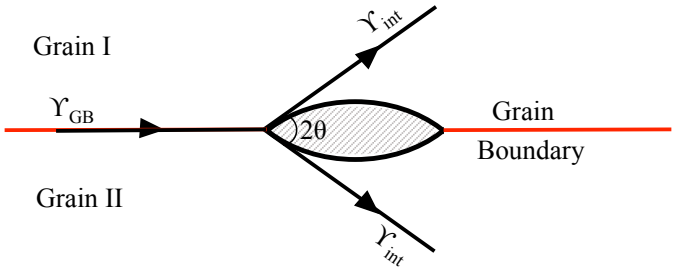


Fig. 5.16 Schematic diagram of an inclusion (shaded area) on a grain boundary (red line). A distribution of the interfacial energies at the point along the grain boundaries which intersects the inclusion interface is shown by γ_{int} and γ_{GB}.

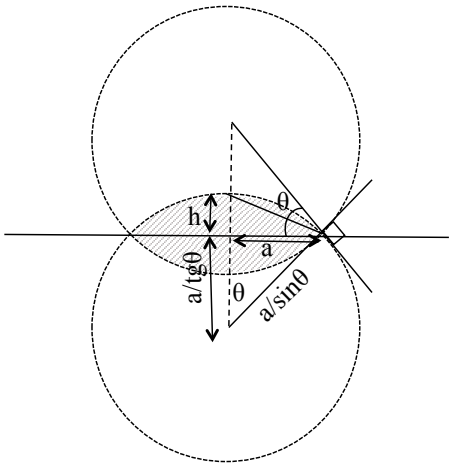


Fig. 5.17 Schematic diagram showing the relationship between interface angle and aspect ratio for a lenticular inclusion.

by

$$\Gamma_{GB} = \gamma_1 + \gamma_2 - \gamma_{GB}, \tag{5.1}$$

correspondingly, the inclusion interfacial strength is defined trough the relation:

$$\Gamma_{int} = \gamma_1 + \gamma_2 - \gamma_{int} \tag{5.2}$$

where γ_1, and γ_2 are energies of the two free surfaces created due to the GB or the inclusion interface cleavage. Also, γ_{GB} and γ_{int} are energies of the GB and the interface respectively.

Figure 5.16 shows an inclusion on a GB and a distribution of interfacial energies. Under the assumption of the local equilibrium, a simple vector balance of the interfacial energies at the point along the GB where it meets the inclusion interface can determine the relative energies of the GB and the inclusion interface. So that

$$\gamma_{GB} = 2\gamma_{int}\cos\theta, \tag{5.3}$$

where θ is the angle formed at the intersection between the tangents to the inclusion interface at the meeting point with the grain boundary. This formula requires that the γ_{int} should be always $\gamma_{int} \geqslant \gamma_{GB}/2$. A simple method, called $\theta/2$ method [220], is used to estimate the angle θ. Assuming that an elliptical inclusion could be approximated to a lenticular inclusion truncated between two circles demonstrated in Figure 5.17, the angle θ can be calculated as:

$$\tan\theta/2 = h/a, \tag{5.4}$$

where h/a is approximated to be the ellipse aspect ratio. Equations 5.3 and 5.4 show that the size of an inclusion located on a GB can be controlled by the relative energy of the GB to the inclusion's interface. Thus, knowing the interfacial energies provides enough information to predict microstructures on the GB and vice versa.

5.3.3.1 Simulation Results

Simulations in this section were conducted to investigate the effect of interfacial strength in a problem of an inclusion located on a GB on crack propagation trajectory and normalised energy possessed by the crack as it moves along the GB towards the inclusion. An initial configuration of the problem is illustrated in Figure 5.15b, where the inclusion is placed in the centre and on the GB with ($x_2 = 0$) equation; deformation of material was not considered in the system. The matrix is subjected to a uniform stress in the x_2 direction. The initial crack length is selected as 10 μm where its crack tip is placed at $(-20, 0)$ μm. The crack is allowed to propagate towards the inclusion and deflect accordingly.

Simulations were performed on sets of hard inclusions, soft inclusions and voids with different sizes and aspect ratios. In the case of hard inclusions, aspect ratios were selected as: $e = l_2/l_1 = 2.5/5 = 0.5$, and $e = l_2/l_1 = 4/5 = 0.8$, while for the soft inclusions and voids they were chosen as: $e = l_2/l_1 = 2.5/5 = 0.5$, and $e = l_2/l_1 = 1/5 = 0.2$. Using formulas 5.3 and 5.4, the relative energy of the GB to the interface was derived by the $\gamma_{GB}/\gamma_{int} = 2.(1-e^2)/(1+e^2)$ formula. SIFs (K) and energies (G) at the crack tip were calculated while the crack was propagating along the GB. Figures 5.18, 5.19, and 5.20 show variation of the normalised energy (G/G_0) and Mode I SIF (K_I/K_{I0}) of the crack; G_0 and K_{I0} are the energy and the SIF of the propagating crack in the similar system but without the inclusion.

When $G < G_0$, it means that the energy release rate associated with a propagating crack in a system containing inclusions is less and the crack can propagate more easily compared with a system without inclusions. Reduction of the energy release rate leads to the increase of the critical remote stress required for the crack to propagate and, hence, apparent enhancement in the fracture toughness of the material. Inversely, increasing the crack energy ($G > G_0$) results in the reduction of the material's toughness.

Figure 5.18 clearly presents both relative energy and SIF values are decreasing as the crack is approaching the hard inclusion (i.e. crack-tip shielding occurs). The crack energy/SIF increases and then decreases as the crack deflects and propagates along the interface of the inclusion. It should be noted that the particular variation of the energy and SIFs depends on the crack incremental size and angle. The fact that added micro-cracks along the inclusions are not symmetric provides an understanding that why the energy and SIF profiles are not

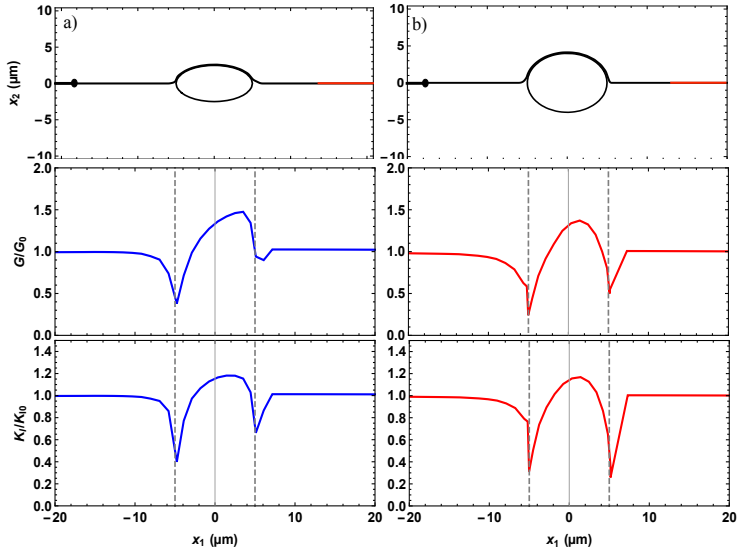


Fig. 5.18 Crack propagation path and evolution of the crack energy and the Mode-I SIF on a GB containing an elliptical hard inclusion are predicted for each set of simulations. Material properties are selected as: $\mu_i/\mu_0 = 10$, $\Gamma_i/\Gamma_0 = 1.1$, $\Gamma_i/\Gamma_{int} = 4$. a) Inclusion size is $e = l_2/l_1 = 0.5$, and, $\Gamma_{GB}/\Gamma_{int} = 0.25$, b) Inclusion size is $e = l_2/l_1 = 0.8$, and $\Gamma_{GB}/\Gamma_{int} = 2.4$. The red line on the schematic of the system shows the GB line.

symmetric and may modify in size for different problems. Also, by considering the size of inclusions, energy variation of cracks and GB energies in Figure 5.18, one can conclude that employing hard inclusions with larger aspect ratio is more appropriate in toughening mechanism. Calculated crack energies and SIFs of the propagating crack in the present model agree with other numerical results using the boundary element method of Bush [100], the symmetric-Galerkin boundary element method (SGBEM) of Kitey [103], and the FEM of Boselli [221] and Ayyar [222].

In the case of a soft inclusion and a void displayed in Figures 5.19 and 5.20, the crack energy increases (amplification) noticeably as the crack approaches the inclusion or the void. In this calculation due to the singularity of the fields at branch points, energy profiles inside the inclusion was not simulated. However, Li *etal*. [223] calculated both numerically and experimentally that the crack energy decreases as crack propagates trough the soft inclusion. As soon as the crack exit the inclusion, the energy increases again and quickly reaches the value of the free crack.

A dramatic variation in the energy and SIF profile at the interface, either shielding or amplification (anti-shielding), is associated with the stress load transfer due to the material mismatch [224] and the deflection of the crack path from Mode *I* to mixed mode propagation ($K_{II}/K_I \neq 0$). It is clear that the hard elastic material ahead of the crack tip carries stresses

higher than those found at a similar distance ahead of a corresponding crack with a softer material. Load transfer to the hard inclusion brings about a stress reduction in the immediate vicinity of the crack; the amount of stress reduction depends on the inclusion stiffness. For a hard inclusion, crack-tip shielding is induced by the load transfer into the hard material. Conversely, in the case of a soft inclusion positioned ahead of the crack tip, the load is transferred from the inclusion itself to the matrix material and this causes an increase of the stress in the crack tip region. Therefore, stress field amplification in front of the crack tip is expected to be seen in the case of soft inclusion. Crack amplification also depends on the relative shear moduli of the soft inclusion and the matrix material; the softer the inclusion, the higher the amplification is. It is manifestly evident that the maximum amplification has to be obtained where a crack approaches voids; the same result achieved in simulations and demonstrated in Figures 5.20, and 5.19. Hence, cracks are more prone to propagate towards voids rather than to soft inclusions of the same size.

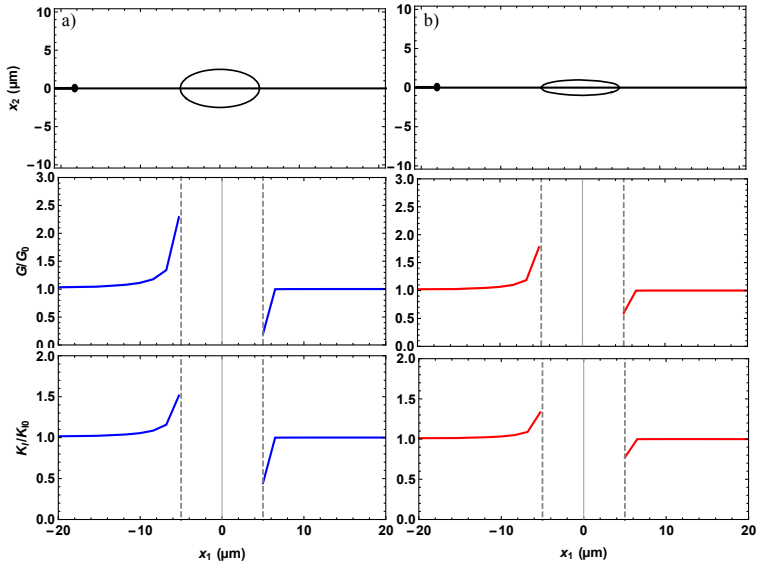


Fig. 5.19 Crack propagation path and evolution of the crack energy and the Mode-I SIF on a GB containing an elliptical soft inclusion are predicted for each set of simulations. Material properties are selected as: $\mu_i/\mu_0 = 0.10$, $\Gamma_i/\Gamma_0 = 0.5$, $\Gamma_0/\Gamma_{int} = 4$. a) Inclusion size is $e = l_2/l_1 = 0.5$, and $\Gamma_{GB}/\Gamma_{int} = 1.60$, b) Inclusion size is $e = l_2/l_1 = 0.2$, and $\Gamma_{GB}/\Gamma_{int} = 0.30$.

Crack deflection and variation of the normalised crack energy and SIF illustrated in the simulations are associated with the crack-inclusion interactions. Interactions between a crack and an inclusion depend on the size and aspect ratio of the inclusion, the relative shear moduli of the inclusion to the matrix material, and the interfacial energies. Figures 5.18, 5.19, and 5.20 show that inclusion with larger size or aspect ratio, and inclusion with

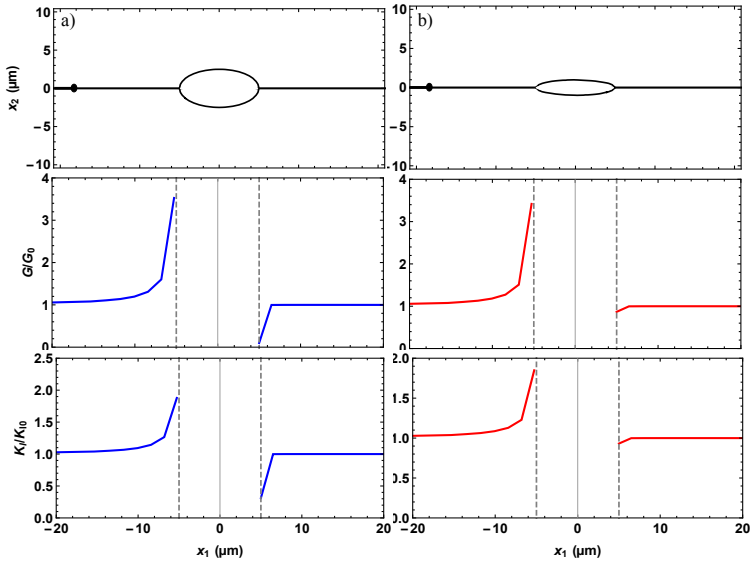


Fig. 5.20 Crack propagation path and evolution of the crack energy and the Mode-I SIF on a GB containing an elliptical hole were predicted for each set of simulations. Material properties are selected as: $\mu_i/\mu_0 = 0.0$, $\Gamma_i/\Gamma_0 = 0.0$, $\Gamma_0/\Gamma_{int} = 1$. a) hole size is $e = l_2/l_1 = 0.5$, and $\Gamma_{GB}/\Gamma_0 = 1.20$, b) hole size is $e = l_2/l_1 = 0.2$, and $\Gamma_{GB}/\Gamma_0 = 1.85$.

a greater difference in the relative shear moduli can deflect crack to the higher degree and hence, offer more significant shielding or amplification. Nevertheless, increasing the size of inclusions is equivalent to provide weak spots, where stresses are concentrated, to make it far easier to fracture. Thus, toughening polycrystalline materials using inclusions on the GBs requires an optimisation of the trade-off between the energy of the GBs and inclusions size and aspect ratio.

5.4 Toughening Mechanism

Engineered materials such as polycrystalline or multi-phase solids are usually limited by their resistance to fracture or fracture toughness rather than their strength. Considerable efforts have been expended to enhance toughness of brittle materials. Micromechanics of toughening in brittle material includes various mechanisms; of particular interest here is a toughening mechanism using inclusions (which in two-dimensional problems can be seen as fibres) reinforcements on the GBs. In general, toughening mechanisms at GBs are associated with directing cracks into the predetermined propagation tortuous path. Direction of the crack extension can be controlled by engineering the GBs in a way that leads to the crack deflecting into the non-maximum energy release rate direction. Reduction of the energy release rate

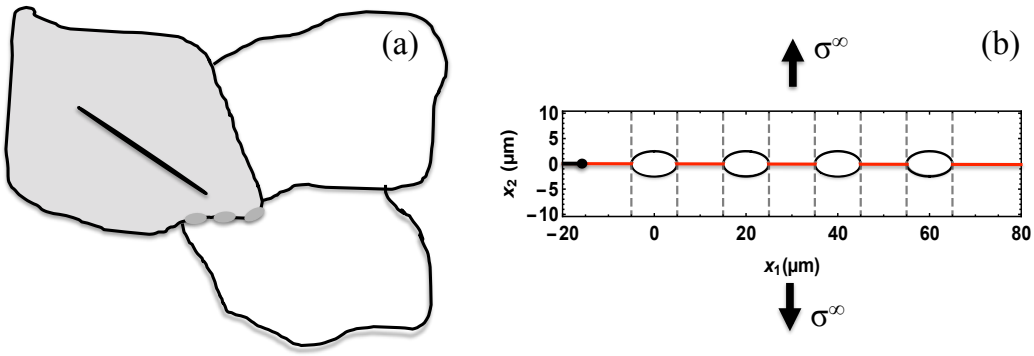


Fig. 5.21 Schematic diagram of a crack propagating towards an array of inclusions on the GB in (a) the polycrystalline structure and (b) in an unbounded solid simulated here as a simplified scenario. Inclusions are assumed to be elliptical in shape and equispaced on a GB.

leads to the increase of the critical remote stress required for the crack to propagate and hence apparent enhancement in the fracture toughness of the material. Effects of an array of soft and hard inclusions (i.e. when the shear modulus of the inclusion is lower or higher than that of the matrix, respectively), on a grain boundary on a crack propagation path, energy and SIF are studied in Sections 5.4.1 and 5.4.2 respectively. It should be noted that here only soft brittle inclusions are studied and the mechanical properties are selected in such a way that the crack can penetrate into the soft inclusions. Temperature effects on chemical and mechanical properties of the material are not considered here.

5.4.1 Array of Soft Inclusions on a Grain Boundary

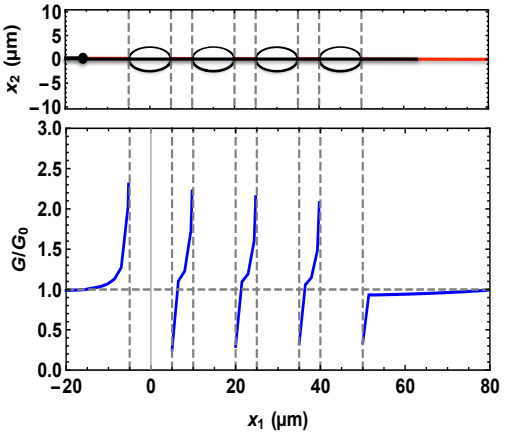
Soft inclusions can improve the fracture toughness of materials by i) storing energy in the inclusion before rupture (this mechanism is in general more important for ductile materials) and, ii) crack deflection mechanisms (of main relevance for brittle materials). Here, the author focused on determining the toughening mechanism induced by crack deflection. The aim is to show that soft inclusions and voids can be used to deflect a crack and cause it to propagate on a predetermined path. Cracks can propagate more easily along a GB containing soft inclusions compared with a pure GB in the absence of impurities. Thus, cracks can deflect and propagate through a tortuous path and release their energy accordingly. Though deflecting a crack path through a predetermined path increases the toughness, the material and GBs should be strong enough to sustain the load and avoid catastrophic failure. So, there is a trade off between increasing toughness and decreasing individual grain and GB strengths and the optimal solution must be always determined. Effects of inclusions on a GB were studied by modelling a system containing an array of equispaced inclusions along the GB.

Figure 5.21b shows an initial configuration of a system schematically. The system is under uniform tension in x_2 direction, and an initial crack of length 10 μm is introduced along the grain boundary; the original crack tip is positioned at $(x_1, x_2) = (-20, 0)$ μm. Preliminarily, the GB and other interfacial energies are fixed; these energies can be obtained from molecular dynamics simulations or experimental results. By pre-selecting the GB and interface energies, and consequently the size of inclusions, the optimal distance between inclusions can be attained.

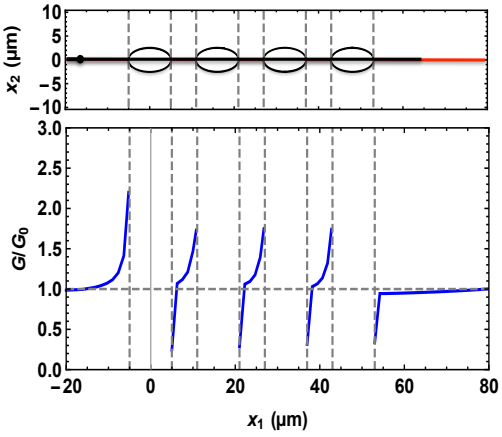
Simulations were performed for soft inclusions (with aspect ratio $e = l_2/l_1 = 2.5/5 = 0.5$) and a matrix material with relative mechanical properties $\mu_i/\mu_0 = 0.1$, and $\nu_i/\nu_0 = 3$, $\Gamma_i/\Gamma_0 = 0.5$, $\Gamma_0/\Gamma_{int} = 4$, and $\Gamma_{GB}/\Gamma_{int} = 1.6$. Figures 5.22a to 5.22d show the influence of the spacing between inclusions on the energy of the evolving crack. In the cases where the distance between two sequential inclusions is less than the major axis of the inclusions (Figures 5.22a, and 5.22b), crack energy amplifications between inclusions are observed. In other words, the crack propagates between inclusions at a higher energy level compared with the system without inclusions. Simulation results predict that increasing spacing between the inclusions can reduce the crack energy and consequently enhance the toughness of the GB (Figures 5.22c). Figure 5.22d shows that interactions between inclusions with spacing more than 1.5 times of the inclusion size ($3l_1$) are negligible. Thus, this structure might not be capable of channeling the crack into a predefined path. Regardless of the GB energy, simulation of this section can be used to study toughening mechanism in the matrix material using a distribution of soft inclusions.

Similar sets of simulations were run for another system, where instead of soft inclusions, elliptical holes of the same size and distance were located on the GB. Maximum energies of the propagating crack in the vicinity of the holes in Figures 5.23a - 5.23d predict that a crack requires less external load to propagate along the array of voids than along the array of soft inclusions. The difference in the average quantities of the maximum energies and maximum SIFs for the crack right at the edge of the elliptical holes and soft inclusions are more than 35% and 20% respectively.

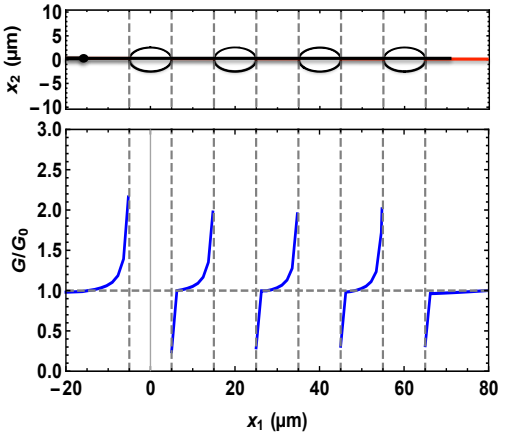
The average quantities of the crack energy and Mode I SIF are calculated and summarised in Table 5.1. Results show that the average energy and SIF at the crack-tip for the case of voids located on the GB are always higher than the same system containing soft inclusions by more than 10%, and 6% respectively. Calculation of the average quantities is consistent with the earlier prediction that the toughness of the GB containing voids is less than the same GB containing soft inclusions. It should be noted that in the current calculations, toughening due to energy dissipation in the soft inclusions is not considered. Including this energy dissipation in calculations strengthen the previous argument that a system containing soft



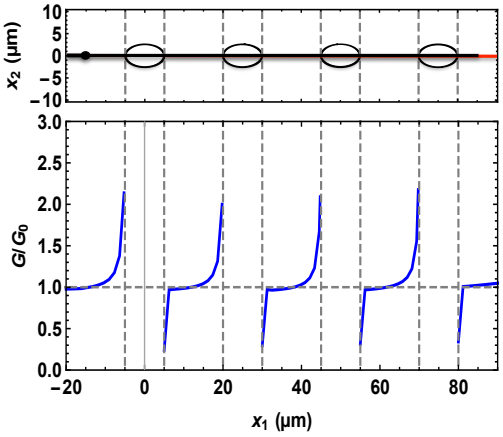
(a) Distance between two sequential inclusions is equal to l_1.



(b) Distance between two sequential inclusions is equal to 1.2 l_1.

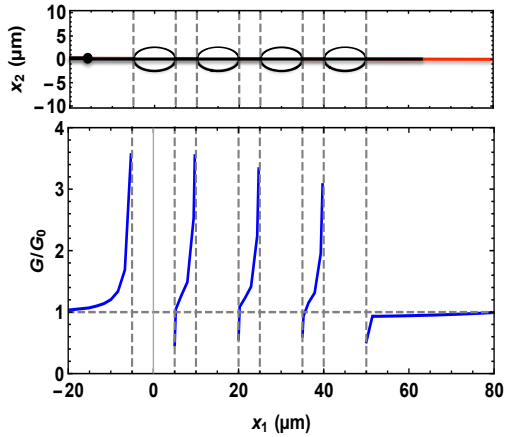


(c) Distance between two sequential inclusions is equal to 2 l_1.

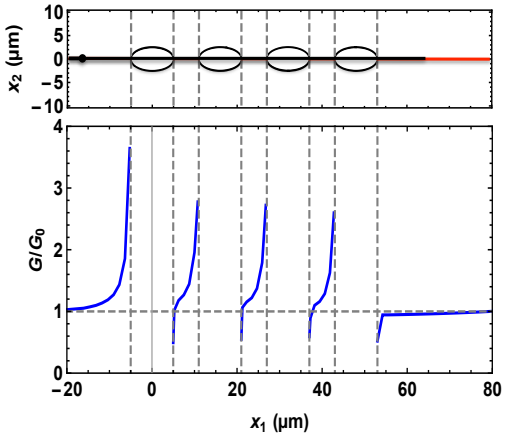


(d) Distance between two sequential inclusions is equal to 3 l_1.

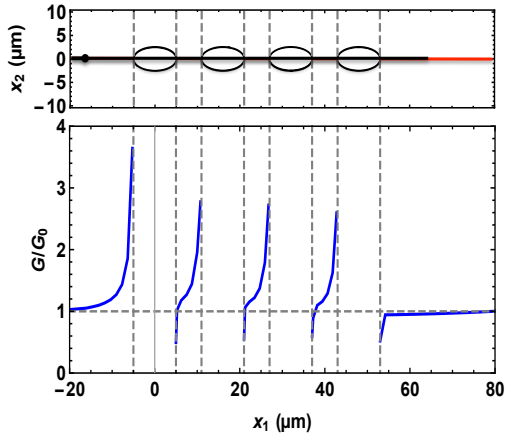
Fig. 5.22 Energy evolution of the crack while it is propagating along the GB containing 4 equispaced soft inclusions with different spacing.



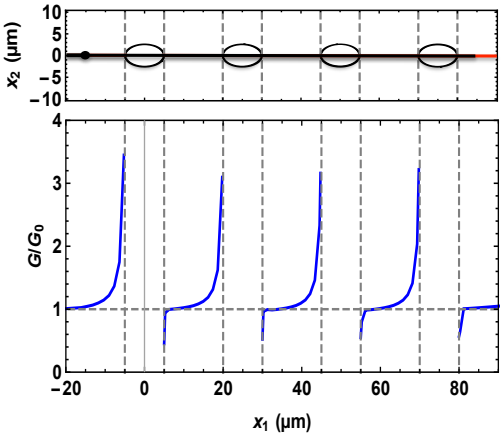
(a) Distance between two sequential holes is equal to l_1.



(b) Distance between two sequential holes is equal to 1.2 l_1.



(c) Distance between two sequential holes is equal to 2 l_1.



(d) Distance between two sequential holes is equal to 3 l_1.

Fig. 5.23 Energy evolution of the crack while it is propagating along the GB containing 4 equispaced elliptical voids with different spacing.

Table 5.1 The average normalised energy and Mode I SIF at the crack-tip are calculated for different toughening mechanisms where soft inclusions, voids, and hard inclusions were located on the GB. The percentage difference of the results for the soft inclusions and voids are calculated. In the last two columns present the normalised quantities for a GB containing hard inclusions.

	Soft Inclusions		Voids		Difference (%)		Hard Inclusions	
Space/$2l_1$	G/G_0	K_I/K_{I0}	G/G_0	K_I/K_{I0}	$\Delta G/G_0$	$\Delta K_I/K_{I0}$	G/G_0	K_I/K_{I0}
0.5	1.16	1.03	1.28	1.10	10.47	6.60	0.88	0.89
0.6	1.08	1.03	1.25	1.09	15.68	6.52	0.89	0.89
1.0	1.13	1.05	1.31	1.12	16.11	6.62	0.89	0.89
1.5	1.12	1.04	1.29	1.11	15.05	6.14	0.89	0.89

inclusions is tougher than the same system containing voids. Results of this section can be extended to a more general case where a matrix material contains several arrays of voids and soft inclusions. Material containing soft inclusions is tougher than the one containing voids. Moreover, the results presented in Table 5.1 show that the average quantities have a minimum value for the situation in which the spacing between to sequential inclusions is $Space/2l_1 = 0.6$; this is the toughest GB structure among all other calculations. It means that there is an optimal distance between either soft inclusions or voids that can maximise the effect of GB toughening mechanism.

5.4.2 Array of Hard Inclusions on a Grain Boundary

Hard inclusions can also be added to a matrix material to increase its toughness. Possible toughening mechanisms attributed to the presence of hard inclusions are micro-cracking, crack deflection, and crack branching. Here, the study is focused on crack deflection mechanism. In toughening mechanism using hard inclusions on a GB, the matrix material transfers part of stresses to the inclusions and modifies stress field distributions at the crack-tip. Thus, the crack is forced to deflect at the crack tip. Crack-deflection plays a pivotal role in the toughening mechanism because it reduces the energy release rate at the crack-tip and consequently, elevates the tolerance of the structure to the external load.

Simulations are performed on a system showed in Figure 5.21b. Inclusions with aspect ratio $e = l_2/l_1 = 4/5 = 0.8$, and matrix material and inclusions with relative mechanical properties such as $\mu_i/\mu_0 = 10$, and $\nu_i/\nu_0 = 1/3, \Gamma_i/\Gamma_0 = 2, \Gamma_i/\Gamma_{int} = 4$, and $\Gamma_{GB}/\Gamma_{int} = 1.12$ are selected to study the toughness enhancement associated with several distributions of the hard inclusions. Figures 5.24a to 5.24d show the crack energy shielding for various GB structures where the shielding effect and the distance between two successive inclusions are inversely related. Evidently, the GB toughness is increased by the presence of inclusions,

and crack propagates along the structure with almost lower energy compared with the system without inclusions. Furthermore, sudden declines in the crack energy at the vicinity of the hard inclusions show that how a propagating crack can be arrested by hard inclusions.

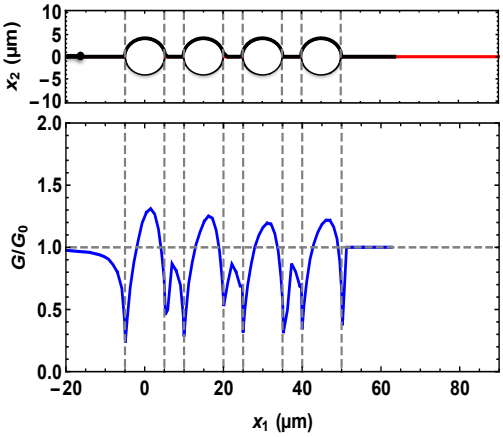
For a more precise quantitative interpretation of the simulation results, average relative energies, and Mode I SIFs are calculated and summarised in Table 5.1. Calculations show that increasing the distance between the inclusions does not change the average quantities of the structures illustrated in Figure 5.24a by more than 1% compared with the one in Figure 5.24d. In reality, if hard inclusions are situated very close together, the average density of the material will be increased, and the hard inclusion agglomeration is expected to occur. Therefore, increasing the spacing between hard inclusions to the point where the interaction between inclusions becomes negligible, should provide a better toughening mechanism. Results of this calculation can be extended to the more generalised toughening mechanism where inclusions are distributed evenly in the matrix material; regardless of the aspect ratio limitation that is caused by the $\gamma_{GB}/\gamma_{int} = 2.(1-e^2)/(1+e^2)$ formula for GBs.

5.4.3 Array Of Inclusions On A Grain Boundary; General Case

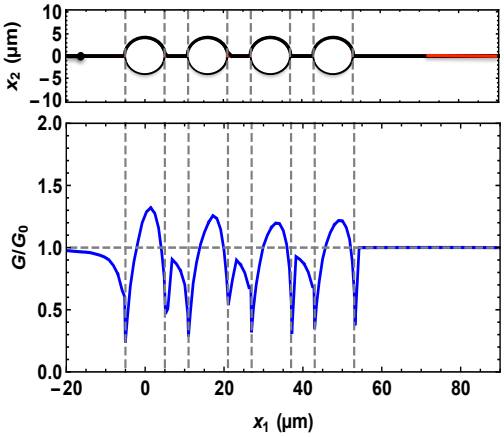
In many polycrystalline materials, macroscopic cracks advance along the grain boundaries, where the strength of the GBs is less than the low cleavage energy of the crystal. Figure 5.25 shows that inclusions accommodated along the GBs can effectively modify the crack propagation path. Crack propagation depends on various factors such as energy and orientation of GBs, interfacial energies, fracture energies, and size and position of inclusions. Also, these factors are interconnected; for example, strength and energy of the GB and the inclusion's interface can be modified by adjusting the size and spacing of the inclusions [60]. Therefore, it appears that the parametric study of the system, even for a simple problem of inclusions on a GB, is impossible because many parameters are involved. Nevertheless, the method is ready to be applied to any specific problems with known parameters.

5.5 Grain Boundary Engineering of Polycrystalline Diamond

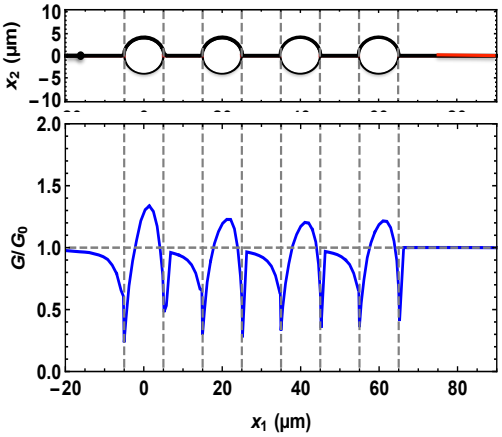
In polycrystalline materials, grain morphology, elastic modulus, and toughness of the individual microstructures and interfaces are the key parameters to study failure mechanisms. Engineering GBs is a concept that can be used in real materials to improve their fracture resistance. Any numerical fracture model, that can simulate crack propagation in materials containing microstructures, has the potential to describe toughening mechanisms in poly-



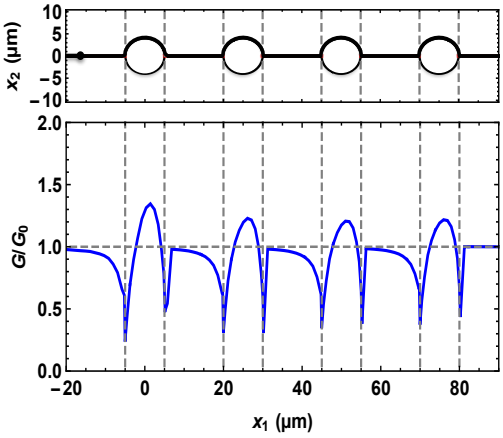
(a) Distance between two sequential hard inclusions is equal to l_1.



(b) Distance between two sequential hard inclusions is equal to 1.2 l_1.



(c) Distance between two sequential hard inclusions is equal to 2 l_1.



(d) Distance between two sequential hard inclusions is equal to 3 l_1.

Fig. 5.24 Energy evolution of the crack while it is propagating along the GB containing 4 equispaced elliptical hard inclusions with different spacing.

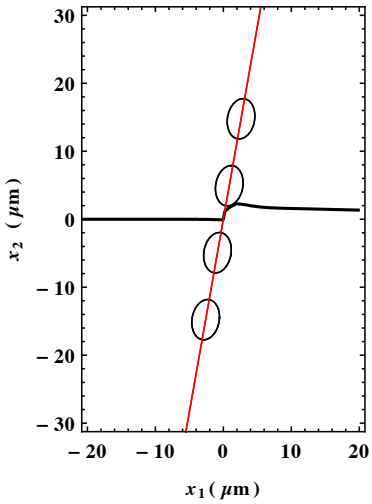


Fig. 5.25 Crack propagation path can be deflected by a GB containing soft inclusions. Deflection mechanisms depend on the GB, the inclusion interface, and the matrix material strength as well as, the relative orientation of GB and the propagating crack.

crystalline materials and provide a framework for microstructural design. In Section 5.4, a toughening mechanism using the microstructural defects was provided. Here, the aim is to incorporate the method into a polycrystalline diamonds. PCDs are diamond grits that have been fused together under high-pressure, high-temperature conditions in the presence of catalytic metals [225, 226]. Strength of PCDs is affected by GB structures and inclusions at GBs. Strength of GBs can be determined using experimental results or numerical calculations such as molecular dynamic simulations [227, 228].

In molecular scale investigations, atomistic modellings provide valuable insights into the relation between microstructures and crack propagation mechanisms at the interfaces. Of particular interest here is GBs where simulations predict the precise mechanism of fracture initiation there [227]. In a system under external load and at a critical local stress, micro-cracks nucleate within the dislocation cores at the GBs and propagate along the interface[229].

Series of molecular dynamics simulations were designed to estimate intergranular cohesion and theoretical fracture strength of individual GBs in PCDs by [230–233]. Simulations were performed using a many-body interatomic potential to investigate behaviour of several symmetrical tilt GBs with $< 001 >$ and $< 011 >$ misorientation axes in diamond when the system is loaded. It was predicted that maximum stresses for samples with GBs are about $30\% - 60\%$ lower than those for the ideal diamond structures. Critical stresses for crack propagation within a GB obtained from dynamic simulations are consistent with those calculated from the Griffith criterion. Also, depending on the GB type, the work of fracture

for various types of GBs is $40\% - 80\%$ lower than that for the $< 111 >$ ideal diamond orientation. Another parameter to study GBs is the GB cleavage energy which is a primary parameter determining GB resistance to crack propagation. The cleavage energies of most $< 001 >$ and $< 011 >$ tilt GB's are about $60\% - 75\%$ of those for the ideal bulk crystals with the same orientation. Although, higher resistance to crack propagation was observed for special type of GBs, crack propagation in polycrystalline diamond samples are predominantly transgranular rather than intergranular.

Another parameter that may significantly contribute to crack propagation and therefore to failure mechanism is the chemistry of materials contributing to GBs and interfaces components. Various catalytic metals such as *W*, *Co*, and *Ni* present during the sintering process in PCDs and remain afterwards. Variation of the exact amount of these catalysts results in different interfacial strengths and mechanical properties [56, 234]. Therefore, reinforcement mechanism such as crack deflection at the interfaces can be accomplished by just varying type or quantity of the additive alloying elements during sintering process. Cobalt-Diamond interfacial energies in the presence of different metallic catalysts are calculated by [235] based on the first-principles or ab initio quantum mechanical theory and in the framework of density functional theory (DFT). DFT, originally developed by Kohn and coworkers [236, 237] has became the most popular and accurate method for electronic structure calculations in condensed matter physics [238, 239].

Ab initio molecular dynamics simulations were performed at high pressure (5 GPa) and high temperature (1500 °C) followed by cooling to room temperature and energy minimisation [235]. Calculations predict that the work of separation for cleavage along the low-index planes of bulk *Co* between (111) atomic planes is 4.08 J/m^2. Cleavage along the (110) and (100) planes has higher work of separation by 0.65 and 0.71 J/m^2, respectively. Work of separation for cleavage in bulk diamond between (111), (110) and (100) atomic planes were derived as 10.18, 10.02, and 16.75 J/m^2 respectively. Work of separation between a *Co* and diamond interface (3.75 J/m^2) is comparable to, and in some cases even smaller than, the work of separation at cobalt phase. Presence of carbon (C-rich interface) and tungsten in the binder phase cobalt tends to lower the cobalt/diamond cleavage energy by 0.1 to 1.25 J/m^2 depending on *C*, and *W* concentration. Also, low concentration of *Ni* at the interface has a small effect on the interface strength. The interfacial energies of inclusion given in Table 5.2 were calculated in stages, where the composition of the binder phase at the inclusion interface was changed from a pure cobalt phase, to cobalt with carbon and subsequently to cobalt with both carbon and tungsten.

Table 5.2 Results of ab initio molecular dynamics simulations at T = 1500 C^0 under a pressure of 5 GPa followed by cooling to room temperature and energy minimisation.

Inclusion	Alloying Elements	Consentration	Interface Strength (J/m^2)
Co	C	C-poor interface	$E_{Co} = 3.69$
Co	C	C-rich interface	$E_{Co-C} = E_{Co} - (0.1\ to\ 0.25)$
Co	C-W	low W concentration	$E_{Co-C} - 0.16$
Co	C-W	high W concentration	$E_{Co-C} - (0.3\ to\ 0.4)$
Co	C-W	W monolayer at the interface	$E_{Co-C} - 1$
Ni	-		$E_{Ni} = 3.5$
Ni	C	low C concentration	$E_{Ni-C} = E_{Ni} - 0.15$
Ni	C	high C concentration	$E_{Ni-C} = E_{Ni} - 0.38$
Ni	C-W		$E_{Ni-C} - (0.2\ to\ 0.5)$

5.5.1 Effect Of Alloying Elements

The aim of this section is to investigate the effect of alloying elements *W*, *C*, *Co*, and *Ni* on the cobalt-diamond interfacial strength and consequently on the crack propagation path. Here, it is assumed that the fracture energy is the same as cleavage energy. However, the work of fracture can exceed the cleavage energy when additional mechanisms of energy dissipation beyond pure bond breaking along the fracture plane involve. For example, the energy dissipation caused by the significant bond bending at loading along different directions.

Simulations were performed using the diamond as the matrix material with shear modulus, $\mu = 570\ GPa$ and Poisson's ratio $\nu = 0.07$ [26], and cobalt as the soft inclusion with shear modulus $\mu = 75\ GPa$ and Poisson's ratio $\nu = 0.31$ [240]. An elliptical cobalt inclusion was located on the GB with cleavage energy 70% of the diamond (111) plane fracture energy. The Co-Diamond (111) interface energies were considered to be $\Gamma_{int} = 3.69$, and 2.5, where the *Co* fracture energy was selected as $\Gamma_{Co} = 4.08$. The inclusion aspect ratio can be derived using the γ_{GB}/γ_{int} ratio; the stronger the GB, the higher the aspect ratio. Simulation results showed that the crack propagation path is identical for two different cases and the crack penetrated through and crossed the inclusion unless the GB energy reached 97% of the diamond fracture energy. In this condition, the crack was deflected by the inclusion and propagated along the inclusion interface. All these calculations are viable for predicting fracture at low temperature. However, PCDs temperature is not constant in operation and increases during the drilling. Elevation of the temperature and the mismatch in the thermal expansion coefficient can potentially modify the crack propagation trajectory.

5.6 Conclusion

This chapter explores the need for developing the advanced engineered GB structures. Many industries working with advanced materials are faced with more advanced requirements on the end-products. The need for greater toughness, tensile strength, less catastrophic failure, and cost efficient manufacturing process are the typical demands.

Composites containing soft and hard inclusions with several GBs and interfacial energies are developed to meet the recent market demands. Here it is shown that a crack approaching a weak GB or inclusion's interface can deflect and release energy. Crack deflection enhances toughness of the materials [14]. Competition between penetration and deflection of crack at interfaces, where the materials on either sides of the interfaces are elastic and isotropic, were studied using different mechanisms proposed in [168], [14–17], [209–212]. In this study an adopted crack propagation mechanism based on the energy distribution at the crack tip and crack coalescence is used.

The effect of the GB orientation and interfacial strength of the GBs and inclusions on crack propagation path are studied. It is shown that variation of the GB and the inclusion interfacial strength could effectively change the crack propagation trajectory in the quasi-static regime and consequently enhance the fracture toughness. Also, crack propagation at the interface depends on the relative orientation of the crack and the interface.

Adding inclusions is a very powerful tool to obtain materials with effective properties in between those of its individual components (matrix material and inclusions) [241]. Understanding the correlation between parameters associated with the presence of inclusions, and the mechanical properties of materials enables one to establish more efficient material design strategies. Hard inclusions can improve toughness of materials via different mechanisms such as micro-cracking, crack deflection, and crack branching [242, 243]. Here, *crack deflection toughening mechanisms* in the presence of hard inclusions are studied. The distance between the hard inclusions should be greater than the size of the inclusions to avoid inclusion clustering, which is not beneficial in terms of increased toughness. Also, simulation results show that soft inclusions and voids in brittle materials can improve the material toughness by *directing a crack into a predetermined propagation path*. Furthermore, considering that additional crack energy dissipation could take place in the presence of soft inclusions considering that they are often ductile (as is the case for Co), the material toughness could be further enhanced in such configurations. However, it should be noted that in our prototypical application, PCDs, inclusions are restricted to relatively low operating temperatures [241, 244] and the effect of temperature variation is not considered in this study.

Chapter 6

Residual Stress and Temperature Effects

6.1 Introduction

Residual stresses are stresses which are locked within a body after inelastic deformations have been experienced. These stresses exist in the material in the absence of the application of any external loads or thermal gradients and are self-equilibrated. Residual stresses can be developed in any mechanical structure through a variety of mechanisms including plastic deformations, temperature gradients, and volumetric changes arising from solidification or phase transformation, and from the differences in thermal expansion coefficients of the existing components.

In this chapter, the effect of residual stresses in general, and the residual thermal stresses associated with the presence of second phase inclusions in particular, on the crack propagation path is studied. Either compressive or tensile residual stresses can deviate crack trajectory. Tensile residual stresses can reduce the performance or cause failures in materials; on the other hand compressive residual stresses can be beneficial and may arrest or retard crack propagation. Results of this study are extended to investigate the influence of residual stresses and thermal stresses on crack propagation in PCD structures.

Here, the crack propagation is modelled using the Discrete Crack Dynamic method, which relies on the prediction of the accurate interactions between different elements of the system using the multipole method. The interfacial effects are also included in the system. The mathematical framework and algorithmic implementation have been explained in details in Chapters 3, 4, and 5. Numerical results at each step are validated using outputs from other numerical techniques and experimental results.

6.2 Residual Stress Effect On The Crack Propagation Path

The effect of residual stress on crack propagation is of a considerable practical significance. Crack propagation in quasi-brittle materials is intensely affected by the tensile and compressive components of residual stresses. It is widely known that the regions of compressive residual stress can retard crack propagation or arrest the crack, while tensile residual stress regions produce the opposite effect. This mainly results from the fact that stress and strain field distributions of a propagating crack changes due to the presence of pre-existing residual stresses.

The aim of this section is to clarify the influence of the residual stresses on the crack propagation trajectory. Superposition techniques are employed most frequently to account for the effect of existing residual stress fields and external loads on crack propagation trajectory [245–247]. This approach is also applied here to measure the total stress fields which is associated with the residual stresses and with the external load and the interactions between crack/inclusions. In this study, the stress field associated with a crack propagating through a residual stress field and subjected to remote tensile loading is computed by assuming some simplified forms of residual stress distribution. However, the method is general and expected to work similarly for any residual stress distributions.

6.2.1 Method Of Approach

Without loss of generality, a known distribution of residual stress in the region around the virtual circle with radius R is considered (please note that the circle does not necessarily correspond to a physical inclusion and the material properties are uniform throughout the sample). The radial component of stress field is defined as $A/(x^2+y^2)$, where the sign of A determines whether the field is tensile or compressive. Also, A specifies the magnitude of the residual stresses. The function of residual stresses σ_{rr} and $\sigma_{\theta\theta} = -\sigma_{rr}$ are defined by

$$\sigma_{rr}(r) = \begin{cases} A/r^2 & r \geqslant R \\ 0 & r < R \end{cases} \tag{6.1}$$

where, $r = \sqrt{x^2+y^2}$ is the radial distance from the centre. The specific distribution of residual stress in Equation 6.1 is similar to thermal residual stresses around circular inclusions that might be caused during the manufacturing process [248, 249]. Effects of thermal residual stresses on crack propagation path are the subject of the next section. Here the study is focused on the influence of distribution of residual stresses on an unbounded solid.

The stress field introduced above changes radially from the perimeter of the virtual circle following $1/r^2$, while the stress fields ahead of the crack vary with a trend which is inversely proportional to the square root of the distance from the crack-tip ($1/\sqrt{r'}$). Constant A can be selected to be large enough to alter the stress fields in the region surrounding the crack-tip and consequently, deflect or arrest the crack. In the DCD method, the crack propagation as a discretised process is modelled by adding a succession of new cracks. Each crack is modelled as a collapsed, zero-stiffness inclusion. However, due to the singularity of the stress fields at the crack-tip, the effect of the residual stresses right at the crack-tip is not sufficient to counteract the singular crack-tip stress field. Therefore, the effect of residual stresses on deflection of crack propagation path can not be captured using the crack propagation criterion at the crack-tip.

To address this issue, the fracture criteria should not be applied right at the crack-tip but at a short distance from that. This distance can be determined at the point where two different methods of calculating the crack propagation direction provide the same results. The first method is the one that has been incorporated in the DCD method for brittle materials. In this method, the exact position of each new crack is determined by searching where the generalised energy release rate is maximised at the curvature of the crack-tip; it is the point where the crack extension starts and propagates in the direction perpendicular to the surface of the initial crack (inclusion). The second method is the maximum tangential stress field using SIFs to predict the crack propagation direction [69]; this method requires the accurate determination of SIFs. In this problem, more accurate SIFs can be determined using the average SIFs over a short distance from the crack-tip in the direction along which the crack propagation is predicted; the short distance is comparable to the crack curvature. It should be noted that there is always some level of uncertainty in predicting the crack propagation path, since the distance to determine SIFs are not fixed and can change depending on the materials under study.

Simulations were performed to validate the mentioned modifications to the fracture criteria. Figure 6.1 shows crack propagation paths and the maximum principle stress fields (at various simulation steps) in a homogeneous solid with the known residual stress distribution. The system is under a uniform tension in x_2 direction and stress fields are normalised with respect to the remote load. The crack is set to propagate in one direction. Crack trajectories were calculated using two different crack propagation methods. An initial crack with 3 μm length is propagated under uniform remote tensile load in the presence of residual stresses corresponding to the expressions in Equation 6.1, where R, and $-A$ are selected as 5 μm and 50 GN respectively. This specific selection of parameters provides a radially compressive stress field distribution with the minimum of -2 GPa on the perimeter of the virtual circle.

In this benchmark test, SIFs are averaged over a short distance, equivalent to the half of the crack curvature. Comparison of two crack trajectories verify the equivalence between the two propagation criteria for brittle fracture adopted here.

The new crack propagation criterion is applied to the system to predict the influence of the residual stresses on the crack propagation path. Below, effects of compressive and tensile residual stresses on the crack trajectory using the crack propagation criterion based on maximum generalised energy release rate are investigated.

6.2.2 Numerical Results

Residual stresses can play a significant role in accelerating or preventing failure of materials. It must be noted that, effects of residual stress distribution depend on the position and the size of the initial crack, and on the external load. Simulations are now conducted to establish the fundamental influences of the compressive and tensile residual stress fields on the crack propagation trajectory. The known distribution of residual stresses were selected according to Equation 6.1. The crack is set to propagate only from the right tip, i.e. toward the residual stresses, and propagation is prevented from the other crack tip. Figure 6.2 predicts crack propagating toward the residual stress field with compressive circumferential stress and radial tensile stress around the virtual circle. Crack will first be deflected by the compressive hoop stress, which is normal to the crack plane. Then, as the crack moves around (normal to tensile radial stress), it can be deflected away by the tensile radial component of the residual stress.

The method was used to predict the effect of the residual stresses relative to the external load on the crack propagation path. Figure 6.3 illustrates the crack propagation path for an initial crack of length 2.6 μm, under an external tensile load. The residual stresses are determined outside of the circular region with radius $R = 5\ \mu m$, and modified by changing constant A. The maximum radial residual stresses on the perimeter of the circle relative to the external load were set as $\sigma_{res}/\sigma_{\infty}$ = 0, 1, and 2; where zero is associated with $A = 0$.

In the case of compressive radial stress, the contrary effect is expected to be seen. Figure 6.4 illustrates the effect of compressive radial residual stress relative to the external load on the crack propagation path for the same system. The minimum radial residual stresses on the perimeter of the virtual circle relative to the external load were set as $\sigma_{res}/\sigma_{\infty}$ = 0, -1, and -2. Figures 6.3, and 6.4 show that by increasing the relative size of the residual stress to the external load, the crack deviation from the straight line becomes more significant. In other words, this confirms that in brittle fracture the lower is the applied load, the more intense the effect of residual stress.

The next set of simulations were run to show the effect of initial crack size and its response to the residual stress and the external load. Figure 6.5 demonstrates that the effect

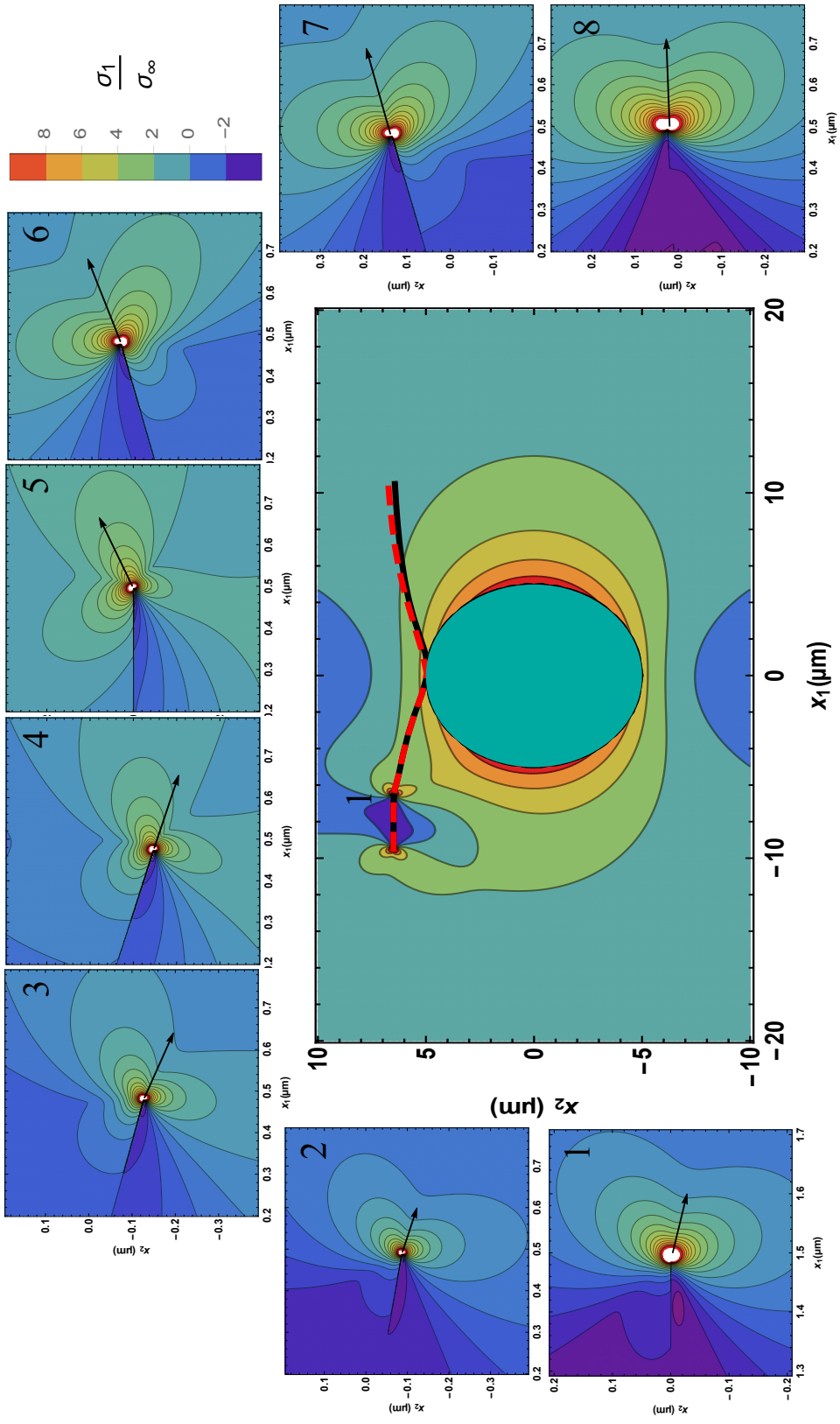


Fig. 6.1 Schematic representation of the crack trajectory and the maximum principle stress fields normalised with respect to the remote load (σ_1/σ_∞). Black and red dashed lines show crack trajectories predicted using SIFs in Equation 4.2 and the two proposed crack propagation criteria. Crack at each simulation step is approximated by a kinked crack, and a kink crack by two sequential cracks. Stress fields at the tip of the second crack are illustrated in different steps where black arrows predict the crack propagation direction in that particular configuration. The crack starts propagating from point 1 and continues until it is far away from the influence of the residual stresses in point 8.

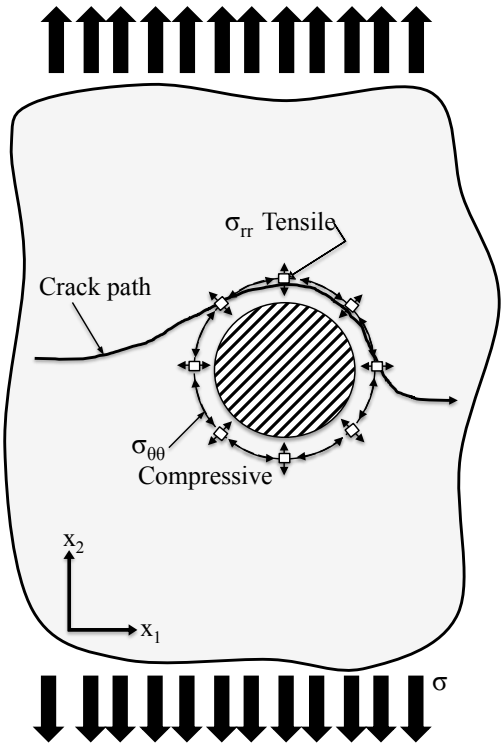


Fig. 6.2 Deflection of the crack by the proposed residual stress in Equation 6.1 and the external far-field load. Propagating crack will first be deflected where the compressive hoop stress in the matrix material is normal to crack plane. As the crack moves around, it will be deflected away where the crack plane is normal to the tensile radial stress.

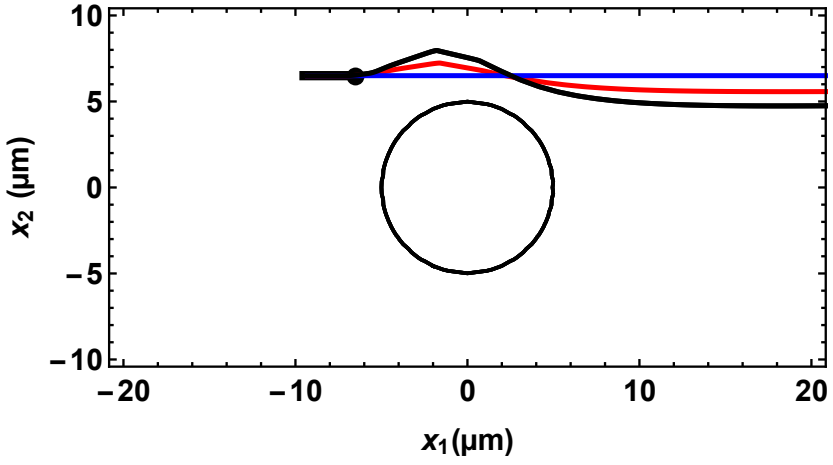


Fig. 6.3 Schematic representation of the crack propagation path for an initial crack of length 2.6 μm, under far-field tension and tensile radial residual stress. The blue, red, and black lines are crack trajectories associated with residual stresses where the magnitude of the stress on the perimeter of the circle relative to the external load are set to 0, 1, and 2.

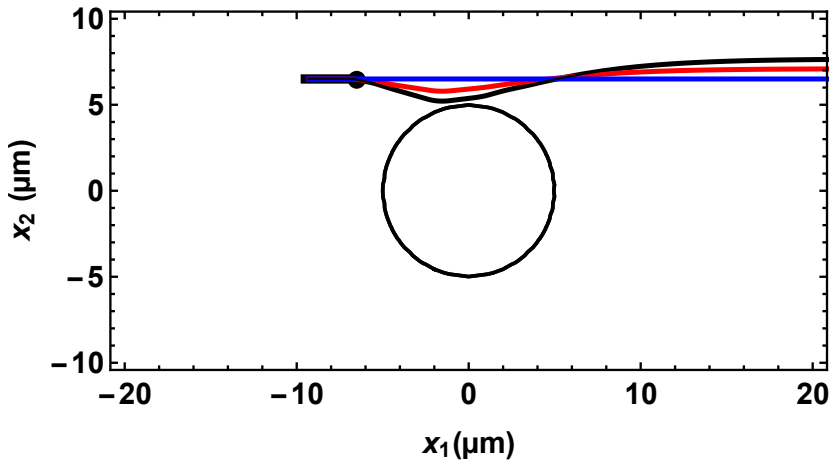


Fig. 6.4 Schematic representation of the crack propagation path for an initial crack of length 2.6 μm, under far-field tension and compressive radial residual stress. The blue, red, and black lines are crack trajectories associated with residual stresses where the magnitude of the stress on the perimeter of the virtual circle relative to the external load were set to 0, -1, and -2.

of residual stress decreases as the crack length increases. Simulations were repeated in the same system with an initial crack of different sizes, where the crack-tip from which the crack propagates (right hand side) was started at the same point. The minimum compressive radial residual stress on the perimeter of the virtual circle relative to the external load was selected to be -2. The small crack deviates more considerably with the residual stress. In general, a short brittle crack is most likely to be arrested, deflected or accelerated by small residual stresses.

It should be noted that effects of residual stress also depend on the position of the original crack relative to the residual stress and the external load. Figure 6.6 shows the trajectory of a crack under tensile far-field load where the initial crack with 30^0 inclination angle has a crack-tip located at point A in Figure 6.6. The maximum tensile radial residual stress on the perimeter of the circle relative to the external load was set to be two. As it is already shown for the horizontal cracks, the crack propagates toward the residual stress field and it is subsequently deflected by the compressive hoop stress and moves around, normal to tensile radial stress.

The effect of residual stress become more significant for finite sized problems than when considering cracks propagating in an infinite plane, and the difference between them increases as crack length or applied stress increases. To this point, effects of the known residual stress distributions in the vicinity of an imaginary circle on the crack propagation path have been studied. The results obtained from the simulations presented here are consistent with the

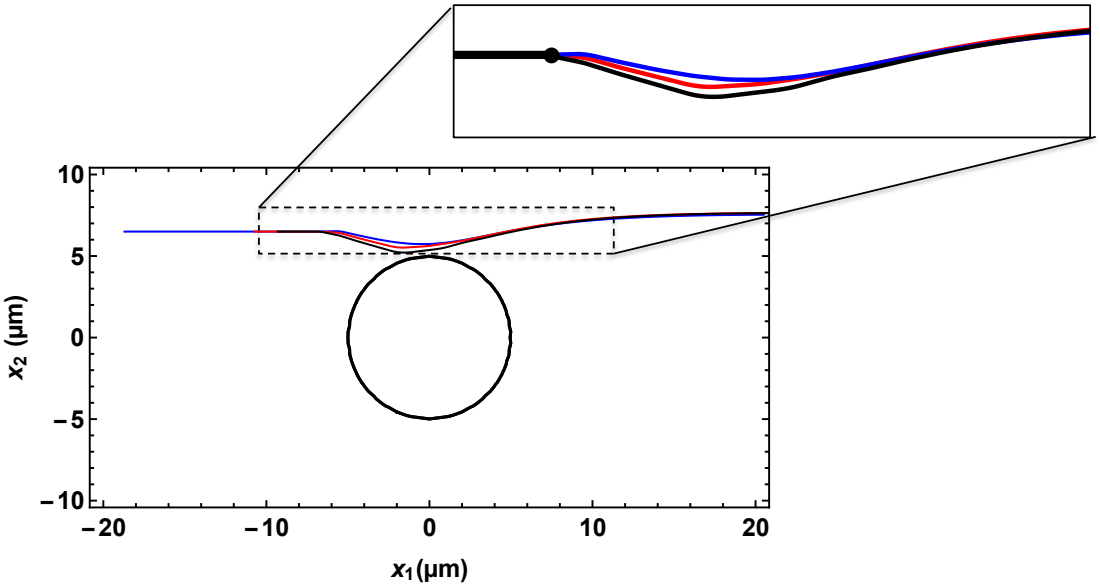


Fig. 6.5 Schematic representation of crack propagation paths under the uniform far-field tension and compressive radial residual stress. The blue, red, and black lines are crack trajectories associated with the initial crack of length 12, 4, and 2.6 μ m respectively.

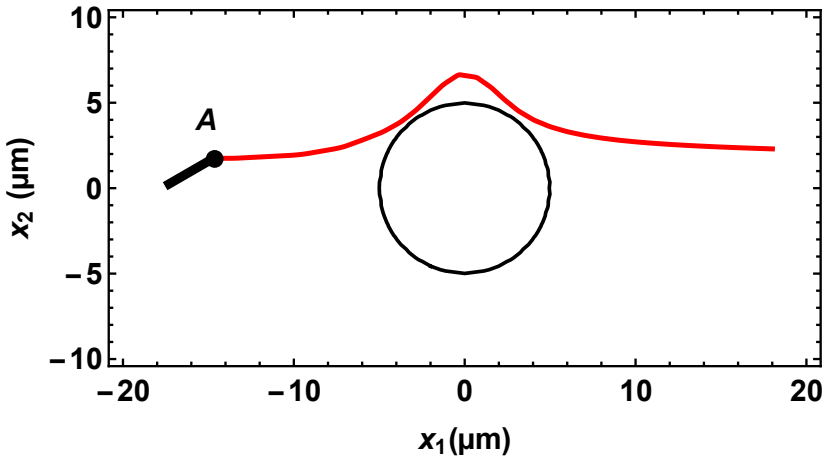


Fig. 6.6 Schematic representation of the crack propagation path of an inclined crack under the far-field tension and tensile radial residual stress.

investigation of Kanazawa *et al.* on the effect of residual stress on brittle fracture propagation [250]. In the next stage of developing the method, effects of residual stress distributions in the presence of the inclusion are investigated. Differences in thermal expansion of inclusions and the matrix material can create residual stress fields in the vicinity of the inclusion. In the following section, the effect of temperature variation and thermal stresses on the crack trajectory are examined.

6.3 Temperature Effect On The Crack Propagation Path

One of the most important factors in fracture of materials containing second phase inclusions is the mismatch of expansion coefficients of the materials; this has not received detailed attention when dealing with the deterministic prediction of crack propagation paths. Differences in thermal expansions of various phases create residual stresses that are developed during cooling or operation processes [251, 252]. Generally, temperature variation induces changes in the size of materials. Increasing or decreasing the temperature results in the expansion or contraction of the structure. To better understand this phenomenon, in 1D the variation in the length (Δl), and temperature (ΔT) are related by the following equation:

$$\Delta l = \alpha l_0 \Delta T \tag{6.2}$$

where α is the thermal expansion coefficient with the unit of $1/\ ^0K$, and l_0 is the original length of the material. If the structure is restrained and prevented from movement while subjected to a temperature change, stresses will develop. This is the case in a system where inclusions are located in a matrix and the two materials are characterised by different thermal expansion and/or stiffness. .

To find the relationship between the changes in temperature and the stress developed in the restrained structure, first it is assumed that the system is unconstrained to move, so that changing the temperature results in variation of the sample size. Then, by forcing reverting the system to its original configuration, the system becomes constrained. This force equals to the amount of stresses that are developed in the system when the temperature is modified. The current investigation is focused on the effect of temperature variation and expansion coefficient mismatch on the crack propagation trajectory. The work is limited to the effects of temperature on the stress distributions around the inclusions, although extensions to include other sources of residual stresses can easily be incorporated in the current strategy.

The procedure of finding thermal stress fields near the inclusion is as follows. The system is decomposed into two sets, one a matrix material with a void and another one, an inclusion of the same size considered in isolation. The total displacements for the two sets can be

calculated separately. Assuming that the whole system is initially in equilibrium and the size of the inclusion matches that of the hole, no force is required to fit the inclusion back into the void in the matrix material. By changing the temperature, both inclusion and void are deformed, and an additional force is necessitated to put the inclusion back into the void. The pressure associated with this additional force on both inclusion and void surfaces is the same and denoted by p_0. The total amount of required force is proportional to the total size variations of the inclusion and void. By equating the force to the amount of stresses that are developed due to the temperature variation, the thermal stress fields are calculated.

6.3.1 Thermal Stress Distribution Around The Circular Inclusions

Consider a small circular inclusion of one material with radius R is embedded in a large matrix of another material. The thermal stress fields of a circular inclusion in 2D are approximated using the ordinary engineering formulas for a thick-walled cylinder [248]. In this calculation, the method is developed by analogy to the model proposed by Selsing [249].

Thermal stress fields of a system containing a circular inclusion with the modulus of elasticity E_i and Poisson's ratio ν_i, and radius R in an infinite isotropic material with the modulus of elasticity E_0 and Poisson's ratio ν_0 can be approximated by a thick-walled cylinder with the inner radius of R, and pressure p_0 when the wall thickness is increased to infinity with zero pressure. Superscripts "i", and "0" are used to denote inclusion and matrix material. The stress fields inside the inclusion for all values of r (the radial distance from the centre) become

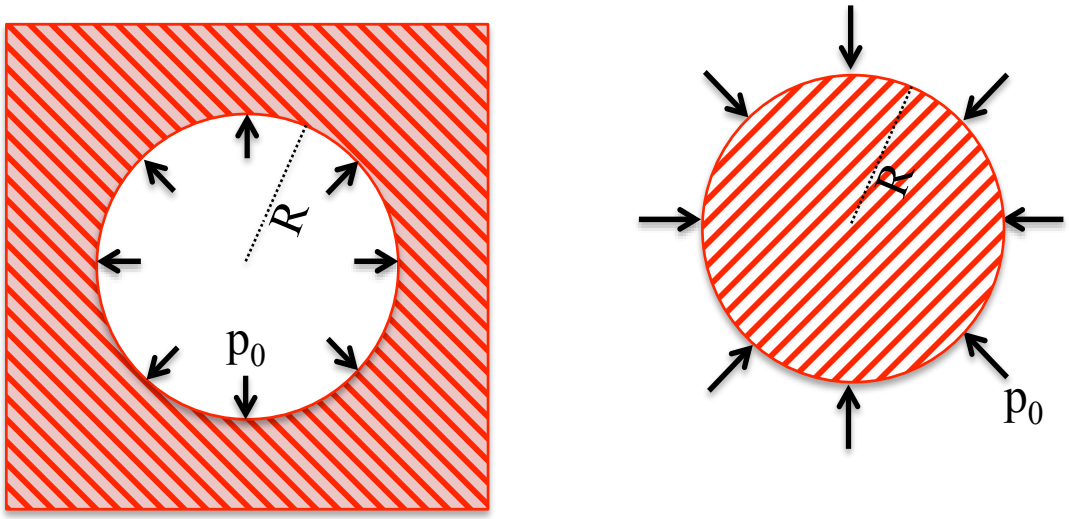
$$\sigma_{rr}^{i} = \sigma_{\theta\theta}^{i} = -p_0. \tag{6.3}$$

Stress fields in the matrix material are

$$\sigma_{rr}^{0} = -\sigma_{\theta\theta}^{0} = -p_0 \frac{R^2}{r^2}. \tag{6.4}$$

By decomposing a system into two sets, one a matrix material with a circular void and another one a circular inclusion in an isolation, and assuming that the whole system is initially in equilibrium , the radial displacements can be calculated separately. It can be assumed that the circular inclusion is forced into the cavity in spite of a misfit in radius Δu; this would apply the same pressure p_0 in the cavity and on the inclusion. The total misfit can be obtained by adding radial deformations.

$$\Delta u = \Delta u_0 + \Delta u_i = p_0 R\left(\frac{1+\nu_0}{E_0} + \frac{1-\nu_i}{E_i}\right) \tag{6.5}$$



(a) (b)

Fig. 6.7 The problem of inclusion in the matrix material is decomposed into two systems: a) a matrix material with a circular void under an internal radial pressure of p_0, b) a circular inclusion under an external radial pressure of p_0.

If the misfit originally was zero and then developed by changing the temperature (ΔT) because of a difference $\Delta\alpha$ in thermal expansion of the matrix material and the inclusion, the variation in radial deformation can be calculated from the following expression:

$$\Delta u = R\,(\alpha_i - \alpha_0)\,(T_2 - T_1) \tag{6.6}$$

By combining equations 6.5, and 6.6 pressure p_0 is obtained.

$$p_0 = \frac{(\alpha_i - \alpha_0)\,(T_2 - T_1)}{\frac{1+\nu_0}{E_0} + \frac{1-\nu_i}{E_i}} \tag{6.7}$$

This value of p_0 yields all the desired components of stress fields when the value is applied to Equations 6.3 and 6.4. The same formula can be derived using the continuity of the stress, and displacement fields [253].

6.3.2 Numerical Results

In this section, crack trajectories in the vicinity of the circular inclusions are predicted. Localised thermal stresses around the inclusion influence the crack path by altering stress fields at the crack-tip. Thermal stress fields are derived for a circular inclusion using Equations 6.4, and 6.7. Simulations are performed for the case where inclusion has higher thermal

expansion than the matrix material. This work can also be extended to study composites with cylindrical fibres.

Superposition of the respective stresses caused by the thermal expansion mismatches, the external load, and by the interaction between crack/inclusions are used to quantify the influence of thermal stresses on the crack propagation path. This approach employed most frequently to account for the effect of existing thermal stresses, residual stress fields and constant amplitude of the external load on crack propagation trajectory [245–247]. Note that the thermal stress fields of the circular inclusion are described in the polar coordinate system. Hence, to perform the calculations using the multipole method as described in Chapters 3 and 4, the stress components have to be converted from the polar coordinate system to the global cartesian system and then from the global system to the local elliptical coordinate system. Consequently, the summation of the thermal stresses and the one caused by inclusion/crack interactions determine the crack trajectory.

To start with, consider a system containing a crack propagating towards a soft inclusion of radius $R = 5\ \mu m$, in an infinite isotropic brittle material. The crack is set to propagate only from the right tip, i.e. toward the residual stresses, and propagation is prevented from the other crack tip. The temperature is decreased from T_0 to T_1. For the particulate inclusion-matrix problem with $\alpha_i > \alpha_0$, the thermal stresses in the inclusion are compressive and constant, and in the matrix material radial and circumferential thermal stresses are tensile and compressive respectively. Radial tensile stresses are larger at the vicinity of the inclusions and decline radially with the distance from the surface of the inclusion.

Simulations are performed on a system containing circular inclusion with the mechanical properties of cobalt, modulus of elasticity $E_i = 220\ GPa$, poisson's ratio $\nu_i = 0.31$ [240], and expansion coefficient $\alpha_i = (13-15) \times 10^{-6} /\ ^0K$ [254], in an infinite slab of diamond material with modulus of elasticity $E_0 = 1220\ GPa$, Poisson's ratio $\nu_0 = 0.07$ [26], and expansion coefficient $\alpha_i = (1-3) \times 10^{-6} /\ ^0K$ [255]. The system is under far-field tension in the x_2 direction and temperature variation of $\Delta T = 1400\ ^0K$. Diamond, cobalt, and cobalt/diamond interface fracture energies are selected respectively as $\Gamma_{Diamond} = 10.18$, $\Gamma_{Co} = 4.08$, and $\Gamma_{int} = 3.0\ J/m^2$ according to the calculations given in [235].

Results of simulation are demonstrated in Figures 6.8, and 6.9, which depict simulations for cracks initiated from different coordinates. The external load is selected in a way that the straight crack with initial size of 2.6 μm can propagate. The maximum component of the radial thermal stress relative to the far-field tension on the inclusion interface becomes 2. The number is chosen to be representative of the application under investigation since the residual stresses in PCDs can be substantial, in a order of 1-2 GPa [256–258]. In Figures 6.8, and 6.9 the initial cracks with angles of 0^0, and 30^0 are positioned with their tips at

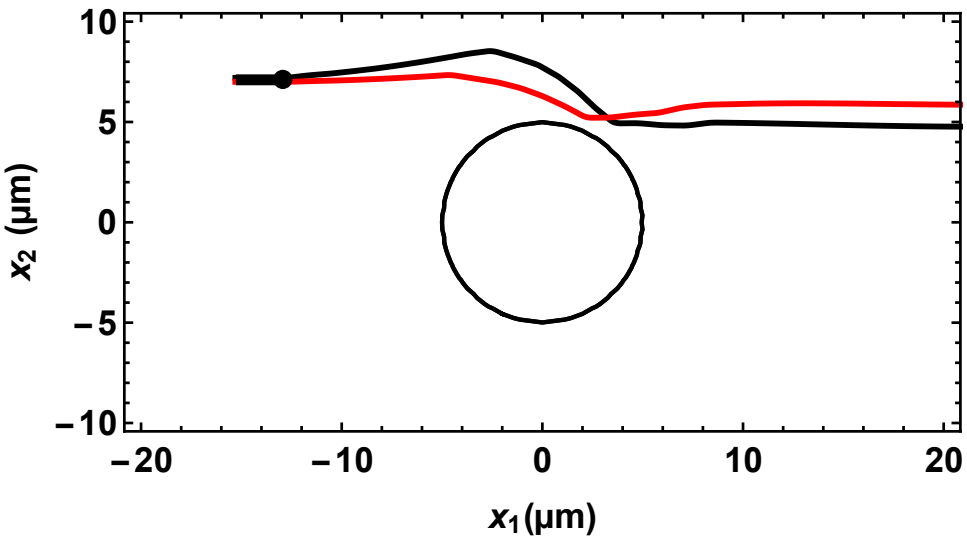


Fig. 6.8 Graph showing the effect of thermal stress and the second phase inclusion on the crack propagation path. Black and red lines illustrate the crack propagation trajectories in the presence and in the absence of thermal stresses respectively.

points (-12, 7), and (-10, 3) respectively. Figures show crack deviation caused by the external load, thermal stresses and interface effects. In both figures, the black, and red lines illustrate the crack propagation trajectories for cases computed in the presence and in the absence of thermal stresses. The average crack energy and SIF are lower by more than 5% and 6% in Figure 6.8, and lower more than 2% and 3% in simulations demonstrated in Figure 6.9, for the calculations in which thermal stress effects were considered compared to those where thermal stresses were not considered.

Figure 6.10 shows the crack propagation path in the presence of thermal stresses for different far-field loads. It is demonstrated that if the applied loading were to have a significant level compared to the thermal stresses, the influence of the thermal stress would only be to lower the crack energy and not to change the crack propagation trajectory. It is cleared that by increasing the far-field load, the crack trajectory tends toward the red line which is the crack propagation path in the absence of the thermal effects.

Calculations performed here show qualitative agreement with other studies given by many authors[259–264]. It can be concluded that the thermal stresses in the configurations studied here by the authors can arrest and deflect crack propagation path in such a way that the material toughness increases. The models and the results provided in this section can be extended to study materials reinforced with fibres or composites with second phase inclusions. It should be noted that with the simple expression proposed for the inclusion thermal stress, one cannot estimate all temperature variation effects. This is because the thermal conductivity,

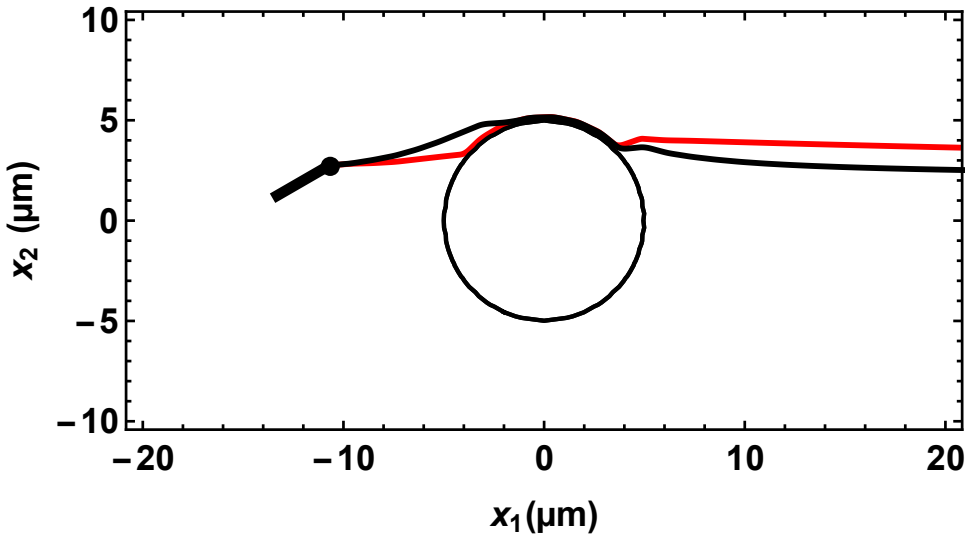


Fig. 6.9 Graph showing the effect of thermal stress, the second phase inclusion and interface strength on the crack propagation path. Black and red lines illustrate the crack propagation trajectories in the presence and in the absence of thermal stresses respectively.

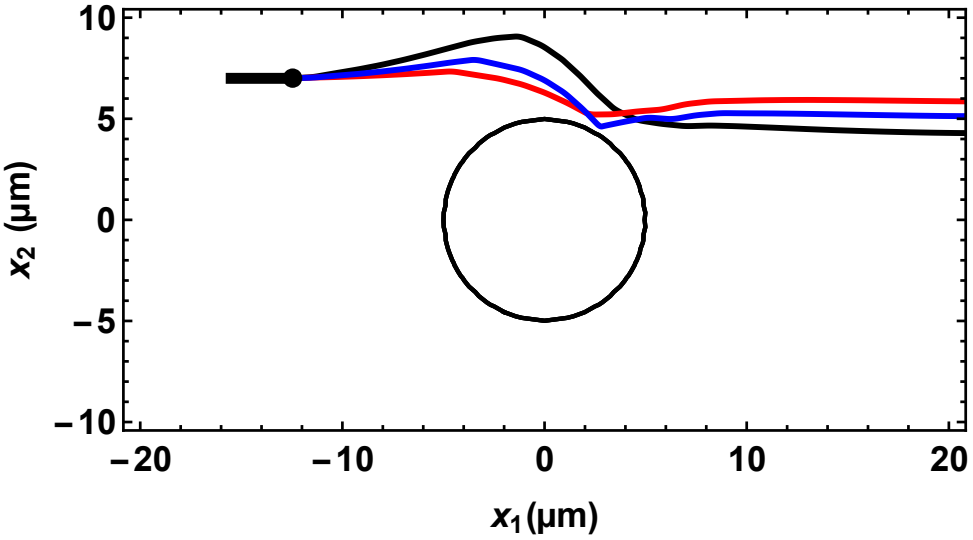


Fig. 6.10 Graph showing the effect of thermal stress relative to the external load, the second phase inclusion and interface strength on the crack propagation path. Black, and blue lines illustrate the crack propagation trajectories for cases where thermal stress was considered and thermal stress on the surface of inclusion relative to the external load was 2 and $2/3$ respectively. The red line shows the crack propagation trajectories for case where thermal stresses were not considered

thermal expansion, Young's modulus, and Poisson's ratio are approximated to be constant values in all temperature ranges. Also, the equations provided in this section hold only for the case of a single inclusion in an infinite isotropic matrix. Although they may represent a satisfactory approximation at low inclusion concentrations, they cannot be generalised. For the system containing many inclusions, predicting the thermal stress requires interactions between thermal stresses of all the elements.

6.4 Fracture Of PCD And Residual Stresses

Investigation on the influence of temperature variation and analysis of the microstructure interactions lead to some valuable insights that can be used to study PCD failure mechanisms. Temperature variation and the differential thermal expansions can induce thermal stresses, which can in turn strongly affect crack propagation paths in PCDs structures.

Figure 6.11 shows the cross section of a PCD sample obtained from a batch with premium performance. The solvent metal catalysts during the operation (at high temperature) can cause an undesirable phase transformation in diamond, converting it to carbon monoxide, carbon dioxide, or graphite. The graphitisation of the diamond depends markedly on the atmosphere around the diamond. In the presence of oxygen, even in minute quantities, apparent graphitisation can be observed at temperatures above 700°C. Metallic binders such as cobalt accelerate the graphitisation process. This problem was addressed by leaching and removing the metallic binders from the working surface of PCDs [56]. This improves the lifetime of the cutters by reducing the vulnerability of the specimen at high temperature. The leaching process gradually removes the binder from the specimen, at least a portion of the first region from the surface to depth of about 0.01 to 0.1 *mm* from the surface. Consequently, microstructure of the PCD is divided into leached and unleached regions (see Figure 6.11b).

A frequent problem in the drilling industry is the failure of cutting tools which is caused by PCDs fracture and chipping. The aim of this section is to investigate the effect of inclusions and thermal stresses in determining the PCDs failure mechanism and chipping. Figure 6.12a shows an example cross-section of a typical cutter after field evaluation. It demonstrate that all the cracks initiated at/near the wear front and then propagated into the bulk; this is a picture of leached cutter, but under the optical microscope in this particular image boundaries are not clear. To gain a more in-depth understanding of thermal effects on fracturing behaviour and its causes, an idealised system is considered here. Figure 6.12b shows a PCD with an ideal clear leached and unleashed boundary. It is postulated that the main crack is propagating close to the boundary of leached and unlatch regions. In Figure 6.13 a symmetric system of inclusions and holes are considered. The crack is located in the

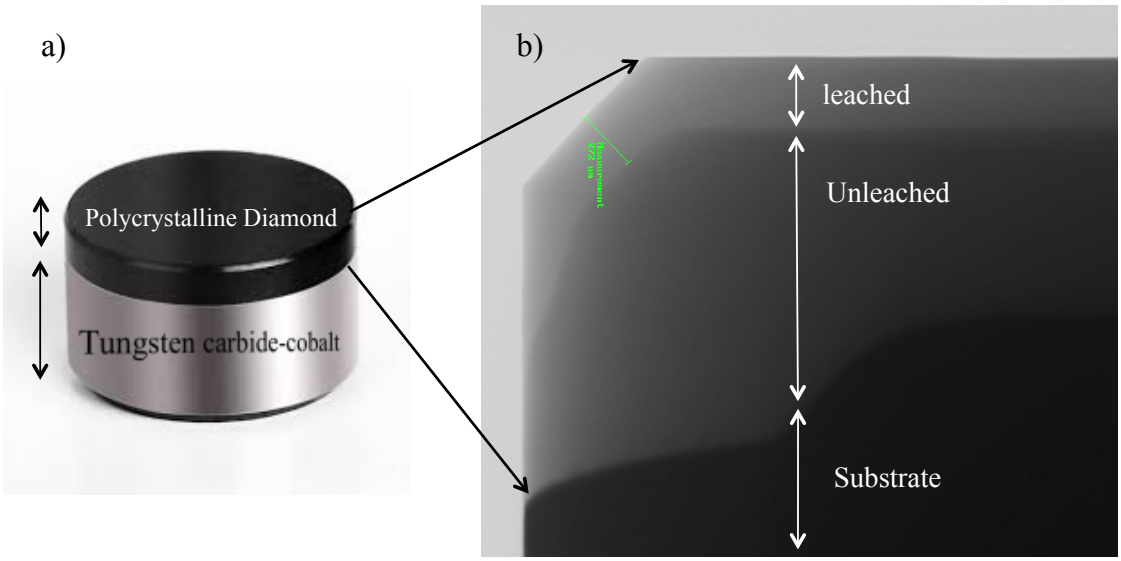


Fig. 6.11 PCD cutter structure: a) photography of a cutter, b) X-ray image of PCD cross-section showing the leach depth of an example cutter (E6 2017). The black, light grey and dark grey parts are showing the substrate, the non-leached, and the leached part of PCD respectively.

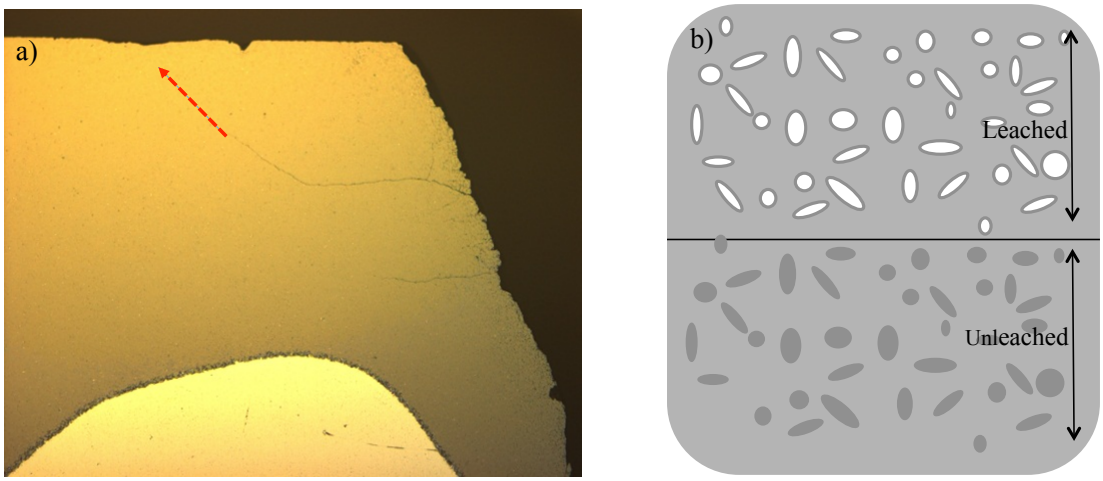


Fig. 6.12 PCD cutter structure: a) a cross-section of a typical cutter after field evaluation showing all the cracks initiating at/near the wear front then propagating into the bulk (E6 2017), b) microstructure of an ideal leached PCD sample.

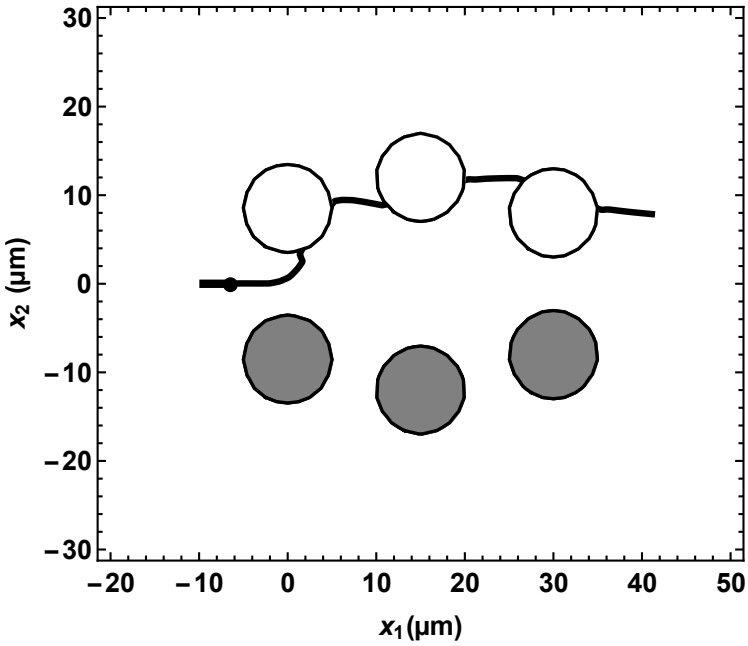


Fig. 6.13 Crack deflection towards holes in a symmetric system containing holes and cobalt inclusions.

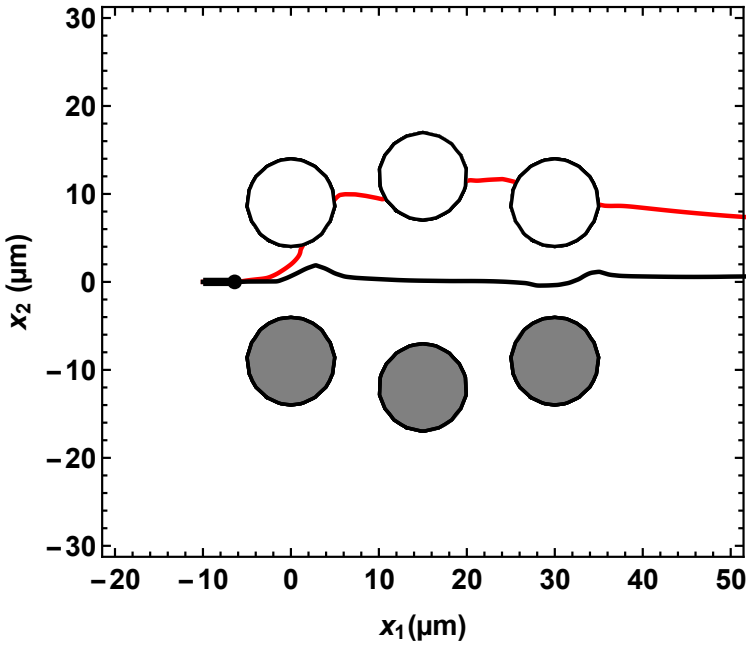


Fig. 6.14 Crack deflection towards holes in a symmetric system containing holes and cobalt inclusions. Red and black lines present crack trajectories in which the thermal stresses are and are not considered respectively.

middle of the system on the symmetric line where inclusions and holes are positioned on opposite sides. The system is under tension in the x_2 direction. Figure 6.13 shows that the crack deviates from the straight line and propagates through the holes in the system where the temperature stresses were neglected.

As mentioned in Section 6.3, Equations 6.4 and 6.7 hold only for the case of a single inclusion in an unbounded homogeneous matrix material, but they represent a satisfactory approximation at low inclusion concentrations [261]. The same approximation is used here to elucidate the effect of thermal stresses in the matrix material, and to find the relationship between thermal stress distribution and failure modes. In the next sets of simulations crack propagation path is predicted and compared for the cases where thermal stresses were also considered. It is assumed that the system is stress free at room temperature.

Figure 6.14 shows modifications in crack propagation paths in a symmetric system containing holes and cobalt inclusions. Red and black lines present crack trajectories in the system in the absence and in the presence of thermal stresses respectively. Result of simulations shows that thermal stresses can modify the crack propagation path and cause failure with fracture being able to navigate through inclusions and holes in the system. Therefore one can conclude that presence of thermal stresses can potentially worsen the chipping process in PCDs. Results of these simulations can be generalised to all thermal stresses initiated either by the mismatch of thermal expansion coefficients between metallic binder and diamond material or by polycrystalline diamond layer and the tungsten carbide substrate [258]. Presence of residual and thermal stresses can considerably change crack trajectories and accelerate chipping and failure mechanisms.

Chapter 7

Conclusions and Future Work

7.1 Conclusion

The subject of this thesis is to develop an all-encompassing two dimensional fracture model for polycrystalline materials in the quasi-static regime, with an ultimate aim to use the method to improve the design and engineer polycrystalline diamonds (PCDs). A polycrystalline material is a system containing several grain boundaries, whose structures can be contaminated with impurities such as inclusions, cracks, and voids. Mechanical properties of the matrix material and inclusions, strength of the interfaces and grain boundaries, and residual stresses are parameters that determine fracture modes and crack propagation trajectories. The ability to predict material behaviours and failure mechanisms of such structures can lead to better designs, improved performance, reduced costs and enhanced safety.

7.1.1 Development of the New Methodology

A new methodology for the study of crack propagation in the presence of interaction inclusions and interfaces was first developed. The development process and the main achievements of this work are listed below.

- In Chapter 2 different numerical and analytical methods to analyse crack-inclusion interactions in elastic solids were reviewed. Their strengths and weaknesses were investigated, and the multipole method was selected for simulation purpose.

- Cracks and inclusions are the basic constituent element of the model, and accurate interactions between them are calculated using the analytical multipole method [135]. The method is explained in Chapter 3 and developed to simulate a finite array of cracks

and inclusions in 3.5. The local field at each point in the system is equivalent to a joint action of the incident far-field and the disturbance fields around all inclusions.

- In Chapter 4, calculated SIFs at the crack-tips (3.5.4), and the full the stress fields (3.5.3) are employed to determine the evolution of a crack in a system while it is interacting with other cracks and inclusions. The method developed to predict crack propagation path in an unbounded solid is explained in 4.4.1 and named Discrete Crack Dynamics.

- In Section 4.5, the method was extended to study finite sized problems using the superposition scheme. In this work, the complex variable boundary element method was combined with the multipole method to study finite sized problems.

- Simulation results presented in Section 4.6 demonstrate that impurity and crack interactions deflect the main crack-path. Interactions between crack and inclusion depend on the size and aspect ratio of the inclusion and the ratio of the inclusion shear modulus to the matrix material shear modulus. It was shown that hard elastic inclusions ahead of the crack-tip carry stresses higher than soft inclusions. Load transfer to hard inclusions brings about a stress reduction near the crack-tip; the amount of stress reduction depends on the inclusion stiffness. For hard inclusions, the crack-tip shielding is induced by load transfer into the hard materials. Conversely, in the case of soft inclusions positioned ahead of the crack-tip, the load is transferred from the inclusion itself to the matrix material and this produces an increase of the stress in the crack-tip region. Therefore, for the problem of soft inclusion, stress field amplification in front of the crack-tip is expected to be seen. Crack amplification also depends on the relative amount of shear modulus of the soft inclusion and the matrix material; the softer the inclusion, the higher the amplification is.

- In Chapter 5 interface effects were incorporated into the simulation code. It was shown that a crack approaching an interface joining two dissimilar materials may arrest or may advance by either deflecting into the interface or penetrating the interface (inter- or intra-granular cracks). This depends on a number of factors including the geometry and relative strength of impurities, grains and grain boundaries.

- Effects of grain boundary strength and orientation on crack propagation path were studied in Section 5.3.1. It is inferred that by decreasing the grain boundary strength, cracks can be deflected to the grain boundary and arrested. Cracks are prone to propagate through grains with low fracture energies but bypass grains with high fracture energies. Crack deflection and arrest can enhance fracture toughness.

- Interfacial strength of inclusions depends on chemistry of the system. Effects of inclusion's interfacial strength were included in the computational code and tested to predict crack deflection in the vicinity of the hard and soft inclusion in Section 5.3.2. Simulation results show that crack propagation trajectory depends not only on the relative amount of shear modulus of materials but also on their interfacial strength. It can be concluded that reducing the interfacial strength can potentially improve materials toughness.

- Grain boundaries may enter and break through inclusions. Interaction of a crack with an inclusion at the grain boundary was investigated in Section 5.3.3. Crack propagation path can be deflected by a GB containing soft and hard inclusions, or voids. Deflection mechanisms depend on GB, inclusion interface, and matrix material strength as well as, the relative orientation of GB and propagating crack, and spacing between inclusions.

- The method was used to find a new toughening mechanism. A single crack channeling into several toughening configurations containing array of elliptical holes, and soft and hard inclusions was studied in detail in Section 5.4 and an optimum configuration for each system was obtained. It was predicted that a system containing soft inclusions is tougher than the same system containing voids.

- In Chapter 6, the method was further extended to study influences of known residual stresses and thermal stresses on crack propagation path. In particular, effects of thermal stresses of a circular cobalt inclusion on crack trajectory in a diamond matrix material was investigated. Finally, the effects of residual stress and thermal stress distributions were investigated on fracture and chipping of PCDs.

7.1.2 Failure Mechanism In PCDs And DCD Method

In PCDs, crack could be initiated by surface flows, micro-scale impurities, inclusions and defects inside diamond grains or at grain boundaries. However, relatively high stress is required to initiate macroscopic cracks from defects and inclusions because they are either small in size or have large crack-tip radii. Loading condition of PCDs during operation is not usually sufficient to initiate a catastrophic fracture, but rather adequate to increase size and number of impurities in a system. Therefore, it is expected that small cracks grow step by step in brittle manner similar to the crack slit in a failed PCD structure demonstrated in Figure 7.1. This gradual crack propagation phenomena was used to model crack propagation in discrete crack dynamic method. In the DCD method, effects of crack-inclusion interactions, GBs, interfaces, and residual stresses on crack propagation path were investigated.

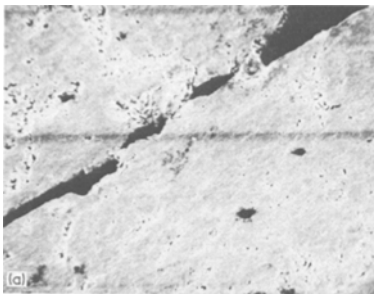


Fig. 7.1 A scanning electron microscope (SEM) test of the crack slit in a failed PCD [19].

It was shown in this work that cracks propagation direction can be changed due to several obstacles such as grain boundaries, interfaces and residual stress distributions. Variations of fracture energy pattern at GBs or changes of the preferred cleavage direction from one grain to another can modify crack trajectories. Crack interactions with inclusions, voids, and interface of inclusions may force the crack to stop, deflect, or bypass inclusions and voids. Distribution of residual stresses and thermal stresses can also alter crack trajectories. The small crack propagates and grows gradually, but at one point it reaches its critical condition where the crack-tip radius, the crack direction, and the local stress distribution become sufficient for the spontaneous crack growth. At that point, instantaneous macroscopic fracture occurs, and the parts fail in a rapid manner.

7.2 Suggestions For Future Work

A straightforward extension of the present work could involve the full fracture model of the more realistic polycrystalline structure containing GBs and inclusions, and residual stresses. The next step should also involve the development of a consistent framework, which incorporates all the codes developed and also provides a user interface to enable the uptake of the simulations tools and their further development. Also, in the DCD method, crack propagation is a discrete process, so the stress fields of the system change sharply at each step. Finding a solution to soften the process of crack propagation would be beneficial to improve the method.

Moreover, the exact determination of temperature variation and associated thermal stresses for elliptical inclusions could be investigated using complex potentials. Also, interactions between inclusion's thermal stresses have not been considered yet. The model presented in this thesis was developed for 2D problems in linear elastic solids. The method could be extended to 3D by changing the constituent elements of the system from ellipses to ellipsoids and accordingly changing the basis functions in series expansions of the complex

potential fields. Dynamic crack growth prediction could be circumvented by deriving elastodynamic solutions for the problem. An elastodynamic BEM solver for the computation of stresses and displacements in the finite domain is already available in [10], so maybe this certainly something that should be pursued to extend the method to solve dynamic problems.

To apply the DCD method to more practical polycrystalline problems and specifically PCDs, inputs of the system such as residual stress distributions, fracture energies, GB energies and crack propagation threshold have to be calculated more accurately by molecular dynamic simulations, or experimental investigations. Crack propagation modes in PCDs depends on the fracture energies at the GBs and other interfaces. A more detailed molecular-scale investigation of interactions at grain boundaries and interfaces between diamond and impurities could bridge the gap between the nano-scale physics and the continuum response.

Also, experimental data shows distinct performance of PCDs produced by Ni and Co binder catalysts [265]. However, macro-scale simulations are not capable of obtaining differences due to the closeness of shear modulus and Poisson's ratios ($\mu_{Ni} = 76 - 82GPa$, $\mu_{Co} = 75GPa$, $\nu_{Ni} = 0.305$, $\nu_{Co} = 0.31$) [266]. Disagreements between Ni and Co catalysts are associated to the chemistry of the problem and can be investigated using molecular dynamic (MD) simulations. Some of the potential issues linked to the use of MD simulations have been preliminarily investigated by the author as reported in Appendix D. Another input of the PCD fracture model is the crack propagation threshold in diamond, which is attributed to the lattice trapping phenomena [267–270]. Crack propagation thresholds can also be obtained using MD simulations [271].

The work would also benefit from additional experimental inputs. For example, fracture properties of individual grains, grain boundaries and interfaces can be obtained experimentally. For example, fracture energy evolution at the micro-scale could be measured using a double cantilever wedging during stable fracture [272]. This work is currently being carried out in another project, although determination of PCD grain boundary strength has proven to be problematic. Also, in-plane residual stress and thermal stress gradient maps at the micro-scale can be measured using the high angular resolution electron backscatter diffraction (EBSD) combined with micro-indentation. This spatial map of stresses can be incorporated into the DCD method to find the effect of residual stresses and thermal stresses on crack propagation path in real microstructures. Figure 7.2 shows typical residual and thermal stress maps of fine and coarse PCD samples.

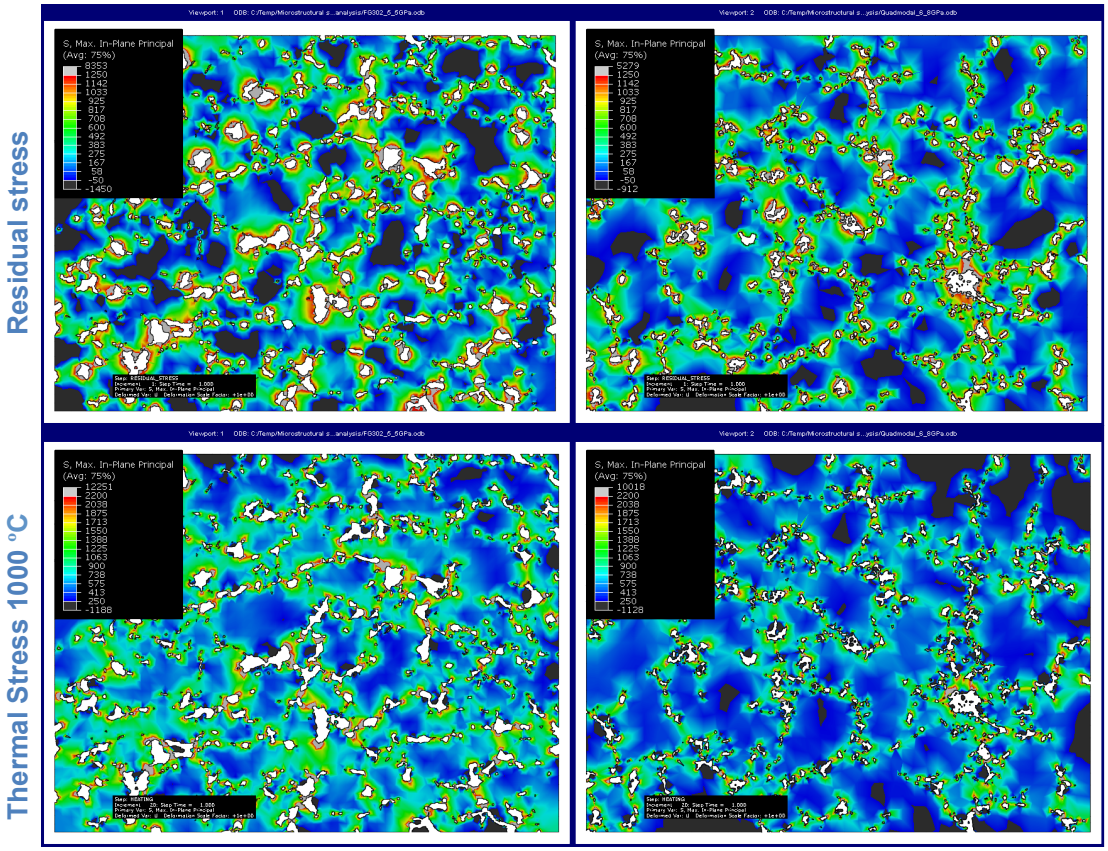


Fig. 7.2 Residual and thermal stresses of fine and coarse unleached PCD samples provided by E6.

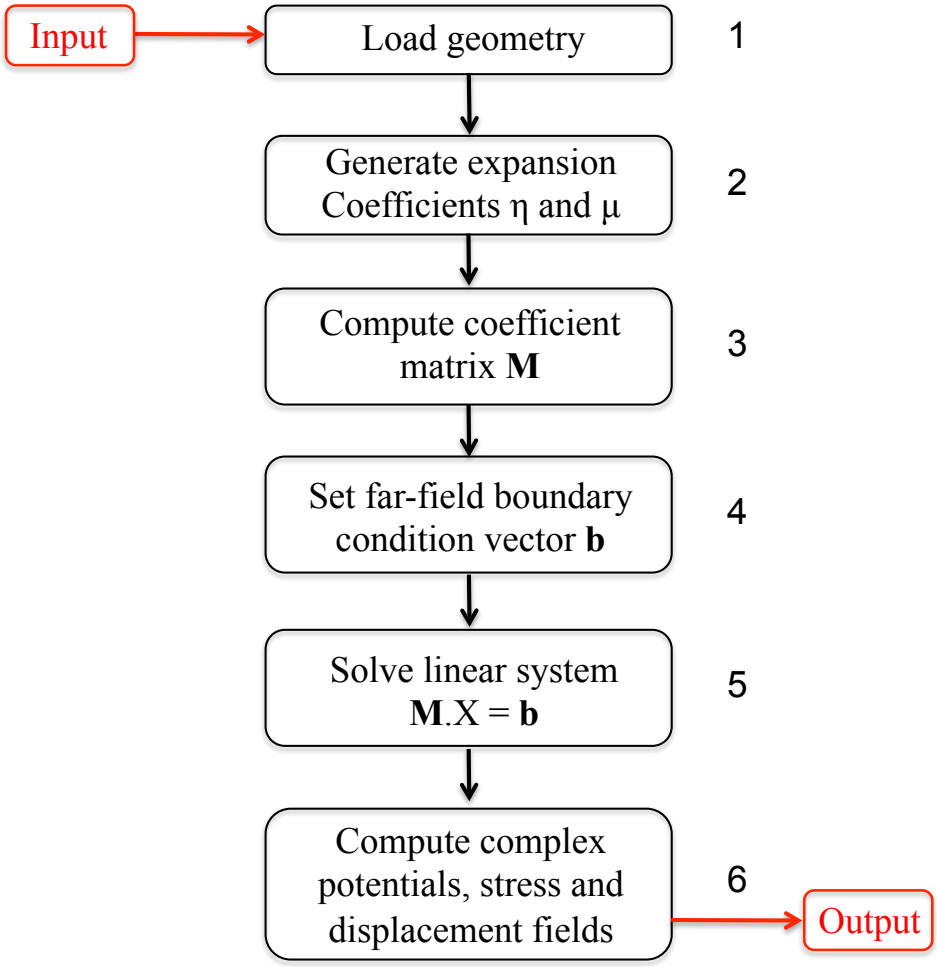


Fig. 7.3 The flow chart of the multipole method displacement and stress fields calculation.

7.3 Summary of Achievements and Algorithms

The achievements of this thesis can be summarised as follows:

- The full stress fields of an unbounded solid containing elliptical inclusions and cracks were calculated using the multipole method according to the algorithm given in Figure 7.3. The method was proposed and developed by Kushch [136] and further developed in this thesis for an arbitrary oriented array of cracks and inclusions.
- Then, the effect of the finite size of the sample studied on stresses and displacements (and, later, on crack propagation) was considered using the linear superposition principle. Here, the complex variable boundary element method was used to study the

complimentary problem of the finite sized body without inclusions. The algorithm is given in Figure 7.4.

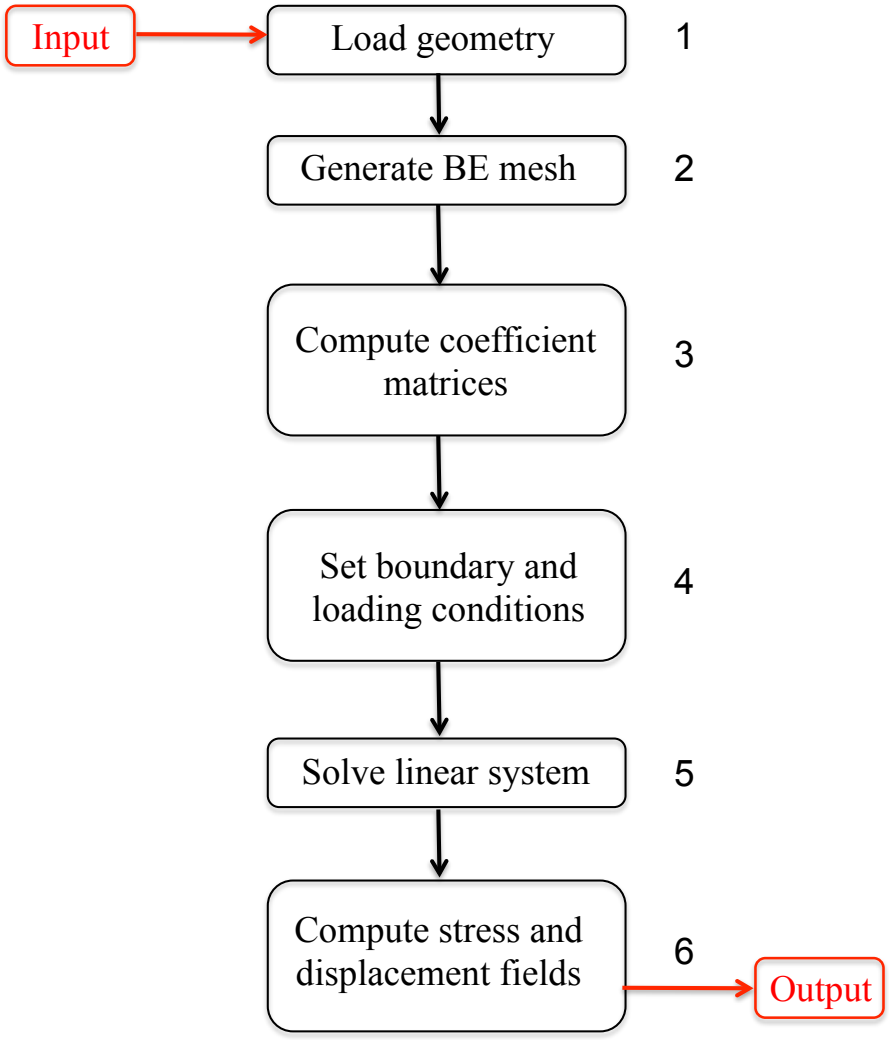


Fig. 7.4 The flow chart of static analysis of CVBEM [10].

- To explicitly model evolution of the individual micro-cracks and their interaction with existing cracks/inclusions a new fracture model was developed; the so called *Discrete Crack Dynamic* (DCD) method using the algorithm given in Figure 7.5 and 7.6.

- *Crack propagation* simulations were successfully performed and tested using numerical solutions and experimental results available from existing benchmark problems.

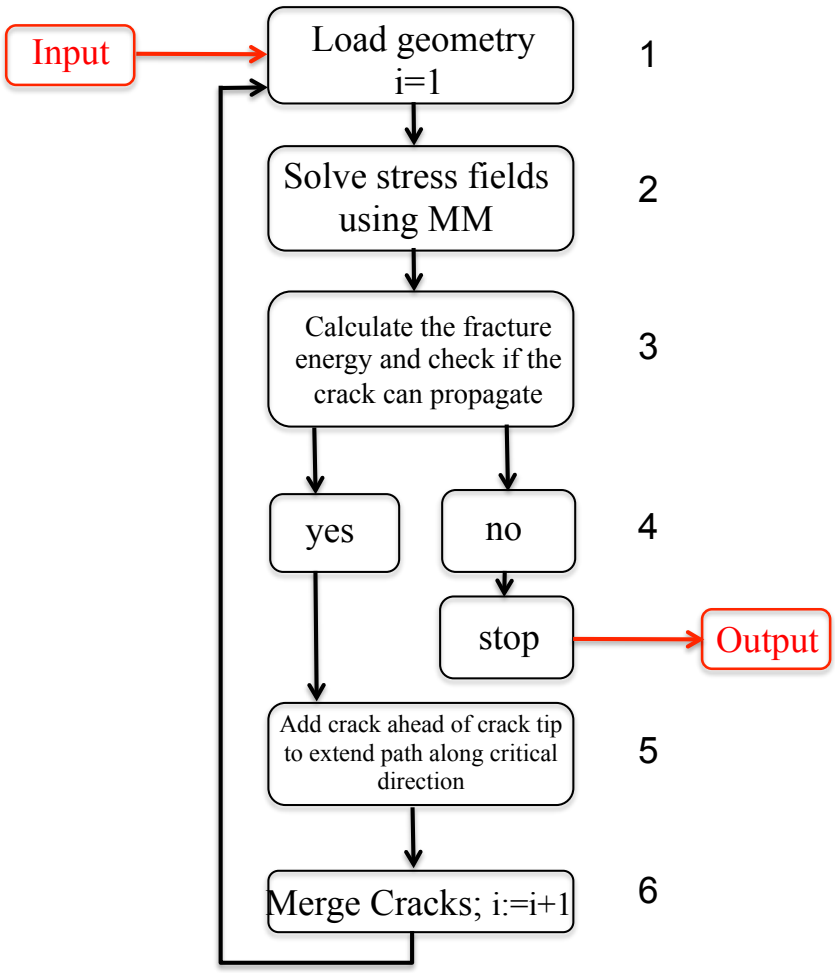


Fig. 7.5 The flow chart of the DCD method to calculate the crack propagation path and its associated energy in the system.

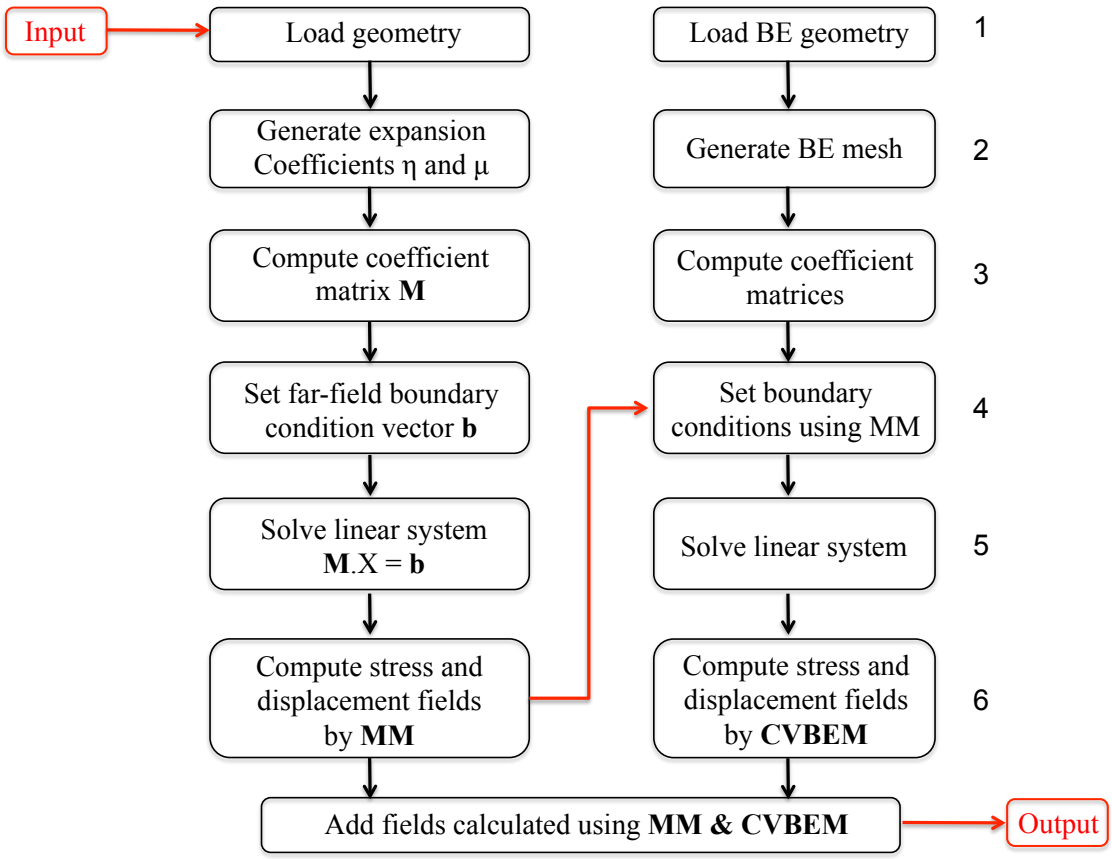


Fig. 7.6 The flow chart of the method used to compute stress and displacement fields in step 2 of the DCD method (Figure 7.5) employed to calculate the crack propagation path and its associated energy in the finite size system.

- The *interface* and *grain boundary* effects were incorporated in the method. Interfaces and grain boundaries were represented explicitly by the fracture energy variation encountered by the crack tip as the crack advances. Results of simulations show how significant changes in interfacial fracture energies can modify the crack propagation path. To add the interfacial effects, positions and energies of the GBs and interfaces were set as inputs in the calculations. When the crack is approaching the interface, a crack propagation criterion based on the maximum of the ratio G/Γ determines the crack propagation direction.

- Finally, *residual* and *thermal stress* effects on crack propagation path were investigated and the effect of second phase soft inclusions with larger thermal expansion coefficient (compared with the matrix material) were studied. Superimposing the residual stress map onto the stress fields of the interacting cracks/inclusions modifies the stress field distributions at the crack-tip and consequently can also change the crack propagation path.

References

[1] F. A. Koch, Tem of standard and some developmental pcd materials., Final DRL/03/D24, Element Six Research Informational Center (Jan 2004).

[2] G. D. Zhan, A. Patin, R. Pillai, R. Gilleylen, M. Castagna, et al., In-situ analysis of the microscopic thermal fracture behavior of pdc cutters using environmental scanning electron microscope, in: IADC/SPE Drilling Conference and Exhibition, Society of Petroleum Engineers, 2014.

[3] S. Natarajan, Enriched finite element methods: advances & applications, Ph.D. thesis, Institute of Mechanics (2011).

[4] M. Kachanov, Elastic solids with many cracks - a simple method of analysis, International Journal of Solids and Structures 23 (1987) 23–43.

[5] Y. Li, L. Tham, Y. Wang, Y. Tsui, A modified kachanov method for analysis of solids with multiple cracks, Engineering Fracture Mechanics 70 (2003) 1115–1129.

[6] A. T. Zehneder, Fracture Mechanics, Vol. 62, Springer, 2012.

[7] T. Willmore, The distribution of stress in the neighbourhood of a crack, Q J Mechanics Appl Math (1949) 53–63.

[8] I. N. Sneddon, M. Lowengrub, crack problems in the classical theory of elasticity, New York ; Chichester : Wiley, 1969.

[9] D. Taylor, Applications of the theory of critical distances to the prediction of brittle fracture in metals and non-metals, in: ECF15, Stockolm 2004, 2013.

[10] A. Zografos, Numerical and experimental investigation of fretting in wheel-hub type bolted joints, Ph.D. thesis, Imperial College London (2011).

[11] H. Haeri, K. Shahriar, M. F. Marji, P. Moarefvand, Cracks coalescence mechanism and cracks propagation paths in rock-like specimens containing pre-existing random cracks under compression, Journal of Central South University 21 (6) (2014) 2404–2414.

[12] C. V. Nielsen, B. N. Legarth, C. F. Niordson, Extended fem modeling of crack paths near inclusions, International Journal for Numerical Methods in Engineering 89 (6) (2012) 786–804.

[13] D. Misseroni, A. Movchan, N. Movchan, D. Bigoni, Experimental and analytical insights on fracture trajectories in brittle materials with voids, International Journal of Solids and Structures 63 (2015) 219–225.

[14] M.-Y. He, J. W. Hutchinson, Kinking of a crack out of an interface, Journal of Applied Mechanics 56 (2) (1989) 270–278.

[15] J. W. Hutchinson, Mixed mode fracture mechanics of interfaces, Metal-ceramic interfaces (1990) 295–306.

[16] J. Cook, J. Gordon, C. Evans, D. Marsh, A mechanism for the control of crack propagation in all-brittle systems, in: Proceedings of the Royal Society of London A: Mathematical, Physical and Engineering Sciences, Vol. 282, The Royal Society, 1964, pp. 508–520.

[17] S. Pompidou, J. Lamon, Analysis of crack deviation in ceramic matrix composites and multilayers based on the cook and gordon mechanism, Composites science and technology 67 (10) (2007) 2052–2060.

[18] K. C. Jajam, H. V. Tippur, Role of inclusion stiffness and interfacial strength on dynamic matrix crack growth: an experimental study, International Journal of Solids and Structures 49 (9) (2012) 1127–1146.

[19] K. Dunn, M. Lee, The fracture and fatigue of sintered diamond compact, Journal of Materials science 14 (4) (1979) 882–890.

[20] A. A. Rubinstein, Macrocrack interaction with semi-infinite microcrack array, International Journal of Fracture 27 (2) (1985) 113–119.

[21] K. K. Lo, Analysis of branched cracks, Journal of Applied Mechanics 45 (4) (1978) 797–802.

[22] Y. Chen, Stress intensity factors for curved and kinked cracks in plane extension, Theoretical and Applied Fracture Mechanics 31 (3) (1999) 223–232.

[23] D. Hills, D. Nowell, Kinked cracks: finding stress intensity factors, in: Applied Stress Analysis, Springer, 1990, pp. 36–50.

[24] A. R. Oganov, R. J. Hemley, R. M. Hazen, A. P. Jones, Structure, bonding, and mineralogy of carbon at extreme conditions, Reviews in Mineralogy & Geochemistry 75 (2013) 47–77.

[25] J. Brookes, The plasticity of diamond, Thesis (June 1992).

[26] J. E. Field, The mechanical and strength properties of diamond., Rep Prog Phys 75 (12) (2012) 126505. doi:10.1088/0034-4885/75/12/126505.

[27] F. Langenhorst, J. Poirier, D. Frost, Tem observations of microscopic inclusions in synthetic diamond, Journal of Materials Science 39 (2004) 1865–1867.

[28] S. Bhagavantam, J. Bhimasenachar, Elastic constants of diamond, Proceedings of the Royal Society of London. Series A, Mathematical and Physical Sciences (1946) 381–384.

[29] V. Chandrasekharan, The influence of optical activity on light scattering in crystals, in: Proceedings of the Indian Academy of Sciences-Section A, Vol. 32, Springer, 1950, pp. 374–378.

[30] M. Grimsditch, A. Ramdas, Brillouin scattering in diamond, Physical Review B 11 (8) (1975) 3139.

[31] R. Krishnan, The scattering of light in diamond and its raman spectrum, in: Proceedings of the Indian Academy of Sciences-Section A, Vol. 26, Springer, 1947, pp. 399–418.

[32] R. Krishnan, V. Chandrasekharan, E. Rajagopal, The four elastic constants of diamond.

[33] H. McSkimin, W. Bond, Elastic moduli of diamond, Physical Review 105 (1) (1957) 116.

[34] H. McSkimin, P. Andreatch Jr, P. Glynn, The elastic stiffness moduli of diamond, Journal of Applied Physics 43 (3) (1972) 985–987.

[35] H. McSkimin, P. Andreatch Jr, Elastic moduli of diamond as a function of pressure and temperature, Journal of Applied Physics 43 (7) (1972) 2944–2948.

[36] R. Vogelgesang, A. Ramdas, S. Rodriguez, M. Grimsditch, T. Anthony, Brillouin and raman scattering in natural and isotopically controlled diamond, Physical Review B 54 (1996) 3989–3999.

[37] M. Eremets, I. Trojan, P. Gwaze, J. Huth, R. Boehler, V. Blank, The strength of diamond, Applied Physics Letters 87 (2005) 141902. doi:DOI10.1063/1.2061853.

[38] A. Neves, M. H. Nazaré, Properties, growth and applications of diamond, no. 26, IET, 2001.

[39] J. Field, C. Freeman, Strength and fracture properties of diamond, Philosophical Magazine A 43 (3) (1981) 595–618.

[40] C. Brookes, V. Howes, A. Parry, Multiple slip in diamond due to a nominal contact pressure of 10 gpa at 1,000 [deg]c, Nature 332 (1988) 139–141.

[41] A. Blumenau, T. Frauenheim, S. Oberg, B. Willems, G. Van Tendeloo, Dislocation structures in diamond: Density-functional based modelling and high-resolution electron microscopy, Defects and Diffusion In Ceramics - an Annual Retrospective Vi 226-228 (2004) 11–30.

[42] R. Z. Khaliullin, H. Eshet, T. D. Kühne, J. Behler, M. Parrinello, Nucleation mechanism for the direct graphite-to-diamond phase transition, Nat Mater 10 (9) (2011) 693–697. doi:10.1038/nmat3078.
URL http://www.hubmed.org/display.cgi?uids=21785417

[43] A. G. G. C. A. C. R. de Vita, A microscopic model for surface-induced diamond-to-graphite transitions, Nature 379 (1996) 523–526.

[44] P. Xiao, G. Henkelman, Communication: From graphite to diamond: reaction pathways of the phase transition, J Chem Phys 137 (10) (2012) 101101–101101. doi:10.1063/1.4752249.
URL http://www.hubmed.org/display.cgi?uids=22979841

[45] I. Suarez-Martinez, G. Savini, G. Haffenden, J.-M. Campanera, M. Heggie, Dislocations of burgers vector c /2 in graphite, Phys. Status Solidi C 4 (2007) 2958–2962.

[46] M. De La Pierre, M. Bruno, C. Manfredotti, F. Nestola, M. Prencipe, C. Manfredotti, The (100),(111) and (110) surfaces of diamond: an ab initio b3lyp study, Molecular Physics 112 (7) (2014) 1030–1039.

[47] S. Ramaseshan, The cleavage properties of diamond, in: Proceedings of the Indian Academy of Sciences-Section A, Vol. 24, Springer, 1946, pp. 114–121.

[48] M. F. Calitz, Mthematical sintering model, numerical and mathematical modelling of PCD Sintering (April 2001).

[49] D. Fedoseev, G. Sokolina, E. Yakovlev, A. Lavrent'ev, O. Lazareva, L. Afanas' eva, Porosity changes in the sintering of diamond powders, Soviet Powder Metallurgy and Metal Ceramics 23 (9) (1984) 683–686.

[50] H. T. Hall, Sintered diamond: A synthetic carbonado, Science 169 (3948) (1970) 868–869.

[51] S. HD, D. Stephens, Sintering of diamond at 1800 degrees-1900 degrees c and 60-65 kbar, AMERICAN CERAMIC SOCIETY BULLETIN 49 (12) (1970) 1030.

[52] I. Sigalas, R. Caveney, M. Bailey, Diamond materials and their applications, Handbook of ceramic hard materials (1833) 478–572.

[53] S. Ozbayraktar, Literature survey on pcd sintering, pCD Sintering (October 1997).

[54] D. Jianxin, Z. Hui, W. Ze, L. Aihua, Friction and wear behavior of polycrystalline diamond at temperatures up to 700 c, International Journal of Refractory Metals and Hard Materials 29 (5) (2011) 631–638.

[55] R. Komanduri, M. Shaw, Wear of synthetic diamond when grinding ferrous metals, Nature 255 (1975) 211–213.

[56] M. K. Keshavan, Y. Zhang, Y. Shen, A. Griffo, M. Janssen, Polycrystalline diamond materials having improved abrasion resistance, thermal stability and impact resistance, uS Patent 7,493,973 (Feb. 24 2009).

[57] Y. Z. L. Chen, Polishing of Diamond Materials, Mechanisms, Modeling and Implementation, no. ISBN 978-1-84996-408-1, Springer, 2013.

[58] M. Yahiaoui, L. Gerbaud, J.-Y. Paris, J. Denape, A. Dourfaye, A study on pcd drill bits quality, Wear 298–299 (0) (2013) 32–41. doi:http://dx.doi.org/10.1016/j.wear.2012.12.026.
URL http://www.sciencedirect.com/science/article/pii/S0043164812004541

[59] K. Faber, A. Evans, Crack deflection processes—i. theory, Acta Metallurgica 31 (4) (1983) 565–576.

[60] M. Mirkhalaf, A. K. Dastjerdi, F. Barthelat, Overcoming the brittleness of glass through bio-inspiration and micro-architecture, Nature communications 5.

[61] G. Noselli, V. S. Deshpande, N. A. Fleck, An analysis of competing toughening mechanisms in layered and particulate solids, International Journal of Fracture 183 (2) (2013) 241–258.

[62] C. E. Inglis, Stresses in a plate due to the presence of cracks and sharp corners, Spie Milestone series MS 137 (1997) 3–17.

[63] A. A. Griffith, The phenomena of rupture and flow in solids, Philosophical transactions of the royal society of london. Series A, containing papers of a mathematical or physical character 221 (1921) 163–198.

[64] G. R. Irwin, Analysis of stresses and strains near the end of a crack traversing a plate, Spie Milestone series MS 137 (167-170) (1997) 16.

[65] H. Westergaard, Bearing pressures and cracks, SPIE MILESTONE SERIES MS 137 (1997) 18–22.

[66] G. P. Cherepanov, Mechanics of Brittle Fracture, Mcgraw-Hill, 1979.

[67] A. T. Zehnder, Lecture notes on fracture mechanics, Available for public use at Cornell University website http://ecommons. library. cornell. edu/bitstream/1813/3075/6/fracture_notes_2008. pdf.

[68] E. Gdoutos, Fracture mechanics criteria and applications, Vol. 10, Springer Science & Business Media, 2012.

[69] F. Erdogan, G. Sih, On the crack extension in plates under plane loading and transverse shear, Fluids Eng. 85 (1963) 519–125.

[70] G. C. Sih, Strain-energy-density factor applied to mixed mode crack problems, International Journal of fracture 10 (3) (1974) 305–321.

[71] G. Sih, A special theory of crack propagation, Mechanics of fracture initiation and propagation (1991) 1–22.

[72] D. Smith, M. Ayatollahi, M. Pavier, The role of t-stress in brittle fracture for linear elastic materials under mixed-mode loading, Fatigue & Fracture of Engineering Materials & Structures 24 (2) (2001) 137–150.

[73] D. Smith, M. Ayatollahi, M. Pavier, On the consequences of t-stress in elastic brittle fracture, in: Proceedings of the Royal Society of London A: Mathematical, Physical and Engineering Sciences, Vol. 462, The Royal Society, 2006, pp. 2415–2437.

[74] K. Palaniswamy, Crack propagation under general in-plane loading, Ph.D. thesis, California Institute of Technology (June 1971).

[75] K. Palaniswamy, W. Knauss, Propagation of a crack under general, in-plane tension, International Journal of Fracture Mechanics 8 (1) (1972) 114–117.

[76] M. Hussain, S. Pu, J. Underwood, Strain energy release rate for a crack under combined mode i and mode ii, in: Fracture Analysis, ASTM STP 560, American Society for Testing and Materials, 1973, pp. 2–28.

[77] J. Chang, J.-q. Xu, Y. Mutoh, A general mixed-mode brittle fracture criterion for cracked materials, Engineering Fracture Mechanics 73 (9) (2006) 1249–1263.

[78] S. Patankar, Numerical heat transfer and fluid flow, CRC press, 1980.

[79] G. Strang, G. J. Fix, An analysis of the finite element method, Vol. 212, Prentice-Hall Englewood Cliffs, NJ, 1973.

[80] O. C. Zienkiewicz, R. L. Taylor, O. C. Zienkiewicz, R. L. Taylor, The finite element method, Vol. 3, McGraw-hill London, 1977.

[81] J. N. Reddy, An introduction to the finite element method, Vol. 2, McGraw-Hill New York, 1993.

[82] S. Li, W. K. Liu, Meshfree particle methods, Springer Science & Business Media, 2007.

[83] S. G. Mogilevskaya, A. Linkov, Complex fundamental solutions and complex variables boundary element method in elasticity, Computational mechanics 22 (1) (1998) 88–92.

[84] A. Munjiza, The combined finite-discrete element method, Wiley Online Library, 2004.

[85] T. Belytschko, T. Black, Elastic crack growth in finite elements with minimal remeshing, International journal for numerical methods in engineering 45 (5) (1999) 601–620.

[86] I. Babuška, U. Banerjee, Stable generalized finite element method (sgfem), Computer Methods in Applied Mechanics and Engineering 201 (2012) 91–111.

[87] I. Babuška, G. Caloz, J. E. Osborn, Special finite element methods for a class of second order elliptic problems with rough coefficients, SIAM Journal on Numerical Analysis 31 (4) (1994) 945–981.

[88] I. Babuška, U. Banerjee, J. E. Osborn, Meshless and generalized finite element methods: a survey of some major results, in: Meshfree methods for partial differential equations, Springer, 2003, pp. 1–20.

[89] T. Belytschko, N. Moës, S. Usui, C. Parimi, Arbitrary discontinuities in finite elements, International Journal for Numerical Methods in Engineering 50 (4) (2001) 993–1013.

[90] T.-P. Fries, T. Belytschko, The extended/generalized finite element method: an overview of the method and its applications, International Journal for Numerical Methods in Engineering 84 (3) (2010) 253–304.

[91] P. Laborde, J. Pommier, Y. Renard, M. Salaün, High-order extended finite element method for cracked domains, International Journal for Numerical Methods in Engineering 64 (3) (2005) 354–381.

[92] J. Dolbow, T. Belytschko, A finite element method for crack growth without remeshing, International journal for numerical methods in engineering 46 (1) (1999) 131–150.

[93] T. Belytschko, R. Gracie, G. Ventura, A review of extended/generalized finite element methods for material modeling, Modelling and Simulation in Materials Science and Engineering 17 (4) (2009) 043001.

[94] S. Bordas, P. V. Nguyen, C. Dunant, A. Guidoum, H. Nguyen-Dang, An extended finite element library, International Journal for Numerical Methods in Engineering 71 (6) (2007) 703–732.

[95] G. Ventura, On the elimination of quadrature subcells for discontinuous functions in the extended finite-element method, International Journal for Numerical Methods in Engineering 66 (5) (2006) 761–795.

[96] Q. Xiao, B. Karihaloo, Improving the accuracy of xfem crack tip fields using higher order quadrature and statically admissible stress recovery, International Journal for Numerical Methods in Engineering 66 (9) (2006) 1378–1410.

[97] K. Park, J. P. Pereira, C. A. Duarte, G. H. Paulino, Integration of singular enrichment functions in the generalized/extended finite element method for three-dimensional problems, International Journal for Numerical Methods in Engineering 78 (10) (2009) 1220–1257.

[98] M. H. Aliabadi, D. Rooke, The boundary element method, Numerical Fracture Mechanics (1991) 90–139.

[99] A. A. Becker, The boundary element method in engineering: a complete course, McGraw-Hill Companies, 1992.

[100] M. Bush, The interaction between a crack and a particle cluster, International Journal of Fracture 88 (3) (1997) 215–232.

[101] C. Wang, W. Libardi, J. Baldo, Analysis of crack extension paths and toughening in a two phase brittle particulate composite by the boundary element method, International journal of fracture 94 (2) (1998) 177–188.

[102] M. Knight, L. Wrobel, J. Henshall, L. De Lacerda, A study of the interaction between a propagating crack and an uncoated/coated elastic inclusion using the be technique, International Journal of Fracture 114 (1) (2002) 47–61.

[103] R. Kitey, A.-V. Phan, H. Tippur, T. Kaplan, Modeling of crack growth through particulate clusters in brittle matrix by symmetric-galerkin boundary element method, International Journal of Fracture 141 (1-2) (2006) 11–25.

[104] R. Williams, A.-V. Phan, H. Tippur, T. Kaplan, L. Gray, Sgbem analysis of crack–particle (s) interactions due to elastic constants mismatch, Engineering fracture mechanics 74 (3) (2007) 314–331.

[105] J. Lei, Q. Yang, Y.-S. Wang, C. Zhang, An investigation of dynamic interaction between multiple cracks and inclusions by tdbem, Composites Science and Technology 69 (7) (2009) 1279–1285.

[106] G. Liu, Y. Gu, An introduction to meshfree methods and their programming. 2005, Springer Berlin. MEMS, NANO and Smart Systems 10 403–408.

[107] J. Dolbow, T. Belytschko, An introduction to programming the meshless element f reegalerkin method, Archives of computational methods in engineering 5 (3) (1998) 207–241.

[108] B. Rao, S. Rahman, An efficient meshless method for fracture analysis of cracks, Computational mechanics 26 (4) (2000) 398–408.

[109] T. Rabczuk, T. Belytschko, Cracking particles: a simplified meshfree method for arbitrary evolving cracks, International Journal for Numerical Methods in Engineering 61 (13) (2004) 2316–2343.

[110] M. Duflot, H. Nguyen-Dang, Fatigue crack growth analysis by an enriched meshless method, Journal of Computational and Applied Mathematics 168 (1) (2004) 155–164.

[111] T. Rabczuk, S. Bordas, G. Zi, A three-dimensional meshfree method for continuous multiple-crack initiation, propagation and junction in statics and dynamics, Computational Mechanics 40 (3) (2007) 473–495.

[112] E. Barbieri, N. Petrinic, M. Meo, V. Tagarielli, A new weight-function enrichment in meshless methods for multiple cracks in linear elasticity, International Journal for Numerical Methods in Engineering 90 (2) (2012) 177–195.

[113] E. Barbier, N. Petrinic, Multiple crack growth and coalescence in meshfree methods with adistance function-based enriched kernel, in: Key Engineering Materials, Vol. 560, Trans Tech Publ, 2013, pp. 37–60.

[114] E. Barbieri, N. Petrinic, Three-dimensional crack propagation with distance-based discontinuous kernels in meshfree methods, Computational Mechanics 53 (2) (2014) 325–342.

[115] M. Kachanov, A simple technique of stress-analysis in elastic solids with many cracks, International Journal of Fracture 28 (1985) R11–R19.

[116] M. Chudnovsky, A. Kachanov, Interaction of a crack with a field of microcracks, International Journal of Engineering Science 21 (1983) 1009–1018.

[117] M. Kachanov, Elastic solids with many cracks and related problems, Academic Press/Elsevier, 1993, Ch. one.

[118] M. Kachanov, E. Montagut, J. Laures, Mechanics of crack-microcrack interactions, Mechanics of Materials 10 (1990) 59–71.

[119] M. Kachanov, E. Montagut, Interaction of a crack with certain microcrack arrays, Engineering Fracture Mechanics 25 (1986) 625–636.

[120] M. Kachanov, On crack - microcrack interactions, International Journal of Fracture 30 (1986) R65–R72.

[121] I. Sevostianov, M. Kachanov, Local minima and gradients of stiffness and conductivity as indicators of strength reduction of brittle-elastic materials, International Journal of Fracture 164 (2010) 147–154. doi:DOI10.1007/s10704-010-9485-6.

[122] M. Kachanov, Effective elastic properties of cracked solids: Critical review of some basic concepts, Appl. Mech. Rev. 45 (1992) 304–335.

[123] I. Sevostianov, M. Kachanov, On some controversial issues in effective field approaches to the problem of the overall elastic properties, Mechanics of Materials 69 (2014) 93–105.

[124] M. Kachanov, On the problems of crack interactions and crack coalescence, International Journal of Fracture 120 (2003) 537–543.

[125] X.-Q. Feng, J.-Y. Li, S.-W. Yu, A simple method for calculating interaction of numerous microcracks and its applications, International Journal of Solids and Structures 40 (2003) 447–464.

[126] L. Ma, X. Wang, X.-Q. Feng, S.-W. Yu, Numerical analysis of interaction and coalescence of numerous microcracks, Engineering Fracture Mechanics 72 (2005) 1841–1865.

[127] X.-Q. Feng, S.-W. Yu, Damage micromechanics for constitutive relations and failure of microcracked quasi-brittle materials, International Journal of Damage Mechanics 19.

[128] L. Gorbatikh, S. Lomov, I. Verpoest, On stress intensity factors of multiple cracks at small distances in 2-d problems, International Journal of Fracture 143 (2007) 377–384. doi:DOI10.1007/s10704-007-9070-9.

[129] H. Horii, S. Nemat-Nasser, Elastic fields of interacting inhomogeneities, International Journal of Solids and Structures 21 (1985) 731–745.

[130] J. C. Maxwell, A Treatise on Electricity and Magnetism, Dover Publications, 1881.

[131] L. N. McCartney, A. Kelly, Maxwell's far-field methodology applied to the prediction of properties of multi-phase isotropic particulate composites, Proceedings of the Royal Society A-Mathematical Physical and Engineering Sciences 464 (2008) 423–446.

[132] L. N. McCartney, Maxwell's far-field methodology predicting elastic properties of multiphase composites reinforced with aligned transversely isotropic spheroids, Philosophical Magazine 90 (2010) 4175–4207. doi:DOI10.1080/14786431003752142.

[133] S. G. Mogilevskaya, S. L. Crouch, Combining maxwell's methodology with the bem for evaluating the two-dimensional effective properties of composite and microcracked materials, Computational Mechanics 51 (2013) 377–389.

[134] S. G. Mogilevskaya, S. L. Crouch, H. K. Stolarski, A. Benusiglio, Equivalent inhomogeneity method for evaluating the effective elastic properties of unidirectional multi-phase composites with surface/interface effects, International Journal of Solids and Structures 47 (2010) 407–418. doi:DOI10.1016/j.ijsolstr.2009.10.007.

[135] V. Kushch, Effective properties of heterogeneous materials, Vol. 193 of Solid Mechanics and Its Applications, Springer, 2013, Ch. Multipole Expansion Method in Micromechanics of Composites, pp. 97–197.

[136] V. Kushch, Micromechanics of composites multipole expansion approach, Burlington : Elsevier Science, 2013.

[137] V. Kushch, Elastic equilibrium of a medium containing a finite number of arbitrarily oriented spheroidal inclusions, International Journal of Solids and Structures 35 (1998) 1187–1198.

[138] V. Kushch, Interacting cracks and inclusions in a solid by multipole expansion method, International Journal of Solids and Structures 35 (1998) 1751–1762.

[139] V. Kushch, A. Sangani, Stress intensity factor and effective stiffness of a solid containing aligned penny-shaped cracks, International Journal of Solids and Structures 37 (2000) 6555–6570.

[140] V. Kushch, S. Shmegera, V. Buryachenko, Interacting elliptic inclusions by the method of complex potentials, International Journal of Solids and Structures 42 (2005) 5491–5512.

[141] S. Benzley, Representation of singularities with isoparametric finite elements, International Journal for Numerical Methods in Engineering 8 (3) (1974) 537–545.

[142] J. Dolbow, N. Moës, T. Belytschko, Discontinuous enrichment in finite elements with a partition of unity method, Finite elements in analysis and design 36 (3) (2000) 235–260.

[143] G. Wells, R. De Borst, L. Sluys, A consistent geometrically non-linear approach for delamination, International Journal for Numerical Methods in Engineering 54 (9) (2002) 1333–1355.

[144] J. Remmers, R. de Borst, A. Needleman, A cohesive segments method for the simulation of crack growth, Computational mechanics 31 (1-2) (2003) 69–77.

[145] E. M. Patton, Crack path prediction near an elliptical inhomogeneity, Tech. rep., DTIC Document (1991).

[146] B. J. Alder, T. Wainwright, Studies in molecular dynamics. i. general method, The Journal of Chemical Physics 31 (2) (1959) 459–466.

[147] H. Cleveringa, E. Van der Giessen, A. Needleman, Comparison of discrete dislocation and continuum plasticity predictions for a composite material, Acta Materialia 45 (8) (1997) 3163–3179.

[148] E. Van der Giessen, A. Needleman, Discrete dislocation plasticity: a simple planar model, Modelling and Simulation in Materials Science and Engineering 3 (5) (1995) 689.

[149] Mathematica, Multipole expansion (2014).
URL http://scienceworld.wolfram.com/physics/MultipoleExpansion

[150] V. Kushch, S. Shmegera, L. Mishnaevsky, Meso cell model of fiber reinforced composite: Interface stress statistics and debonding paths, International Journal of Solids and Structures 45 (2008) 2758–2784.

[151] N. I. Muskhelishvili, Some basic problems of the mathematical theory of elasticity, Springer, 1954.

[152] J. Yardley, A. Reuben, R. McPhedran, The transport properties of layers of elliptical cylinders, Proceedings of the Royal Society A-Mathematical Physical and Engineering Sciences.

[153] J. Yardley, R. McPhedran, N. Nicorovici, L. Botten, Addition formulas and the rayleigh identity for arrays of elliptical cylinders, Phys. Rev. E 60 (5).

[154] V. Panasyuk, E. Buina, Critical stress diagrams for brittle materials with defects of the cusped void/crack type, Soviet materials science: a transl. of Fiziko-khimicheskaya mekhanika materialov/Academy of Sciences of the Ukrainian SSR 3 (5) (1968) 427–432.

[155] L. Berezhnitskii, Propagation of cracks terminating at the edge of a curvilinear hole in a plate, Materials Science 2 (1) (1967) 16–23.

[156] V. Panasyuk, L. Berezhnitskii, Limit equilibrium of plates with sharp stress raisers, Materials Science 1 (4) (1966) 293–301.

[157] A. Carpinteri, A. R. Ingraffea, Fracture mechanics of concrete: Material characterization and testing: Material Characterization and Testing, Vol. 3, Springer Science and Business Media, 2012.

[158] R. G. Hoagland, G. T. Hahn, A. R. Rosenfield, Influence of microstructure on fracture propagation in rock, Rock Mechanics 5 (2) (1973) 77–106.

[159] Z. Li, S. P. Shah, Localization of microcracking in concrete under uniaxial tension, Materials Journal 91 (4) (1994) 372–381.

[160] M. Ortiz, Microcrack coalescence and macroscopic crack growth initiation in brittle solids, International Journal of Solids and Structures 24 (3) (1988) 231–250.

[161] W. Pompe, H. A. Bahr, G. Gille, W. Kreher, Increased fracture toughness of brittle materials by microcracking in an energy dissipative zone at the crack tip, Journal of Materials Science 13 (12) (1978) 2720–2723.

[162] C. C. Wu, S. Freiman, R. Rice, J. Mecholsky, Microstructural aspects of crack propagation in ceramics, Journal of Materials Science 13 (12) (1978) 2659–2670.

[163] Z. Zhang, J. Eckert, Unified tensile fracture criterion, Phys. Rev. Lett 94 (2005) 094301.

[164] S. Wei, J. D. Lee, The nonlinear energy method for mixed mode fracture, Engineering Fracture Mechanics 16 (6) (1982) 783–798.

[165] M. Williams, On the stress distribution at the base of a stationary crack, Journal of applied Mechanics 24 (1957) 109–114.

[166] M. R. Ayatollahi, M. R. M. Aliha, Fracture analysis of some ceramics under mixed mode loading, Journal of the American Ceramic Society 94 (2) (2011) 561–569.

[167] M. Mirsayar, A modified maximum tangential stress criterion for determination of the fracture toughness in bi-material notches–part 1: Theory, Engineering Solid Mechanics 2 (4) (2014) 277–282.

[168] H. Ming-Yuan, J. W. Hutchinson, Crack deflection at an interface between dissimilar elastic materials, International Journal of Solids and Structures 25 (9) (1989) 1053 – 1067. doi:http://dx.doi.org/10.1016/0020-7683(89)90021-8.

[169] D. Nowell, D. Dini, Stress gradient effects in fretting fatigue, Tribology international 36 (2) (2003) 71–78.

[170] D. Dini, D. A. Hills, Asymptotic characterisation of nearly-sharp notch root stress fields, International journal of fracture 130 (3) (2004) 651–666.

[171] D. Dini, D. A. Hills, The effect of a crack-tip radius on the validity of the singular solution, Proceedings of the Institution of Mechanical Engineers, Part C: Journal of Mechanical Engineering Science 218 (7) (2004) 693–701.

[172] D. Dini, D. Nowell, I. N. Dyson, The use of notch and short crack approaches to fretting fatigue threshold prediction: Theory and experimental validation, Tribology international 39 (10) (2006) 1158–1165.

[173] P. Cornetti, N. Pugno, A. Carpinteri, D. Taylor, Finite fracture mechanics: A coupled stress and energy failure criterion, Engineering Fracture Mechanics 73 (14) (2006) 2021 – 2033. doi:http://dx.doi.org/10.1016/j.engfracmech.2006.03.010.

[174] D. Taylor, P. Cornetti, N. Pugno, The fracture mechanics of finite crack extension, Engineering Fracture Mechanics 72 (7) (2005) 1021 – 1038. doi:http://dx.doi.org/10.1016/j.engfracmech.2004.07.001.

[175] R. E. Peterson, Notch sensitivity, Metal fatigue (1959) 293–306.

[176] H. Neuber, J. Brock, D. W. T. M. Basin, Theory of Notch Stresses: Principles for Exact Stress Calculation, Translation, J. W. Edwards, 1946.
URL http://books.google.co.uk/books?id=y2c0AAAAMAAJ

[177] M. El Haddad, N. Dowling, T. Topper, K. Smith, J integral applications for short fatigue cracks at notches 16 (1) (1980) 15–30. doi:10.1007/BF00042383.

[178] D. S. Dugdale, Yielding of steel sheets containing slits, Journal of the Mechanics and Physics of Solids 8 (2) (1960) 100–104.

[179] G. I. Barenblatt, The mathematical theory of equilibrium cracks in brittle fracture, Advances in applied mechanics 7 (1962) 55–129.

[180] A. Needleman, A continuum model for void nucleation by inclusion debonding, Journal of applied mechanics 54 (3) (1987) 525–531.

[181] A. Needleman, An analysis of tensile decohesion along an interface, Journal of the Mechanics and Physics of Solids 38 (3) (1990) 289–324.

[182] V. Tvergaard, J. W. Hutchinson, The relation between crack growth resistance and fracture process parameters in elastic-plastic solids, Journal of the Mechanics and Physics of Solids 40 (6) (1992) 1377–1397.

[183] A. Carpinteri, Handbook of fatigue crack propagation in metallic structures, Newnes, 2012.

[184] D. Eberly, Distance from a point to an ellipse in 2d, Magic Software.

[185] V. Kushch, I. Sevostianov, Effective elastic moduli of a particulate composite in terms of the dipole moments and property contribution tensors, International Journal of Solids and Structures 53 (2015) 1–11.

[186] V. I. Kushch, I. Sevostianov, The "rigorous" maxwell homogenization scheme in 2d elasticity: Effective stiffness tensor of composite with elliptic inhomogeneities, Mechanics of Materials 103 (2016) 44–54.

[187] J. D. Eshelby, The determination of the elastic field of an ellipsoidal inclusion, and related problems, in: Proceedings of the Royal Society of London A: Mathematical, Physical and Engineering Sciences, Vol. 241, The Royal Society, 1957, pp. 376–396.

[188] T. Mura, Micromechanics of defects in solids, Springer Science & Business Media, 2013.

[189] L. Berezhnitskii, V. Panasyuk, R. Arone, Interaction of collinear cracks, Soviet Materials Science 7 (2) (1973) 189–191.

[190] A. Mehdi-Soozani, I. Miskioglu, C. Burger, T. Rudolphi, Stress intensity factors for interacting cracks, Engineering fracture mechanics 27 (3) (1987) 345–359.

[191] W. Peng, J.-C. Sung, Interactions of two arbitrarily oriented cracks in a homogeneous anisotropic medium, Applied Mathematical Modelling 27 (9) (2003) 701 – 715. doi:http://dx.doi.org/10.1016/S0307-904X(03)00076-3.

[192] E. Gdoutos, Problems of mixed mode crack propagation, Vol. 2, Springer Science & Business Media, 2012.

[193] A. Chudnovsky, A. Dolgopolsky, M. Kachanov, Elastic interaction of a crack with micro cracks, in: ICF6, New Delhi (India) 1984, 1984.

[194] J. W. Hutchinson, Crack tip shielding by micro-cracking in brittle solids, Acta metallurgica 35 (7) (1987) 1605–1619.

[195] D. K. Shum, J. W. Hutchinson, On toughening by microcracks, Mechanics of Materials 9 (2) (1990) 83–91.

[196] B. Bilby, G. Cardew, The crack with a kinked tip, International Journal of Fracture 11 (4) (1975) 708–712.

[197] B. Cotterell, J. Rice, Some remarks on elastic crack-tip stress fields, Int. J. Fract 16 (1980) 155–169.

[198] S. Suresh, Crack deflection: implications for the growth of long and short fatigue cracks, Metallurgical Transactions A 14 (11) (1983) 2375–2385.

[199] H. Kitagawa, R. Yuuki, T. Ohira, Crack-morphological aspects in fracture mechanics, Engineering Fracture Mechanics 7 (3) (1975) 515–529.

[200] S. Bechtle, T. Fett, G. Rizzi, S. Habelitz, G. A. Schneider, Mixed-mode stress intensity factors for kink cracks with finite kink length loaded in tension and bending: application to dentin and enamel, Journal of the mechanical behavior of biomedical materials 3 (4) (2010) 303–312.

[201] A. Zografos, D. Dini, A combined bem/contact asymptotics (bem-ca) semi-analytical formulation for the assessment of fretting damage in bolted joints, Procedia Engineering 1 (1) (2009) 201–204.

[202] R. Fenner, Force field superposition analysis of three-dimensional stress concentrations, Journal of strain analysis for engineering design 37 (5) (2002) 445–457.

[203] M. Patrıcio, R. Mattheij, Crack propagation analysis, CASA report (2007) 07–03.

[204] M. Meggiolaro, A. Miranda, J. Castro, L. Martha, Stress intensity factor equations for branched crack growth, Engineering fracture mechanics 72 (17) (2005) 2647–2671.

[205] H. Horii, S. Nemat-Nasser, Brittle failure in compression: splitting, faulting and brittle-ductile transition, Philosophical Transactions of the Royal Society of London A: Mathematical, Physical and Engineering Sciences 319 (1549) (1986) 337–374.

[206] S. Nemat-Nasser, H. Horii, Compression-induced nonplanar crack extension with application to splitting, exfoliation, and rockburst, Journal of Geophysical Research: Solid Earth (1978–2012) 87 (B8) (1982) 6805–6821.

[207] P.-O. Bouchard, Damage and discrete crack propagation modelling: Some results and challenges for 2d and 3d configurations, in: ICF11-International Conference on Fracture, 2005, pp. 6–pages.

[208] E. Patton, M. Santare, Crack path prediction near an elliptical inclusion, Engineering fracture mechanics 44 (2) (1993) 195–205.

[209] O. Buyukozturk, Interface fracture and crack propagation in concrete composites, in: Micromechanics of Concrete and Cementitious Composites, Presses Polytechniques et Universitaires Romandes Lausanne, 1993, pp. 203–212.

[210] J. Dundurs, Effect of elastic constants on stress in a composite under plane deformation, Journal of Composite Materials 1 (3) (1967) 310–322.

[211] F. Erdogan, G. Sih, On the crack extension in plates under plane loading and transverse shear, Journal of Fluids Engineering 85 (4) (1963) 519–525.
URL http://dx.doi.org/10.1115/1.3656897

[212] J. Rice, G. C. Sih, Plane problems of cracks in dissimilar media, Journal of Applied Mechanics 32 (2) (1965) 418–423.
URL http://dx.doi.org/10.1115/1.3625816

[213] J. R. Rice, Limitations to the small scale yielding approximation for crack tip plasticity, Journal of the Mechanics and Physics of Solids 22 (1) (1974) 17–26.

[214] Y. Zhou, Z. Yang, Z. Lu, Dynamic crack propagation in copper bicrystals grain boundary by atomistic simulation, Materials Science and Engineering: A 599 (2014) 116–124.

[215] Y. Chen, S. Pan, M. Zhou, D. Yi, D. Xu, Y. Xu, Effects of inclusions, grain boundaries and grain orientations on the fatigue crack initiation and propagation behavior of 2524-t3 al alloy, Materials Science and Engineering: A 580 (2013) 150–158.

[216] C. Holzapfel, W. Schäf, M. Marx, H. Vehoff, F. Mücklich, Interaction of cracks with precipitates and grain boundaries: Understanding crack growth mechanisms through focused ion beam tomography, Scripta Materialia 56 (8) (2007) 697–700.

[217] Y. Li, Z. Ou, Z. Duan, F. Huang, Interaction between matrix crack and elliptic inclusion under dynamic loadings, Journal of Theoretical and Applied Mechanics 51.

[218] K. Jajam, H. Tippur, An experimental investigation of dynamic crack growth past a stiff inclusion, Engineering Fracture Mechanics 78 (6) (2011) 1289–1305.

[219] G. S. Rohrer, "introduction to grains, phases, and interfaces—an interpretation of microstructure," trans. aime, 1948, vol. 175, pp. 15–51, by cs smith, Metallurgical and Materials Transactions B 41 (3) (2010) 457–494.

[220] C. Dahlgren, T. Sunqvist, Phagocytosis and hydrophobicity: a method of calculating contact angles based on the diameter of sessile drops, Journal of immunological methods 40 (2) (1981) 171–179.

[221] J. Boselli, P. Pitcher, P. Gregson, I. Sinclair, Numerical modelling of particle distribution effects on fatigue in al–sic p composites, Materials Science and Engineering: A 300 (1) (2001) 113–124.

[222] A. Ayyar, N. Chawla, Microstructure-based modeling of crack growth in particle reinforced composites, Composites Science and technology 66 (13) (2006) 1980–1994.

[223] R. Li, S. Wu, E. Ivanova, A. Chudnovsky, K. Sehanobish, C. Bosnyak, Finite element model and experimental analysis of crack–inclusion interaction, Journal of applied polymer science 50 (7) (1993) 1233–1238.

[224] Y. Sugimura, P. Lim, C. Shih, S. Suresh, Fracture normal to a bimaterial interface: effects of plasticity on crack-tip shielding and amplification, Acta Metallurgica et Materialia 43 (3) (1995) 1157–1169.

[225] Z. Z. Fang, Sintering of advanced materials, Elsevier, 2010.

[226] R. M. Hazen, The diamond makers, Cambridge University Press, 1999.

[227] V. R. Coffman, J. P. Sethna, Grain boundary energies and cohesive strength as a function of geometry, Physical review B 77 (14) (2008) 144111.

[228] H. Beladi, G. S. Rohrer, The relative grain boundary area and energy distributions in a ferritic steel determined from three-dimensional electron backscatter diffraction maps, Acta materialia 61 (4) (2013) 1404–1412.

[229] P. Lejcek, Grain boundary segregation in metals, Vol. 136, Springer Science & Business Media, 2010.

[230] O. Shenderova, D. W. Brenner, Atomistic simulations of structures and mechanical properties of polycrystalline diamond: Symmetrical $< 001 >‹$ tilt grain boundaries, Physical Review B 60 (10) (1999) 7053.

[231] O. Shenderova, D. Brenner, A. Omeltchenko, X. Su, L. H. Yang, A. Nazarov, Multi-scale modeling of polycrystalline diamond, in: Technical Proceedings MSM, Citeseer, 1999, pp. 61–64.

[232] O. Shenderova, D. Brenner, A. Omeltchenko, X. Su, L. Yang, Atomistic modeling of the fracture of polycrystalline diamond, Physical Review B 61 (6) (2000) 3877.

[233] D. W. Brenner, O. A. Shenderova, Theory and modelling of diamond fracture from an atomic perspective, Philosophical Transactions of the Royal Society of London A: Mathematical, Physical and Engineering Sciences 373 (2038) (2015) 20140139.

[234] M. K. Keshavan, Y. Zhang, Y. Shen, A. Griffo, M. Janssen, Polycrystalline diamond materials having improved abrasion resistance, thermal stability and impact resistance., US Patent Application Publication US20130067827 A1 (13/676,070).

[235] E. 6, Effect of alloying wc-co binder with ni on sintering of diamond powders.

[236] P. Hohenberg", Inhomogeneous electron gas, Physical Review 136 (3B) (1964) B864–B871. doi:10.1103/PhysRev.136.B864.

[237] W. Kohn, L. J. Sham, Self-consistent equations including exchange and correlation effects, Physical review 140 (4A) (1965) A1133.

[238] R. Stowasser, R. Hoffmann, What do the kohn-sham orbitals and eigenvalues mean? what do the kohn-sham orbitals and eigenvalues mean?, Journal of the American Chemical Society 121 (14) (1999) 3414–3420. arXiv:http://pubs.acs.org/doi/pdf/10.1021/ja9826892, doi:10.1021/ja9826892.
URL http://pubs.acs.org/doi/abs/10.1021/ja9826892

[239] D. Chong, O. Gritsenko, E. Baerends, Interpretation of the kohn–sham orbital energies as approximate vertical ionization potentials, Journal of Chemical Physics 116 (5) (2002) 1760–1772.

[240] H. Doi, Y. Fujiwara, K. Miyake, Y. Oosawa, A systematic investigation of elastic moduli of wc-co alloys, Metallurgical and Materials Transactions 1 (5) (1970) 1417–1425.

[241] F. Riley, 2nd European Symposium on Engineering Ceramics, Springer Science & Business Media, 2012.

[242] D. Lloyd, Particle reinforced aluminium and magnesium matrix composites, International Materials Reviews 39 (1) (1994) 1–23.

[243] I. Ibrahim, F. Mohamed, E. Lavernia, Particulate reinforced metal matrix composites—a review, Journal of materials science 26 (5) (1991) 1137–1156.

[244] P. Descamps, J. Tirlocq, F. Cambier, Ceramic matrix composites: properties and applications, in: 3rd European Symposium on Engineering Ceramics, Springer, 1991, pp. 109–125.

[245] D. Nelson, Effects of residual stress on fatigue crack propagation, in: Residual stress effects in fatigue, ASTM International, 1982.

[246] J. LaRue, S. Daniewicz, Predicting the effect of residual stress on fatigue crack growth, International Journal of Fatigue 29 (3) (2007) 508–515.

[247] C. Liljedahl, J. Brouard, O. Zanellato, J. Lin, M. Tan, S. Ganguly, P. E. Irving, M. Fitzpatrick, X. Zhang, L. Edwards, Weld residual stress effects on fatigue crack growth behaviour of aluminium alloy 2024-t351, International Journal of Fatigue 31 (6) (2009) 1081–1088.

[248] N. Tutuncu, Stresses in thick-walled fgm cylinders with exponentially-varying properties, Engineering Structures 29 (9) (2007) 2032–2035.

[249] J. Selsing, Internal stresses in ceramics, Journal of the American Ceramic Society 44 (8) (1961) 419–419.

[250] T. Kanazawa, H. Oba, S. Machida, The effect of welding residual stress on brittle fracture propagation, Journal of Zosen Kiokai 1961 (109) (1961) 359–369.

[251] A. Evans, The role of inclusions in the fracture of ceramic materials, Journal of Materials Science 9 (7) (1974) 1145–1152.

[252] D. Marshall, A. Evans, M. Drory, Transformation toughening in ceramics, Fracture mechanics of ceramics 6 (1983) 289–307.

[253] S. Seo, D. Mishra, C. Park, S.-H. Yoo, Y. Pak, Energy release rates for a misfitted spherical inclusion under far-field mechanical and uniform thermal loads, European Journal of Mechanics-A/Solids 49 (2015) 169–182.

[254] F. Cverna, Thermal properties of metals, ASM International, Materials Park, OH.

[255] G. A. Slack, S. Bartram, Thermal expansion of some diamondlike crystals, Journal of Applied Physics 46 (1) (1975) 89–98.

[256] T.-P. Lin, M. Hood, G. A. Cooper, R. H. Smith, Residual stresses in polycrystalline diamond compacts, Journal of the American Ceramic Society 77 (6) (1994) 1562–1568.

[257] K. Bertagnolli, R. Vale, Understanding and controlling residual stresses in thick polycrystalline diamond cutters for enhanced durability, Finer Points(USA), 12 (1) (2000) 20.

[258] C. Feng, X. Gen, G.-p. Xu, et al., Thermal residual stress of polycrystalline diamond compacts, Transactions of Nonferrous Metals Society of China 20 (2) (2010) 227–232.

[259] B.-N. Kim, M. Watanabe, M. Enoki, T. Kishi, Simulation of crack propagation process in particle-dispersed composites, Materials Transactions, JIM 37 (3) (1996) 404–408.

[260] M.-O. Nandy, S. Schmauder, B.-N. Kim, M. Watanabe, T. Kishi, Simulation of crack propagation in alumina particle-dispersed sic composites, Journal of the European Ceramic Society 19 (3) (1999) 329–334.

[261] R. Davidge, T. J. Green, The strength of two-phase ceramic/glass materials, Journal of Materials Science 3 (6) (1968) 629–634.

[262] Z. Li, H. Jia, H. Ma, W. Guo, X. Liu, G. Huang, R. Li, X. Jia, Fem analysis on the effect of cobalt content on thermal residual stress in polycrystalline diamond compact (pdc), Science China Physics, Mechanics and Astronomy 55 (4) (2012) 639–643.

[263] M. Taya, S. Hayashi, A. S. Kobayashi, H. Yoon, Toughening of a particulate-reinforced ceramic-matrix composite by thermal residual stress, Journal of the American Ceramic Society 73 (5) (1990) 1382–1391.

[264] G. Wei, P. Becher, Improvements in mechanical properties in sic by the addition of tic particles, Journal of the American Ceramic Society 67 (8) (1984) 571–574.

[265] X. Boland, J.N.; Li, Microstructural characterisation and wear behaviour of diamond composite materials, Materials 3 (2010) 1390–1419.

[266] T. U. of Sheffield, U. WebElements Ltd, http://www.webelements.com (2012).

[267] D. Bernstein, N Hess, Lattice trapping barriers to brittle fracture, Phys. Rev. Lett. 91.

[268] S. Huang, S. Zhang, T. Belytschko, S. S. Terdalkar, T. Zhu, Mechanics of nanocrack: Fracture, dislocation emission, and amorphization, Journal of the Mechanics and Physics of Solids 57 (2009) 840–850. doi:DOI10.1016/j.jmps.2009.01.006.

[269] J. R. Kermode, T. Albaret, D. Sherman, N. Bernstein, P. Gumbsch, M. C. Payne, G. Csnyi, A. De Vita, Low-speed fracture instabilities in a brittle crystal, Nature 455.

[270] R. Thomson, C. Hsieh, V. Rana, Lattice trapping of fracture cracks, Journal of Applied Physics 42 (1971) 3154–3160.

[271] M. J. Buehler, H. Tang, A. C. van Duin, W. A. Goddard III, Threshold crack speed controls dynamical fracture of silicon single crystals, Physical Review Letters 99 (2007) 165502. doi:DOI10.1103/PhysRevLett.99.165502.

[272] T.-S. Jun, Z. Zhang, G. Sernicola, F. P. Dunne, T. B. Britton, Local strain rate sensitivity of single α phase within a dual-phase ti alloy, Acta Materialia 107 (2016) 298–309.

[273] Brenner, Empirical potential for hydrocarbons for use in simulating the chemical vapor deposition of diamond films, Phys Rev B Condens Matter 42 (15) (1990) 9458–9471.

[274] D. W. Brenner, O. A. Shenderova, J. A. Harrison, S. J. Stuart, B. Ni, S. B. Sinnott, A second-generation reactive empirical bond order (rebo) potential energy expression for hydrocarbons, Journal of Physics-Condensed Matter 14 (2002) 783–802.

[275] L. Pastewka, M. Mrovec, M. Moseler, P. Gumbsch, Bond order potentials for fracture, wear, and plasticity, MRS Bulletin 37 (2012.94) (2012) 493–503.

[276] L. Pastewka, A. Klemenz, P. Gumbsch, M. Moseler, Screened empirical bond-order potentials for si-c, PhysRevB 87 (205410).

[277] L. Pastewka, P. Pou, R. Prez, P. Gumbsch, M. Moseler, Describing bond-breaking processes by reactive potentials: Importance of an environment-dependent interaction range, Phys. Rev. B 78 (2008) 161402.

[278] L. Pastewka, S. Moser, P. Gumbsch, M. Moseler, Anisotropic mechanical amorphization drives wear in diamond, Nat Mater 10 (1) (2011) 34–8. doi:10.1038/nmat2902.

[279] J. Fineberg, Tribology: Diamonds are forever - or are they?, Nat Mater 10 (1) (2011) 3–4. doi:10.1038/nmat2926.

[280] Tersoff, Modeling solid-state chemistry: Interatomic potentials for multicomponent systems, Phys Rev B Condens Matter 39 (8) (1989) 5566–5568.

[281] L. Pastewka, Atomistica package (2014).

[282] S. Plimpton, Fast parallel algorithms for short-range molecular-dynamics, Journal of Computational Physics 117 (1995) 1–19.
URL LAMMPSWWWSite

Appendix A

Conformal Mapping And Branch Points

When both inclusion and the matrix material were the same, the results were such that no trace of inclusion was found in the fields of matrix material. Despite discontinuity at branch points and the branch cut errors given in figure A.1 are machine sized errors. Figure A.2 showes stress and displacement field distributions throughout the system for the case where matrix material and inclusions are different. Stress fields inside the inclusion are not thoroughly accurate and they become reliable far away from the branch points.

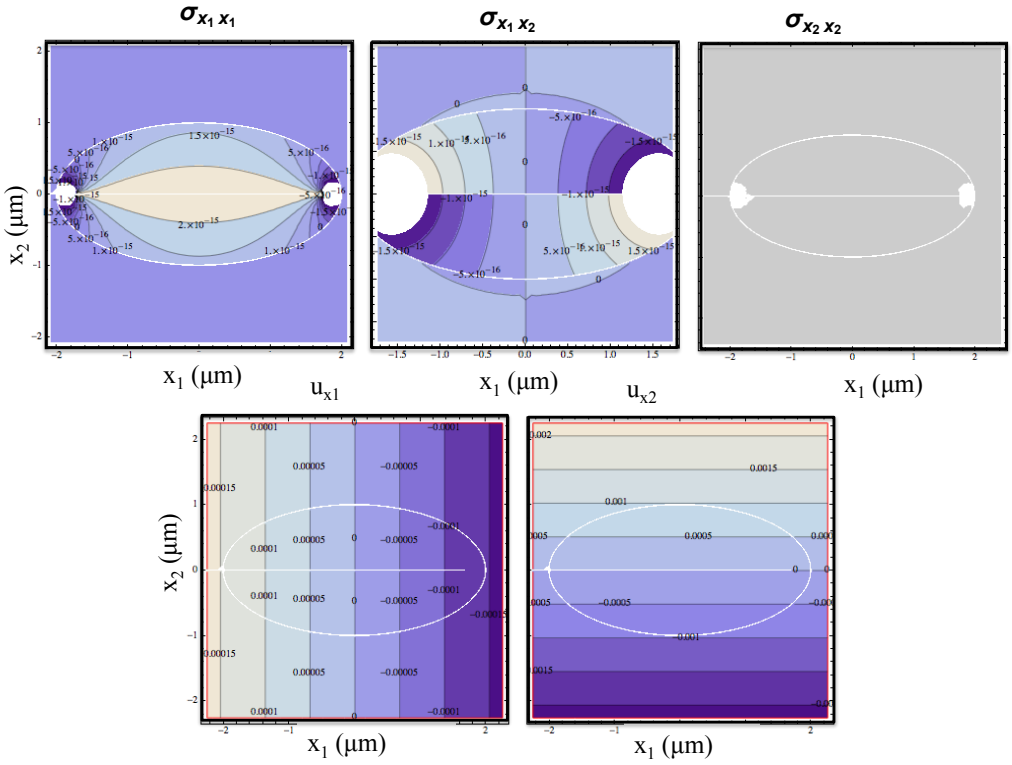


Fig. A.1 Mode I stress fields and displacement fields of elliptic inclusion with aspect ratio $l_2/l_1 = 1/2$. Matrix material and inclusion have the same material.

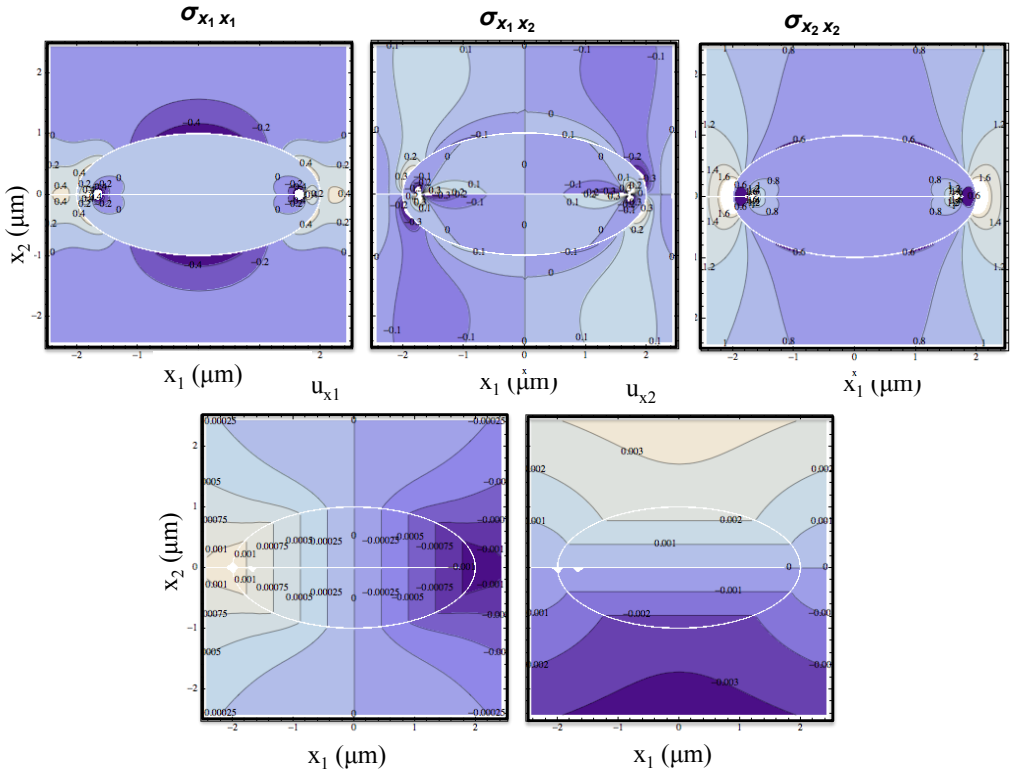


Fig. A.2 Mode I stress fields and displacement fields of elliptic inclusion with aspect ratio $l_2/l_1 = 1/2$. Matrix material and inclusion are selected with mechanical properties $\mu_0 = 478$ GPa and $\nu_0 = 0.07$, and $\mu_1 = 75$ GPa and $\nu_1 = 0.31$ respectively.

Appendix B

Finite Array Of Inclusion; Expansion Coefficient

B.1 Introduction

This section is concluded with three parts dealing with a derivation of the a_{npq}, and b_{npq}, and associated coefficients of the uniform far-field load. While this section is of considerable mathematical interest, it is not central to study crack/inclusion interactions in earlier sections. The reader may pass directly to Section B.1.1 at this time and refer back when necessary. Before addressing the main derivation of the coefficients, some lemmas are introduced and proved.

B.1.0.1 Lemma 1

$$\begin{aligned} \varphi_p^{s\prime} &= \frac{\partial \varphi_p^s}{\partial y_p} \\ &= \frac{\partial(\varphi_{pq}^r)}{\partial y_p} e^{i\theta_{pq}} = \frac{\partial(\varphi_{pq}^r)}{\partial y_q} \frac{\partial y_q}{\partial y_p} e^{i\theta_{pq}} \end{aligned} \tag{B.1}$$

where $\frac{\partial y_q}{\partial y_p} = e^{-i\theta_{pq}}$, so

$$\boxed{\varphi_p^{s\prime} = \varphi_{pq}^{r\prime}.} \tag{B.2}$$

B.1.0.2 Lemma 2

$$\begin{aligned} z_q &= -Z_{pq} + z_p \\ y_q e^{i\theta_q} &= -Z_{pq} + y_p e^{i\theta_p} \end{aligned} \tag{B.3}$$

$$\boxed{y_q = -Z_{pq}e^{-i\theta_q} + y_p e^{-i\theta_{pq}}} \tag{B.4}$$

B.1.0.3 Lemma 3

In the first step, the formula $(v_p + \frac{1}{v_p})\frac{\partial v_p^{-n}}{\partial z_p}$ has to be determined, where $y_p = \frac{D_p}{2}(v_p + \frac{1}{v_p})$ and $v_p = \exp\xi_p$.

$$\begin{aligned}(v_p + \frac{1}{v_p})\frac{\partial v_p^{-n}}{\partial z_p} &= \frac{\partial v_p^{-n+1}}{\partial z_p} + \frac{\partial v_p^{-n-1}}{\partial z_p} - \frac{2}{d_p}v_p^{-n} \\ &= \sum_{m\pm}(\mu^{pq}_{n-1,m} + \mu^{pq}_{n+1,m})v_q^{-m} - \frac{2}{d_p}v_p^{-n}\end{aligned} \tag{B.5}$$

then,

$$\begin{aligned}y_p\varphi_p^{s\prime} &= z_p e^{-i\theta_p}\frac{\partial}{\partial y_p}\varphi_p^s = z_p e^{-i\theta_p}\frac{\partial\varphi_p^s}{\partial z_p}\frac{\partial z_p}{\partial y_p} = z_p\frac{\partial\varphi_p^s}{\partial z_p} \\ &= \frac{d_p}{2}(v_p + \frac{1}{v_p})\sum_{n=1}^{\infty}A_{np}\frac{\partial v_p^{-n}}{\partial z_p} \\ &= \frac{d_p}{2}\sum_{n=1}^{\infty}A_{np}\sum_{m\pm}(\mu^{pq}_{n-1,m} + \mu^{pq}_{n+1,m})v_q^{-m} - \sum_{n=1}^{\infty}A_{np}\sum_{m\pm}\eta^{pq}_{n,m}v_q^{-m}\end{aligned} \tag{B.6}$$

Thus,

$$\boxed{y_p\varphi_p^{s\prime} = \sum_{m\pm}\left\{\sum_{n=1}^{\infty}A_{np}\left[\left(\mu^{pq}_{n-1,m} + \mu^{pq}_{n+1,m}\right)\frac{d_p}{2} - \eta^{pq}_{n,m}\right]\right\}v_q^{-m}} \tag{B.7}$$

B.1.0.4 Lemma 4

$$\boxed{\varphi_p^{s\prime} = e^{i\theta_p}\sum_{n=1}^{\infty}A_{np}\frac{\partial v_p^{-n}}{\partial z_p} = e^{i\theta_p}\sum_{m\pm}\left(\sum_{n=1}^{\infty}A_{np}\mu^{pq}_{n,m}\right)v_q^{-m}} \tag{B.8}$$

B.1.0.5 Lemma 5

$$\frac{v_p^{-n-1}}{\sinh\xi_p} = 2\frac{v_p^{-n-1}}{v_p - \frac{1}{v_p}} \tag{B.9}$$

$$\frac{\partial v_p^{-n}}{\partial z_p} = -\frac{2n}{d_p}\frac{v_p^{-n}}{v_p - \frac{1}{v_p}} \tag{B.10}$$

$$\frac{v_p^{-n}}{v_p - \frac{1}{v_p}} = -\frac{d_p}{2n}\frac{\partial v_p^{-n}}{\partial z_p} = -\frac{d_p}{2n}\sum_{m\pm}\mu_{n,m}^{pq} v_q^{-m} \tag{B.11}$$

So,

$$\boxed{\frac{v_p^{-n-1}}{\sinh\xi_p} = -\frac{d_p}{n+1}\sum_{m\pm}\mu_{n+1,m}^{pq} v_q^{-m}} \tag{B.12}$$

B.1.0.6 Lemma 6

$$\sum_{m\pm} m\frac{v_q^{-m-1}}{\sinh\xi_q} a_{mpq} = 2\sum_{m\geqslant 1} m a_{mpq}\frac{v_q^{-m-1} - v_q^{m+1}}{v_q - \frac{1}{v_q}} = 2\sum_{m\geqslant 1}\frac{m}{v_q} a_{mpq}\frac{v_q^{-m} - v_q^{m}}{v_q - \frac{1}{v_q}} \tag{B.13}$$

Thus,

$$\boxed{a_{mpq} = a_{-mpq}} \tag{B.14}$$

B.1.0.7 Lemma 7

$$\begin{aligned}
&\sum_{m\pm} m\, a_{mpq}\frac{\sinh\zeta_{0q}}{\sinh\xi_q}\left(\frac{v_q}{v_{0q}} - \frac{v_{0q}}{v_q}\right) v_q^{-m} \\
&= \sum_{m\pm} m\, a_{mpq}\left[\left(1 - v_{0q}^{-2}\right) v_q^{-m} - \frac{1}{2}(v_{0q} - \frac{1}{v_{0q}})^2\frac{v_q^{-m-1}}{\sinh\xi_q}\right]
\end{aligned} \tag{B.15}$$

The second term can be written as:

$$\begin{aligned}
&-\frac{1}{2}(v_{0q} - \frac{1}{v_{0q}})^2\sum_{m\pm} m\, a_{mpq}\frac{v_q^{-m-1}}{\sinh\xi_q} \\
&= -(v_{0q} - \frac{1}{v_{0q}})^2\sum_{m>0} a_{mpq}\frac{m}{v_q}\frac{v_q^{-m} - v_q^{m}}{v_q - \frac{1}{v_q}} \\
&= -(v_{0q} - \frac{1}{v_{0q}})^2\sum_{m>0}\sum_{k=0}^{m-1} a_{mpq} m\, v_q^{2k-m} \\
&= -(v_{0q} - \frac{1}{v_{0q}})^2\sum_{m\pm}\sum_{k=0}^{\infty} |2k+m|\, a_{|2k+m|pq} m\, v_q^{-m}
\end{aligned} \tag{B.16}$$

Using Formula B.23, we have:

$$\begin{aligned}
&-\frac{1}{2}(v_{0q}-\frac{1}{v_{0q}})^2\sum_{m\pm} m\, a_{mpq}\frac{v_q^{-m-1}}{\sinh\xi_q} \\
&=-(v_{0q}-\frac{1}{v_{0q}})^2\sum_{m\pm}\sum_{n\geqslant 1}\sum_{k=0}^{\infty}|2k+m|A_{np}e^{-i\theta_{pq}}\eta^{pq}_{n,|2k+m|}\, v_q^{-m}
\end{aligned} \tag{B.17}$$

Thus, Equation B.15 becomes:

$$\boxed{\begin{aligned}
&\sum_{m\pm} m\, a_{mpq}\frac{\sinh\zeta_{0q}}{\sinh\xi_q}\left(\frac{v_q}{v_{0q}}-\frac{v_{0q}}{v_q}\right)v_q^{-m} \\
&=\sum_{m\pm}\sum_{n=1}^{\infty}\left\{ m\, A_{np}e^{-i\theta_{pq}}\eta^{pq}_{nm}\left(1-v_{0q}^{-2}\right)\right. \\
&\left.-(v_{0q}-\frac{1}{v_{0q}})^2\sum_{k=0}^{\infty}|2k+m|A_{np}e^{-i\theta_{pq}}\eta^{pq}_{n,|2k+m|}\right\}v_q^{-m}
\end{aligned}} \tag{B.18}$$

B.1.1 Expansion Coefficients: a_{npq}

The singular disturbance field induced by the pth inclusion u_p^s ($\lim_{|z|\to\infty}|u_p^s|=0$) can be expanded to the regular field in the qth coordinate system. The transformation from the y local coordinate system requires a rotational transformation of the coordinate systems.

$$\begin{aligned}
u_p^s(z_p) &= u_{pq}^r(z_q) \\
u_p^s(y_p)e^{i\theta_p} &= u_{pq}^r(y_q)e^{i\theta_q}
\end{aligned} \tag{B.19}$$

Both $u_p^s(y_p)$ and $u_{pq}^r(y_q)$ are written in terms of complex potentials 3.8 format:

$$\begin{aligned}
u_p^s(y_p) &= \kappa\varphi_p^s(y_p)-(y_p-\bar{y_p})\overline{\varphi_p^{s\prime}(y_p)}-\overline{\psi_p^s(y_p)} \\
u_{pq}^r(y_q) &= \kappa\varphi_{pq}^r(y_q)-(y_q-\bar{y_q})\overline{\varphi_{pq}^{r\prime}(y_q)}-\overline{\psi_{pq}^r(y_q)}
\end{aligned} \tag{B.20}$$

where $\varphi_{pq}^{r\prime}(y_q)=\frac{\partial\varphi_{pq}^r}{\partial y_q}$ and $\varphi_p^{s\prime}(y_p)=\frac{\partial\varphi_p^s}{\partial y_p}$. By equating similar terms in $u_p^s(z_p)$ and $u_{pq}^r(z_q)$, the coefficients a_{mpq} and b_{mpq} can be derived. By applying Equation B.20 to φ_p^s, we obtain

$$\varphi_p^s(y_p)=\varphi_{pq}^r(y_p)e^{i\theta_{pq}} \tag{B.21}$$

$$\begin{aligned}\sum_{m=1}^{\infty} A_{mp} e^{-i\theta_{pq}} v_p^{-m} &= \sum_{n=-\infty}^{\infty} a_{npq} v_q^{-n} \\ \sum_{m=1}^{\infty} A_{mp} e^{-i\theta_{pq}} \left\{ \sum_{n\geqslant 1} \eta_{mn}^{pq} v_q^{-n} \right\} &= \sum_{n=-\infty}^{\infty} a_{npq} v_q^{-n}\end{aligned} \tag{B.22}$$

from where,

$$\boxed{a_{npq} = \sum_{m=1}^{\infty} A_{mp} e^{-i\theta_{pq}} \eta_{mn}^{pq}.} \tag{B.23}$$

B.1.2 Expansion Coefficients: b_{npq}

Determination of b_{npq} is somewhat more complicated sand requires to equate the second term in Equation B.20 as:

$$\left((\overline{y_p} - y_p)\overline{\varphi_p^{s\prime}} - \overline{\psi_p^s}\right) e^{-i\theta_{pq}} = (\overline{y_q} - y_q)\overline{\varphi_{pq}^{r\prime}} - \overline{\psi_{pq}^r}. \tag{B.24}$$

By substituting y_q, and $\overline{y_q}$ from B.4 into B.24 and using Lemma B.2, $\overline{\psi_{pq}^r}$ is derived as:

$$\overline{\psi_{pq}^r} = (-\overline{Z_{pq}} e^{i\theta_q} + Z_{pq} e^{-i\theta_q})\overline{\varphi_p^{s\prime}} + \overline{y_p}(e^{i\theta_{pq}} - e^{-i\theta_{pq}})\overline{\varphi_p^{s\prime}} + \overline{\psi_p^s} e^{-i\theta_{pq}} \tag{B.25}$$

and then $\psi_{pq}^{r\prime}$ is determined by finding the conjugate of the function.

$$\psi_{pq}^r = (-Z_{pq} e^{-i\theta_q} + \overline{Z_{pq}} e^{i\theta_q})\varphi_p^{s\prime} + y_p(e^{-i\theta_{pq}} - e^{i\theta_{pq}})\varphi_p^{s\prime} + \psi_p^s e^{i\theta_{pq}} \tag{B.26}$$

Using Lemmas B.7, and B.8, ψ_{pq}^r is re-written as:

$$\begin{aligned}\psi_{pq}^r = \sum_{m\pm} \Bigg\{ &\sum_{n=1}^{\infty} e^{i\theta_p} A_{np} \mu_{n,m}^{pq} (-Z_{pq} e^{-i\theta_q} + \overline{Z_{pq}} e^{i\theta_q}) \\ &+ \sum_{n=1}^{\infty} A_{np} \left[(\mu_{n-1,m}^{pq} + \mu_{n+1,m}^{pq}) \frac{d_p}{2} - \eta_{n,m}^{pq} \right] (e^{-i\theta_{pq}} - e^{i\theta_{pq}}) \Bigg\} v_q^{-m} + \psi_p^s e^{i\theta_{pq}}\end{aligned} \tag{B.27}$$

Here, ψ_p^s is presented using the formula derived by Kushch [140] where,

$$\psi_p^s = \sum_{m\pm} \left\{ \sum_{n=1}^{\infty} \left[B_{np} \eta_{n,m}^{pq} - n A_{np} (1 - v_{0p}^{-2}) \eta_{n,m}^{pq} - \frac{d_p}{2} (v_{0p} - \frac{1}{v_{0p}})^2 \frac{n A_{np}}{n+1} \mu_{n+1,m}^{pq} \right] \right\} v_q^{-m} \tag{B.28}$$

Substituting Equation B.28 into B.27 results into ψ_{pq}^r as:

$$\begin{aligned}\psi^r_{pq} = \sum_{m\pm}\sum_{n=1}^{\infty}\Bigg\{\mathbf{A_{np}}\Bigg\{e^{i\theta_p}\mu^{pq}_{n,m}(-Z_{pq}e^{-i\theta_q}+\overline{Z_{pq}}e^{i\theta_q})\\ +\left[(\mu^{pq}_{n-1,m}+\mu^{pq}_{n+1,m})\frac{d_p}{2}-\eta^{pq}_{n,m}\right](e^{-i\theta_{pq}}-e^{i\theta_{pq}})\\ -ne^{i\theta_{pq}}(1-v_{0p}^{-2})\eta^{pq}_{n,m}-\frac{d_p}{2}(v_{0p}-\frac{1}{v_{0p}})^2e^{i\theta_{pq}}\frac{n}{n+1}\mu^{pq}_{n+1,m}\Bigg\}\\ +\mathbf{B_{np}}e^{i\theta_{pq}}\eta^{pq}_{n,m}\Bigg\}v_q^{-m}\end{aligned} \tag{B.29}$$

On the other hand, complex potential $\psi^r_{pq}(y_q)$ is defined (Equation: **??**) as :

$$\psi^r_{pq}(y_q) = \sum_{m\pm}\left[b_{mpq} - ma_{mpq}\frac{\sinh\zeta_{0q}}{\sinh\xi_q}\left(\frac{v_q}{v_{0q}}-\frac{v_{0q}}{v_q}\right)\right]v_q^{-m} \tag{B.30}$$

Using Lemma B.18, $\psi^r_{pq}(y_q)$ becomes:

$$\begin{aligned}\psi^r_{pq}(y_q) = \sum_{m\pm}\Bigg\{b_{mpq} - \sum_{n=1}^{\infty}\Bigg\{m\,A_{np}e^{-i\theta_{pq}}\eta^{pq}_{nm}(1-v_{0q}^{-2})\\ -\left(v_{0q}-\frac{1}{v_{0q}}\right)^2\sum_{k=0}^{\infty}|2k+m|A_{np}e^{-i\theta_{pq}}\eta^{pq}_{n,|2k+m|}\Bigg\}\Bigg\}v_q^{-m}\end{aligned} \tag{B.31}$$

By equating Equations B.31 and B.29, coefficients b_{npq}s are derived for ($n > 0$) as follow:

$$
\begin{aligned}
b_{npq} &= \sum_{n=1}^{\infty} B_{mp} e^{-i\theta_{pq}} \eta_{mn}^{pq} \\
&= \sum_{n=1}^{\infty} A_{mp} \Bigg\{ \left[n e^{-i\theta_{pq}} (1 - v_{0q}^{-2}) - m e^{i\theta_{pq}} (1 - v_{0p}^{-2}) \right] \eta_{mn}^{pq} \\
&\quad - \frac{d_p}{2} \frac{m}{m+1} \left(v_{0p} - \frac{1}{v_{0p}} \right)^2 \mu_{m+1,n}^{pq} \\
&\quad + \left(v_{0q} - \frac{1}{v_{0q}} \right)^2 \sum_{k=0}^{\infty} |2k+n| \eta_{m,|2k+n|}^{pq} \\
&\quad + \left(\overline{z_{pq}} e^{i\theta_q} - z_{pq} e^{-i\theta_q} \right) e^{i\theta_p} \mu_{m,n}^{pq} \\
&\quad + \left[(\mu_{m-1,n}^{pq} + \mu_{m+1,n}^{pq}) \frac{d_p}{2} - \eta_{mn}^{pq} \right] (e^{-i\theta_{pq}} - e^{i\theta_{pq}}) \Bigg\}
\end{aligned}
\tag{B.32}
$$

For $(n < 0)$, we can either use

$$
\begin{aligned}
b_{npq} &= \sum_{n=1}^{\infty} B_{mp} e^{-i\theta_{pq}} \eta_{mn}^{pq} \\
&= \sum_{n=1}^{\infty} A_{mp} \Bigg\{ \left[n e^{-i\theta_{pq}} (1 - v_{0q}^{-2}) - m e^{i\theta_{pq}} (1 - v_{0p}^{-2}) \right] \eta_{mn}^{pq} \\
&\quad - \frac{d_p}{2} \frac{m}{m+1} \left(v_{0p} - \frac{1}{v_{0p}} \right)^2 \mu_{m+1,n}^{pq} \\
&\quad + \left(v_{0q} - \frac{1}{v_{0q}} \right)^2 \sum_{k=\mathbf{1}}^{\infty} |2k+n| \eta_{m,|2k+n|}^{pq} \\
&\quad + \left(\overline{z_{pq}} e^{i\theta_q} - z_{pq} e^{-i\theta_q} \right) e^{i\theta_p} \mu_{m,n}^{pq} \\
&\quad + \left[(\mu_{m-1,n}^{pq} + \mu_{m+1,n}^{pq}) \frac{d_p}{2} - \eta_{mn}^{pq} \right] (e^{-i\theta_{pq}} - e^{i\theta_{pq}}) \Bigg\}
\end{aligned}
\tag{B.33}
$$

or use the equation below, where the $(n > 0)$.

$$
b_{-npq} = b_{npq} - 2a_{npq} |n| \sinh 2\xi_{0q} \tag{B.34}
$$

B.1.3 Expansion Coefficient Of Uniform Far-Field Load

Complex potentials for uniform far-field loading have to be selected as a linear function of z due to constraints imposed by the displacement and traction in the complex potential form

(Equations 3.13, and 3.14). Potentials are chosen as:

$$\varphi_0 = \Gamma_1 z; \qquad \psi_0 = \Gamma_2 z \tag{B.35}$$

Here, u_{0q}, and u_{00q} are displacement fields caused by the far-field loading in the global (z) coordinate, and in the local y_q coordinate systems respectively. By substituting φ_0, and ψ_0 into u_{0q} and using formulas $z = Z_q + z_q$, and $z_q = y_q e^{i\theta_q}$, u_{0q} is derived in terms of u_{00q}.

$$\begin{aligned} u_{0q}(z) &= \kappa\varphi_0(z) - (z-\bar{z})\overline{\varphi_0'(z)} - \overline{\psi_0(z)} \\ &= \kappa\Gamma_1 z - (z-\bar{z})\overline{\Gamma_1} - \overline{\Gamma_2 z} \\ &= \left(\kappa\Gamma_1 Z_q - (Z_q - \overline{Z_q})\overline{\Gamma_1} - \overline{\Gamma_2 Z_q}\right) + \left(\kappa\Gamma_1 z_q - (z_q - \overline{z_q})\overline{\Gamma_1} - \overline{\Gamma_2 z_q}\right) \\ &= u_{00q}(Z_q) + u_{01q}(z_q) \end{aligned} \tag{B.36}$$

As far-field load is a regular field at infinity, complex potentials should obey

$$\begin{aligned} \varphi^r_{0q}(y_q) &= \sum_{m\pm} a_{m0q} v_q^{-m} \\ \psi^r_{0q}(y_q) &= \sum_{m\pm} \left[b_{m0q} - m a_{m0q} \frac{\sinh\zeta_{0q}}{\sinh\xi_q} \left(\frac{v_q}{v_{0q}} - \frac{v_{0q}}{v_q} \right) \right] v_q^{-m} \end{aligned} \tag{B.37}$$

where 0 denotes the far-field load. Using formula $a_{mpq} = a_{-mpq}$, and $b_{mpq} = b_{-mpq} + 2m a_{mpq} \sinh 2\zeta_{0q}$, complex potentials are derived as:

$$\begin{aligned} \varphi^r_{0q}(y_q) &= a_{00q} + a_{10q}(v_q^{-1} + v_q) \\ \psi^r_{0q}(y_q) &= b_{00q} + \frac{2z_q}{d_q} \left[b_{-10q} + a_{10q} \left(1 - \frac{1}{v_{0q}^2} \right) \right] \end{aligned} \tag{B.38}$$

Using the the $u_{0q}(z) = e^{i\theta_q} u_q(y_q)$ relation between displacements in coordinate systems z, and y_q, complex potentials in the y_q coordinate are predicted. Displacements are calculated by:

$$u_{0q}(z) = u_{00q}(Z_q) + \left(\kappa\Gamma_1 z_q - (z_q - \overline{z_q})\overline{\Gamma_1} - \overline{\Gamma_2 z_q}\right) \tag{B.39}$$

$$u_q(y_q) = \kappa\varphi^r_{0q}(y_q) - (y_q - \bar{y_q})\overline{\varphi^{r\,\prime}_{0q}(y_q)} - \overline{\psi^r_{0q}(y_q)} \tag{B.40}$$

Displacement u_q contains two parts, a constant term and a linear function of coordinate.

$$u_q(y_q) = \left(\kappa\varphi_{00} - (y_q - \bar{y_q})\overline{\varphi'_{00}} - \overline{\psi_{00}}\right) + \left(\kappa\varphi_{01}(y_q) - (y_q - \bar{y_q})\overline{\varphi'_{01}(y_q)} - \overline{\psi_{01}(y_q)}\right) \tag{B.41}$$

Using formulas B.38, and B.39, expansion coefficients are determined as follow:

$$u_{00q}(Z_q) = (\kappa a_{00q} - \overline{b_{00q}})e^{i\theta_q} = \kappa\Gamma_1 Z_q - (Z_q - \overline{Z_q})\overline{\Gamma_1} - \overline{\Gamma_2}\overline{Z_q} \tag{B.42}$$

$$\varphi_{01} = e^{-i\theta_q}\Gamma_1 z_q = \frac{2a_{10q}}{d_q} z_q \tag{B.43}$$

Hence,

$$\boxed{a_{10q} = a_{-10q} = \frac{D_q\Gamma_1}{2}.} \tag{B.44}$$

Determination of b_{10q} is somehow involved. All remaining terms in Equations B.39, and B.41 are equated. Thus,

$$\psi_{01}(y_q)e^{i\theta_q} = z_q(\Gamma_2 - \Gamma_1) + z_q e^{-2i\theta_q}\Gamma_1 \tag{B.45}$$

Substituting $\psi_{01}(y_q)$ to the formula using Equation B.38 results the expansion coefficient of unifor far-field as:

$$\boxed{b_{-10q} = \frac{e^{2i\theta_q}D_q}{2}(\Gamma_2 - \Gamma_1) + \frac{a_{10q}}{v_{0q}^2}.} \tag{B.46}$$

In the case of far stress tensor $\mathbf{S} = s_{ij}$, Γ_1, and Γ_2 are:

$$\begin{aligned} \Gamma_1 &= \frac{s_{11} + s_{22}}{8\mu} \\ \Gamma_2 &= \Gamma_1 + \frac{s_{22} - s_{11} + 2is_{12}}{4\mu} \end{aligned} \tag{B.47}$$

Appendix C

Minimum Distance From A Point To An Ellipse

Point $\mathbf{P} = (y_{11}, y_{21})$, demonstrated in Figure C.1, is a point outside an ellipse that is centred at the origin of the local y_q coordinate system, the ellipse equation is:

$$\frac{y_{1q}^2}{D_q^2 \cosh^2 \zeta_{0q}} + \frac{y_{2q}^2}{D_q^2 \sinh^2 \zeta_{0q}} = 1 \tag{C.1}$$

Any point on the surface of the ellipse is given by parameterisation $\mathbf{x} = (y_{1q}, y_{2q})$, where

$$(y_{1q}, y_{2q}) = (D_q \cosh \zeta_{0q} \cos \eta_q, D_q \sinh \zeta_{0q} \sin \eta_q) \tag{C.2}$$

and $\eta \in [0, 2\pi]$. Any square distance from any arbitrary point $\mathbf{P}$ to any point $\mathbf{y} = (y_{1q}, y_{2q})$ on the ellipse perimeter is

$$F(\eta_q) = |\mathbf{y} - \mathbf{P}|^2 \tag{C.3}$$

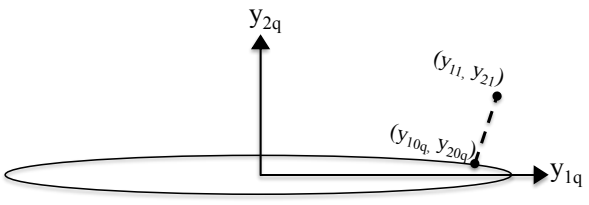


Fig. C.1 Minimum distance from point $\mathbf{P} = (y_{11}, y_{21})$ to an ellipse in the local y_q coordinate system.

A global minimum of the function gives the minimum path and obeys the analytical formula

$$F'(\eta_q) = 2(\mathbf{y} - \mathbf{P}).\mathbf{y}' = 0 \tag{C.4}$$

This formula is equivalent to the $((y_{1q} - y_{11}), (y_{2q} - y_{21})).(y'_{1q}, y'_{2q}) = 0$ or to the $(y_{1q} - y_{11})y'_{1q} + (y_{2q} - y_{21})y'_{2q} = 0$. Now consider the problem where the point on the ellipse and the distance (Δ) from that are known. What is the **P** coordinate system? If the point on the perimeter of the ellipse is given by (y_{10q}, y_{20q}), where

$$\begin{aligned} y_{10q} &= D_q \cosh \zeta_{0q} \cos \eta_{0q} \\ y_{20q} &= D_q \sinh \zeta_{0q} \sin \eta_{0q} \end{aligned} \tag{C.5}$$

then, coordinate (y_{11}, y_{21}) for the distance Δ will be derived by solving two equations.

$$\begin{aligned} &(\cosh \zeta_{0q}^2 - \sinh \zeta_{0q}^2) D_q \cos \eta_{0q} \sin \eta_{0q} - y_{11} \cosh \zeta_{0q} \sin \eta_{0q} + y_{21} \sinh \zeta_{0q} \cos \eta_q = 0 \\ &(y_{11} - D_q \cosh \zeta_{0q} \cos \eta_{0q})^2 + (y_{21} - D_q \sinh \zeta_{0q} \sin \eta_{0q})^2 = \Delta^2 \end{aligned} \tag{C.6}$$

Also, to verify if the point **p** is situated outside the ellipse, the condition, $\frac{y_{11}^2}{D_q^2 \cosh^2 \zeta_{0q}} + \frac{y_{21}^2}{D_q^2 \sinh^2 \zeta_{0q}} > 1$ has to be fulfilled. In DCD method, both η_{0q} and ζ_{0q} are determined by employing the maximum tangential method on the surface of the q_{th} ellipse.

Appendix D

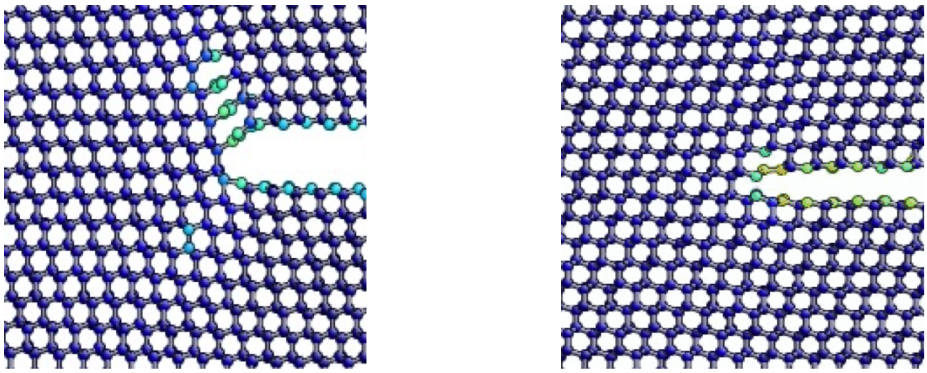
Notes On The Use Of Atomistic Simulations

The reliability of atomistic simulations depends on the use of appropriate interatomic forces and energies. A class of empirical band order potentials, Tersoff, reactive empirical bond order (REBO) [273], REBO2 [274], screened REBO2 (REBO2Scr) [275], and screened Tersoff bond order (TSCR) [275, 276] potentials, are being used for covalent materials including carbon.

Tersoff proposed an explicit expression for the bond order that was able to describe bonding in ambient and high-pressure phases of group IV elements. Brenner adapted the coefficient of Teresoff-style potential empirically to describe the covalent bonding interactions of carbon in a broad range of bonding environments [273]. He extended the potential to a second generation (REBO2) to provide the most accurate description of bond energies, lengths, and elastic properties [274].

Despite the numerous successes, the REBO2 potential has been known to fail under certain circumstances. The most significant failures occur when the bonds are significantly stretched beyond their equilibrium distances by external forces; for example, under large external loads or in the vicinity of the crack tip. Although in a brittle material such as diamond, crack propagation in the form of bond breaking is expected, preliminary simulations run using this potential have shown that the REBO2 potential predicts the crack to emit dislocations and blunting (Figure D.1 a).

This unphysical behaviour does not mean that the bond order approach fails conceptually. This failure simply originates from the applied fitting scheme that leads to two different problems. Computational expenses could be minimised by assuming that the bond integral and the repulsive potential are short ranged. The brittle behaviour can be restored by limiting the interactions to the first-nearest neighbour shell while allowing the bond lengths to vary



(a) (b)

Fig. D.1 (a) Unphysical behaviour at diamond crack tip using REBO2 potential, a crack in diamond blunts. (b) Bond braking in diamond using REBO2Scr potential.

smoothly over a longer range. According to an empirical screening function approach [277], two atoms interact as long as there is no third atom in the bonding area that screens the interaction. This system was transferred to Brenner's REBO2 to produce a screened second generation reactive empirical bond order (REBO2Scr) potential [275]. This new REBO2 potential corrects the fracture problem (see Figure D.1 b) [278, 279].

Although REBO2Scr potential improves the description of amorphous carbon (a-C) and hydrocarbon (a-C:H) phases as well as brittle fractures in diamond structure, it can not produce a correct order of surface energy for diamond crystallographic planes. Therefore, to produce a reliable simulation of crack propagation and (cracks) interaction in diamond material, another improved screened potential must be used.

The bond-order approach can be systematically derived from the tight-binding approximation [275], thus in principle, bond order potential must be transferable to a wide number of situations. It is also apparent that the screening function can be applied to different force fields to enlarge the interaction range similar to REBO2. The same approach with extra correction has been applied to the Teresoff potential [276].

Adaptations are implemented in the Tersoff's third-generation potential (TIIIScr) [280]. Since this approach is more rigorous compared to REBO2Scr potential, it is expected to better predict the physical behaviour of carbon structures. The most accurate molecular dynamic simulations of diamond can be performed using LAMMPS and ATOMISTICA packages [281, 282]. The most appropriate potential for diamond and carbon allotropes is implemented in the ATOMISTICA package and it is recommended that the use of these package is pursued in future research.